

Coherent Dynamics of Spinor Bose-Einstein Condensates

Dissertation
zur Erlangung des Doktorgrades
des Departments Physik
der Universität Hamburg

vorgelegt von
Jochen Kronjäger
aus Trier

Hamburg
2007

Gutachterin/Gutachter der Dissertation: Prof. Dr. Klaus Sengstock
Prof. Dr. Daniela Pfannkuche
Prof. Dr. G.V. Shlyapnikov

Gutachter der Disputation: Prof. Dr. Klaus Sengstock
Prof. Dr. Werner Neuhauser

Datum der Disputation: 26. Juni 2007

Vorsitzender des Prüfungsausschusses: Dr. Klaus Petermann

Vorsitzender des Promotionsausschusses: Prof. Dr. Günter Huber

Dekan der Fakultät für Mathematik,
Informatik und Naturwissenschaften: Prof. Dr. Arno Frühwald

Zusammenfassung

Seit der Realisierung von Bose-Einstein Kondensaten in Alkaligasen im Jahr 1995 haben diese sich zu vielseitigen Forschungsobjekten entwickelt. Ein besonders faszinierender Zweig sind Spinor-Kondensate in optischen Fallen, die die außergewöhnlichen Quantengas-Eigenschaften von Bose-Einstein Kondensaten auf den Spin als Freiheitsgrad ausdehnen. Spinor-Kondensate ermöglichen es, Magnetismus in Quantengasen zu erforschen, und verbinden so diese zwei ausgesprochen fruchtbaren Gebiete der Physik. Seit den ersten grundlegenden Experimenten 1998 ist das Gebiet erst in den letzten Jahren in bemerkenswerter Weise wieder aufgelebt. In diesem Zusammenhang leistet die vorliegende Arbeit einen bedeutenden Beitrag zum gegenwärtigen Verständnis der Physik der Spinor-Kondensate.

Die vorliegende Arbeit behandelt kohärente Dynamik in Spinor-Kondensaten und ihre Grenzen, Dekohärenz und Dämpfung. Aufbauend auf einer hochentwickelten Apparatur zur Erzeugung großer Spinor-Kondensate in einer optischen Falle, wurden experimentelle Methoden zur Präparation und Manipulation des Spinzustands sowie zur Kontrolle der Umgebungsparameter entwickelt und verfeinert. Neben den technischen Aspekten wurde insbesondere auch das Verständnis der Spindynamik, deren mathematische Beschreibung ebenso wie intuitive Vorstellungen, erheblich weiterentwickelt.

Als ein wichtiger Punkt wurde die Methode der Rabi- und Ramsey-Oszillationen mittels Anregung durch hochfrequente Magnetfelder auf Spin-1 und Spin-2 Systeme verallgemeinert. Angewendet auf Spinor-Kondensate ergeben sich daraus Rückschlüsse auf Dekohärenzmechanismen und deren Zeitskalen. Inhärente Spindynamik wurde anhand eines besonderen, vollständig transversal magnetisierten Anfangszustands untersucht, der robust in der Präparation ist und empfindlich auf Wechselwirkungseffekte reagiert.

Ein zentrales Ergebnis der vorliegenden Arbeit ist die erstmalige Beobachtung einer Spindynamik-Resonanz sowohl in ferro- als auch in antiferromagnetischen Kondensaten. Die Resonanz kann auf die Konkurrenz von quadratischem Zeeman-Effekt und spinabhängiger Wechselwirkung zurückgeführt werden; sie ist äquivalent zu nichtlinearer Phasen Anpassung bei optischem Vierwellmischen.

Weiterhin wurde gezeigt, dass die Einmoden-Näherung, obwohl sie jegliche räumliche Abhängigkeit des Spins vernachlässigt, die experimentellen Ergebnisse detailliert widerspiegelt. Ihre Gültigkeit ist jedoch durch Thermalisierung und räumliche Strukturbildung begrenzt, und beide Prozesse werden umfassend analysiert. Im Rahmen dieser Arbeit konnten erstmals auch analytische Lösungen der Spindynamik in Einmoden-Näherung gefunden werden.

Das besonders interessante Phänomen der räumlichen Strukturbildung wird anhand von Spin-2 Kondensaten in einer eindimensionalen optische Falle weiter untersucht. Die entstehenden beinahe regelmäßigen Spin-Muster sind ästhetisch faszinierend, und zerfallen in chaotische Strukturen. Als Ursachen der Strukturbildung werden spontane Musterbildung infolge einer dynamischen Instabilität sowie Rest-Inhomogenitäten im Magnetfeld diskutiert.

Der experimentelle Befund der Strukturbildung wird durch eine numerische Analyse der Einmoden-Spindynamik in Spin-2 Kondensaten ergänzt, die eindeutige Anzeichen für deterministisches Chaos in diesem nichtlinearen komplexen System ergibt.

Darüberhinaus werden in dieser Arbeit experimentelle Techniken vorgestellt, die in zukünftigen Untersuchungen zum Einsatz kommen werden. Ein Raman-Lasersystem ermöglicht die lokale Manipulation des Spinzustands eines ausgedehnten Kondensats, beispielsweise um Solitonen zu präparieren. Die Nutzung von räumlich inkohärentem Licht und kurzen Pulsen zur interferenzfreien Abbildung von Bose-Einstein Kondensaten wird diskutiert; alternativ oder ergänzend dazu besteht die Möglichkeit, Absorptionbilder rechnerisch zu verarbeiten, um Interferenzen zu eliminieren.

Das heute bedeutend weiter entwickelte Verständnis der Einmoden-Spindynamik, zu dem die vorliegende Arbeit einen wesentlichen Beitrag liefert, stellt eine gute Grundlage dar um die faszinierenden Fragen aktueller und zukünftiger Forschung an Spinor-kondensaten anzugehen.

Abstract

Since the realization of Bose-Einstein condensation in alkali gases in 1995, Bose-Einstein condensates (BEC) have developed into a versatile subject of research. A particularly intriguing variant, extending the extraordinary properties of BEC as quantum gases to the spin as a degree of freedom, are spinor BEC in optical traps. Spinor BEC allow the study of magnetism in quantum gases, merging these two fascinating branches of physics. After the pioneering experiments in 1998, the past few years have seen a remarkable burst of activity on the topic of spinor BEC. In this context, the present thesis constitutes a significant contribution to the current understanding of spinor BEC physics.

The present thesis deals with the coherent dynamics of spinor condensates, and with the mechanisms leading to decoherence and damping. Building on a highly optimized apparatus for the production of large spinor BEC in an optical trap, experimental methods used for the preparation and manipulation of the spin state and the control of environmental parameters had to be developed and sophisticated. Parallel to the experimental aspects, a better understanding of spinor BEC dynamics, including mathematical modeling and intuitive pictures, had to be developed.

The techniques of radio-frequency induced Rabi and Ramsey oscillations have been generalized to spin-1 and spin-2 systems and, applied to spinor BEC, provide insight into the mechanisms and time scales of decoherence. Inherent spin-mixing dynamics is studied using a particular initial state, a fully transversely magnetized state, which combines ease of preparation and sensitivity to interaction effects.

As a central result of this thesis, a fundamental resonance phenomenon in the spin-mixing dynamics of both ferromagnetic and anti-ferromagnetic spinor BEC is demonstrated for the first time. This resonance is a result of competition between the quadratic Zeeman effect and the spin-dependent interaction energy, and is analogous to nonlinear phase-matching in optical four-wave mixing.

The single-mode approximation (SMA), neglecting any spatial variations of the spin state, is shown to reproduce the experimentally observed population dynamics in great detail. However, its validity is limited by thermalization processes and spatial structure formation – both of these effects are analyzed in detail. In the context of the present thesis, analytical solutions of the SMA equations of spin dynamics could be obtained for the first time.

The particularly intriguing phenomenon of spatial structure formation is further studied with spin-2 BEC in a single-beam optical trap providing a 1D geometry. Beautiful, almost regular spin patterns are observed to emerge from a homogeneous initial state and to decay into chaos. Spontaneous pattern formation due to a dynamical instability as well as residual magnetic field gradients are discussed as the origin of the observed structure.

The experimental observation of structure formation is complemented by a numerical analysis of the single-mode dynamics of spin-2 BEC, uncovering clear evidence of deterministic chaos in this nonlinear complex system.

Moreover, the present work introduces experimental tools that will be useful for future studies. A Raman laser system allows to manipulate the spin state of a BEC locally, e.g. in order to prepare solitons. Using spatially incoherent light and short pulses is discussed as a way of avoiding interference fringes in absorption imaging of condensates. Alternatively or additionally, absorption images may be post-processed on a computer to eliminate fringes.

The greatly improved understanding of single-mode spinor dynamics, to which the work at hand has significantly contributed, provides a firm basis for tackling the intriguing questions raised by current and future research on spinor BEC.

Publikationen

Im Rahmen der vorliegenden Arbeit sind die folgenden wissenschaftlichen Veröffentlichungen entstanden.

Publications

The following research articles have been published in the course of this thesis.

- [1] J. Kronjäger, C. Becker, P. Navez, K. Bongs and K. Sengstock, *Magnetically tuned spin dynamics resonance*, Phys. Rev. Lett. **97** 110404 (2006)
- [2] J. Kronjäger, C. Becker, M. Brinkmann, R. Walser, P. Navez, K. Bongs and K. Sengstock. *Evolution of a spinor condensate: Coherent dynamics, dephasing, and revivals*, Phys. Rev. A **72**, 063619 (2005)
- [3] M. Erhard, H. Schmaljohann, J. Kronjäger, K. Bongs and K. Sengstock. *Bose-Einstein condensation at constant temperature*, Phys. Rev. A **70**, 031602(R) (2004)
- [4] M. Erhard, H. Schmaljohann, J. Kronjäger, K. Bongs and K. Sengstock. *Measurement of a mixed-spin-channel Feshbach resonance in ^{87}Rb* , Phys. Rev. A **69**, 032705 (2004)
- [5] H. Schmaljohann, M. Erhard, J. Kronjäger, K. Bongs and K. Sengstock. *Dynamics and thermodynamics in spinor quantum gases*, Appl. Phys. B **79**, 1001 (2004)
- [6] H. Schmaljohann, M. Erhard, J. Kronjäger, M. Kottke, S. van Staa, J. J. Arlt, K. Bongs and K. Sengstock. *Magnetism in ultracold quantum gases*, Journal of Modern Optics **51**, 1829 (2004)
- [7] H. Schmaljohann, M. Erhard, J. Kronjäger, M. Kottke, S. van Staa, L. Cacciapuoti, J. J. Arlt, K. Bongs and K. Sengstock. *Dynamics of $F = 2$ Spinor Bose-Einstein Condensates*, Phys. Rev. Lett. **92**, 040402 (2004)
- [8] H. Schmaljohann, M. Erhard, J. Kronjäger, M. Kottke, S. van Staa, J. J. Arlt, K. Bongs and K. Sengstock. *Spin Evolution in Ultracold Quantum Gases*, Laser Physics **14**, 1252 (2004)

Contents

1	Introduction	1
2	Spinor Bose-Einstein condensates (BEC)	5
2.1	Introduction to spinor Bose-Einstein condensates	5
2.2	Single atom spin-1 and spin-2 physics	6
2.2.1	Quantum mechanical description	6
2.2.2	Classical interpretation	14
2.2.3	Decoherence and damping	16
2.3	Interacting spinor Bose-Einstein condensates	19
2.3.1	Mean-field description	19
2.3.2	Single-mode approximation (SMA)	22
2.3.3	Ground states and phase separation	25
2.3.4	Coherent dynamics	27
2.3.5	The four-wave mixing picture	29
2.3.6	Beyond SMA	31
3	Experimental setup and characterization	35
3.1	Preparing ^{87}Rb BEC	35
3.2	Optical dipole trap	35
3.3	Detection	40
3.4	Magnetic field control	42
3.5	Spin state preparation	47
4	Additional experimental tools	52
4.1	Fringe reduction in absorption images	52
4.1.1	Interference fringes in absorption imaging	52
4.1.2	Post-processing: algorithmic fringe reduction	53
4.1.3	Random scattering: imaging with spatially incoherent light	57
4.1.4	Ultrashort pulses: absorption imaging in the Rabi regime	66
4.2	Raman laser system	68
4.2.1	State manipulation via Raman transitions	68
4.2.2	A phase-locked diode laser system	70
4.2.3	Characteristics of the Raman laser system	71
5	Spin dynamics of a transversely magnetized state	73
5.1	Why this initial state?	73
5.2	Probing coherence in the Zeeman regime ($F = 1$)	75
5.3	Effects of interaction in the Zeeman regime ($F = 1$)	79

5.4	Observation of the crossover resonance ($F = 2$)	85
5.5	Thermalization effects ($F = 1$)	86
5.6	Validity of the SMA ($F = 2$)	90
6	Structure formation on elongated spinor BEC	95
6.1	Spinor dynamics beyond single-mode approximation	95
6.2	Preparation and analysis of elongated BEC	96
6.3	Observation of a dynamical instability in $F = 2$	101
7	Chaotic dynamics in $F = 2$	112
7.1	Signatures of chaos	112
7.2	Trajectory statistics	114
7.3	Phase space dynamics	118
7.4	Discussion and outlook	123
8	Summary and outlook	132
A	Coordinate systems	134
B	Elementary nonlinear dynamics	135
C	Optical four-wave mixing	137

Chapter 1

Introduction

The realization of *Bose-Einstein Condensation* in dilute atomic gases in 1995 earned E. A. Cornell, C. E. Wieman and W. Ketterle the 2001 Nobel Prize in Physics and incited a rush of activity that has grown into a whole new field of research. Bose-Einstein condensation is a phase transition occurring in ensembles of identical bosonic particles, where the absolute ground state is macroscopically occupied below the transition temperature. The macroscopic wavefunction associated with a Bose-Einstein condensate, which can easily reach a size of a few tenths of a millimeter, renders it a fascinating testing ground for quantum mechanics, where the wave-like properties of matter can be observed almost “by eye”. Beautiful experiments have demonstrated the fundamental properties of BEC as giant matter waves. Questions regarding the interpretation of quantum mechanics and touching the foundations of our understanding of the microscopic world – “do independent particles interfere?” – have become experimentally accessible. Today, research on and with Bose-Einstein condensates is widely ramified. BEC have been applied in precision measurements [9, 10] and quantum information processing [11]; beautiful examples of fundamental research include the observation vortex lattices in rotating condensates [12, 13, 14] and the Hanbury Brown Twiss effect of atoms in optical lattices [15, 16], to name only a few.

The interest of physicists in *magnetism* is much older. While electro-magnetism was comprehensively described by Maxwell’s equations at the end of the 19th century, a satisfactory explanation of ferromagnetism was not found until the advent of quantum mechanics and in particular the discovery of the quantized spin by O. Stern and W. Gerlach in 1922 [17, 18]. It turned out that magnetism in materials in general relies on the magnetic moments of atoms and electrons, generated by their internal angular momentum or spin. The mechanism determining their relative orientation was identified in 1928 by W. Heisenberg [19] as the exchange interaction, arising from the interplay of the Pauli exclusion principle and the Coulomb interaction of electrons. Despite 80 years of research since, and despite the enormous technological relevance of magnetic materials today, the details of magnetism are not yet fully understood and remain an active area of research.

Spinor Bose-Einstein condensates consist of particles with non-zero internal angular momentum or spin, whose orientation in space is not externally constrained. Spinor Bose-Einstein condensates extend the extraordinary properties of a BEC to the spin as a degree of freedom and allow the study of magnetism in quantum gases, merging these two fascinating branches of physics.

The pioneering experiments with spinor BEC were performed not long after the realization of BEC in the group of W. Ketterle. The first observation of a BEC with spin degree of freedom [20] in an optical trap, together with seminal theoretical work by T.-L. Ho [21], T. Ohmi and K. Machida [22], established the basic techniques and notions of spinor BEC physics.

The Ketterle group studied a spin-1 system, namely Na in the $F = 1$ hyperfine state. They were the first to study the ground state of a spinor BEC experimentally and to recognize the importance of spin conservation and the quadratic Zeeman effect [23]. They also established the validity of the mean-field description proposed in [21, 22], which is now widely acknowledged as a successful approximation. Further important results include the interpretation of ground states and domain formation in terms of a phase diagram [23] and the first observation of spontaneous de-mixing of spin states, explained by energetic arguments [24].

In parallel, the group of E. A. Cornell established a magnetically trapped two-component mixture of ^{87}Rb in different hyperfine states as a quasi-spin-1/2 system [25]. Important results were the demonstration of coherence, i.e. a well-defined relative phase, of the two components in the condensed state [26, 27], as well as decoherence and its consequences in the non-condensed fraction [28]. Collective excitations in a thermal ensemble were studied both above [29, 30] and below [31] the transition temperature, as well as their interaction with the condensed part in the latter case.

Following the ground-breaking work of W. Ketterle and E. A. Cornell, the field was revitalized by experiments performed in the group of M.-S. Chapman and in our group in Hamburg. Two main questions determined the track: on the one hand, what are the characteristics of spin-2 systems in general [32, 33] and ^{87}Rb in particular [34]; on the other hand, is it possible to observe coherent oscillations in spinor BEC [35]. Both questions were addressed in the Hamburg group, resulting in the classification of spin-2 spinor ground states at finite magnetic field in terms of a phase diagram [36] and in a direct experimental confirmation of the predicted ground state of ^{87}Rb $F=2$ [7]. The observation of coherent spinor oscillations however turned out to be difficult in both $F = 2$ (Hamburg group [8, 7]) and $F = 1$ (Chapman group [37]).

Today, still only a handful of groups are engaged in experimental research on spinor BEC [38, 39, 40, 41, 42], despite the spectacular prospects associated with the implementation of optical lattices [43]. In contrast, theoretical approaches to spinor BEC are diverse, ranging from the tried and tested mean-field approximation (e.g. [44, 45, 46, 47], to name a few recent papers utilizing this approach) to exact many-body calculations (e.g. [35, 48, 49]).

The first observation of clearly coherent spinor oscillations in both $F = 1$ and $F = 2$ condensates is one of the highlights of the present work – independent work on $F = 1$ in the group of Chapman has appeared simultaneously [50], beautifully complementing our results. We have also been the first to systematically apply the Rabi and Ramsey methods, known from spin-1/2 physics but extended to $F \geq 1$ condensates, establishing them as a versatile tool for the preparation and analysis of spinor BEC. These experiments and the theoretical models developed in their context have tremendously advanced our comprehension of spinor BEC dynamics.

At the core of this understanding is the concept of the single-mode approximation (SMA), claiming that the spin state of a trapped condensate does not vary in space. The present thesis highlights the usefulness of the single-mode approximation in the interpretation of dynamical phenomena and at the same time explores its limits. In fact, it takes

one step beyond those limits in presenting first results on spontaneously formed spatial spin patterns in antiferromagnetic $F = 2$ ^{87}Rb . However, single-mode $F = 2$ spinor dynamics holds yet another surprise – behind the innocent face of quantum mechanics, spin dynamics is a beautiful example of nonlinear dynamics in a complex system.

In the following, an overview of the contents of this thesis is presented, in the form of a short abstract for each chapter.¹

Technical note – The symmetry axis or quantization axis is in some cases referred to as x -axis in this work, in contrast to the usual convention (z -axis). Appendix A clarifies this issue.

¹For the reader's convenience, each abstract is repeated at the beginning of the respective chapter.

Chapter 2 – Spinor Bose-Einstein condensates Mathematical tools as well as intuitive pictures used in the description of spin-1 and spin-2 ensembles are summarized. In the first part, the generalization of well-known spin-1/2 physics to spin- F is developed and key concepts such as Rabi and Ramsey oscillations and the Bloch sphere are discussed. The second part deals with the mean-field description of interacting spinor Bose-Einstein condensates, focusing on dynamics in the single-mode approximation but also covering related topics such as ground states and pattern formation.

Chapter 3 – Experimental setup and characterization The observation and manipulation of ultra-cold spinor gases is a technically demanding task and requires a complex experimental setup together with an experimentalist’s ability to master it. Many of the key techniques covered in this chapter, in particular the control of the magnetic field and the preparation of spin states, had to be specially developed or improved in order to achieve the results of the following chapters.

Chapter 4 – Additional experimental tools This chapter covers two rather peripheral experimental aspects, that yet turn out to be quite rewarding distractions, uncovering beautiful physics. In the first part, various methods aimed at reducing the disturbance of absorption images by interference fringes – a problem well known to anyone working in the field of ultracold gases and probably of much wider impact, considering the importance of laser light in modern imaging technology. The second part describes the construction of flexible and easy-to-use light source for driving Raman transitions between the hyperfine ground states of ^{87}Rb .

Chapter 5 – Spin dynamics from a rotated stretched state This chapter, covering those of our spinor BEC experiments that can be analyzed under the single-mode paradigm, is the heart of this thesis. It turns out that fully transversely magnetized states are particularly suited to observe fascinating new types of spinor dynamics, such as the resonance phenomenon central to this chapter. The contents of this chapter has been the subject of two peer-reviewed publications: work on $F = 1$ can be found in Kronjäger et al., Phys. Rev. A **72**, 063619 (2005) [2], work on $F = 2$ in Kronjäger et al., Phys. Rev. Lett. **97**, 110404 (2006) [1].

Chapter 6 – Structure formation in elongated spinor BEC Evidence of spontaneous pattern formation in anti-ferromagnetic $F = 2$ ^{87}Rb condensates as well as a critical analysis thereof is presented in this chapter. Similar phenomena have been observed before in *ferromagnetic* spinor condensates only, where they are easily interpreted as spontaneous symmetry breaking or demixing of components. This interpretation is not applicable to our observations. Possible explanations discussed here include a *dynamical instability* or a *twisting* of the order parameter by magnetic field gradients, both leading to the breakdown of the single-mode approximation.

Chapter 7 – Chaotic dynamics in $F = 2$ A thorough numerical and analytical treatment of the *equations of motion of symmetric $F = 2$ spin dynamics in the single mode approximation* unravels the complex and actually chaotic dynamics of this system. A comprehensive treatise of this topic is beyond the scope of the present work, but an attempt is made to introduce the reader to the beauty of nonlinear dynamics and deterministic chaos, which in fact is a ubiquitous phenomenon in nature.

Chapter 2

Spinor Bose-Einstein condensates (BEC)

Mathematical tools as well as intuitive pictures used in the description of spin-1 and spin-2 ensembles are summarized. In the first part, the generalization of well known spin-1/2 physics to spin- F is developed and key concepts such as Rabi and Ramsey oscillations and the Bloch sphere are discussed. The second part deals with the mean-field description of interacting spinor Bose-Einstein condensates, focusing on dynamics in the single-mode approximation but also covering related topics such as ground states and pattern formation.

2.1 Introduction to spinor Bose-Einstein condensates

Spinor condensates consist of bosonic particles possessing an *internal* degree of freedom, namely the orientation of their spin. While the theory describing the *external* degrees of freedom of a Bose-Einstein condensate is well known (see e.g. [51, 52, 53]), the particular features of spinor Bose-Einstein condensates are the subject of the present chapter.

First and foremost, the order parameter of a spinor BEC becomes a multi-component *spinor* wave-function. Compared to general multi-component Bose-Einstein condensates, e.g. of atoms in different hyperfine states [54, 26] or of different isotopes [55], spinor condensates are distinguished by the symmetry of the spinor order parameter. Under rotations of the coordinate system, spinor components transform into one another according to the laws of the corresponding symmetry group. In other words, the number of particles in each component is not fixed. Internal dynamics may change the individual populations, only restricted by the conservation of the total spin.

Bose-Einstein condensates of alkali gases are weakly interacting, meaning they can be well described in the mean-field approximation, which is an effective single-particle theory. Nevertheless, interactions are important and generally even dominate over kinetic energy in the ground state. Extending the formalism to spinor BEC, interactions become dependent on the internal state, leading to complex nonlinear dynamics of the internal degrees of freedom and a rich manifold of ground states.

This chapter starts with a review of the quantum mechanics of single-particle spin physics with emphasis on the particularities of spin-1 and spin-2 particles, as compared to the well-known spin-1/2 or two-level case with its intuitive classical interpretation, the

Bloch sphere. Understanding single-particle spin physics is the basis for the analysis and interpretation of many-particle spinor systems.

The second half of this chapter addresses the mean-field theory of spinor condensates, and in particular the consequences of state-dependent interaction. We concentrate on dynamical aspects, which are at the core of the present work as a whole. We also point out the analogy of spinor BEC and nonlinear optics, both obeying wave equations that share essential features.

2.2 Single atom spin-1 and spin-2 physics

2.2.1 Quantum mechanical description

The quantum mechanical description of single-particle spinor physics is based on a Hamiltonian constructed from

1. the respective F -manifold of atomic energy levels in an axial magnetic field B_0 ; the energy dependence on B_0 is taken into account to second order (linear and quadratic Zeeman effect)
2. the linear interaction with a relatively small, time-dependent transverse field $B_\perp(t)$ produced by a radio frequency antenna.

In the regime of magnetic interaction energy much smaller than the fine structure splitting ΔE_{LS} , the hyperfine Hamiltonian including an external magnetic field \vec{B} can be written (following [56])

$$\mathbf{H}_{\text{HFS}} = A \vec{\mathbf{I}} \cdot \vec{\mathbf{J}} - (g_K \mu_K \vec{\mathbf{I}} - g_J \mu_B \vec{\mathbf{J}}) \cdot \vec{B} \quad (2.1)$$

where $\vec{\mathbf{I}}$ and $\vec{\mathbf{J}}$ are the angular momentum operators of the nuclear and electronic (including orbital) spin, respectively, μ_K and μ_B are the nuclear and Bohr magneton and g_K and g_J the corresponding Landé factors¹. At zero field, $\vec{\mathbf{I}}$ and $\vec{\mathbf{J}}$ couple to the total spin $\vec{\mathbf{F}} = \vec{\mathbf{I}} + \vec{\mathbf{J}}$, and the energy levels are simultaneous eigenstates of \mathbf{I}^2 , \mathbf{J}^2 , \mathbf{F}^2 , \mathbf{F}_z with energies $E_{\text{HFS}} = \frac{A}{2} ((F(F+1) - I(I+1) - J(J+1)))$.

A small magnetic field $\vec{B} = B_0 \vec{e}_z$ lifts the m_F degeneracy and – using linear perturbation theory – leads to Zeeman levels $E_{\text{LZE}} = g_F \mu_B B_0 m_F \equiv \hbar p m_F$. Second order perturbation theory adds a term quadratic in B_0 and m_F , $E_{\text{QZE}} = \hbar q m_F^2$. In the case of alkali atoms in S -states with $J = \frac{1}{2}$, the Breit-Rabi formula [56] allows to diagonalize (2.1) exactly:

$$E \left(F = I \pm \frac{1}{2}, m_F \right) = -\frac{\Delta E_{\text{hfs}}}{2(2I+1)} - m_F g_K \mu_K B_0 \pm \frac{\Delta E_{\text{hfs}}}{2} \sqrt{1 + \frac{4m_F}{2I+1} x + x^2} \quad (2.2)$$

$$\text{with } x = \frac{g_J \mu_B + g_K \mu_K}{\Delta E_0} B_0 \quad (2.3)$$

¹All four quantities are positive with the sign convention chosen here [57]. The Bohr magneton $\mu_B = \frac{e\hbar}{2m_e c} \approx h \times 1.4 \text{ MHz/G}$ and the nuclear magneton $\mu_K = \frac{e\hbar}{2m_p c} \approx h \times 760 \text{ Hz/G}$ determine the order of magnitude of Zeeman energy shifts. For the electronic ground state of ^{87}Rb , the Landé factor is $g_J \approx 2$ and the corresponding nuclear g factor $g_K \approx 2.75$. Since $\mu_K \ll \mu_B$, the nuclear contribution to the Zeeman effect can be neglected for the purposes of the present work.

$\Delta E_{\text{hfs}} \equiv \hbar\omega_{\text{hfs}} = A(I + 1/2)$ is the hyperfine splitting of the two states $F = I \pm \frac{1}{2}$ at zero magnetic field. Expanded to second order in B_0 , we get for the case of ^{87}Rb with $I = \frac{3}{2}$

$$E_{\text{LZE}} = m_F \mu_B B_0 \left(\pm \frac{g_j}{4} - \frac{(3 \pm 1)\mu_K}{4\mu_B} g_K \right) \approx \pm \frac{1}{2} m_F \mu_B B_0 \quad (2.4)$$

$$E_{\text{QZE}} = \pm \frac{\mu_B^2 B_0^2}{4\Delta E_{\text{hfs}}} \left(g_j + \frac{\mu_K}{\mu_B} g_K \right)^2 \left(1 - \frac{m_F^2}{4} \right) \approx \pm \frac{\mu_B^2 B_0^2}{4\Delta E_0} (4 - m_F^2) \quad (2.5)$$

where \pm refers to the case $F = I \pm \frac{1}{2}$, respectively, i.e. $F = 1$ and $F = 2$. It thus turns out that in very good approximation, the Zeeman effect (both linear and quadratic) in ^{87}Rb $F = 1$ and $F = 2$ is equal in magnitude but of opposite sign.

The Wigner-Eckart theorem guarantees that $|F, m_F\rangle$ are still energy eigenstates. The magnetic field dependent part of (2.1) is frequently reduced to

$$\mathbf{H}_{\text{ZE}} \equiv \mathbf{H}_{\text{LZE}} + \mathbf{H}_{\text{QZE}} = -\hbar p \mathbf{F}_z + \hbar q \mathbf{F}_z^2 \quad (2.6)$$

with $|p| = \frac{1}{2} \frac{\mu_B}{\hbar} B_0$ and $|q| = \frac{p^2}{\omega_{\text{hfs}}}$. For $F = 2$ ($F = 1$) both p and q are negative (positive).

Besides the constant offset $B_0 \vec{e}_z$, the magnetic field can have a time-dependent perpendicular component, e.g. produced by a radio frequency antenna, $\vec{B} = B_0 \vec{e}_z + \hat{b} \cos(\omega t) \vec{e}_y$. Since the amplitude of such a time-dependent field is typically well within the linear regime, the quadratic Zeeman effect can be neglected and the corresponding time-dependent Hamiltonian reads

$$\mathbf{H}_{\text{rf}} = -g_F \mu_B \hat{b} \cos(\omega t) \mathbf{F}_y. \quad (2.7)$$

Before we proceed to look at the dynamics induced by $\mathbf{H}_{\text{ZE}} + \mathbf{H}_{\text{rf}}$, it is convenient to transform to a *rotating coordinate system*. For a coordinate system rotating around the z -axis at angular velocity ω_0 , the time-dependent transformation operator is diagonal,

$$\mathbf{T} = e^{-i\omega_0 t \mathbf{F}_z}. \quad (2.8)$$

It commutes with \mathbf{H}_{ZE} , but due to its explicit time dependence adds a term $i\hbar \dot{\mathbf{T}} \mathbf{T}^{-1} = +\hbar\omega_0 \mathbf{F}_z$ to the effective Zeeman Hamiltonian in the rotating frame,

$$\tilde{\mathbf{H}}_{\text{ZE}} = \mathbf{T} \mathbf{H}_{\text{ZE}} \mathbf{T}^{-1} + i\hbar \dot{\mathbf{T}} \mathbf{T}^{-1} = -\hbar p \mathbf{F}_z + \hbar q \mathbf{F}_z^2 + \hbar\omega_0 \mathbf{F}_z. \quad (2.9)$$

The off-diagonal part \mathbf{H}_{rf} transforms to

$$\mathbf{T} \mathbf{H}_{\text{rf}} \mathbf{T}^\dagger = -\frac{g_F \mu_B \hat{b}}{4i} (e^{i\omega t} + e^{-i\omega t}) (e^{-i\omega_0 t} \mathbf{F}_+ - e^{i\omega_0 t} \mathbf{F}_-) \quad (2.10)$$

with $\mathbf{F}_\pm = \mathbf{F}_x \pm i\mathbf{F}_y$. The *rotating wave approximation* (RWA) consists in expanding the product and keeping only terms oscillating at the *difference* frequency $\omega - \omega_0$ (assuming both have the same sign). This approximation is used extensively in all kinds of near-resonant two-level problems and is generally considered adequate if the two frequencies are sufficiently close [58]. In RWA, the full Hamiltonian in the rotating frame reads

$$\tilde{\mathbf{H}} = -\hbar(p - \omega_0) \mathbf{F}_z + \hbar q \mathbf{F}_z^2 - \frac{g_F \mu_B \hat{b}}{2} \left(\cos(\omega - \omega_0) \mathbf{F}_y + \sin(\omega - \omega_0) \mathbf{F}_x \right). \quad (2.11)$$

In principle, the frequency of rotation ω_0 is. However, the choice $\omega_0 = \omega$ turns out to be particularly useful in situations where $\hat{b} \neq 0$, since $\tilde{\mathbf{H}}$ then becomes time-independent.

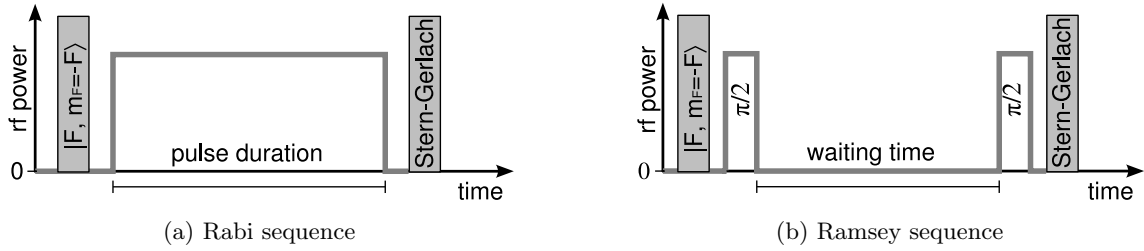


Figure 2.1: Experimental rf pulse sequence for the Rabi and Ramsey oscillations.

The Schrödinger equation of the *full* multi-level problem can be solved formally in the rotating wave approximation, where the Hamiltonian is time-independent,

$$i\hbar|\dot{\zeta}\rangle = \tilde{\mathbf{H}}|\zeta\rangle \quad \Leftrightarrow \quad |\zeta(t)\rangle = e^{-i\frac{\tilde{\mathbf{H}}}{\hbar}t} |\zeta(0)\rangle. \quad (2.12)$$

Since $\tilde{\mathbf{H}}$ is a $(2F + 1)$ -dimensional matrix, the exponential can be calculated numerically using standard linear algebra techniques. Alternatively, the super-operator formalism of Section 2.2.3 may be applied, in which the time evolution of the *density matrix* is calculated in a similar way.

It is instructive to solve the Schrödinger equation with $\mathbf{H} = \mathbf{H}_{\text{ZE}} + \mathbf{H}_{\text{rf}}$ for some special cases:

- *Larmor rotation* is evolution under $\mathbf{H}_{\text{LZE}} = -\hbar p \mathbf{F}_z$ only, $\hat{b} = 0$ and $q = 0$. Since an axial magnetic field B_0 is always present in experiments, Larmor rotation is the fundamental type of dynamics of any *superposition* of m_F states.
- *Rabi oscillations* arise from the coupling Hamiltonian \mathbf{H}_{rf} , with constant radio frequency amplitude \hat{b} . Rf-induced Rabi oscillations, typically lasting only fractions of a cycle, are the most important tool for the preparation of spin states used in this work (Section 3.5).
- *Ramsey fringes* are the result of a *sequence* of rf-driven and free evolution in the presence of \mathbf{H}_{ZE} , consisting of two Rabi quarter-cycles separated by a variable delay time. The Ramsey sequence can be regarded as an interferometer in spin space. Ramsey fringes yield information on the decay of coherence during the delay time and have been used in the present work for the characterization of magnetic field fluctuations (Section 3.4) and for probing the coherence of spinor Bose-Einstein condensates and thermal clouds (Section 5.2).

Larmor rotation

In the simplest non-trivial case of a purely linear Zeeman effect and no radio frequency coupling, the equations of motion can be solved in the fixed frame of reference in terms of observables, which has the advantage of being independent of the particular value of F . From the Heisenberg picture we obtain

$$\langle \dot{\mathbf{A}} \rangle = \frac{i}{\hbar} \langle [\mathbf{H}, \mathbf{A}] \rangle \quad (2.13)$$

for any observable $A \equiv \langle \mathbf{A} \rangle$. Applied to the spin components and \mathbf{H}_{LZE} , using $[\langle \mathbf{F}_x \rangle, \langle \mathbf{F}_y \rangle] = i\langle \mathbf{F}_z \rangle$ and cyclic permutations [59],

$$\dot{F}_x = +pF_y \quad \text{and} \quad \dot{F}_y = -pF_x. \quad (2.14)$$

These equations describe *Larmor rotation* of the spin vector around the z -axis, at the Larmor frequency $\omega_L = |p|$. F_z is a constant of the motion, $\dot{F}_z = 0$.

Switching to the rotating frame, we note that the Larmor frequency is replaced by the *detuning* $|\tilde{p}| = |p - \omega_0|$. Obviously, in the frame rotating exactly at the Larmor frequency, $\tilde{p} = 0$ and the system appears stationary.

The quadratic Zeeman effect introduces another energy scale $\hbar q$. Its effect is most easily calculated using matrix representation. Since it is diagonal in the basis of m_F states, it acts on the relative phases of superposition states only. The time evolution operator corresponding to \mathbf{H}_{QZE} is

$$e^{-iqF_z^2 t} \stackrel{F=1}{=} e^{-iqt} \begin{pmatrix} 1 & & & \\ & e^{iqt} & & \\ & & & 1 \end{pmatrix} \quad (2.15)$$

$$\stackrel{F=2}{=} e^{-4iqt} \begin{pmatrix} 1 & & & & & \\ & e^{3iqt} & & & & \\ & & e^{4iqt} & & & \\ & & & & e^{3iqt} & \\ & & & & & 1 \end{pmatrix} \quad (2.16)$$

where the pre-factors are arbitrary since they only add a global phase corresponding to a global energy shift.

Take, for example, the fully transversely magnetized state $|\zeta_{\pi/2}\rangle$ (see the following sections on Rabi oscillations and the Ramsey sequence) with $\langle \mathbf{F}_x \rangle = F$,

$$|\zeta_{\pi/2}\rangle \stackrel{F=1}{=} \left(\frac{1}{2} \quad \frac{1}{\sqrt{2}} \quad \frac{1}{2} \right)^T, \quad (2.17)$$

$$\stackrel{F=2}{=} \left(\frac{1}{4} \quad \frac{1}{2} \quad \sqrt{\frac{3}{8}} \quad \frac{1}{2} \quad \frac{1}{4} \right)^T. \quad (2.18)$$

Applying the time evolution operator of the quadratic Zeeman effect to this initial state, the expectation value

$$\langle F_x(t) \rangle = \langle \zeta_{\pi/2} | e^{+iq\mathbf{F}_z^2 t} \mathbf{F}_x e^{-iq\mathbf{F}_z^2 t} | \zeta_{\pi/2} \rangle \quad (2.19)$$

can be calculated straight-forwardly. For $F = 1$, the result is $\langle \mathbf{F}_x(t) \rangle = \cos(qt)$, while the remaining components of the spin vector remain zero, $\langle \mathbf{F}_y(t) \rangle = \langle \mathbf{F}_z(t) \rangle = 0$. We will get back to this in the context of the Ramsey fringes below.

Rabi oscillations

Rabi oscillations [60] in the original sense occur in two-level or spin-1/2 systems, where obviously no quadratic Zeeman effect exists. A similar phenomenon is observed in higher spin (multilevel ladder) systems when the quadratic Zeeman effect is small or negligible. The latter case can again be solved in terms of observables, independent of the value of F .

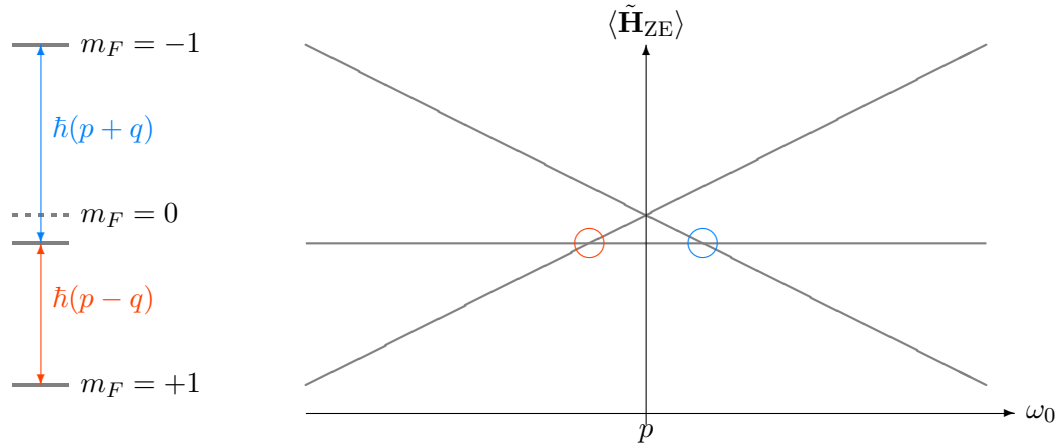


Figure 2.2: Detuning of transitions by the quadratic Zeeman effect ($F = 1$). LEFT: Level scheme for finite B_0 . RIGHT: Dressed-state energy $\langle \tilde{\mathbf{H}}_{\text{ZE}} \rangle$ in the rotating frame versus angular frequency ω_0 . \mathbf{H}_{QZE} splits the three-fold level-crossing into separate resonances, two of which satisfy $\Delta m_F = \pm 1$ (circles).

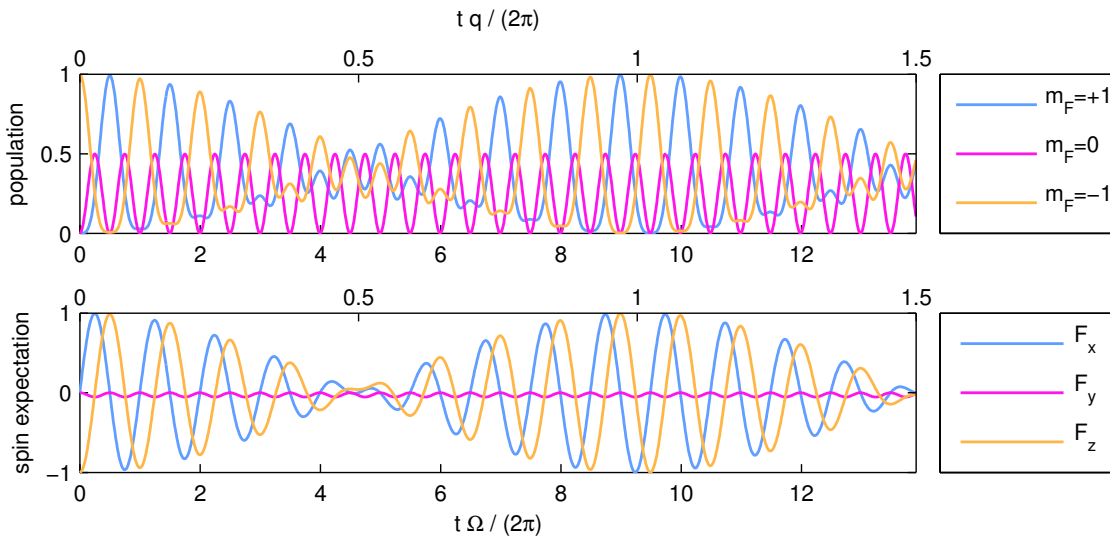


Figure 2.3: Rabi oscillations in $F = 1$ including the quadratic Zeeman effect. The plots have been numerically calculated from RWA solutions of the Schrödinger equation (2.12) with the parameters $\tilde{p} = 0$ and $q \approx 0.11\Omega_0$. Note the double scale of the horizontal axis, showing time in units of $2\pi/q$ as well as $2\pi/\Omega_0$.

In the rotating wave approximation the Hamiltonian becomes time-independent for $\omega_0 = \omega$:

$$\tilde{\mathbf{H}} = -\hbar\tilde{p}\mathbf{F}_z + \hbar q\mathbf{F}_z^2 - \frac{g_F\mu_B\hat{b}}{2}\mathbf{F}_y \quad (2.20)$$

where $\tilde{p} = p - \omega$ represents the detuning between the Larmor frequency and the excitation frequency.

Neglecting the quadratic Zeeman effect ($q = 0$) and assuming resonance ($\tilde{p} = 0$), the spin vector evolves according to

$$\dot{F}_x = -\Omega_0 F_z \quad \dot{F}_y = 0 \quad \dot{F}_z = +\Omega_0 F_x. \quad (2.21)$$

This is a rotation – in the rotating frame! – of the spin vector around the y -axis at the Rabi frequency $\Omega_0 = \frac{g_F\mu_B\hat{b}}{2\hbar}$. This is analogous to the two-level case except for the fact that the spin vector $\vec{F} = (F_x, F_y, F_z)$ does not fully characterize the quantum-mechanical state for $F > 1/2$.

For nonzero detuning, but still negligible quadratic Zeeman effect, the Hamiltonian (2.20) takes the form of the generator of a rotation at angular velocity $\Omega = \sqrt{\tilde{p}^2 + \Omega_0^2}$ around an axis $\vec{n} = \frac{\tilde{p}}{\Omega}\vec{e}_z + \frac{\Omega_0}{\Omega}\vec{e}_y$,

$$\tilde{\mathbf{H}} = -\hbar\Omega \vec{n} \cdot \vec{F} \quad \text{where} \quad |\vec{n}| = 1. \quad (2.22)$$

This is analogous to the two-level case [58] and describes a gradual transition from resonant Rabi oscillations ($\vec{n} = \vec{e}_y$, $\Omega = \Omega_0$) to Larmor rotation at large detunings ($\vec{n} \rightarrow \vec{e}_z$, $\Omega \rightarrow \tilde{p}$).

As in the case of Larmor rotation, the quadratic Zeeman effect introduces another energy scale q . Intuitively, the radio frequency driving field couples to $\Delta m_F = \pm 1$ transitions; the quadratic Zeeman effect detunes the different transitions which otherwise are all degenerate. Taking $F = 1$ as an example, there are two transitions with $\Delta m_F = \pm 1$ (Fig. 2.2). Superimposing two slightly detuned oscillators generally yields a *beat signal* at the difference frequency, and the same result is obtained in the case of Rabi oscillations. The “beat” picture is an intuitive explanation for qualitative features that distinguish $F \geq 1$ from the two-level case.

Exact solutions of the equations of motion can be calculated numerically, and an example for $F = 1$ is presented in Fig. 2.3, where the beat note is readily identified. Starting from $|\zeta(0)\rangle = (0, 0, 1)$, the *populations* $\rho_{+1} = |\zeta_{+1}|^2$ and $\rho_{-1} = |\zeta_{-1}|^2$ oscillate exactly π out of phase at the Rabi frequency, while $\rho_0 = |\zeta_0|^2$ oscillates at twice the Rabi frequency. This reflects the rotation of the *spin vector* around the y -axis: $F_z = \pm F$ corresponds to $\rho_{\pm 1} = 1$, while $F_z = 0$, corresponding to $\rho_0 = 1/2$, occurs twice per cycle at $F_x = +F$ and $F_x = -F$. Accordingly, F_z and F_x oscillate $\pi/2$ out of phase. The beat note resulting from the quadratic Zeeman effect is visible in both F_z and F_x as well as ρ_{+1} and ρ_{-1} , but is hardly noticeable in ρ_0 . The quadratic Zeeman effect also leads to a small oscillation of F_y at twice the Rabi frequency. A small detuning would also show up in small oscillations of F_y , however at the same frequency and in phase with F_z .

Ramsey fringes

A powerful technique to study coherences, well known in two-level systems, is Ramsey interferometry [61]. Generally speaking, a wave packet is split in two and reunited after a period of free evolution, leading to interference fringes depending on the phase difference accumulated by the two parts. In the language of two-level systems, a beam-splitting

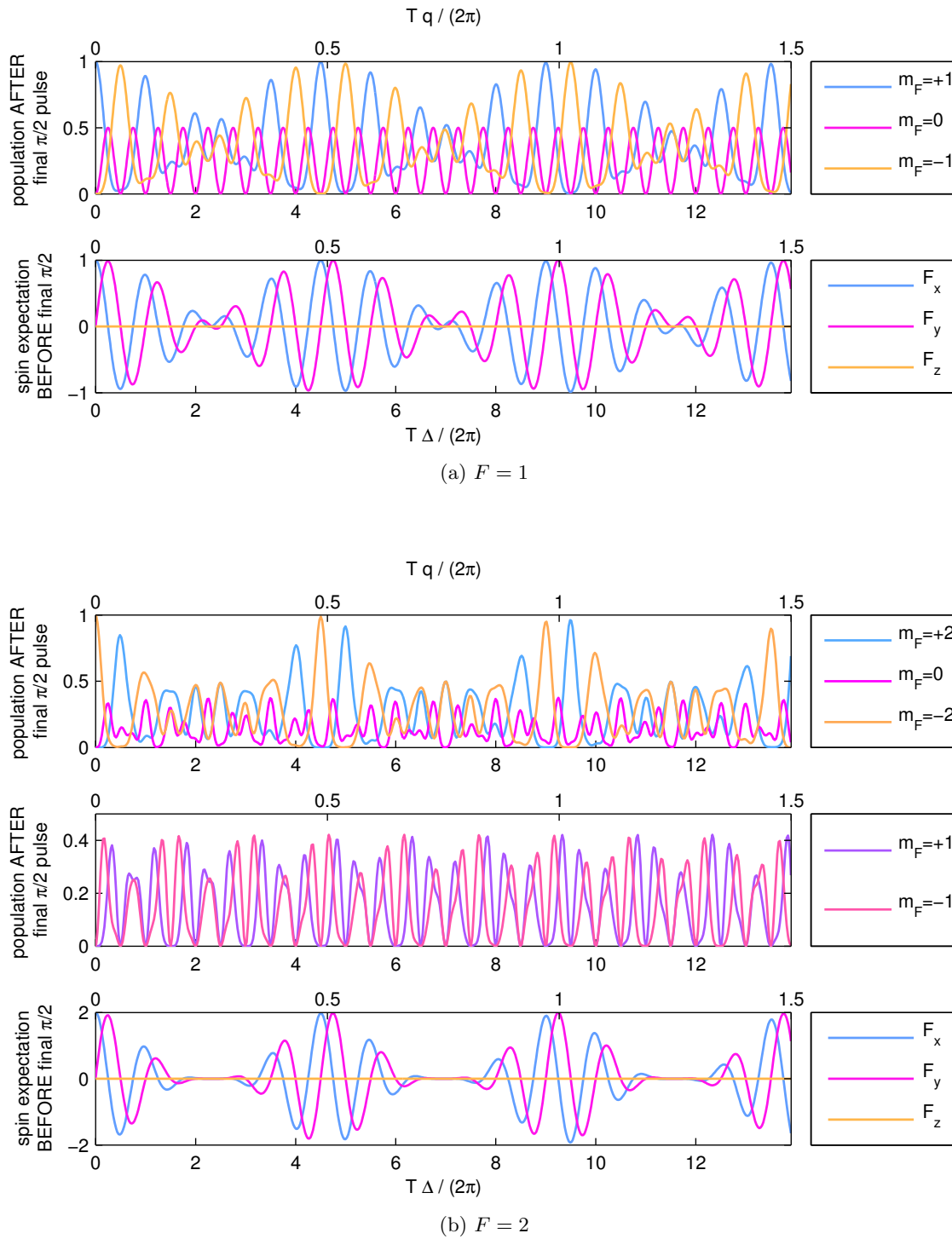


Figure 2.4: Ramsey fringes including quadratic Zeeman effect for (a) $F = 1$ and (b) $F = 2$, calculated numerically assuming ideal $\pi/2$ -pulses. In both cases, the detuning $\Delta \equiv \tilde{\nu}$ sets the time scale of the fast oscillations, and the quadratic Zeeman effect $q \approx 0.11\Delta$ determines the beat period. Note the double scale of the horizontal axis, showing time in units of $2\pi/q$ as well as $2\pi/\Delta$.

(radio frequency or light) pulse prepares the system in a superposition of internal states evolving at different rates according to their energy difference; a second pulse mixes the states once again, leading to population oscillations known as *Ramsey fringes* depending on the energy splitting and the time interval of free evolution between pulses.

The generalization to $F > 1/2$ performed here is straight forward. The time evolution during a Ramsey sequence takes place in three steps:

1. *beam-splitting* radio frequency pulse of duration τ and amplitude \hat{b} , such that $\Omega_0\tau = \pi/2$ (so-called $\pi/2$ -pulse). If τ is short compared to the time scale of the quadratic Zeeman effect q^{-1} , the latter may be neglected and the simplified Rabi picture discussed above applies.
2. *free evolution* governed by linear and quadratic Zeeman effect over time T .
3. *beam-combining* radio frequency $\pi/2$ -pulse of the same amplitude and duration as the first pulse.

In general, the evolution during the radio frequency pulses is described by the full Hamiltonian $\mathbf{H}_{\text{ZE}} + \mathbf{H}_{\text{rf}}$. The $\pi/2$ -pulse can be thought of as an instantaneous transformation when its duration τ is much smaller than other time scales of the system, here in particular that of the quadratic Zeeman effect q^{-1} and the detuning² \tilde{p}^{-1} ,

$$\mathbf{R}_{\pi/2} = \lim_{\substack{\tau \rightarrow 0 \\ \Omega_0\tau = \pi/2}} e^{-\frac{i}{\hbar}(\mathbf{H}_{\text{ZE}} + \mathbf{H}_{\text{rf}})\tau} = \lim_{\tau \rightarrow 0} e^{+i(\tilde{p}\mathbf{F}_z - q\mathbf{F}_z^2)\tau + i\frac{\pi}{2}\mathbf{F}_y} = e^{+i\frac{\pi}{2}\mathbf{F}_y} \quad (2.23)$$

$$F \equiv 1 \quad \begin{pmatrix} 1/2 & 1/\sqrt{2} & 1/2 \\ -1/\sqrt{2} & 0 & -1/\sqrt{2} \\ 1/2 & -1/\sqrt{2} & 1/2 \end{pmatrix} \quad (2.24)$$

$$F \equiv 2 \quad \begin{pmatrix} 1/4 & 1/2 & \sqrt{6}/4 & 1/2 & 1/4 \\ -1/2 & -1/2 & 0 & 1/2 & 1/2 \\ \sqrt{6}/4 & 0 & -1/2 & 0 & \sqrt{6}/4 \\ -1/2 & 1/2 & 0 & -1/2 & 1/2 \\ 1/4 & -1/2 & \sqrt{6}/4 & -1/2 & 1/4 \end{pmatrix} \quad (2.25)$$

$\mathbf{R}_{\pi/2}$ in fact is the transformation operator for a 90° active rotation around the y -axis, or, equivalently, for a (passive) rotation of the coordinate system such that the z -axis takes the place of the former x -axis. Applying $\mathbf{R}_{\pi/2}$ to a stretched state $| -F \rangle$ with $F_z = -F$ results in a fully transversely magnetized state $|\zeta_{\pi/2}\rangle$ with $F_x = F$; another pulse $\mathbf{R}_{\pi/2}$ transforms $|\zeta_{\pi/2}\rangle$ to the the opposite stretched state $| +F \rangle$.

It follows that measuring F_z after the final beam-combining $\pi/2$ -pulse is actually equivalent to measuring F_x *before* the final rotation. Similarly, the first beam-splitting pulse can be regarded as preparing a fully transversely magnetized state. During the period of free evolution, the linear Zeeman effect then induces a Larmor rotation at the detuning \tilde{p} in the rotating frame, while the quadratic Zeeman effect introduces a beat note of the order of q , as discussed in the previous section on Larmor rotation.

²From the Rabi formula (2.22), neglecting the quadratic Zeeman effect but not the detuning, one obtains a width of the resonance of the order of the resonant Rabi frequency Ω_0 . For a $\pi/2$ -pulse, the Rabi frequency is inversely proportional to the pulse duration τ , $\Omega_0 = \frac{\pi}{2\tau}$. The width of the resonance is thus the same as expected from the Fourier-limited spectral width of the pulse envelope.

Fig. 2.4 illustrates the Ramsey sequence and the resulting population dynamics for both $F = 1$ and $F = 2$. In $F = 1$, the dynamics is similar to Rabi oscillations, except that F_x and F_y are now oscillating in quadrature instead of F_z and F_x , and $F_z = 0$ exactly. As expected from the considerations for Larmor rotation in the presence of a quadratic Zeeman shift, the period of oscillations of F_x and F_y is $2\pi/\tilde{p}$ and the beat period introduced by the quadratic Zeeman effect is π/q . Note the phase jumps caused by the change of sign of the envelope function $\cos(qT)$ at its zero-crossings. In $F = 2$, the time scales of both the oscillation and the beat note are the same as in $F = 1$, but the details differ significantly. In particular, population dynamics appears quite irregular, even though no nonlinearity is present here. The shape of the beat envelope of F_x, F_y oscillations also differs. This is caused by harmonics of $\cos(qT)$, resulting from the phase factors in the time evolution operator (2.16).

2.2.2 Classical interpretation

The dynamics of a driven two-level system can be mapped to the classical dynamics of an angular momentum \vec{s} under the influence of a torque $\vec{\Omega}$. This is expressed by the Bloch equations [58],

$$\dot{\vec{s}} = -\vec{\Omega} \times \vec{s} \quad \text{with} \quad \vec{\Omega} = \begin{pmatrix} 0 \\ \Omega_0 \cos(\omega t) \\ \omega_0 \end{pmatrix} \quad \text{and} \quad \vec{s} = \begin{pmatrix} \langle \sigma_1 \rangle \\ \langle \sigma_2 \rangle \\ \langle \sigma_3 \rangle \end{pmatrix}. \quad (2.26)$$

The connection to quantum mechanics is established by identifying the components of \vec{s} as expectation values of observables σ_i . The operators σ_i are the Pauli matrices,

$$\sigma_1 = \begin{pmatrix} 0 & 1 \\ 1 & 0 \end{pmatrix} \quad \sigma_2 = \begin{pmatrix} 0 & i \\ -i & 0 \end{pmatrix} \quad \sigma_3 = \begin{pmatrix} 1 & 0 \\ 0 & -1 \end{pmatrix} \quad (2.27)$$

The Pauli matrices not only play the role of angular momentum operators, $\mathbf{F}_i = \frac{1}{2}\sigma_i$, but also form a basis in which any spin-1/2 density matrix ρ can be expanded,

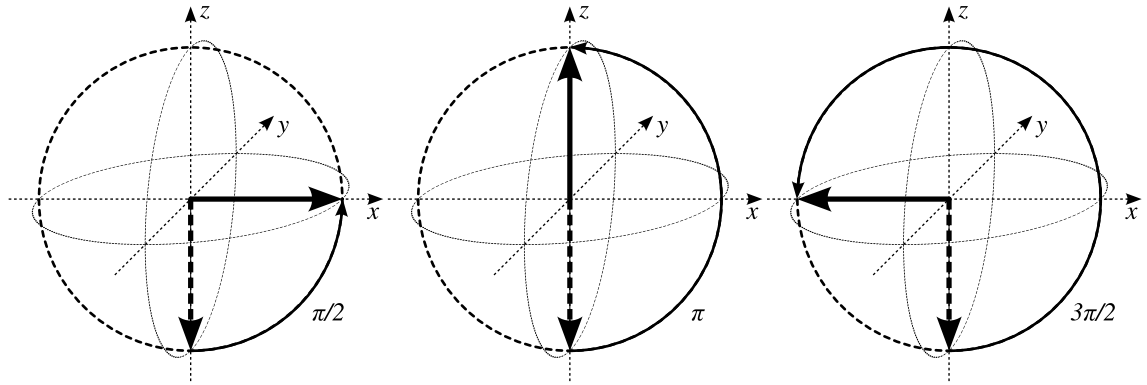
$$\rho = \sum_{i=1,2,3} \alpha_i \sigma_i \quad \text{with} \quad \alpha_i = \frac{1}{2} \text{Tr} \rho \sigma_i = \langle \mathbf{F}_i \rangle \quad (2.28)$$

The tip of the *Bloch vector* \vec{s} , or equivalently the spin vector (F_x, F_y, F_z) , moves on the surface of the *Bloch sphere*. For $F = 1/2$, the surface of the Bloch sphere contains *all* possible physical states. This is a consequence of the fact that the group of 3D rotations $O(3)$ and the group of special unitary transformations $SU(2)$ on \mathbb{C}^2 are isomorphic [62], and is not true for any Hilbert space dimension larger than two. It also implies that in $F = 1/2$, *every* state is a stretched state in a properly chosen coordinate system.

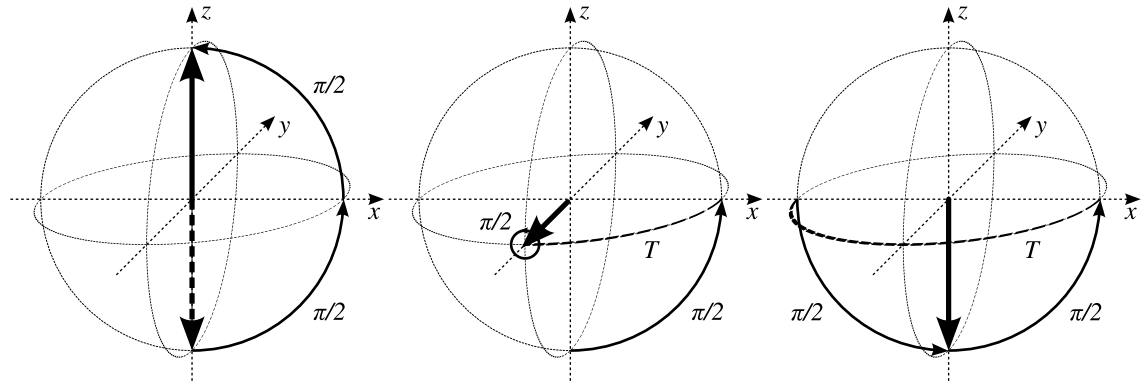
For $F > 1/2$, the spin vector is still useful to visualize dynamics on the Bloch sphere, but only as long as the state remains a stretched state with respect to some direction in space. For purely linear Zeeman dynamics including rf drive, any stretched state remains stretched since the time evolution operator $e^{-i\frac{\mathbf{H}}{\hbar}t}$ is just a rotation around $\vec{n} = (0, \Omega_0, p)/\sqrt{p^2 + \Omega_0^2}$,

$$e^{-i(-p\mathbf{F}_z - \Omega_0\mathbf{F}_y)t} = e^{i\varphi\vec{n}\cdot\vec{\mathbf{F}}}, \quad (2.29)$$

equivalent to a change in coordinate system. The quadratic Zeeman effect however destroys this picture.



(a) Rabi oscillations (resonant rf drive for time t). From left to right: $F_z(\Omega_0 t = \pi/2) = 0$, $F_z(\Omega_0 t = \pi) = F$, $F_z(\Omega_0 t = 3\pi/2) = 0$.



(b) Ramsey fringes (two $\pi/2$ -pulses separated by time T , detuned by $\Delta = \omega - \omega_0$). $F_z(\Delta \cdot T = 0) = F$, $F_z(\Delta \cdot T = \pi/2) = 0$, $F_z(\Delta \cdot T = \pi) = -F$.

Figure 2.5: Bloch sphere: Rabi and Ramsey oscillations in the rotating frame with the initial state is on the negative z -axis, $F_z = -F$, $F_x = F_y = 0$. Compare to Fig. 2.3 (Rabi) and Fig. 2.4 (Ramsey).

For example, consider Rabi oscillations in the presence of a quadratic Zeeman shift, as shown in Fig. 2.3. The initial state $|-1\rangle$ can be represented on the Bloch sphere, compare to Fig. 2.5. However, at the beat nodes $t = (2n+1)\pi/q$, all components of the spin vector (F_x, F_y, F_z) vanish, which is obviously not compatible with any state on the surface of the Bloch sphere. The same occurs at the beat nodes of Ramsey fringes with quadratic Zeeman effect (Fig. 2.4).

It is possible to construct a generalized Bloch vector for an N -level system obeying an equation of motion similar to (2.26) [63]. The method is based on a suitably chosen set of $N \times N$ basis matrices \mathbf{q}_i , in which the density matrix is expanded, $\rho = \sum_{i=1}^{N^2-1} \alpha_i \mathbf{q}_i$. The expansion coefficients α_i form the components of the Bloch vector $\vec{s} = (\alpha_1, \dots, \alpha_{N^2-1})$. However, this is an abstract vector in a high dimensional space \mathbb{R}^{N^2-1} , and its construction is somewhat arbitrary since it depends on the choice of basis matrices with different proposals offering specific advantages [64, 65, 66]. We will return to the topic in the following section in the context of the so-called super-operator formalism, where we will also go into the details of the expansion of the density matrix.

2.2.3 Decoherence and damping

Decoherence of a quantum mechanical state arises as a result of interaction of the quantum mechanical system under study with a “bath” of external degrees of freedom, whose details are unknown. E.g. a single atom as a constituent of a thermal ensemble, or a Bose-Einstein condensate interacting with its thermal cloud may suffer from decoherence. The description of decoherence as a statistical phenomenon is based on the density matrix formulation of quantum mechanics.

The density matrix ρ is defined as a statistical mixture of pure states $|\psi_i\rangle$ with weight p_i ,

$$\rho = \sum_i p_i |\psi_i\rangle\langle\psi_i| \quad \text{with} \quad \sum_i p_i = 1, \quad (2.30)$$

and obeys an equation of motion that follows from the Schrödinger equation, the *von-Neumann* equation

$$\dot{\rho} = -\frac{i}{\hbar} [\mathbf{H}, \rho] \quad \text{with Hamiltonian } \mathbf{H}. \quad (2.31)$$

Density matrices describing pure states, in contrast to statistical mixtures, are distinguished by $\text{Tr } \rho^2 = 1$. An observable A , corresponding to an operator \mathbf{A} , is calculated from

$$A = \text{Tr } \rho \mathbf{A}. \quad (2.32)$$

The density matrix formalism thus incorporates both quantum mechanical and statistical averaging into a single formalism.

The von-Neumann equation conserves not only $\text{Tr } \rho = 1$ (normalization) but also $\text{Tr } \rho^2$, which means that a pure state always remains pure. Thus it cannot describe decoherence, which is generally associated with the decay of off-diagonal elements of the density matrix. The *Lindblad-form* [67] is the most general amendment of the equation of motion fulfilling certain physical requirements, namely the conservation of the trace $\text{Tr } \rho$, complete

positivity of ρ , and Markovianity³ [68, 69]. The Lindblad form reads

$$\dot{\rho} = -\frac{i}{\hbar}[\mathbf{H}, \rho] + \frac{1}{2} \sum_k \left([\mathbf{L}_k \rho, \mathbf{L}_k^\dagger] + [\mathbf{L}_k, \rho \mathbf{L}_k^\dagger] \right) \quad (2.33)$$

$$= -\frac{i}{\hbar}[\mathbf{H}, \rho] - \frac{1}{2} \sum_k \left(\mathbf{L}_k^\dagger \mathbf{L}_k \rho + \rho \mathbf{L}_k^\dagger \mathbf{L}_k - 2\mathbf{L}_k \rho \mathbf{L}_k^\dagger \right) \quad (2.34)$$

The *Lindblad-operators* \mathbf{L}_k are arbitrary operators in Hilbert space. They have to be chosen in a suitable way such that they lead to the desired decoherence effect, or they may be calculated from a microscopic theory of the interaction with some specific environment. A common condition narrowing the range of operators and simplifying the physical interpretation is that the \mathbf{L}_k must be observables (hermitian operators) themselves. In this case, the Lindblad-von-Neumann equation (2.34) is equivalent to an averaged random unitary evolution [70, 71].

In the simple case of a fixed Hamiltonian \mathbf{H}_0 with a perturbation of randomly varying strength $\alpha(t)\mathbf{H}_R$, commuting with \mathbf{H}_0 , the Lindblad-equation can be derived by elementary means as the equation of motion of the averaged density matrix. $\alpha(t)$ is assumed to be a random walk with $[\alpha(t)] = 0$ and $[\alpha(t)\alpha(t')] = \sigma^2\delta(t-t')$, where $[\cdot]$ denotes the ensemble average of α . Since the time-dependent Hamiltonian $\mathbf{H}(t) = \mathbf{H}_0 + \alpha(t)\mathbf{H}_R$ commutes with itself at all times, $[\mathbf{H}(t), \mathbf{H}(t')] = 0$, the time-evolution operator $\mathbf{U}(t_2, t_1)$ that propagates the density matrix as $\rho(t_2) = \mathbf{U}(t_2, t_1)\rho(t_1)\mathbf{U}^\dagger(t_2, t_1)$ is simply given by

$$\mathbf{U}(t_2, t_1) = e^{-\frac{i}{\hbar} \int_{t_1}^{t_2} \mathbf{H}(t') dt'} = e^{-\frac{i}{\hbar} \mathbf{H}_0 t} e^{-\frac{i}{\hbar} \mathbf{H}_R \int_{t_1}^{t_2} \alpha(t') dt'} \quad (2.35)$$

Expanding the product

$$e^{-\frac{i}{\hbar} \mathbf{H}_R \int_{t_1}^{t_2} \alpha(t') dt'} \rho(t_1) e^{\frac{i}{\hbar} \mathbf{H}_R \int_{t_1}^{t_2} \alpha(t') dt'} \quad (2.36)$$

to second order in $\beta = \int_{t_1}^{t_2} \alpha(t') dt'$ we obtain

$$\rho(t_1) + \frac{i}{\hbar} \beta [\rho(t_1), \mathbf{H}_R] + \frac{\beta^2}{\hbar^2} \left(-\frac{1}{2} \mathbf{H}_R^2 \rho(t_1) + \mathbf{H}_R \rho(t_1) \mathbf{H}_R - \frac{1}{2} \rho(t_1) \mathbf{H}_R^2 \right), \quad (2.37)$$

and taking the ensemble average we arrive at

$$[\rho(t_2)] = e^{-\frac{i}{\hbar}(t_2-t_1)\mathbf{H}_0} \left[\rho(t_1) - \frac{1}{2} \frac{\sigma^2}{\hbar^2} (t_2 - t_1) (\mathbf{H}_R^2 \rho(t_1) + \rho(t_1) \mathbf{H}_R^2 - 2\mathbf{H}_R \rho(t_1) \mathbf{H}_R) \right] e^{\frac{i}{\hbar}(t_2-t_1)\mathbf{H}_0}. \quad (2.38)$$

The fact that only the *time difference* appears in this equation reflects the *statistical* time invariance of the problem. Taking the time derivative in the limit $t_2 \rightarrow t_1$, we obtain an equation of motion of the Lindblad form for the ensemble-averaged density matrix,

$$[\dot{\rho}] = -\frac{i}{\hbar}[\mathbf{H}_0, [\rho]] - \frac{1}{2} (\mathbf{L}^2[\rho] + [\rho]\mathbf{L}^2 - 2\mathbf{L}[\rho]\mathbf{L}), \quad (2.39)$$

with a single Lindblad operator $\mathbf{L} = \mathbf{L}^\dagger = \frac{\sigma}{\hbar} \mathbf{H}_R$. Assuming ergodicity, the ensemble average may also be substituted by a time average.

³In this context, Markovianity means that the quantum dynamical map $\Theta(t) : \rho(0) \rightarrow \rho(t)$ possesses a semi-group structure, i.e. $\Theta(t_1 + t_2) = \Theta(t_1)\Theta(t_2)$. This is what remains of the properties of the unitary time evolution operator $T(t) : |\psi(0)\rangle \rightarrow |\psi(t)\rangle$ of the Schrödinger picture.

An example where the above arguments apply would be a Ramsey experiment with an ensemble of thermal particles in a confining potential and subject to an inhomogeneous magnetic field. Provided the particle trajectories are sufficiently irregular, the inhomogeneity will look like a temporally fluctuating magnetic field, and by determining the population of spin states we actually measure the ensemble average of the diagonal elements of the density matrix. The Hamiltonian \mathbf{H}_R in this case is just proportional to \mathbf{F}_z .

The Lindblad-von-Neumann equation (2.34) is still a linear ordinary differential equation with respect to the components of ρ . In other words, regarding ρ as a vector in the space \mathcal{O} of hermitian operators⁴, the equation of motion can be written in the form $\dot{\rho} = \mathbf{M}\rho$, where \mathbf{M} is an operator on \mathcal{O} , also called *super-operator*. \mathcal{O} is of the dimension N^2 if the original Hilbert space is N -dimensional, but conservation of trace reduces the dimension to $N^2 - 1$. For practical calculations, ρ and \mathbf{M} are mapped to \mathbb{R}^{N^2-1} and $\mathbb{R}^{(N^2-1)\times(N^2-1)}$, respectively, by expanding ρ in a set of suitable basis matrices \mathbf{q}_i . The (real) expansion coefficients of $\rho = \sum_i \alpha_i \mathbf{q}_i$ form a vector in \mathbb{R}^{N^2-1} , and the abstract super-operator \mathbf{M} reduces to a $(N^2 - 1) \times (N^2 - 1)$ matrix.

For example, a suitable set of basis matrices for $F = 1$ are the *Gell-Mann matrices*⁵

$$\mathbf{q}_1 = \begin{pmatrix} 1 & 0 & 0 \\ 0 & 0 & 0 \\ 0 & 0 & -1 \end{pmatrix} \quad \mathbf{q}_2 = \sqrt{\frac{1}{3}} \begin{pmatrix} 1 & 0 & 0 \\ 0 & -2 & 0 \\ 0 & 0 & 1 \end{pmatrix} \quad (2.40)$$

$$\mathbf{q}_3 = \begin{pmatrix} 0 & 1 & 0 \\ 1 & 0 & 0 \\ 0 & 0 & 0 \end{pmatrix} \quad \mathbf{q}_4 = \begin{pmatrix} 0 & i & 0 \\ -i & 0 & 0 \\ 0 & 0 & 0 \end{pmatrix} \quad (2.41)$$

$$\mathbf{q}_5 = \begin{pmatrix} 0 & 0 & 0 \\ 0 & 0 & 1 \\ 0 & 1 & 0 \end{pmatrix} \quad \mathbf{q}_6 = \begin{pmatrix} 0 & 0 & 0 \\ 0 & 0 & i \\ 0 & -i & 0 \end{pmatrix} \quad (2.42)$$

$$\mathbf{q}_7 = \begin{pmatrix} 0 & 0 & 1 \\ 0 & 0 & 0 \\ 1 & 0 & 0 \end{pmatrix} \quad \mathbf{q}_8 = \begin{pmatrix} 0 & 0 & i \\ 0 & 0 & 0 \\ -i & 0 & 0 \end{pmatrix} \quad (2.43)$$

Note that all basis matrices are traceless, owing to the fact that the trace of ρ can be absorbed in the expansion coefficient of the identity matrix and ignored since it is fixed. The basis matrices closely resemble the spin matrices: $\mathbf{F}_z = \mathbf{q}_1$, $\mathbf{F}_y = \frac{1}{\sqrt{2}}(\mathbf{q}_4 + \mathbf{q}_6)$ and $\mathbf{F}_x = \frac{1}{\sqrt{2}}(\mathbf{q}_3 + \mathbf{q}_5)$. \mathbf{q}_2 , \mathbf{q}_7 and \mathbf{q}_8 are related to higher powers of the spin operators.

The above set of basis matrices possesses a particularly useful property, they form an *orthonormal basis* with respect to the scalar product⁶ $(\mathbf{u}, \mathbf{v}) \equiv \text{Tr } \mathbf{u} \mathbf{v}$, $(\mathbf{q}_i, \mathbf{q}_j) = 2\delta_{ij}$. This makes the calculation of expansion coefficients very easy.

For $F = 1/2$, the Pauli matrices (2.27) may serve as an orthonormal basis, and their expansion coefficients form the *Bloch vector* as discussed in the previous section. Once again, it becomes clear that the spin vector, the expansion coefficients of the spin matrices, is a full description of the system *only* in the case of $F = 1/2$.

⁴Note that the space \mathcal{O} of hermitian operators is a *real* vector space, i.e. allows only scalar multiplication with *real* numbers. In contrast, a general Hilbert space is a *complex* vector space.

⁵This set of matrices is named after Murray Gell-Mann, who introduced it as a generalization of Pauli matrices. [72]

⁶Note that this scalar product on the (real) vector space \mathcal{O} is in fact always real since $(\text{Tr } \mathbf{u} \mathbf{v})^* = \text{Tr } \mathbf{u}^\dagger \mathbf{v}^\dagger = \text{Tr } \mathbf{u} \mathbf{v}$

The super-operator approach is used in this work to numerically simulate the dynamics of non-interacting $F = 1$ ensembles including decoherence, implemented as a Lindblad operator proportional to \mathbf{F}_z , $\mathbf{L} = \gamma\mathbf{F}_z$. These simulations can then be compared to experimental data (Chapter 5). In our experiments on Rabi and Ramsey oscillations in $F = 1$, interactions are small enough to be neglected even in the condensed fraction. Of course, the formalism can also be used to simulate coherent dynamics, e.g. Fig. 2.3 and Fig. 2.4 ($F=1$) have been calculated using the super-operator method with a Lindblad operator set to zero.

2.3 Interacting spinor Bose-Einstein condensates

2.3.1 Mean-field description

Bose-Einstein condensates in dilute gases of weakly interacting particles are customarily described by the Gross-Pitaevskii equation (see e.g. the review article [51] and references therein),

$$i\hbar\dot{\Phi}(\vec{r}, t) = \left(-\frac{\hbar^2\nabla^2}{2m} + V_{\text{ext}}(\vec{r}) + \hbar g|\Phi(\vec{r}, t)|^2 \right) \Phi(\vec{r}, t). \quad (2.44)$$

In this version for a single-component or spin-0 gas, $\Phi(\vec{r}, t)$ is the space- and time-dependent *order parameter* of the condensate, which can be interpreted as a wave function or state vector in the single-particle Hilbert space. The Gross-Pitaevskii equation (2.44) is then identified as the single-particle Schrödinger equation with an additional nonlinear term representing the average effect of all remaining particles on any single one (*mean field*). Formally, the Gross-Pitaevskii equation is derived from the *energy functional*

$$H = \int d^3\vec{r} \left[\Phi^*(\vec{r}) \left(-\frac{\hbar^2\nabla^2}{2m} + V_{\text{ext}}(\vec{r}) \right) \Phi(\vec{r}) + \frac{\hbar}{2}g|\Phi(\vec{r})|^4 \right] \quad (2.45)$$

as the variational derivative with respect to Φ^* . Note that Φ is normalized to the total number of particles N , thus $|\Phi|^2$ is the density of particles.

The interaction of particles, described by a two-body potential $V_{\text{int}}(\vec{r}_1 - \vec{r}_2)$, is reduced to an effective contact interaction $\hbar g\delta(\vec{r}_1 - \vec{r}_2)$ in the *s-wave scattering* limit, applicable in a dilute gas at low energies. The coupling constant $g = \frac{4\pi\hbar a}{m}$ is related⁷ to the s-wave scattering length a .

The Gross-Pitaevskii equation can be cast into dimensionless form [53] by choosing suitable length and time scales,

$$\begin{aligned} \Phi &= \bar{n}\tilde{\Phi} & \bar{n} &= \text{arbitrary} \\ V_{\text{ext}} &= U\tilde{V}_{\text{ext}} & U &= \hbar g\bar{n} \\ \vec{r} &= L\tilde{\vec{r}} & L &= \sqrt{\frac{\hbar}{2mg\bar{n}}} \\ t &= T\tilde{t} & T &= \frac{1}{g\bar{n}} \end{aligned} \quad \text{with} \quad (2.46)$$

resulting in

$$i\partial_{\tilde{t}}\tilde{\Phi} = \left(-\nabla_{\tilde{\vec{r}}}^2 + \tilde{V}_{\text{ext}} + |\tilde{\Phi}|^2 \right) \tilde{\Phi}. \quad (2.47)$$

⁷Note that like the Zeeman parameters p and q , g has the dimension of an angular frequency. As a result, the relation of a and g differs by one \hbar from [51].

The *healing length* $\xi = \sqrt{\frac{\hbar}{2mg\bar{n}}}$ thus emerges naturally as the length scale that makes the Gross-Pitaevskii equation dimensionless, independent of the external potential⁸. The healing length is characterized by a balance of kinetic and interaction energy, $\frac{\hbar^2}{2m\xi^2} = \hbar g\bar{n}$. In situations where both compete, e.g. when the wave function is forced to zero by a hard wall [52] or in the core of a vortex [53], it defines the length scale across which the wave function actually varies.

Generalizing to spin- F particles, $\Phi(\vec{r}, t)$ is replaced by a $(2F + 1)$ -component wave function $\Phi_m(\vec{r}, t)$, $m = -F \dots + F$. If an additional external potential depends on the spin orientation, it is also replaced with a $2F + 1$ -component version; for the time being, we assume that this is *not* necessary, ignoring linear and quadratic Zeeman effect.

The most general interaction term would have $(2F + 1) \times (2F + 1)$ entries, i.e. g becomes a $(2F + 1) \times (2F + 1)$ matrix. Rotational symmetry however allows to greatly reduce the number of parameters [21]: Two identical spin- F particles (bosons, i.e. F is integer) colliding may form a total spin $F_{\text{tot}} = 0, 2, \dots, 2F$ depending on the relative orientation of the colliding particles. Odd F_{tot} are forbidden in the s-wave limit due to total symmetry of the combined spatial and spin wave function. Owing to rotational symmetry, the scattering length depends only on the total spin F_{tot} , i.e. there are $F + 1$ potentially different scattering lengths a_0, \dots, a_{2F} , and the effective interaction potential takes the form

$$V_{\text{int}}(\vec{r}_1 - \vec{r}_2) = \delta(\vec{r}_1 - \vec{r}_2) \frac{4\pi\hbar^2}{m} \sum_{f=0,2,\dots,2F} a_f \mathbf{P}_f, \quad (2.48)$$

where \mathbf{P}_f are projectors on the subspace $F_{\text{tot}} = f$. In order to calculate the spin-dependent mean-field potential, it is useful to rewrite the projectors as products of single-particle spin operators. For $F = 1$ and $F = 2$, the commonly used decompositions are [22, 21, 32]

$$F = 1 : \mathbf{P}_0 = \frac{1}{3}(1 - \vec{\mathbf{F}}_1 \cdot \vec{\mathbf{F}}_2) \quad \mathbf{P}_2 = \frac{1}{3}(2 + \vec{\mathbf{F}}_1 \cdot \vec{\mathbf{F}}_2), \quad (2.49)$$

$$F = 2 : \mathbf{P}_2 = \frac{1}{7}(4 - \vec{\mathbf{F}}_1 \cdot \vec{\mathbf{F}}_2 - 10\mathbf{P}_0) \quad \mathbf{P}_4 = \frac{1}{7}(3 + \vec{\mathbf{F}}_1 \cdot \vec{\mathbf{F}}_2 + 3\mathbf{P}_0). \quad (2.50)$$

In the case of $F = 2$, the projection on total spin $F_{\text{tot}} = 0$ is needed besides the identity operator and $\vec{\mathbf{F}}_1 \cdot \vec{\mathbf{F}}_2$. Alternatively, it is possible to use $\vec{\mathbf{F}}_1^2 \cdot \vec{\mathbf{F}}_2^2$ instead of \mathbf{P}_0 , leading to different expansion coefficients [36].

The interaction potential then takes the form

$$V_{\text{int}}(\vec{r}_1 - \vec{r}_2) = \hbar\delta(\vec{r}_1 - \vec{r}_2)(g_0 + g_1\vec{\mathbf{F}}_1 \cdot \vec{\mathbf{F}}_2 + \frac{5}{4}g_2\mathbf{P}_0) \quad (2.51)$$

with

$$F = 1 : g_0 = \frac{4\pi\hbar}{m} \frac{a_0 + 2a_2}{3} \quad g_1 = \frac{4\pi\hbar}{m} \frac{a_2 - a_0}{3} \quad \frac{5}{4}g_2 = 0 \quad (2.52)$$

$$F = 2 : g_0 = \frac{4\pi\hbar}{m} \frac{4a_2 + 3a_4}{7} \quad g_1 = \frac{4\pi\hbar}{m} \frac{a_4 - a_2}{7} \quad \frac{5}{4}g_2 = \frac{4\pi\hbar}{m} \frac{7a_0 - 10a_2 + 3a_4}{7} \quad (2.53)$$

⁸Other choices are possible, e.g. in a harmonic external potential $V_{\text{ext}} = \frac{1}{2}m\omega^2 r^2$ the oscillator length $a_{\text{ho}} = \sqrt{\frac{\hbar}{m\omega}}$ provides another natural length scale $L = a_{\text{ho}}$ [51]. While in principle equivalent, different choices are more or less useful depending on the physical situation.

and the energy functional leading to the Gross-Pitaevskii equation becomes

$$H = \int d^3\vec{r} \sum_k \left[\Phi_k^*(\vec{r}) \left(-\frac{\hbar^2 \nabla^2}{2m} + V_{\text{ext}}(\vec{r}) \right) \Phi_k(\vec{r}) + \frac{\hbar}{2} \left(g_0 n(\vec{r})^2 + g_1 N^2 |\vec{F}(\vec{r})|^2 + g_2 N^2 |S_0(\vec{r})|^2 \right) \right] \quad (2.54)$$

where

$$n(\vec{r}) \equiv \sum_i |\Phi_i(\vec{r})|^2 \quad (2.55)$$

$$\vec{F} \equiv (F_x, F_y, F_z) \quad \text{and} \quad F_\alpha(\vec{r}) \equiv \frac{1}{N} \sum_{ij} \Phi_i^*(\vec{r}) (F_\alpha)_{ij} \Phi_j(\vec{r}) \quad (2.56)$$

$$S_0(\vec{r}) \equiv \frac{1}{N} (\Phi_{-2} \Phi_2 - \Phi_{-1} \Phi_1 + \Phi_0^2 / 2) \quad (2.57)$$

\vec{F} and S_0 are normalized such that when integrated over space, the result is the average spin and the average spin-singlet amplitude *per particle*. Accordingly, their contribution to the total energy scales with the square of the particle number.

The multicomponent Gross-Pitaevskii equation itself is easily recovered (though lengthy) by taking the derivative of the energy functional,

$$i\hbar \dot{\Phi}_k(\vec{r}, t) = \frac{\partial H}{\partial \Phi_k^*(\vec{r}, t)}. \quad (2.58)$$

The spinor wave function $\Phi_k(\vec{r}, t)$ can always be written as product of two functions, one absorbing the total density and one representing the local spin state,

$$\Phi_k(\vec{r}, t) = \phi(\vec{r}, t) \zeta_k(\vec{r}, t) \quad \text{with} \quad \int d^3r |\phi|^2 = N \quad \text{and} \quad \sum_k |\zeta_k|^2 = 1 \quad (2.59)$$

With this re-definition, the Gross-Pitaevskii equation is the sum of contributions of the total density and of the spin state plus a coupling term,

$$0 = \zeta_k \left\{ -i\hbar \dot{\phi} - \frac{\hbar^2 \nabla^2}{2m} \phi + V_{\text{ext}} \phi + \hbar g_0 |\phi|^2 \phi \right\} \quad (2.60)$$

$$+ \phi \left\{ -i\hbar \dot{\zeta}_k - \frac{\hbar^2 \nabla^2}{2m} \zeta_k + \hbar g_1 |\phi|^2 \sum_\alpha \langle F_\alpha \rangle \sum_l (F_\alpha)_{kl} \zeta_l + \hbar g_2 |\phi|^2 S_0 (-1)^k \zeta_{-k}^* \right\} \quad (2.61)$$

$$- \frac{\hbar^2}{2m} \nabla \phi \cdot \nabla \zeta_k \quad (2.62)$$

with

$$\langle F_\alpha \rangle \equiv \sum_{ij} \zeta_i^* (F_\alpha)_{ij} \zeta_j \quad S_0 \equiv \zeta_{-2} \zeta_2 - \zeta_{-1} \zeta_1 + \zeta_0^2 / 2. \quad (2.63)$$

Each of the terms in curly brackets $\{\cdot\}$ is a Gross-Pitaevskii equation of its own. Neglecting the coupling term (2.62), the Gross-Pitaevskii equation for the total density (2.60) can be solved without knowledge of the spin state ζ_k , and then is a parameter only in the Gross-Pitaevskii equation for the spin state (2.61).

By analogy with the *healing length* $\xi = \sqrt{\frac{\hbar}{2mg_n}}$ that characterizes the competition between kinetic energy and interaction energy of the *total density* ϕ , the *spin healing length* may be defined for the *spin state* from (2.61). Since in $F \geq 2$ there are several ways the spin state can vary in space, each weighted with a different interaction parameter g_n , this definition is arbitrary to some extent. For ^{87}Rb $F = 2$, g_1 and g_2 are of the same order of magnitude, but the states considered in this work turn out to have small S_0 and are thus insensitive to g_2 . We therefore choose to define the spin healing length using g_1 , $\xi_s = \sqrt{\frac{\hbar}{2mg_1n}}$.

2.3.2 Single-mode approximation (SMA)

The Gross-Pitaevskii equation for the spin- F gas is significantly simplified by the assumption that *spatial and spin degrees of freedom decouple*. This is expressed in a product ansatz for the wave function,

$$\Phi_k(\vec{r}, t) \equiv \phi(\vec{r})\zeta_k(t) \quad \text{with} \quad \int d^3\vec{r}|\phi|^2 = N \quad \text{and} \quad \sum_k |\zeta_k|^2 = 1 \quad (2.64)$$

This ansatz is known as the *single mode approximation* [35] (also used implicitly in [22, 21]), and it differs from the general re-definition (2.59) by the assumptions that ϕ is fixed in time and ζ_k does not vary in space. This approximation is generally considered reasonable if the spin-dependent part of the interaction energy is small, i.e. $g_{1,2} \ll g_0$ [35] (also compare [73] for a more detailed analysis of the validity of the SMA). Summing over m_F states and integrating over space, respectively, the energy functional (2.54) decomposes into a *spin-independent part* that takes the same form as for a single-component gas,

$$H_0 = \int d^3\vec{r} \phi^*(\vec{r}) \left(-\frac{\hbar^2 \nabla^2}{2m} + V_{\text{ext}}(\vec{r}) + \frac{\hbar}{2} g_0 |\phi(\vec{r})|^2 \right) \phi(\vec{r}), \quad (2.65)$$

and a *spin-dependent part* that takes the average density $\langle n \rangle \equiv \int |\phi|^4 d^3\vec{r} / N$ as a parameter,

$$H_{\text{spin}} = \frac{\hbar}{2} N \langle n \rangle \left(g_1 \langle \vec{F} \rangle^2 + g_2 |S_0|^2 \right) \quad (2.66)$$

with

$$\langle F_\alpha \rangle \equiv \sum_{ij} \zeta_i^* (F_\alpha)_{ij} \zeta_j \quad S_0 \equiv \zeta_{-2} \zeta_2 - \zeta_{-1} \zeta_1 + \zeta_0^2 / 2. \quad (2.67)$$

Since both parts are connected only by the weighting factor $\langle n \rangle$ in H_{spin} , the total ground state can be found by minimizing them independently. The spatial wave function in the ground state thus can be found as the solution of a time-independent single-component Gross-Pitaevskii equation, using methods well known from scalar Bose-Einstein condensates such as the Thomas-Fermi approximation. Minimizing H_{spin} on the other hand is a finite dimensional problem and as such much easier to solve.

As an example, for a Bose-Einstein condensate in a harmonic trap the Thomas-Fermi approximation predicts an inverted parabolic density $|\phi(\vec{r})|^2$. In this case the average density is $\langle n \rangle = \frac{4}{7} n_0$, where n_0 is the peak density at the center of the trap. n_0 is related to the chemical potential μ through $n_0 = \mu / g_0$.

Dynamics in single mode approximation is equivalent to the homogeneous spinor Bose gas if we assume that $\phi(\vec{r})$ remains fixed, e.g. in the ground state of H_0 . This assumption is plausible if the spin-independent interaction energy is much larger than the

spin-dependent one, effectively freezing out spatial degrees of freedom. The time dependent Gross-Pitaevskii equation for the spin components ζ_k is obtained from (2.66) by differentiation with respect to ζ_k^* ,

$$i\hbar N \dot{\zeta}_k = \frac{\partial H_{\text{spin}}}{\partial \zeta_k^*}. \quad (2.68)$$

The particle number N on the left hand side is a result of the normalization of the spatial wave function, $\int |\phi(\vec{r})|^2 = N$. It cancels with a corresponding factor in H_{spin} , such that the equations of motion for the spinor components do not depend on the absolute particle number.

The Zeeman effect enters into (2.54) as an additional external potential which is homogeneous in space but depends on spin orientation, $V_{\text{ZE},mm'}(\vec{r}) = -\hbar pm \delta_{mm'} + \hbar q m^2 \delta_{mm'}$, leading to an additional term in the spin-dependent energy functional,

$$H_{\text{spin}} = \frac{\hbar}{2} N \langle n \rangle \left(g_1 \langle \vec{F} \rangle^2 + g_2 |S_0|^2 \right) + \hbar N \left(-p \langle F_z \rangle + q \langle F_z^2 \rangle \right) \quad (2.69)$$

with $\langle F_z^2 \rangle \equiv \sum_{ijk} \zeta_i^* (F_z)_{ik} (F_z)_{kj} \zeta_j$.

The resulting equations of motion [74] are cited here for reference (also compare [75] (F=1) and [76] (F=2)), with the additional shorthand $|A_F|^2 = \langle F_x \rangle^2 + \langle F_y \rangle^2$:

$$A_2 = 2(\zeta_{+2} \zeta_{+1}^* + \zeta_{-2}^* \zeta_{-1}) + \sqrt{6}(\zeta_{+1} \zeta_0^* + \zeta_{-1}^* \zeta_0) \quad (2.70)$$

$$A_1 = 2(\zeta_{+1} \zeta_0^* + \zeta_{-1}^* \zeta_0) \quad (2.71)$$

Spin equations of motion for $F = 2$

$$\left. \begin{aligned} i\dot{\zeta}_{+2} &= \frac{g_1 \langle n \rangle}{2} [+4F_z \zeta_{+2} + 2A_2 \zeta_{+1}] + \frac{g_2 \langle n \rangle}{2} S_0 \zeta_{-2}^* + (-2p + 4q) \zeta_{+2} \\ i\dot{\zeta}_{+1} &= \frac{g_1 \langle n \rangle}{2} [+2F_z \zeta_{+1} + \sqrt{6} A_2 \zeta_0 + 2A_2^* \zeta_{+2}] - \frac{g_2 \langle n \rangle}{2} S_0 \zeta_{-1}^* + (-p + q) \zeta_{+1} \\ i\dot{\zeta}_0 &= \frac{g_1 \langle n \rangle}{2} [\sqrt{6} (A_2 \zeta_{-1} + A_2^* \zeta_{+1})] + \frac{g_2 \langle n \rangle}{2} S_0 \zeta_0^* \\ i\dot{\zeta}_{-1} &= \frac{g_1 \langle n \rangle}{2} [-2F_z \zeta_{-1} + \sqrt{6} A_2^* \zeta_0 + 2A_2 \zeta_{-2}] - \frac{g_2 \langle n \rangle}{2} S_0 \zeta_{+1}^* + (+p + q) \zeta_{-1} \\ i\dot{\zeta}_{-2} &= \frac{g_1 \langle n \rangle}{2} [-4F_z \zeta_{-2} + 2A_2^* \zeta_{-1}] + \frac{g_2 \langle n \rangle}{2} S_0 \zeta_{+2}^* + (+2p + 4q) \zeta_{-2} \end{aligned} \right\} F = 2 \quad (2.72)$$

Spin equations of motion for $F = 1$

$$\left. \begin{aligned} i\dot{\zeta}_{+1} &= g_1 \langle n \rangle [+F_z \zeta_{+1} + A_1 \zeta_0] + (-p + q) \zeta_{+1} \\ i\dot{\zeta}_0 &= g_1 \langle n \rangle [A_1^* \zeta_{+1} + A_1 \zeta_{-1}] \\ i\dot{\zeta}_{-1} &= g_1 \langle n \rangle [-F_z \zeta_{-1} + A_1^* \zeta_0] + (+p + q) \zeta_{-1} \end{aligned} \right\} F = 1 \quad (2.73)$$

Note that these equations of motion conserve

- the norm $\sum_m |\zeta_m|^2$,
- the z -component of the spin $F_z = \sum_m m |\zeta_m|^2$,
- the energy H_{spin} .

Additionally, the equations are invariant under the transformation $\mathbf{T} : \zeta_{+m} \rightarrow \zeta_{-m}$, which becomes obvious if we bear in mind that under this transformation, $F_z \rightarrow -F_z$ and $A_F \rightarrow A_F^*$ while S_0 is invariant. T is in fact nothing but the equivalent of *parity* in spin space. Obviously, \mathbf{T} is its own inverse, $\mathbf{T}^{-1} = \mathbf{T}$.

The spin Hilbert space \mathcal{H} can be decomposed into a *symmetric subspace* \mathcal{H}^s and an *antisymmetric subspace* \mathcal{H}^a with respect to the parity operator \mathbf{T} . Each of the subspaces is a vector space as is easily verified, \mathcal{H}^s and \mathcal{H}^a are orthogonal to each other, and the full Hilbert space is the direct sum of both, $\mathcal{H} = \mathcal{H}^s \oplus \mathcal{H}^a$. Writing the right hand side of (2.72) or (2.73) as a *nonlinear* operator $i\dot{|\zeta\rangle} = \mathcal{F}(|\zeta\rangle)$, the fact that the equation of motion conserves parity means that

$$\mathcal{F}(\mathbf{T}|\zeta\rangle) = \mathbf{T}\mathcal{F}(|\zeta\rangle). \quad (2.74)$$

Thus, if $|\zeta\rangle$ is an eigenstate of \mathbf{T} , $\mathbf{T}|\zeta\rangle = \pm|\zeta\rangle$, it follows that the time derivative $i\dot{|\zeta\rangle} = \mathcal{F}(|\zeta\rangle)$ is also an eigenstate of \mathbf{T} with the same eigenvalue. In other words, starting in one of the subspaces, the evolution is *confined to this subspace* for all times. Note however that due to the nonlinearity of \mathcal{F} it is generally *not* possible to calculate the dynamics of an arbitrary state by decomposing it into its symmetric and antisymmetric part.

The situation is different if the equations of motion are *linearized* in the neighborhood of a certain state $|\bar{\zeta}\rangle$ that is stationary or part of a trajectory. The dynamics of a small deviation $|\epsilon\rangle$ is given by the *Jacobi matrix* of F taken at $|\bar{\zeta}\rangle$,

$$\dot{\epsilon}_k = \sum_j \left. \frac{\partial F_k}{\partial \zeta_j} \right|_{\bar{\zeta}} \epsilon_j \quad \text{or} \quad i\dot{|\epsilon\rangle} = \partial F|\epsilon\rangle. \quad (2.75)$$

Now ∂F is a linear operator commuting with T . The symmetric and antisymmetric component of an arbitrary deviation will evolve separately, without influence on each other. ∂F can be diagonalized in the symmetric and antisymmetric subspace separately, which is important for the calculations of Lyapunov exponents (see Chapter 7 and Chapter B).

In this work, the focus will be on dynamics in the symmetric subspace, and the equations of motion for this special case will be used frequently. Note that $F_z = 0$ and $A_F = A_F^*$ in this case.

Symmetric spin equations of motion

$$\left. \begin{aligned} i\dot{\zeta}_2 &= \frac{g_1\langle n \rangle}{2} A_2 2\zeta_1 + \frac{g_2\langle n \rangle}{2} S_0 \zeta_2^* + (-2p + 4q)\zeta_2 \\ i\dot{\zeta}_1 &= \frac{g_1\langle n \rangle}{2} A_2 \left[\sqrt{6}\zeta_0 + 2\zeta_2 \right] - \frac{g_2\langle n \rangle}{2} S_0 \zeta_1^* + (-p + q)\zeta_1 \\ i\dot{\zeta}_0 &= \frac{g_1\langle n \rangle}{2} A_2 2\sqrt{6}\zeta_1 + \frac{g_2\langle n \rangle}{2} S_0 \zeta_0^* \end{aligned} \right\} F = 2 \quad (2.76)$$

$$\left. \begin{aligned} i\dot{\zeta}_1 &= g_1\langle n \rangle A_1 \zeta_0 + (-p + q)\zeta_1 \\ i\dot{\zeta}_0 &= g_1\langle n \rangle 2A_1 \zeta_1 \end{aligned} \right\} F = 1 \quad (2.77)$$

$$\begin{aligned} A_2 &= 4\text{Re} \zeta_2 \zeta_1^* + 2\sqrt{6}\text{Re} \zeta_1 \zeta_0^* \\ A_1 &= 4\text{Re} \zeta_1 \zeta_0^* \\ S_0 &= \zeta_2^2 - \zeta_1^2 + \zeta_0^2/2 \end{aligned} \quad (2.78)$$

Table 2.1: Recently calculated scattering lengths and measured differences cited from [78]. Calculated and measured differences agree within error-bars; for $F = 1$, the measurement is significantly more precise, while for $F = 2$ errors are about the same.

predicted scattering lengths			measured differences		
	$F = 1$	$F = 2$		$F = 1$	$F = 2$
a_0/a_B	101.78 ± 0.2	87.93 ± 0.2	$(a_2 - a_0)/a_B$	-1.07 ± 0.09	3.51 ± 0.54
a_2/a_B	100.40 ± 0.1	91.28 ± 0.2	$(a_4 - a_2)/a_B$	—	6.95 ± 0.35
a_4/a_B	—	98.98 ± 0.2			

2.3.3 Ground states and phase separation

The mean-field ground state of an interacting spinor condensate is defined as the spinor $|\zeta_0\rangle$ that minimizes the energy functional. Of course, the ground state spinor may be ambiguous; in particular, rotational symmetry will lead to degeneracy. The ground state is always stationary, i.e. $\partial H_{\text{spin}}/\partial \zeta_k^* = 0$ (2.68), however there may be stationary states that are *not* ground states, in particular, since the spin energy functional is bounded both from below and above, there will also be a stationary state of *maximum* energy.

The ground states of the mean-field Hamiltonian (2.69) *without* quadratic Zeeman effect have been first analyzed in [22, 21] ($F = 1$) and [32] ($F = 2$). Depending on the scattering lengths, $F = 1$ spinor gases at zero magnetic field can be classified into either *ferromagnetic* (ground state is stretched) or *anti-ferromagnetic* (also referred to as *polar*) ground state has ($\vec{F} = 0$). For $F = 2$ gases, a so-called *cyclic* phase comes into play. This phase is distinguished by a non-vanishing spin-singlet pair amplitude ($S_0 \neq 0$) [32]. For alkali gases, the classification as either ferromagnetic, anti-ferromagnetic or cyclic is a property of the atomic species and the hyperfine state under study.

At finite magnetic field, these phases are modified due to the quadratic Zeeman effect; also, conservation of magnetization restricts the accessibility of the absolute ground state in typical experimental situations. The state of lowest energy depending on magnetization and magnetic field is identified in the *phase diagram* of a given atomic species. Phase diagrams for $F = 2$ have been first calculated in Holger Schmaljohann's PhD thesis [36]; The ground states for $F = 1$ have been worked out in [23]. *Structured* ground states arise from field gradients and can be understood on the basis of phase diagrams in a local density approximation [23, 77].

According to the most recent precision measurements [78, 79] of scattering lengths as well as several experiments aimed directly at the observation of the ground state in a spinor condensate,

- ^{87}Rb $F = 1$ is *ferromagnetic* [37, 50, 2],
- ^{87}Rb $F = 2$ is most probably *anti-ferromagnetic*, but very close to cyclic [7, 1].

Values for the scattering lengths a_f and coupling coefficients g_i are given in Tab. 2.1 and Tab. 2.2, respectively. For all calculations and fits in this work, the measured values of g_1 and g_2 from Tab. 2.2 have been used; the value of g_0 has been calculated from the predicted scattering lengths of Tab. 2.1.

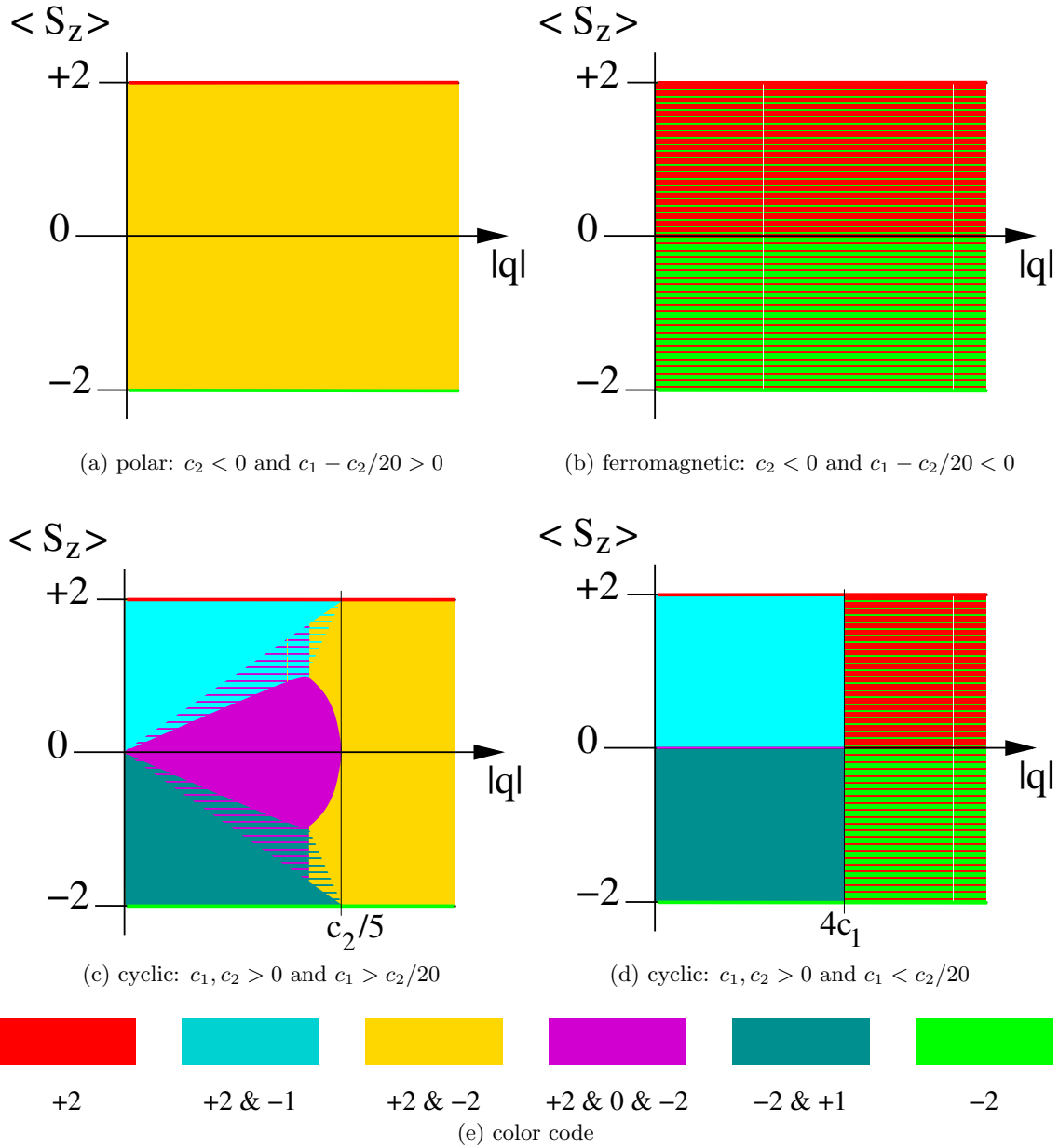


Figure 2.6: Phase diagrams for the ground state of $F = 2$ spinor condensates (from [36]). In this graph $\langle S_z \rangle \equiv F_z$ is the preserved z -component of the spin or magnetization, while $c_1 \equiv g_1 \langle n \rangle / 2$ and $c_2 \equiv g_2 \langle n \rangle$. Solid colored areas indicate that the ground state is a mixture of m_F -states, while in hatched areas components are immiscible and phase separation occurs.

Table 2.2: Calculated and measured coupling parameters, cited from [78]. g_2 is hard to determine: as the authors of [78] note, depending on details of the fitting procedure, even the sign of g_2 may change. Note that $g_2 \equiv 4c_2$ when comparing values to [78].

predicted and measured coupling parameters				
	measured		predicted	
	$F = 1$	$F = 2$	$F = 1$	$F = 2$
$g_1/(4\pi a_B \hbar/m)$	-0.36 ± 0.04	$+0.99 \pm 0.06$	-0.46	$+1.10$
$g_2/(4\pi a_B \hbar/m)$	—	-2.12 ± 2.32	—	-0.20
$g_0/(4\pi a_B \hbar/m)$	—	—	100.86	94.58
$4\pi a_B \hbar/m = 2\pi \times 7.73 \times 10^{-14} \text{ Hz cm}^3$				

2.3.4 Coherent dynamics

The solution of the equations of motion (2.73) and (2.72) is in general rather complicated due to their nonlinearity. It is possible, however, to obtain analytical results in some special cases.

For $F = 1$, conservation of spin and energy as well as normalization and global phase invariance reduce the number of degrees of freedom to just two, e.g. the population ρ_o of $m_F = 0$ and a relative phase $\theta \equiv \theta_{+1} + \theta_{-1} - 2\theta_0$ [75], where $\zeta_m = \sqrt{\rho_m} e^{i\theta_m}$. This system is integrable, and in fact for the particular initial condition $\zeta(0) = \zeta_{\pi/2}$ an analytic solution can be obtained [74, 2]. The time-dependent spinor amplitudes can be written in terms of Jacobi elliptic functions [80]

$$\zeta_0(t) = \frac{s}{\sqrt{2}} \left[\frac{(1-k) \text{sn}_k(\frac{qt}{2})}{1-k \text{sn}_k^2(\frac{qt}{2})} - \frac{i \text{cn}_k(\frac{qt}{2}) \text{dn}_k(\frac{qt}{2})}{1+k \text{sn}_k^2(\frac{qt}{2})} \right] \quad (2.79a)$$

$$\zeta_{\pm}(t) = \mp \frac{s e^{\pm i p t}}{2} \left[\frac{\text{cn}_k(\frac{qt}{2}) \text{dn}_k(\frac{qt}{2})}{1-k \text{sn}_k^2(\frac{qt}{2})} - \frac{i(1+k) \text{sn}_k(\frac{qt}{2})}{1+k \text{sn}_k^2(\frac{qt}{2})} \right] \quad (2.79b)$$

where $s = \exp(-i(g_1 \langle n \rangle - q)t/2)$ is a dynamic global phase and $k = g_1 \langle n \rangle / q$ is the ratio of interaction energy to quadratic Zeeman effect. For the directly measurable populations, the solution simplifies to

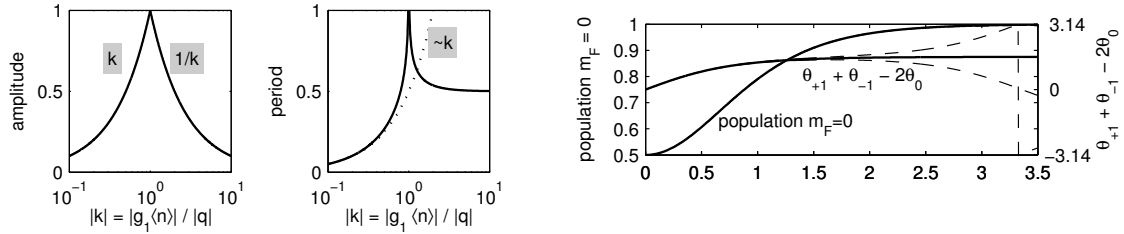
$$|\zeta_0(t)|^2 = (1 - k \text{sn}_k^2(qt))/2, \quad (2.80a)$$

$$|\zeta_{\pm 1}(t)|^2 = (1 + k \text{sn}_k^2(qt))/4. \quad (2.80b)$$

Fig. 2.7 illustrates the analytic solution across a wide range of k and in the particular case $k = 1$.

For small $|k| \ll 1$, the Jacobi elliptic functions can be approximated by ordinary trigonometric ones, i.e., $\text{sn}_k(x) \approx \sin(x)$, $\text{cn}_k(x) \approx \cos(x)$, $\text{dn}_k(x) \approx 1$. Thus, the populations of Eqs. (2.80) oscillate with an amplitude given by k , and a period which is π/q for small $|k|$.

In the opposite regime, $|k| \gg 1$, the identity $\text{sn}_k(x) = \frac{1}{k} \text{sn}_{1/k}(kx)$ leads to another trigonometric approximation, $\text{sn}_k(x) \approx \sin(kx)/k$. In this regime, populations oscillate with amplitude $1/k$ and period $\pi/(g_1 \langle n \rangle)$.



(a) Amplitude and period of population oscillations, according to the analytic solution (2.80). The period diverges to infinity at $|k| = 1$.

(b) Population and phase dynamics at and around resonance $|k| = 1.00 \pm 0.01$, starting from $\zeta_{\pi/2}$.

Figure 2.7: Resonance in $F = 1$ spin dynamics starting from the fully transversely magnetized state.

The crossover region $|k| \approx 1$ exhibits a maximum of the amplitude, while the oscillation period diverges. In other words, at $|k| = 1$ the evolution becomes aperiodic, and the $m_F = 0$ population asymptotically approaches 1. The experimental observation of this spin dynamics resonance is a central result of the present work (Chapter 5).

The analytic solution also offers a clear way to determine the magnetic properties of the system as k is negative/positive for ferromagnetic/anti-ferromagnetic systems, resulting in an increase/decrease of $|\zeta_0|^2$ at the beginning of the oscillation (if $q > 0$ as is the case for ^{87}Rb $F = 1$).

Owing to the larger number of degrees of freedom (Chapter 7), the equations of motion for ^{87}Rb $F = 2$ are not integrable and no exact analytic solution exists. However, in the limiting cases of very small and very large quadratic Zeeman effect q , approximate solutions for the initial condition $\zeta(0) = \zeta_{\pi/2}$ have been obtained [74, 1].

In the Zeeman regime ($q \rightarrow \infty$), the populations are, to first order in g_1 and g_2 ,

$$|\zeta_0|^2 = \frac{3}{8} \left\{ 1 + \frac{g_1 \langle n \rangle}{2q} \left[2(1 - \cos(2qt)) + \frac{1}{2}(1 - \cos(4qt)) \right] - \frac{g_2 \langle n \rangle}{2q} \left[\frac{1}{4}(1 - \cos(2qt)) - \frac{1}{64}(1 - \cos(8qt)) \right] \right\} \quad (2.81a)$$

$$|\zeta_1|^2 = \frac{1}{4} \left\{ 1 - \frac{g_1 \langle n \rangle}{2q} \left[\frac{3}{4}(1 - \cos(2qt)) - \frac{1}{12}(1 - \cos(6qt)) \right] + \frac{g_2 \langle n \rangle}{2q} \left[\frac{3}{16}(1 - \cos(2t)) - \frac{1}{48}(1 - \cos(6qt)) \right] \right\} \quad (2.81b)$$

$$|\zeta_2|^2 = \frac{1}{16} \left\{ 1 - \frac{g_1 \langle n \rangle}{2q} \left[3(1 - \cos(2qt)) + \frac{3}{2}(1 - \cos(4qt)) + \frac{1}{3}(1 - \cos(6qt)) \right] + \frac{g_2 \langle n \rangle}{2q} \left[\frac{1}{12}(1 - \cos(6qt)) - \frac{3}{64}(1 - \cos(8qt)) \right] \right\} \quad (2.81c)$$

Note that all terms related to g_2 have pre-factors roughly one order of magnitude smaller than those related to g_1 . As a result, these terms are minor contributions only, even if $g_2 \approx g_1$, a possibility indicated by recent measurements [78], in contrast to earlier

predictions (compare Tab. 2.2). The fundamental frequency of oscillation is q/π with an amplitude $\propto \frac{g_1 \langle n \rangle}{q}$, both as in the case of $F = 1$.

In the opposite limit, the interaction regime $q \rightarrow 0$, the approximate populations are given by

$$|\zeta_0|^2 = \frac{3}{8} \left[1 + \frac{q}{2g_1 \langle n \rangle} (1 - \cos(4g_1 \langle n \rangle t)) \right] \quad (2.82a)$$

$$|\zeta_1|^2 = \frac{1}{4} \quad (2.82b)$$

$$|\zeta_2|^2 = \frac{1}{16} \left[1 - \frac{3q}{2g_1 \langle n \rangle} (1 - \cos(4g_1 \langle n \rangle t)) \right] \quad (2.82c)$$

In this limit and to first order, terms related to g_2 drop out completely, which can be understood from the fact that $S_0 = 0$ for the initial state $\zeta_{\pi/2}$. The frequency of oscillation $2g_1 \langle n \rangle / \pi$ is determined by the same mean-field interaction term as in $F = 1$.

2.3.5 The four-wave mixing picture

In the following we will develop some more qualitative physical insights by an interpretation of the resonance phenomenon in terms of *phase matching* in four-wave mixing (see Fig. 2.8). We will do this by means of $F = 1$ as an example; the concept, however, applies to $F = 2$ as well.

In contrast to nonlinear optics or four-wave mixing in single component condensates [81] we do not deal with wave vector or momentum modes [82, 83] but with spin modes. This view is justified, as we are considering trapped samples in a single momentum state. Spin mixing dynamics is then formally equivalent to collinear optical four-wave mixing: electro-magnetic modes characterized by frequencies ϖ_m and corresponding wave numbers $k_m = n\varpi_m/c$ (with index of refraction n) can be identified with m_F states $|m\rangle$ and their linear Zeeman energies $\omega_m = -pm$. Both kinds of modes have slowly-varying amplitudes $A_m(z)$ or $\zeta_m(t)$, compared to their wavelength or Larmor frequency, respectively. Time in the spinor case takes the role of the z -coordinate in optics. The quadratic Zeeman effect qm^2 plays the role of the dispersion $n(\varpi)$ in a linear medium, and finally spin interactions are analogous to $\chi^{(3)}$ nonlinear effects in suitable media [35, 84]. Fig. 2.8 summarizes these relationships.

Along these lines, we identify in the $F = 1$ spinor equations of motion (2.73), e.g. for ζ_{+1} , linear dispersion, *self- and cross phase modulation* terms and *four-wave mixing* terms:

$$\begin{aligned} i\dot{\zeta}_{+1} &= g_1 \langle n \rangle |\zeta_{+1}|^2 \zeta_{+1} && \textit{self-PM} \\ &+ g_1 \langle n \rangle [2|\zeta_0|^2 - |\zeta_{-1}|^2] \zeta_{+1} && \textit{cross-PM} \\ &+ g_1 \langle n \rangle 2\zeta_0 \zeta_0 \zeta_{-1}^* && \textit{four-wave mixing} \\ &+ q\zeta_{+1} && \textit{linear dispersion} \end{aligned} \quad (2.83)$$

p has been eliminated by choosing a suitable rotating frame, in analogy to choosing $k = \frac{\sqrt{\epsilon}}{c}\varpi$ for electro-magnetic modes. In both cases, the effect is to cancel trivial rapid oscillations.

The exact optical analogue to $F = 1$ spin dynamics is *degenerate collinear four-wave mixing* with three modes⁹ $\varpi_{+1}, \varpi_0, \varpi_{-1}$ and $2\varpi_0 = \varpi_{+1} + \varpi_{-1}$. The optical equations of

⁹Note that the term “four-wave mixing” refers to products of the form $A_2 A_3 A_4^*$ appearing at the right hand side of \dot{A}_1 , regardless how many *distinguishable* modes are involved.

spinor $\zeta_m(t)e^{i\omega_m t}$	Index $\pm, 0$	slowly-varying amplitude $\zeta_m(t)$	Rotating frame $\omega_m = mp$	time t
electro-magnetic $A_m(z)e^{i(k_m z - \varpi_m t)}$	frequency ϖ_m	slowly-varying amplitude $A_m(z)$	wave number $k_m = \frac{n}{c}\varpi_m$	distance z

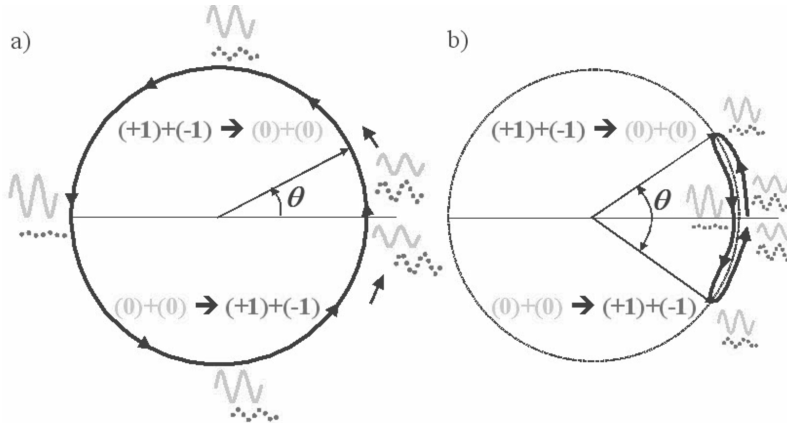


Figure 2.8: Four-wave mixing picture. TOP: Comparison of terms. BOTTOM: Schematic representation in a) the quadratic Zeeman regime and b) the mean field regime. The direction of spin mixing is indicated in the upper and lower half of the circle symbolizing the relative phase θ . For $\theta > 0$ the (0) mode (upper waves) get populated, while for $\theta < 0$ the (+1) and (-1) mode (lower waves) increase.

motion for this case are worked out in Appendix C. The equations of motion for $F = 2$ also contain products of three amplitudes only that can be classified in a similar way. In the following, both the spin component $m_F = m$ and the electro-magnetic mode ϖ_m will be referred to as (m) .

In view of the optical analogy it is obvious, that phase matching considerations are essential to understand the resonance in spinor four-wave mixing. The important point is, that the value of the relative phase of the initial and final modes determines the direction of wave mixing. In our case the (0) wave will be populated if the combined phase of the (+1) + (-1) waves is ahead of twice the (0) wave phase, i.e. $\theta = \theta_{+1} + \theta_{-1} - 2\theta_0 \in [0.. \pi]$ and it will be depopulated, if $\theta \in [\pi..2\pi]$ (modulo 2π).

In our system, the competition between mean field driven dephasing or *self- and cross-phase modulation* (tending to decrease θ) and quadratic Zeeman shift or *linear dispersion* (tending to increase θ) determines the evolution of the system. Most importantly the evolution depends on the relative size of the quadratic Zeeman energy shift and the maximally achievable mean field shifts, as shown in Fig. 2.8. For large magnetic fields, i.e. always negligible mean field energy shifts, θ will continuously grow, i.e. the (± 1) wave evolves faster than the (0) wave, and the population transfer shows an oscillatory behavior depending on which wave is lagging behind at which instant (Fig. 2.8a). In this regime the oscillation period is expected to be given by $\frac{\pi}{q}$. Furthermore the oscillation amplitude, which depends on the unidirectional mixing time, should be proportional to this period.

For small magnetic fields the mean field energy shift grows with increasing population in the (0) wave, until it exceeds the quadratic Zeeman shift and thus reverses the evolution of θ , i.e. the (0) wave will speed up and decrease its lag behind the (± 1) wave, eventually overtaking it. In this case θ will remain confined in the interval $[-\pi.. \pi]$ and oscillate

around $\theta = 0$ (Fig. 2.8b). In this regime the population oscillation amplitude is expected to decrease with decreasing q , i.e. at lower magnetic field, as less population transfer is necessary to create a mean field energy of the order of the quadratic Zeeman shift.

In the resonance region at intermediate magnetic field, the relative movement of the (0) and (± 1) waves is very slow, with θ being on the border of oscillation and continuous increase. This leads to long time unidirectional spin mixing and thus maximum amplitude.

2.3.6 Beyond SMA

In single-mode approximation, the complexity of a multi-component Bose-Einstein condensate, e.g. a spinor condensate, is reduced to a finite number of *internal* degrees of freedom. This approach has been very successful in advancing our understanding of spinor BEC, and in predicting and explaining fundamental aspects of its dynamics. However, it remains an approximation of limited validity. Both usefulness and limitations of the SMA become clear in our experiments (see Chapter 5 and Chapter 6).

In many cases, and in particular in our experiments, the initial state prepared by various techniques of spin manipulation is ideally *homogeneous*, in the sense that it complies to the single-mode paradigm. Small spatial fluctuations may however be expected from technical imperfections (such as gradients of magnetic or radio frequency field, see Section 3.4) as well as finite temperature or even quantum fluctuations, both not covered by the usual mean-field description of a condensate in terms of a wave function (Section 2.3.1). We will thus focus on the question how a (nearly) homogeneous state may develop into a strongly structured one, a phenomenon known as *spontaneous pattern* or *structure formation*.

Pattern formation in spatially extended nonlinear systems is an ubiquitous phenomenon and subject of ongoing research. A common mechanism for spontaneous pattern formation is *linear instability* of a homogeneous or continuous-wave solution: linearizing the equations of motion around the homogeneous stationary state¹⁰, one obtains a linear wave equation for small deviations. Expanding in a suitable basis of modes such as plain waves $e^{i(kx-\omega t)}$, the wave equation becomes diagonal with a dispersion relation $\omega(k)$ that can be complex in general. The imaginary part of the frequency ω describes *damping* ($\text{Im } \omega < 0$) or *exponential growth* ($\text{Im } \omega > 0$). In the latter case, the corresponding mode is *linearly unstable* and an arbitrarily small initial population will grow to a significant amplitude in finite time. Once a mode has grown to a point where it can no longer be considered a small deviation, nonlinear dynamics takes over and stabilizes the pattern at some finite amplitude. The geometry and size of the pattern is in good approximation given by the *most unstable mode*.

In the context of Bose-Einstein condensates, the linear stability analysis can be carried out classically on the basis of the Gross-Pitaevskii equation alone (see e.g. the review paper [85] which is however limited to single-component BEC), or quantum-mechanically as a Bogoliubov analysis (e.g. [86] where the two-component case is treated). In any case, as is generally true in pattern forming systems, it is essential to take into account the kinetic energy. It is the balance of kinetic and interaction energy that distinguishes certain modes, a fact that is also reflected by the observation that generally the *healing length* $\xi = \sqrt{\frac{\hbar}{2mgn}}$ defines the scale of the spatial modulations.¹¹ This is in contrast to the situation discussed

¹⁰The argument can be extended to homogeneous trajectories and is then analogous to the concept of Lyapunov exponents, where the tangential space now comprises inhomogeneous deviations as well.

¹¹Depending on whether modulations of the total density or of the spin composition are of interest, $g = |g_0|$ or $g = |g_1|$, respectively; n is the typical particle density. At a typical density of $1 \times 10^{14} \text{ cm}^{-3}$,

in [23, 77] (see Section 2.3.3), where the width of domain boundaries but not the size of the domains is determined by the spin healing length.

As an example illustrating the concepts and implications of dynamical instability, consider an anti-ferromagnetic ^{87}Rb $F = 2$ condensate in the $m_F = 0$ state, $\zeta = (0, 0, 1, 0, 0)$. Following [76], there are two degenerate Bogoliubov modes $e^{i(kx - \omega(k)t)}$ proportional to $(0, 1, 0, 0, 0)$ and $(0, 0, 0, 1, 0)$, respectively, with eigen-energies

$$\omega^2(k) = (\epsilon_k + q)(\epsilon_k + q + 6g_1\langle n \rangle - \frac{2}{5}g_2\langle n \rangle) \quad \text{where} \quad \epsilon_k = \frac{\hbar}{2m}k^2 \quad (2.84)$$

These modes can grow exponentially in time if $\omega^2(k) < 0$. ω^2 as a function of ϵ_k describes a parabola with two zeros, $-q$ and $-q + 6g_1\langle n \rangle - \frac{2}{5}g_2\langle n \rangle$, and is negative for

$$|q| - 6|g_1|\langle n \rangle - \frac{2}{5}|g_2|\langle n \rangle < \epsilon_k < |q|, \quad (2.85)$$

where the correct signs of the parameters ($q < 0, g_1 > 0, g_2 < 0$) have been taken into account explicitly. The minimum of the parabola is at $\epsilon_k^0 = |q| - 3\langle n \rangle (|g_1| + \frac{1}{12}|g_2|)$. The interaction parameters g_1 and g_2 can be combined into an effective parameter $\bar{g} = |g_1| + \frac{1}{12}|g_2|$ that can be used to define a corresponding spin healing length $\bar{\xi} = \sqrt{\frac{\hbar}{2m\bar{g}\langle n \rangle}}$. This healing length is a natural scale of the wavelength $\lambda = 2\pi/k$ of a given mode.

Since $\epsilon_k \geq 0$, several cases have to be distinguished, depending on the sign of the lower limit $|q| - 6\bar{g}\langle n \rangle$ and ϵ_k^0 .

- If $3\bar{g}\langle n \rangle > |q|$, the minimum of the parabola is on the negative ϵ_k -axis and physically not accessible. The fastest growing mode in this case is the homogeneous $k = 0$ mode. Wave vectors up to $k = |q|$, corresponding to a minimum wavelength $\lambda_{\min} = 2\pi\sqrt{\frac{\hbar}{2m|q|}}$, are also unstable and may produce patterns at the scale of

$$\frac{\lambda_{\min}}{\bar{\xi}} = 2\pi\sqrt{\frac{\bar{g}\langle n \rangle}{q}}. \quad (2.86)$$

- For zero magnetic field $q = 0$, $m_F = 0$ is stable with respect to the considered mode¹² at any finite wavelength or $k > 0$. The homogeneous mode $k = 0$ is marginally stable.
- If $3\bar{g}\langle n \rangle < |q| < 6\bar{g}\langle n \rangle$, the fastest growing mode is given by ϵ_k^0 and has a wavelength

$$\frac{\lambda_0}{\bar{\xi}} = \frac{2\pi}{\sqrt{\frac{|q|}{\bar{g}\langle n \rangle} - 3}}. \quad (2.87)$$

The homogeneous mode $k = 0$ is still unstable, too.

- If $|q| > 6\bar{g}\langle n \rangle$, the homogeneous mode is no longer unstable. A linear stability analysis *not* taking into account the kinetic energy, e.g. of the SMA equations of motion, will falsely suggest that $m_F = 0$ is stable at high magnetic field. The Bogoliubov analysis reveals that this is not true – $m_F = 0$ is unstable for any finite magnetic field, and in the present case the fastest growing mode is given by λ_0 .

the spin healing length using g_1 is $\xi = 2.7 \mu\text{m}$ in $F = 2$ and $\xi = 4.3 \mu\text{m}$ in $F = 1$.

¹²In fact, the same applies to the remaining modes, which are proportional to $(1, 0, 0, 0, 0)$ and $(0, 0, 0, 0, 1)$. See reference [76] for more details.

Pattern formation in single- and two-component condensates has been the subject of several theoretical studies (e.g. [87, 88, 86]; see also the review article [85]). Spinor condensates differ from these not only in the number of components, but also in the particular coupling that allows conversion between the spin components. In the language of nonlinear optics, spinor condensates feature not only self- and cross-phase modulation, but also four-wave mixing.

Nevertheless, domain formation analogous to that in early spinor BEC experiments [23] (Section 2.3.3) has been observed in two-component ($F = 1, m_F = -1$) plus ($F = 2, m_F = +1$) ^{87}Rb condensates [31]. *Thermal* ensembles show similar patterns which have been identified as *spin waves* [30, 29]. In both cases, the length scale of structures is rather large, of the order of the condensate dimensions. Small-scale structure has been seen to emerge in the condensed system [27], as a result of external gradients “winding up” the phase of the pseudo-spinor up to a point where kinetic energy comes into play and the SMA fails even locally. We will resume the discussion of this particular mechanism in the context of our own observations of pattern formation in Chapter 6.

Pattern formation in $F = 1$ condensates has been studied in a series of publications, partly triggered by the recent advances in the experimental possibilities (see below) and in the general understanding of mean-field spin dynamics. Both analytical [89, 44, 90] and numerical [91, 92, 93] studies consistently predict the existence of a modulational instability in the ferromagnetic case, while the anti-ferromagnetic case is dynamically stable. The patterns generated depend (among others) on the dimensionality of the sample and include topological defects such as vortices [46].

A corresponding analysis for $F = 2$ spinor condensates has been performed in [94] for the case of zero magnetic field. In a more recent study including the quadratic Zeeman effect [76], it is shown among others that the $m_F = 0$ state in ^{87}Rb is dynamically unstable against modes populating the $m_F = \pm 1$ and $m_F \pm 2$ states *at any finite magnetic field*. Numerical simulations by the same authors [95], analogous to $F = 1$ [90], have also demonstrated the dynamical instability.

Pattern formation due to dynamical instability has been experimentally observed in single-component Bose-Einstein condensates with attractive interactions, where it leads to collapse [96, 97, 98] or formation of soliton trains [99, 100], as well as in spinor condensates. The first observation of spontaneous domain formation in $F = 1$ sodium [24] is in fact a realization of the immiscible two-component case [86], because only two m_F components $m_F = +1, 0$ are involved. At high magnetic offset field (15 G in [24]) these are immiscible and thus any homogeneous mixture is unstable with respect to local phase separation. In contrast, the ferromagnetic instability at negligible magnetic field has recently been observed in $F = 1$ ^{87}Rb [41] using an in-situ imaging technique that is directly sensitive to the transverse magnetization [101].

In $F = 2$ spinor dynamics starting from $m_F = 0$, the formation of dips and corresponding peaks in $m_F = 0$ and $m_F = \pm 1$, respectively, has been observed [38, 6] and interpreted as a local density effect. Structure formation in general, and in particular by the local density mechanism, has been proposed as a reason for apparent damping of coherent spin oscillations in $F = 2$ [1, 95]. This aspect is discussed in more detail in Section 5.6.

Chapter 6 of this work is dedicated to the *direct observation of pattern formation* in elongated $F = 2$ BEC. The quasi-1D geometry offers two important advantages: a large axial extension of the condensates enables the observation of long-wavelength modes, while a comparatively tight transverse confinement suppresses structure formation in the direction of detection, which otherwise would be averaged and appear as damping or loss

of contrast (compare Section 5.6). As a result, local density dynamics as well as previously unknown, strong wave-like modulations of the spin populations have been observed.

Chapter 3

Experimental setup and characterization

The observation and manipulation of ultra-cold spinor gases is a technically demanding task and requires a complex experimental setup together with an experimenter's ability to master it. Many of the key techniques covered in this chapter, in particular the control of the magnetic field and the preparation of spin states, had to be specially developed or improved in order to achieve the results of the following chapters.

3.1 Preparing ^{87}Rb BEC

Our experimental apparatus (Fig. 3.1) forms a complete setup for the creation, preparation and detection of spinor BEC of ^{87}Rb in $F = 1$ and $F = 2$. We prepare ^{87}Rb BEC in a magnetic trap using a setup optimized for stability and large particle numbers: a 2D-3D MOT system collects up to about 10^{10} atoms in 20 s, which are additionally cooled in an optical molasses and optically pumped to $F = 1$. The $F = 1, m_F = -1$ fraction¹ is loaded into a magnetic trap, compressed by increasing the radial trap steepness and cooled further using radio frequency forced evaporation over 20 s. Any residual $F = 2$ atoms are removed during the first of three rf ramps with low-power resonant light. We end up with nearly pure BEC of several 10^6 atoms in the magnetic trap. The apparatus has been described in detail in two PhD theses [57, 36].

In the course of this work, the whole setup has been moved to a brand new laboratory, and on this occasion has been further improved in terms of stability (mechanical as well as temperature) and immunity to electromagnetic interference (EMI). Additionally, of course, it has undergone modifications necessary to perform specific measurements. In the following, several experimental aspects of special relevance to spinor BEC are discussed in-depth.

3.2 Optical dipole trap

An important prerequisite for studying spin dynamics is to separate spatial from internal degrees of freedom as far as possible. An optical dipole trap provides a spin-independent

¹Further optical pumping within the $F = 1$ manifold has proven unnecessary. It is also ineffective due to re-pumping to $F = 2$ on transitions where laser frequencies are available from our system.

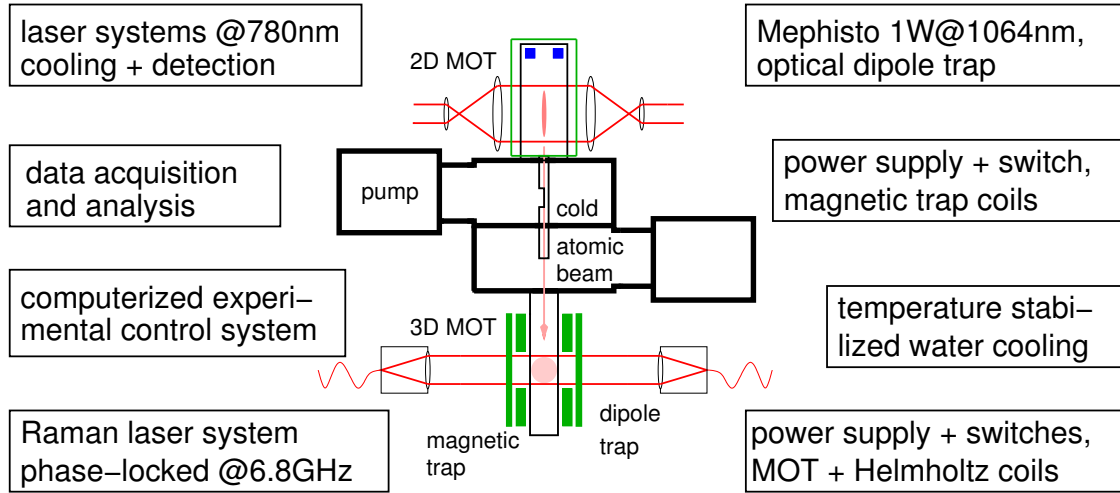
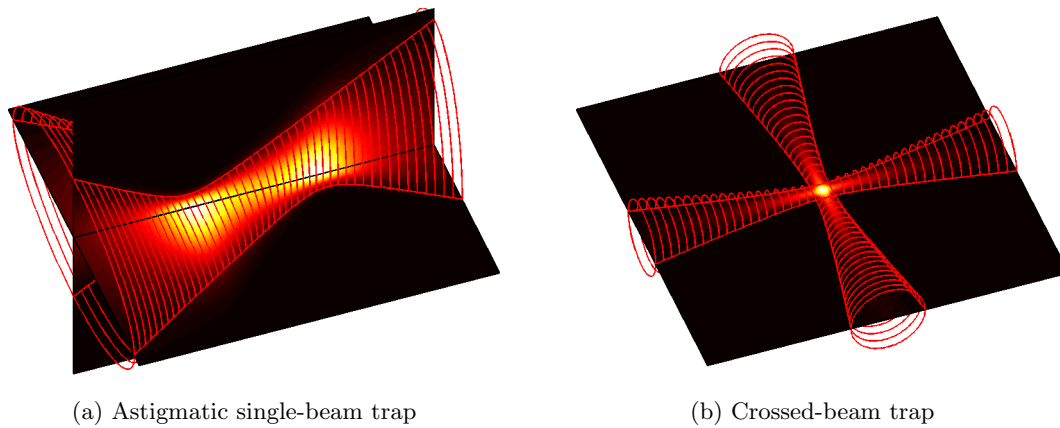


Figure 3.1: Schematic experimental setup.

Figure 3.2: Schematic beam geometries of the astigmatic and crossed-beam optical dipole traps. Shown are the $1/e^2$ beam diameter (red wire frame) and the intensity distribution (colored sections).

trapping potential for atoms [102], assuming the light used is sufficiently far detuned from the atomic resonance and linearly polarized. In a red-detuned trap, the atoms are localized at the intensity maximum, and the potential is harmonic to first approximation.

Our experiment uses light from a single-mode Nd:YAG laser (Mephisto by InnoLight) at 1064 nm, guided to the vacuum chamber in single-mode optical fibers and finally applied in one or two focused beams in three different geometries, as sketched in Fig. 3.2. These correspond to different trap geometries with characteristic advantages and disadvantages for certain experiments.

The trap geometry mostly used in this work and first implemented due to its simplicity is the astigmatic single focused beam (Fig. 3.2a). This geometry was invented in [36, 57] as a compromise providing sufficiently tight axial confinement and strong vertical support, but only moderate overall tightness (measured in terms of the average trap frequency $\bar{\omega} = (\omega_x \omega_y \omega_z)^{1/3}$). Astigmatism is deliberately introduced using a cylindrical lens. A

Table 3.1: Trapping frequencies and power scaling of the optical dipole traps used in this work. Data for the crossed-beam trap is taken from [104]. For the stigmatic trap, compare Fig. 3.3.

	at power	ω_x	ω_y	ω_z
astigmatic	$P = 48 \text{ mW}$	$2\pi \times 16.7 \text{ Hz}$	$2\pi \times 118 \text{ Hz}$	$2\pi \times 690 \text{ Hz}$
crossed-beam	$P_x = P_y = 15 \text{ mW}$	$2\pi \times 92 \text{ Hz}$	$2\pi \times 103 \text{ Hz}$	$2\pi \times 138 \text{ Hz}$
	optical power	ω_x	ω_y	ω_z
astigmatic	P (single beam)	$\propto \sqrt{P}$	$\propto \sqrt{P}$	$\propto \sqrt{P}$
crossed-beam	$P_{x,y}$ (beam in x, y dir.)	$\propto \sqrt{P_y}$	$\propto \sqrt{P_x}$	$\propto \sqrt{P_x + P_y}$

beam diameter of $d \approx 50 \text{ mm}$ at the focusing lens² ($f = 250 \text{ mm}$) leads to a tightly focused beam waist of $w_0 \approx 6 \mu\text{m}$, neglecting adverse effects of the cylindrical lens and other sources of error. In a first approximation, the effect of the cylindrical lens is to produce two foci separated by a distance $\delta \approx 4 \text{ mm}$ and having a beam waist of w_0 in one and $400 \mu\text{m}$ in the other transverse direction [36]. Only the vertically tight focus is suitable to support atoms against gravity. Trapping frequencies for this geometry have been measured using dipole oscillations of a BEC as well as parametric heating (see Fig. 3.3 and Tab. 3.1).

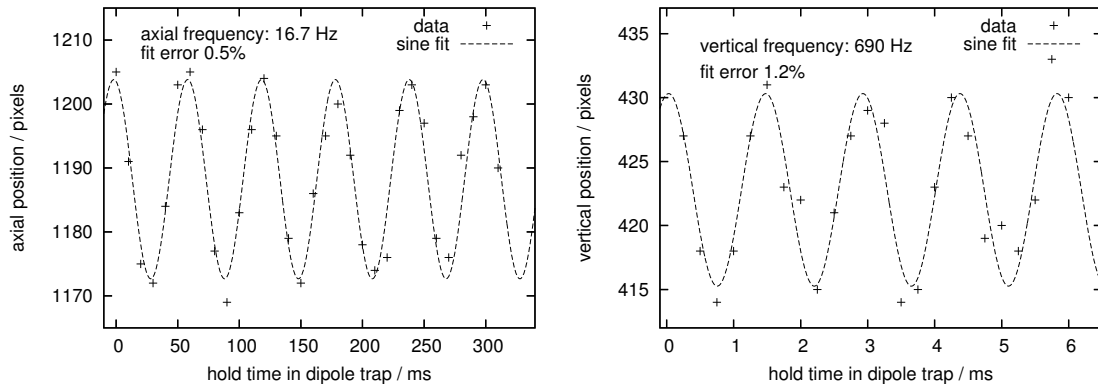
Experimental data from Section 5.5 and Section 5.3 can be employed to check the properties of the astigmatic trap. The relevant quantities extracted from two representative datasets are summarized in Tab. 3.2. The condensed (N_0) and total (N) particle numbers as well as the temperature T are obtained from bimodal fits to absorption images. Assuming a harmonic trap, the critical temperature T_c is then calculated from $N_0/N = 1 - (T/T_c)^3$ and the average trap frequency from $k_B T_c = 0.94 \hbar \bar{\omega}^{(T)} N^{1/3}$ [51]. On the other hand, the average density of the condensate $\langle n \rangle$ can be obtained from fits to the spin population oscillations observed in Section 5.3, and the trap frequency can be calculated via $\bar{\omega}^{(n)} = \frac{\hbar}{m a^2} (14\pi \langle n \rangle a^3)^{5/6} (15N_0)^{-1/3}$ [51]³. The scattering length $a = g_0 \frac{m}{4\pi \hbar} \approx 5.3 \text{ nm}$ corresponds to the spin-independent coefficient g_0 of the contact interaction (Section 2.3.1).

Obviously, none of the experimental methods leads to results consistent with the power scaling law from Tab. 3.1, neither the absolute values nor the ratio of frequencies at different optical power conforms to our expectations. Both experimental methods depend on the accuracy of the number of particles N or N_0 , but only to the power of $1/3$. Thus, in order to explain a discrepancy by a factor of $2 \dots 3$ in either absolute value or ratio, an error in the number of particles of nearly one order of magnitude has to be assumed, which appears implausible. A more realistic conjecture is that due to *gravitational sag*, the optical potential is skewed in such a way that it deviates strongly from the harmonic shape assumed in all formulae. Additionally, the minimum of the trap is shifted away from the maximum of optical intensity, and the trap frequencies may be modified even if the harmonic approximation still holds. Since the amount of gravitational sag depends on the optical power, the scaling laws of Tab. 3.1 no longer hold.

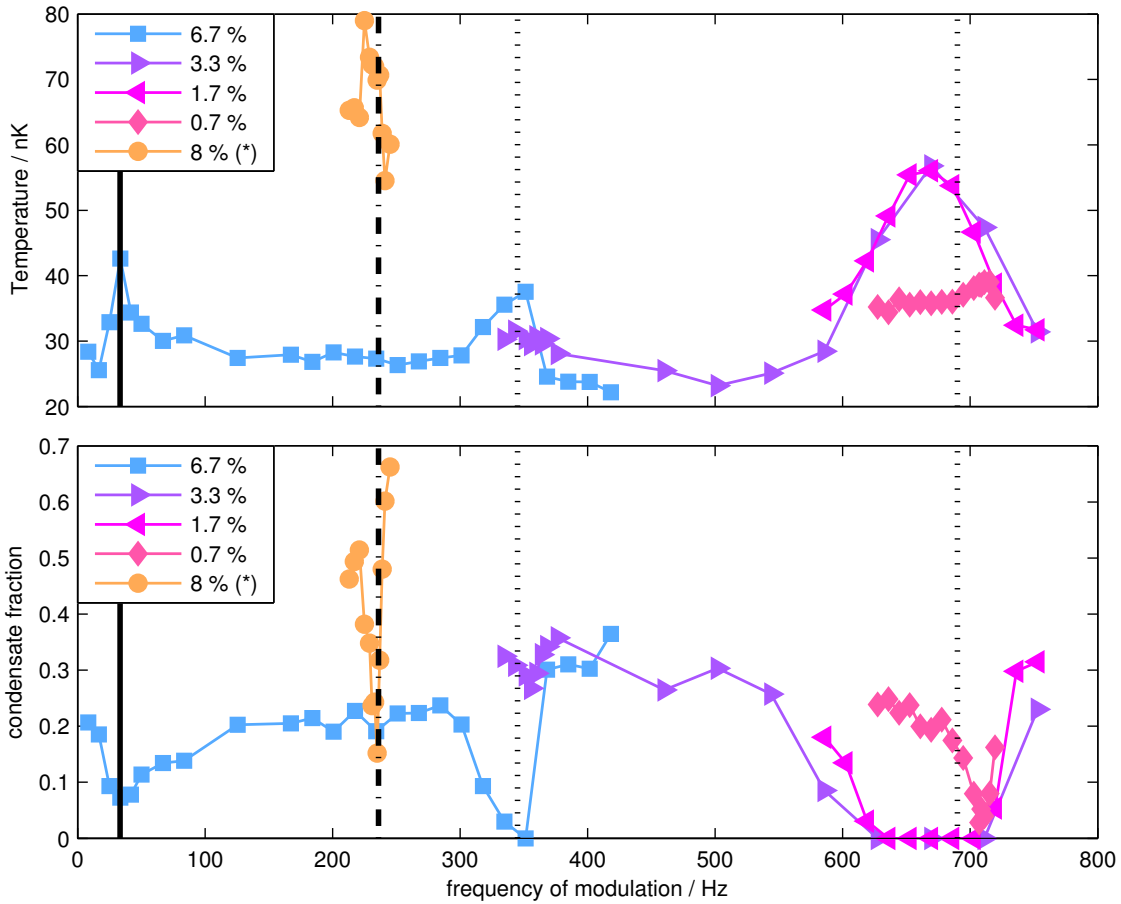
In an effort to provide a more isotropic potential, Christoph Becker has implemented the crossed-beam geometry in our experiment. Details of the setup will be covered in his PhD thesis [105] (to be published). This type of trap is more flexible since the confinement

²The Gaussian beam emerging from the fiber end is slightly truncated by the aperture of the lens. See [103] for construction details and [57] for a thorough analysis of the astigmatic beam shape.

³Note that $\langle n \rangle = 4/7 \hat{n}$, where \hat{n} is the peak condensate density at the trap minimum, see Section 2.3.2.



(a) Center-of-mass oscillations of a cloud of atoms in the astigmatic single-beam trap, used to determine the trapping frequencies in Tab. 3.1. The measurements have been performed at 48 mW optical power.



(b) Parametric heating spectra for various modulation depths. Measurements have been taken at 68 mW or 48 mW (marked (*)) optical power; modulation frequencies have been scaled to 48 mW. Vertical lines mark $2 \times f_x$ and $2 \times f_y$ (where $2\pi f_{x,y,z} = \omega_{x,y,z}$) as well as $1 \times f_z$ and $0.5 \times f_z$. Excitation at the vertical trap frequency and sub-harmonics is possible since gravitational sag shifts the trap center.

Figure 3.3: Determination of the trap frequencies of the astigmatic single-beam trap.

Table 3.2: Comparison of average frequencies of the astigmatic dipole trap, obtained by various methods. $\bar{\omega}$ is scaled according to Tab. 3.1, $\bar{\omega}^{(T)}$ and $\bar{\omega}^{(n)}$ are calculated from measured critical temperatures and densities, respectively (see text for details).

power [mW]	experimental data				calculated from data			scaled
	T/nK	$N/10^5$	$N_0/10^5$	n/cm^{-3}	T_c/nK	$\bar{\omega}^{(T)}/\text{s}^{-1}$	$\bar{\omega}^{(n)}/\text{s}^{-1}$	$\bar{\omega}/\text{s}^{-1}$
44	64	5.0	3.8	0.68×10^{14}	104	$2\pi \times 29$	$2\pi \times 23$	$2\pi \times 106$
107	205	8.3	2.9	1.9×10^{14}	229	$2\pi \times 54$	$4\pi \times 96$	$2\pi \times 165$

in all three directions is given by the *transverse* intensity gradients of the two beams only, which can be independently adjusted. The beams have circular cross-sections and are focused to $w_0 \approx 25 \mu\text{m}$; equal power ideally leads to an aspect ratio of $\omega_x : \omega_y : \omega_z = 1 : 1 : \sqrt{2}$ of the trap. Condensates in this trap are tightly localized in all directions and should conform much better to the single-mode approximation (Section 2.3.2) than in the astigmatic single-beam trap. Tab. 3.1 lists representative trapping frequencies, determined in a similar way as for the astigmatic trap. Details of this measurement can be found in Sebastian Schnelle's Diploma thesis [104].

The last variant simply consists of just one of the beams of the crossed dipole trap. The resulting potential shows extremely low confinement in axial direction ($\omega_x \approx \omega_y/100$ based on the measured beam waist), leading to the formation of very elongated Bose-Einstein condensates in this waveguide-like structure. This geometry is useful for observing spatial structure formation; however, the extreme shape also introduces several technical and physical complications (Chapter 6). The transverse trapping frequency can be deduced from the measurement of the crossed beam trap (Tab. 3.1).

Intensity fluctuations of the dipole trap translate to fluctuations of the trapping frequencies and may lead to heating via the mechanism of parametric excitation [106]. It is therefore important to keep intensity noise low, in particular the Fourier components at twice the trap frequencies where parametric excitation is resonant. Fluctuations may result from intensity noise of the laser source itself as well as mechanical and acoustic noise modulating the coupling efficiency and polarization properties of the fiber used to guide the light to the experiment.

Fig. 3.4 shows the Fourier spectrum of the light intensity measured behind the fiber using a battery-powered photodetector and an FFT audio analyzer (Rohde & Schwarz UPL). The most dominant features result from line frequency modulation, and are suppressed by a factor of more than 1000 even in the worst case. The broad-band noise floor at -100 dB corresponds to a spectral noise density⁴ of -110 dB/Hz . Assuming a typical trap frequency of 690 Hz , this noise translates [106] to a heating rate of $\Gamma = \frac{\langle \dot{E} \rangle}{\langle E \rangle} = 5 \cdot 10^{-5} \text{ s}^{-1}$, which is completely negligible on typical experimental time scales.

⁴The FFT analyzers spectral filter is normalized to a peak value of 1. This means that the rms power of a single-frequency signal can be directly read from the peak of the curve. On the other hand, this means that the spectral power density of noise is displayed in terms of total power integrated over the effective filter bandwidth (approx. 10 Hz here for the solid curves)

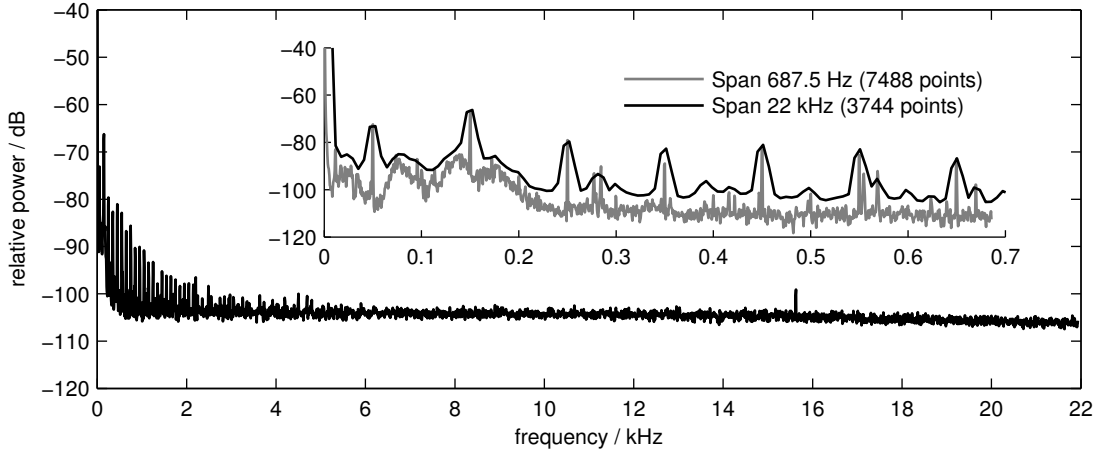


Figure 3.4: Intensity noise of the astigmatic single-beam dipole trap. Note that “relative power” refers to the photodiode signal (i.e. 60 dB correspond to a factor of 1000 in light intensity) and is normalized to the DC signal level. Electronic noise is negligible; it has been checked that with the laser blocked, the noise level is > 60 dB lower throughout the spectral range.

3.3 Detection

After release from the optical dipole trap and free expansion during time-of-flight, our spinor condensates are imaged using the standard absorption technique [107]. In order to obtain information about the spin state, individual m_F -components are separated in a magnetic field gradient (Stern-Gerlach technique). Thus, spin state populations can be measured in total or spatially resolved, but phases needed for a complete characterization of the quantum mechanical state are not accessible.⁵

In order to have a well defined quantization axis \vec{e}_x during Stern-Gerlach separation, a large offset field $B_{x,\text{offs}}$ is applied. For the interpretation of certain experiments, specifically for magnetic field compensation (Section 3.4), it is important to know whether this offset field is switched on adiabatically or not. In the former case, any spin state is just rotated together with the quantization axis, in the latter case it is projected onto the new axis. Variations of B_x on a time scale much shorter than Larmor precession in the transverse field B_\perp lead to projection. On the other hand, adiabatic evolution occurs when the speed of rotation of the magnetic field, $|\dot{\vec{B}}|/|\vec{B}|$, is much less than the Larmor frequency $\frac{gF\mu_B}{\hbar}|\vec{B}|$. Changes in spin populations with respect to \vec{e}_x due to adiabatic rotation can be neglected when the angle between \vec{B} and \vec{e}_x is sufficiently small, the same condition as applies to the final offset field. This means, that the offset field $B_{x,\text{offs}}$ has to rise to a value sufficiently large to neglect the transverse field, in a time small compared to the transverse Larmor

⁵Measuring populations corresponds to projecting the spin onto a quantization axis; the populations are the diagonal elements of the density matrix. In principle, it is possible to obtain the *full* density matrix using tomography, i.e. several projections on different axes. For a spin- F system, in general $4F + 1$ projections are needed [108]. Tomography has not been performed in the course of this work due to technical restrictions. The simplest possibility using active rotation by rf pulses (Section 2.2.2) would require a level of shot-to-shot reproducibility at least one order of magnitude beyond the (already excellent) capabilities of the current setup. Methods relying on switched magnetic fields [109] are technically demanding and could not be implemented to date.

Table 3.3: Key parameters of imaging lenses used in the course of this work. The observed resolution is also limited by the pixel size ($6.8\mu\text{m} \times 6.8\mu\text{m}$) of the camera. The diffraction limit s has been calculated according to the Rayleigh-criterion, where $s = 1.22 \frac{\lambda f}{D} \approx 1.22 \frac{\lambda}{2NA}$. (D diameter, f focal length, NA numerical aperture of lens).

	achromats	B. Halle
working distance	120 mm	105 mm
numerical aperture	0.16	0.20
magnification	$1\times, 2.17\times, 3.75\times$	$2.58\times, 9.9\times$
resolution (diffraction limit)	$2.8\mu\text{m}$	$2.3\mu\text{m}$
resolution (best observed)	$3.6\mu\text{m} @ 3.75\times$	$< 2.2\mu\text{m}$

frequency. Assuming linear growth,

$$\frac{\Delta B_{x,\text{offs}}}{\Delta t} \gg \frac{g_F \mu_B}{\hbar} B_{\perp}^2 = \frac{2\pi \times 700 \text{ kHz}}{G} B_{\perp}^2 \quad (3.1)$$

The growth rate of the offset field $\partial B_{x,\text{offs}}/\partial t$ has been estimated from current measurements as $\approx 0.1\text{G}/\mu\text{s}$. This implies non-adiabatic switching for transverse fields $B_{\perp} \ll 150\text{mG}$, which is typically fulfilled after and during the compensation of residual magnetic fields. This is important for the interpretation of Stern-Gerlach images during the compensation procedure.

The optical setup for absorption detection consists of an illuminating laser beam, an imaging lens and a CCD camera. The laser beam is fiber-coupled and collimated to a diameter of several centimeters, illuminating the atoms at typically 20% saturation ($\approx 0.3\text{mW}/\text{cm}^2$). Depending on the density of the atomic cloud, the laser is resonant or detuned up to one linewidth of the atomic transition (6 MHz). In order to minimize the spin dependence of the absorption cross-sections [57], the polarization is chosen parallel to the quantization axis (π polarization).

The imaging lens consists of two 40 mm diameter achromatic lenses mounted back-to-back in earlier measurements⁶, and is now a custom-designed multi-lens objective (B. Halle Nachfl. GmbH, Berlin). Key parameters of the respective lenses are summarized in Tab. 3.3. The imaging systems have been characterized and put into operation together with Thomas Garl (home-made system) [110] and Lars Neumann (B. Halle objective) [111] as part of their diploma theses; more details can be found therein.

The CCD camera (SenSys 3200ME) takes three pictures in a row for each run of the experiment. (1) The absorption image I^{abso} , (2) the same image after the atoms have fallen down (reference image) I^{ref} and (3) a dark image I^{dark} where the illuminating laser beam is off. Each image takes about 4s to read out, while the exposure time, defined by the duration of the detection laser pulse, is typically only $50\mu\text{s}$. From the three images, the optical column density of the absorbing atomic cloud is calculated,

$$n_{\text{OD}} = -\ln\left(\frac{I^{\text{abso}} - I^{\text{dark}}}{I^{\text{ref}} - I^{\text{dark}}}\right) \quad (3.2)$$

This is the standard procedure [107] to eliminate background light as well as the structure of the illuminating beam (Gaussian profile, dust particles, interference fringes).

⁶dating from before April 2006

Table 3.4: Characteristics of the compensation coil cube, calculated using Ampère’s law. The measured value for B_x is 275 ± 1 mG/A, in good agreement with the calculation. The comparison may serve as an error estimate for the remaining coefficients.

coil pair	quantity	coefficient	unit
Helmholtz horizontal	B_x, B_y	0.286	G/A
Anti-Helmholtz horizontal	$\partial B_x / \partial x$	0.034	G/(A cm)
Helmholtz vertical	B_z	0.521	G/A

It turns out, however, that part of the pattern is not fixed but varies in time on a millisecond scale [112], limiting the effectiveness of the above procedure. We have therefore developed an algorithm for additional post-processing of the images. The basic idea of post-processing is to construct for each absorption image an artificial best-fit reference image from the set of all reference images (of the same day or series) [57, 112]. This is then used instead of the original reference image to calculate the optical density in the usual way. Another simple way of avoiding a large part of the smallest-scale fringes is to use a quarter-wave plate in front of the camera. This seems to suppress the parasitic resonator formed between the camera chip and the vacuum cell through the imaging lenses. The fringe problem is discussed again in more detail in Section 4.1.

3.4 Magnetic field control

Every experiment takes place at finite magnetic field \vec{B}_0 . Precise control of this offset field and its fluctuations is crucial for any experiment involving spinor physics. Ideally, \vec{B}_0 is assumed to have a constant magnitude B_0 and a fixed direction \vec{e}_x (labeled x -axis by convention). In our experiment, the actual magnetic field during hold time in the dipole trap is composed of the desired axial offset field, produced by dedicated offset field coils, and residual static (DC) and dynamic (AC) fields.

The coils used to compensate and generate magnetic fields have been described in [57]. They are wound along the edges of a cube of dimensions $x \times y \times z = 28 \text{ cm} \times 28 \text{ cm} \times 18 \text{ cm}$. Several pairs of 2×10 turns each are available for each direction. The pairs can be used in Helmholtz⁷ as well as anti-Helmholtz configuration. The BEC is situated approximately at the center of the assembly. Some characteristics of the coils are summarized in Tab. 3.4 for reference.

The dominant source of static residual fields, above any technical sources, is the earth’s magnetic field, which is of the order of 0.5 G [113]. Technical sources comprise e.g. the permanent magnets of the ion vacuum pumps, the permanently running coils and dispensers of the 2D MOT, and residual magnetization in the steel parts of the apparatus⁸. We employ computer-controlled constant-current driven compensation coils to cancel static stray fields down to about 0.5 mG in the transverse direction and about 2 mG in the axial direction, following the procedure outlined below.

⁷For simplicity, the terms “Helmholtz” and “anti-Helmholtz” are used not only for the classical Helmholtz configuration of circular coils separated by half their diameter, but for any equivalent topology, irrespective of dimensions.

⁸The vacuum apparatus and the surface of the optical table are made of non-magnetic A4 steel, bolts and other hardware is usually made of A2 steel which is only slightly magnetic.

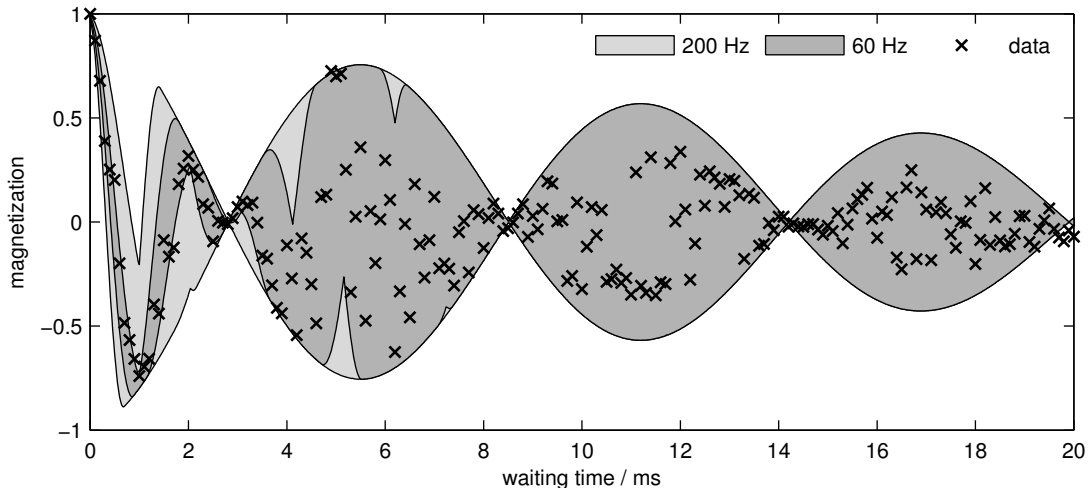


Figure 3.5: Ramsey experiment in $F = 1$ at 1.1 G offset field. Colored area indicate the expected envelope assuming a detuning of 480 ± 60 Hz and 480 ± 200 Hz, respectively. The theoretical model includes exponential damping (Section 2.2.3, $\gamma^2 = 100 \text{ s}^{-1}$).

The fundamental problem in cancelling magnetic stray fields is the lack of knowledge of these fields at the position of the atomic cloud. The way out consists in using the atoms themselves as a magnetic sensor. The following procedure requires a working spinor BEC experiment, namely production of BEC in a dipole trap and Stern-Gerlach analysis. Reasonable starting values for the compensation coils are those used for the optical molasses.

After evaporation in the magnetic trap, atoms are in a pure $F = 1, m_F = -1$ state⁹. With a sufficiently high offset field $B_0 = B_{\text{ini}}$, only the single corresponding Stern-Gerlach separated cloud should be populated. In a first step, the axial compensation is roughly adjusted by setting the offset field temporarily to $B_0 = 0$ and ensuring that several m_F components are populated. This means that the resulting field is more or less transverse.

In the next step, the offset field B_0 is gradually reduced from its initial value B_{ini} until a small population in $m_F = 0$ appears. Adjusting the currents through the transverse compensation coils, this population has to be minimized until it is not visible any more. The offset field is then further reduced, the compensation currents are re-adjusted and the procedure is repeated until no further improvement is seen. On a good day (and with properly compensated gradients, see below), this means that the compensation currents are finally adjusted by only 1 mA, corresponding to ≈ 0.3 mG.

In a last step, the residual axial field is cancelled. This is done by setting one of the transverse directions off its correct value by several mG. Ideally, the resulting field at $B_0 = 0$ is purely transversal and the population distribution seen after Stern-Gerlach is symmetric around $m_F = 0$. The axial compensation current is adjusted to achieve a distribution as symmetric as possible. The minimum step size achievable by this criterion is several times larger than that for the transverse directions.

As a check for good compensation, it is useful to set again $B_0 = 0$ now using the correct currents for all compensation coils. Compensation is perfect, if all m_F components are populated and *spatially structured* (Fig. 3.6). The latter means that field variations across

⁹For simplicity, we use $F = 1$ as an example. The procedure for $F = 2, m_F = +2$ is analogous.

the condensate are of the same order as the residual field. With good compensation, an offset field of $30 \text{ mG} \hat{=} 100 \text{ mA}$ should be sufficient to suppress any population other than $m_F = -1$ below the visibility limit. With transverse compensation adjusted to 1 mA accuracy, even $3 \text{ mG} \hat{=} 10 \text{ mA}$ are sufficient; however, since stray fields seem to drift on the time scale of hours it is not advisable to rely on this ultra-low offset¹⁰. Additionally, it is possible to obtain rf resonance frequencies (Section 3.5) for various offset field values, and obtain the residual field from the offset of the linear relationship; the result is again of the order of mG.

Dynamic (AC) fields usually oscillate at multiples of the line frequency (50 Hz) with an amplitude of the order of a few mG. They can be minimized to some degree by keeping power supplies and other line-operated equipment far from the vacuum chamber. In addition, it is useful to synchronize the experiment to the mains cycle – this improves shot-to-shot reproducibility, and stabilizes the magnetic field seen by the atoms at least for hold times much shorter than the mains period. Fig. 3.5 shows the result of a Ramsey experiment (see Section 2.2.1 and Section 5.2) at 1.1 G offset. Each data point corresponds to a single run of the experiment, lasting about a minute. The visibility of Ramsey fringes up to the first beat node implies a shot-to-shot fluctuation of less than $\pm 60 \text{ Hz}$, corresponding to less than 0.1 mG .

Since the line frequency is not sufficiently stable on the time scale of seconds or minutes, the experimental sequence control has been modified to pause on demand and wait for a line-generated trigger signal to continue. This wait-for-trigger state is invoked just before the critical part of the experimental sequence.

The next level of compensation is to take the variation of magnetic fields across the condensate into account, or to first order the gradient $\partial B_{\{x,y,z\}}/\partial\{x,y,z\}$. With nine components of the gradient matrix and only one constraint $\nabla \cdot \vec{B} = 0$, complete compensation is not feasible. However, it is possible to single out the two or three dominant gradients. First, at finite offset $\vec{B}_0 = B_0 \vec{e}_x$, small transverse components contribute only quadratically to the total magnitude, whereas axial fluctuations enter linearly. Second, the extension of the atomic cloud is largest in axial direction, except in the crossed dipole trap where it is more or less spherical. Therefore the most important gradient is $\partial B_x/\partial x$, which can be compensated (at the cost of additional transverse gradients) using a pair of anti-Helmholtz coils. Of the transverse gradients of B_x , only $\partial B_x/\partial z$ has been compensated using a pair of small off-axis Helmholtz coils. While the $\partial B_x/\partial x$ compensation adds only a very small residual field, the significant additional offset field produced by $\partial B_x/\partial z$ compensation has to be taken into account in the compensation procedure. The effect of gradient compensation is directly visible in spinor BEC in the crossed-beam dipole trap (Fig. 3.8).

Best compensation of $\partial B_x/\partial x$ is achieved at $0.5 \pm 0.1 \text{ A}$, indicating a magnetic field gradient of the order of 15 mG/cm , which in x -direction is reduced by compensation to a residual gradient of $\partial B_x/\partial x \approx 3 \text{ mG/cm}$. At the same time, however, other components may increase by the same amount. Across a typical condensate elongation of $100 \mu\text{m}$, this residual gradient causes dephasing between adjacent Zeeman sublevels at a rate of $\approx 2\pi \times 20 \text{ Hz}$.

Another estimate of residual gradients can be obtained from the fact that patterns as illustrated in Fig. 3.6 are observed only when the Helmholtz compensation currents are

¹⁰It has been observed that after several hours, the compensation currents have to be re-adjusted by $1 \dots 2 \text{ mA}$. Switching off the power supplies of cameras used to monitor the MOTs makes changes of the same order of magnitude necessary, as does interrupting the experimental cycle for a few minutes.

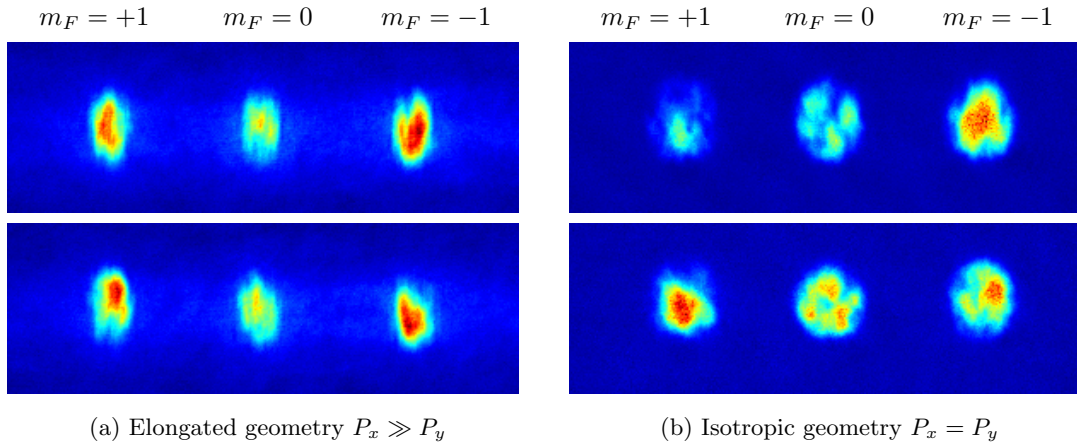


Figure 3.6: Typical structured spinor condensates in the crossed dipole trap at zero offset field, indicating optimum stray field and gradient compensation. Gradient compensation currents are those deduced from Fig. 3.7 and Fig. 3.8. The pattern as well as the relative population of spin states varies randomly from shot to shot, probably due to AC stray fields. Since the hold time at zero offset field is comparatively long, the line trigger is ineffective in this case.

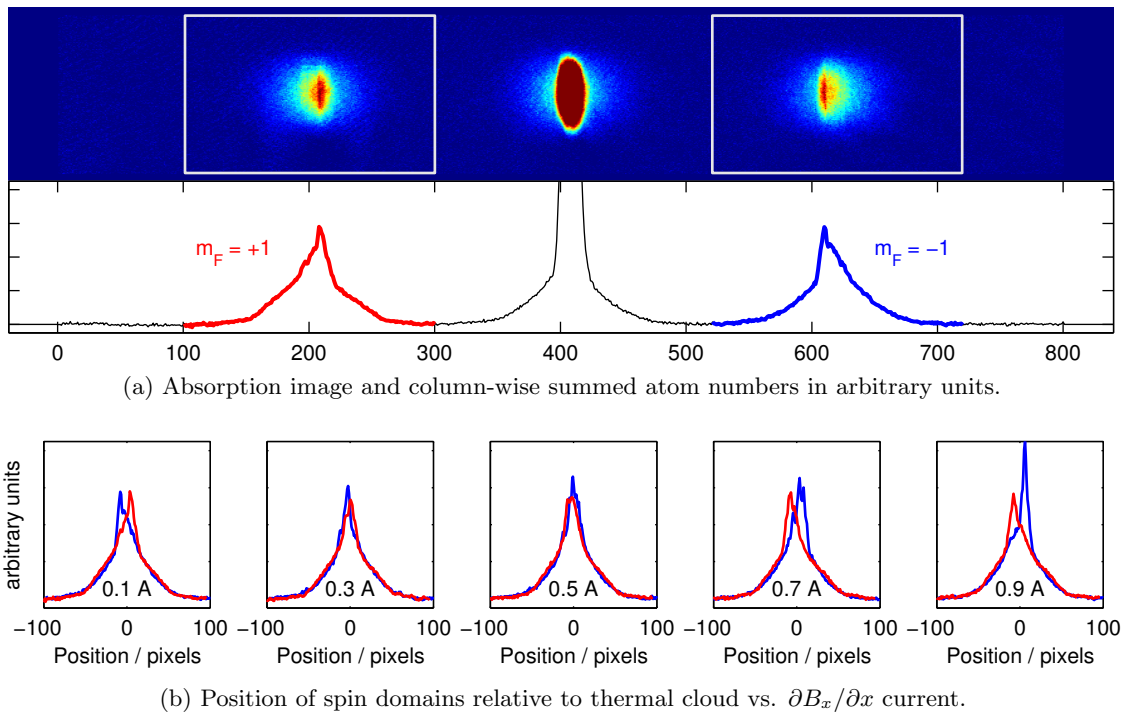


Figure 3.7: Gradient compensation in the astigmatic dipole trap (selected examples). Demixing of spin components occurs after preparation with $\pi/2$ pulse (Section 2.2.1) at 0.7 G offset field; $\partial B_x / \partial x$ leads to a deterministic spatial separation. From this experiment, an optimum compensation current of about 0.4 A could be deduced, consistent with Fig. 3.8.

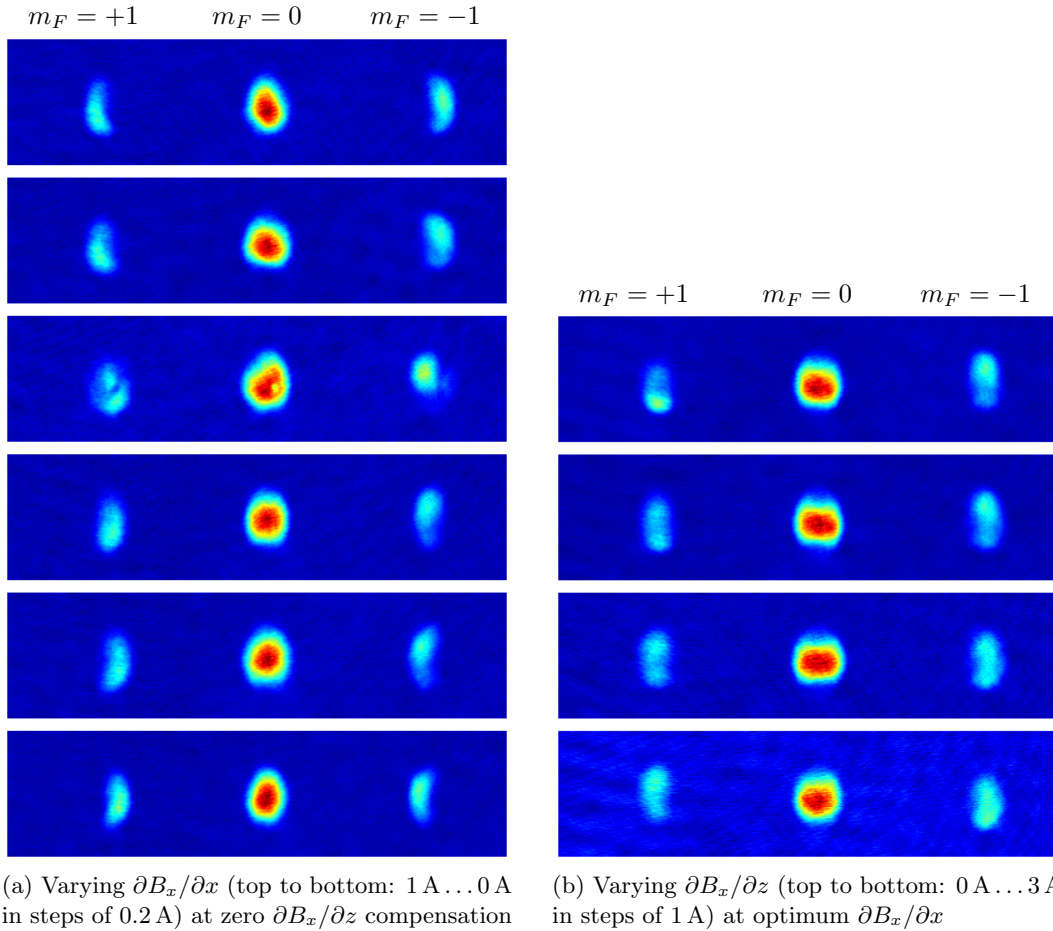


Figure 3.8: Selected images of spinor condensates in the crossed dipole trap at zero offset field, demonstrating gradient compensation. This kind of experiment has been used to find the optimum compensation currents. In the left column, it can be seen how the $m_F = \pm 1$ components separate under the influence of the magnetic field gradient and swap places when it changes sign (from both “outwards” with respect to $m_F = 0$ at the center to both “inwards”). In the right column, similar behavior can be seen in the vertical direction depending on the vertical gradient. Optimum compensation currents deduced from these images are 0.5 A for $\partial B_x/\partial x$ (left) and 2 A for $\partial B_x/\partial z$ (right).

Table 3.5: Examples of initial states that can be prepared from $|1, -1\rangle$ using microwave sweeps, adiabatic rf sweeps and pulses. Notation: $|1, -1\rangle \equiv (0, 0, 1)$ etc.

$(0, 0, 1)$			$\xrightarrow{\pi/2}$	$(\frac{1}{2}, \frac{1}{\sqrt{2}}, \frac{1}{2})$
$(0, 0, 1)$	$\xrightarrow{\text{rf sweep}}$	$(0, 1, 0)$	$\xrightarrow{\pi/2}$	$(\frac{1}{\sqrt{2}}, 0, -\frac{1}{\sqrt{2}})$
$(0, 0, 1)$	$\xrightarrow{\text{rf sweep}}$	$(0, 1, 0)$	$\xrightarrow{\pi/4}$	$(\frac{1}{2}, \frac{1}{\sqrt{2}}, -\frac{1}{2})$
$(0, 0, 1)$	$\xrightarrow{\text{mw sweep}}$	$(0, 0, 0, 0, 1)$	$\xrightarrow{\pi/2}$	$(\frac{1}{4}, \frac{1}{2}, \sqrt{\frac{3}{8}}, \frac{1}{2}, \frac{1}{4})$
$(0, 0, 1)$	$\xrightarrow{\text{mw sweep}}$	$(0, 0, 1, 0, 0)$	$\xrightarrow{\pi/2}$	$(\sqrt{\frac{3}{8}}, 0, -\frac{1}{2}, 0, \sqrt{\frac{3}{8}})$
$(0, 0, 1)$	$\xrightarrow{\text{mw sweep}}$	$(0, 0, 0, 0, 1)$	$\xrightarrow{\text{rf sweep}}$	$(0, 0, 0, 1, 0)$
			$\xrightarrow{\pi/2}$	$(\frac{1}{2}, \frac{1}{2}, 0, -\frac{1}{2}, -\frac{1}{2})$

optimized at the mA-level, corresponding to changes in offset field of 0.3 mG. Assuming that the local spin composition reflects the local magnetic field orientation, field variations across the condensate should be well below this value. This estimate is compatible with the previous paragraph, though slightly less stringent.

The Helmholtz compensation or offset field coils themselves may be the source of an unwanted *variable* gradient.¹¹ Estimating the gradient caused by only an axial deviation (± 1 cm) of the actual condensate position from the symmetry point of the coil pair, a variable gradient of up to 4 mG/(A cm) may be expected realistically. This is of the same order of magnitude as the achievable accuracy of gradient compensation.

3.5 Spin state preparation

The main tools used in this work for state preparation and manipulation are radio frequency driven transition between m_F substates within a hyperfine manifold, and microwave driven transitions between $F = 1$ and $F = 2$. Both rely on the BEC or atomic cloud being in a pure state ($F = 1, m_F = -1$) after evaporation in the magnetic trap. Also, both methods are naturally first-order sensitive to the magnetic field, and precise knowledge of the Zeeman splitting at a given offset field is necessary. The same rf techniques used for the preparation of spin states can also be employed to determine the Larmor frequency in the first place; as a by-product, we gain a precise value for the magnetic offset field.

We distinguish three basic techniques, each relying on specific experimental parameters and providing specific degrees of freedom for the manipulation of the spin state.

Spin rotations

At small offset field, where the quadratic Zeeman splitting is small compared to the Rabi frequency of the rf coupling (a few kHz), the dynamics of an initially stretched state is well described by the classical spin picture (Section 2.2.2). In the frame of reference rotating at the rate of the radio frequency, applying rf power induces a rotation around the x -axis at the rate of the Rabi frequency, while just waiting corresponds to a rotation around

¹¹The coils are not in true Helmholtz configuration, i.e. the curvature of the magnetic field as a function of the position does not vanish at the symmetry point.

the z -axis at the rate of the detuning between radio and Larmor frequency. Arbitrary rotations can be achieved by rf pulse sequences; many sophisticated techniques have been developed in the context of nuclear magnetic resonance (NMR) [114].

Practically, the correct frequency and pulse duration are roughly known from experience. Precise values for the Larmor frequency are found by choosing an approximate π -pulse of $80 \mu\text{s}$ and adjusting the frequency for maximum rotation away from the initial $|F, -F\rangle$ state; ideally, a π -pulse at zero detuning will transfer all atoms to the opposite stretched state $|F, +F\rangle$. The Rabi frequency is then adjusted by varying the amplitude such that a pulse duration of $40 \mu\text{s}$ corresponds to a $\pi/2$ pulse, i.e. leads to a symmetric distribution of the population over all m_F states. If necessary the procedure is iterated. Using this protocol, the Larmor frequency can be obtained to a precision of about 1 kHz.

For improved precision, the π -pulse is split into two $\pi/2$ -pulses (Ramsey sequence) and the waiting time between them is gradually increased from $10 \mu\text{s}$ up to 1 ms, while the frequency is continuously adjusted for maximum population of $|F, +F\rangle$ as before. Care has to be taken not to increase the waiting time by more than a factor of two in each step, in order to keep the rotation due to detuning always within $\pm\pi$. The resulting precision of the Larmor frequency is about 100 Hz. The Larmor frequencies obtained this way are slightly different (by less than 1%) in $F = 1$ and $F = 2$ at the same B_0 , and also depend very slightly on the depth of the dipole trap (less than 0.1%).

A $\pi/2$ -pulse is also employed to prepare the particular superpositions $\zeta_{\pi/2} = (1/2, 1/\sqrt{2}, 1/2)$ in $F = 1$ and $\zeta_{\pi/2} = (1/4, 1/2, \sqrt{3}/8, 1/2, 1/4)$ in $F = 2$ at low offset fields up to 3 G, corresponding to a Larmor frequency of 2.1 MHz and a quadratic Zeeman effect of the order of 1 kHz maximum (Section 2.3.4). Both states are fully transversely magnetized states, $\zeta_{\pi/2} = e^{i\frac{\pi}{2}\mathbf{F}_y} \zeta_{-F}$ where $\zeta_{-F} = (0, 0, 1)$ or $(0, 0, 0, 0, 1)$, respectively.

The specific advantage of spin rotations is that the relative phases of different m_F components are well defined. Use of the technique is neither limited to stretched states nor to $\pi/2$ pulses. E.g., a $\pi/2$ pulse applied to a pure $|F = 2, m_F = 0\rangle$ state can be used to prepare a superposition of $m_F = \pm 2$ and $m_F = 0$ only, a state that is characterized by the absence of g_1 coupling (Section 2.3.1); other useful examples can be found in Tab. 3.5. Pulse areas $\ll \pi/2$ can be employed to generate small “seed” populations in m_F states adjacent to a single strongly populated one at a well defined phase.

Rf adiabatic passage

The characteristic regime for spin rotations is that of a negligible quadratic Zeeman effect. As a result, *all* transitions between adjacent m_F levels are degenerate. At larger offset field, where the quadratic Zeeman effect is of the order of 100 kHz and thus much larger than the Rabi frequency of the rf coupling, this degeneracy is lifted. Transitions between specific m_F levels can be selectively addressed by tuning the radio frequency (Fig. 3.10).

Rf *sweeps* can be used to adiabatically transfer population between specific m_F sub-states, enabling access to non-stretched states, e.g. $|1, -1\rangle \rightarrow |1, 0\rangle$. Superpositions can be prepared as well by sweeping more quickly, violating adiabaticity; however, in this case the phases are not well defined. This technique has been used extensively in earlier experiments of our group [36, 57]. The offset field is chosen at 26 G, corresponding to a linear Zeeman splitting of 18 MHz and transition frequencies between m_F components spaced at 47 kHz due to the quadratic Zeeman effect. Sweeping over 50 kHz in 1 ms is sufficient to ensure adiabaticity [57].

While the use of quick rf sweeps to generate mixtures is problematic, adiabatic sweeps

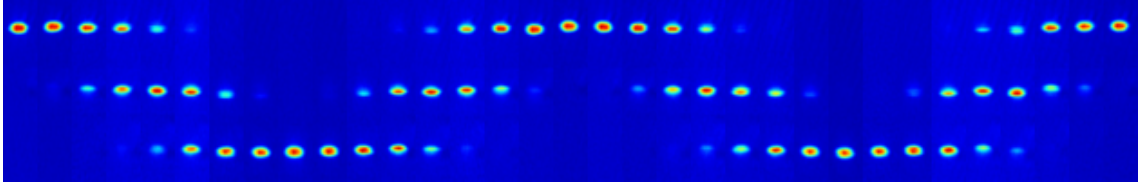


Figure 3.9: Rabi-like oscillations in $F = 1$, driven by continuously applied rf. The condensate is initially prepared in $F = 1, m_F = -1$ (top row) and is driven through a superposition of all three m_F -states to a pure $m_F = +1$ state, before the dynamics is reversed. The pictures are taken at intervals of $10 \mu\text{s}$. (pictures resized - not to scale.)

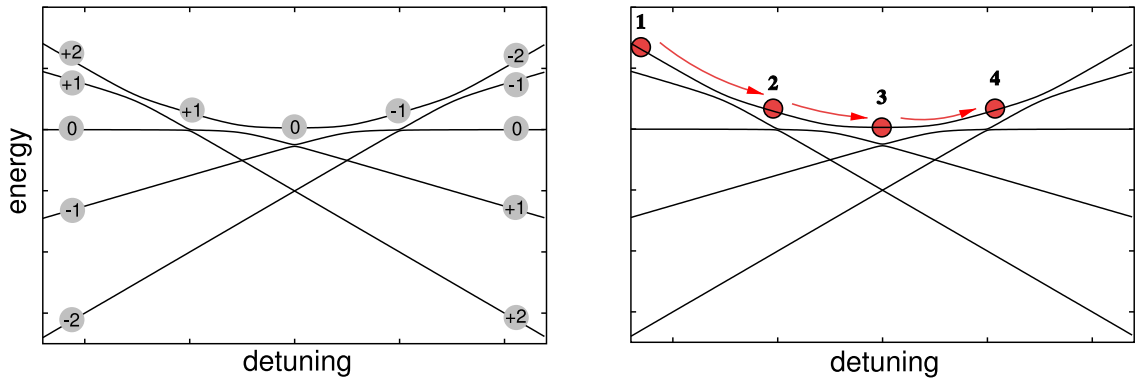


Figure 3.10: Schematic level diagram of dressed m_F states versus detuning of the radio frequency from the Larmor frequency. LEFT: The quadratic Zeeman effect lifts the degeneracy of the resonance. Without it, all levels would intersect at zero detuning. Coupling of adjacent levels ($\Delta m_F = \pm 1$) turns level intersections into avoided crossings. RIGHT: Sweeping the radio frequency, a population prepared in $m_F = +2$ adiabatically follows the dressed state across avoided intersections and ends as a pure $m_F = -1$ population when the sweep is interrupted between resonances. (see also [57])

are an invaluable tool due to their robustness. Used to prepare initial states for subsequent rotation by pulses, they also greatly increase the range of mixtures accessible by the latter technique (see also Tab. 3.5).

Hyperfine transitions $F = 2 \leftrightarrow F = 1$

A microwave field at the hyperfine frequency of ≈ 6.8 GHz can drive transitions between specific m_F levels belonging to different hyperfine manifolds. Even at small offset field, m_F levels can be selectively addressed by tuning the precise microwave frequency according to the linear Zeeman effect. Selection rules limit possible transitions to $\Delta m_F = \pm 1$. For complete population transfer, adiabatic sweeps have proven useful; pulses may be used as well, in particular for superpositions. E.g., starting from $F = 1, m_F = -1$ it is thus possible to transfer to $F = 2, m_F = 0$ or $F = 2, m_F = -2$ in a single sweep. Fig. 3.12 shows how by continuation of this sweep, the population can be successively transferred in a zig-zag way through all available m_F values, alternating between $F = 1$ and $F = 2$.

The microwave frequency does not need extra adjustment when the Larmor frequency has been determined by the procedure described above. The achievable Rabi frequency for the $|1, -1\rangle \leftrightarrow |2, -2\rangle$ transition is approximately $\Omega_0 = 2\pi \times 10$ kHz, a fully adiabatic sweep may cover a range of detunings of 400 kHz in 0.5 ms.

Apart from the possibility of preparing mixtures, the advantage of using microwave transitions is that switching between $F = 1$ and $F = 2$ is possible without changing anything in the experimental sequence before loading the dipole trap; in particular loading and evaporating in the magnetic trap is always done in $F = 1$.

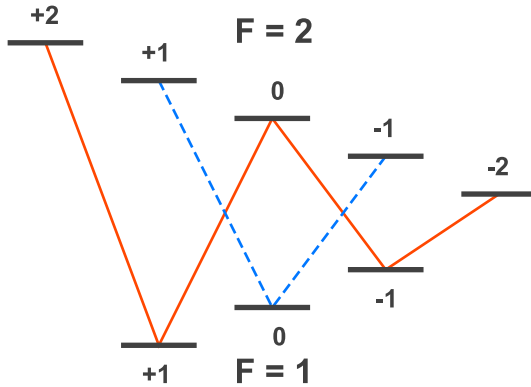
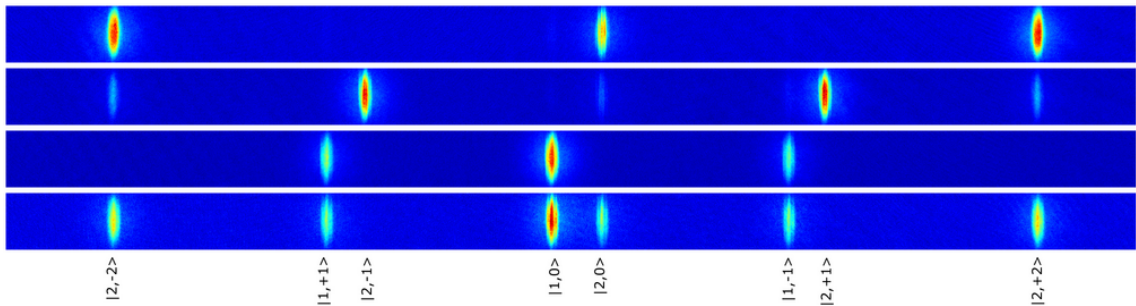
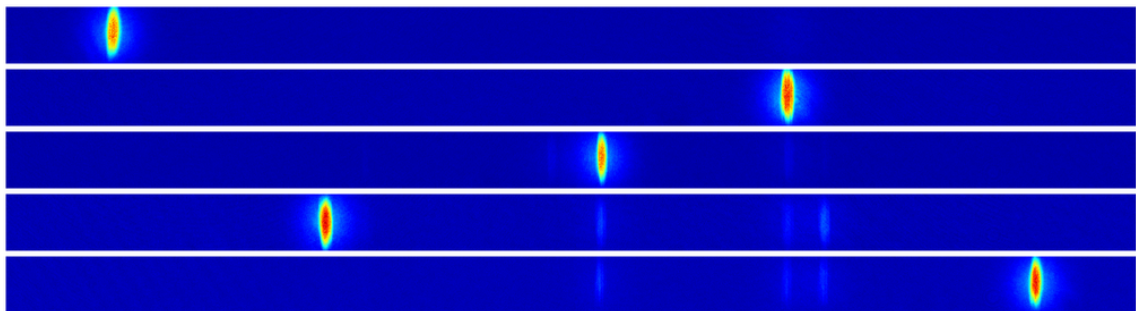


Figure 3.11: Preparation scheme using microwave sweeps. Each colored path can be traversed in a single sweep, taking the population along from one $|F, m_F\rangle$ state to the next. In the example below, we start in $|F = 2, m_F = -2\rangle$ and follow the solid path to $|F = 2, m_F = +2\rangle$.



(a) Various superpositions of $F = 2$ and $F = 1$, used to calibrate Stern-Gerlach imaging. $F = 1$ and $F = 2$ positions differ due to the quadratic Zeeman effect.



(b) Successive preparations using successive microwave sweeps. From top to bottom: $|2, -2\rangle \rightarrow |1, -1\rangle \rightarrow |2, 0\rangle \rightarrow |1, +1\rangle \rightarrow |2, +2\rangle$. The individual sweeps can also be combined into a single one spanning all transitions.

Figure 3.12: Preparation of $F = 2$ and $F = 1$ using microwave sweeps.

Chapter 4

Additional experimental tools

This chapter covers two rather peripheral experimental aspects, that yet turn out to be quite rewarding distractions, uncovering beautiful physics. In the first part, various methods aimed at reducing the disturbance of absorption images by interference fringes – a problem well known to anyone working in the field of ultracold gases and probably of much wider impact, considering the importance of laser light in modern imaging technology. The second part describes the construction of flexible and easy-to-use light source for driving Raman transitions between the hyperfine ground states of ^{87}Rb .

4.1 Fringe reduction in absorption images

4.1.1 Interference fringes in absorption imaging

Absorption imaging of atomic clouds requires highly monochromatic light within the linewidth of the atomic transition used, which usually means laser light. It is well known that illumination by laser light produces all kinds of interference patterns, even in the case of random scattering leading to so-called speckle patterns. This is an unavoidable consequence of the monochromaticity of laser light, although in principle the size of structures may be pushed down to the scale of the wavelength of the light and thus below the size of the detector elements (e.g. CCD pixels).

In our experiment, as in many others, diffraction from impurities, such as dust particles or scratches, and interference between surfaces of optical elements lead to an illuminating beam profile contaminated with structures of all length scales, from the pixel size to the field of view. The standard procedure [107] of BEC absorption imaging, in which the optical density of the atomic cloud is recovered by calculating pixel-wise the ratio of light intensities with and without absorbing atoms, is expected to eliminate structures together with the overall Gaussian beam profile of the illumination.

This strategy in fact works well and removes interference fringes as well as the Gaussian profile to a large degree. However, the method is limited by the *movement* of the fringes during the time between taking the absorption and the reference image. This movement is caused by mechanical vibrations or even changes in air flow. Since the patterns result from interference, they are sensitive to length changes of the order of the light wavelength as well as modulations of the index of refraction caused e.g. by changing air temperature. There are several obvious possibilities to at least alleviate the problem.

- Reducing mechanical vibration and air turbulence helps (Fig. 4.1), but in the end such minute variations as the patterns are sensitive to are beyond control.
- Reducing the time between the absorption and the reference image also helps, but in order to practically eliminate the structures, this time has to be cut down to the millisecond level, which is only possible using specialized cameras¹. Fig. 4.1 demonstrates both the effect of noise and waiting time.
- If optical elements leading to particularly annoying fringes are identified, measures can be taken to suppress their tendency to oscillation, they may be cleverly re-arranged to inhibit interference or simply cleansed of dust particles.

As an example, in our experiment the interferometer formed by the camera (window or chip) and most probably the glass cell has turned out to make a big contribution to moving fringes. Due to the large separation of the “cavity mirrors” it is particularly sensitive. The quality of images could be significantly improved by inserting a quarter-wave plate in front of the camera, rotating the polarization of reflected light and depriving it of its ability to interfere with illuminating light.

In the following, three more complex and expensive methods to eliminate fringes if the obvious ones fail will be presented. One of them, post-processing on a computer, is routinely employed in our analysis of absorption images. Although generally proven useful, we have shown only recently, together with Diploma student Martin Brinkmann, that post-processing is actually able to reduce noise in images to the photon shot-noise limit. The technique of illuminating with randomly scattered light has been developed to improve image quality where post-processing meets its limits. It has been characterized experimentally, but currently the cost (in time, mainly) of integrating the method into the running experiment is not justified by the limited improvement of image quality it provides under certain conditions. Finally, I propose an idea of using short, spectrally broad pulses, driving the atomic transition coherently, which possesses a certain elegance but has not yet been implemented, not least due to the costly technical challenge it poses.

4.1.2 Post-processing: algorithmic fringe reduction

In the standard procedure of absorption imaging, three images are taken in every run of the experiment: the absorption image I^{abso} , a reference image I^{ref} using the same parameters but with no atoms present, and a dark image I^{dark} taken at the same exposure time but without illumination. Ideally, I^{abso} and I^{ref} will show the same spatial light distribution, including the illuminating beam profile and interference fringes, except for the presence of atoms. The atomic cloud is assumed not to modify interference fringes. Thus, the optical column density calculated pixel-wise as [107]

$$n_{\text{OD}} = -\ln \left(\frac{I^{\text{abso}} - I^{\text{dark}}}{I^{\text{ref}} - I^{\text{dark}}} \right) \quad (4.1)$$

should be free of interference fringes and should have a homogeneous background.

As a matter of fact, this is not the case due to movement of the fringes in the time between taking the absorption and the reference image: I^{ref} does not fit I^{abso} . However,

¹Interline CCD cameras such as the PCO Pixelfly QE possess the ability of taking two pictures within a few milliseconds, and have proven to be very useful [115]. Images taken with the PCO Pixelfly QE at our experiment show virtually no remaining interference fringes in the calculated optical density distribution.

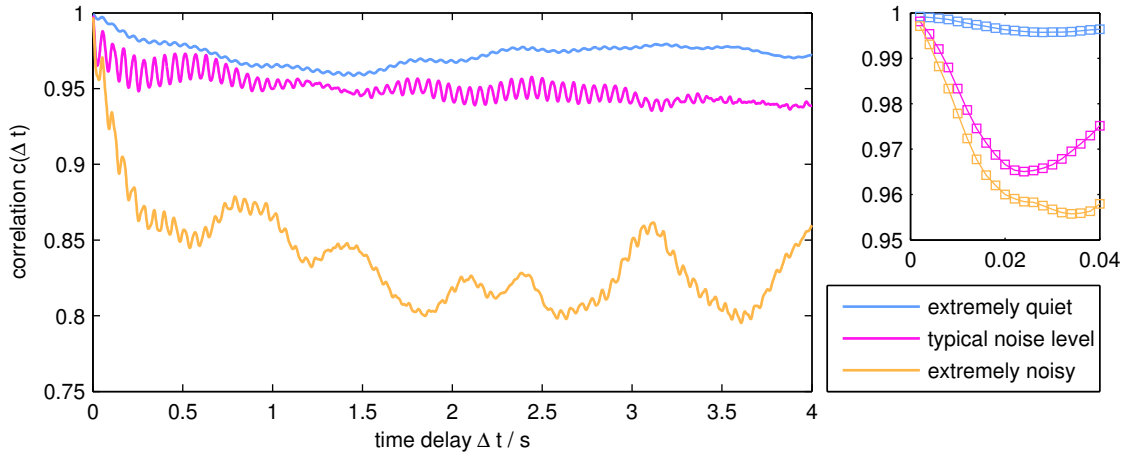
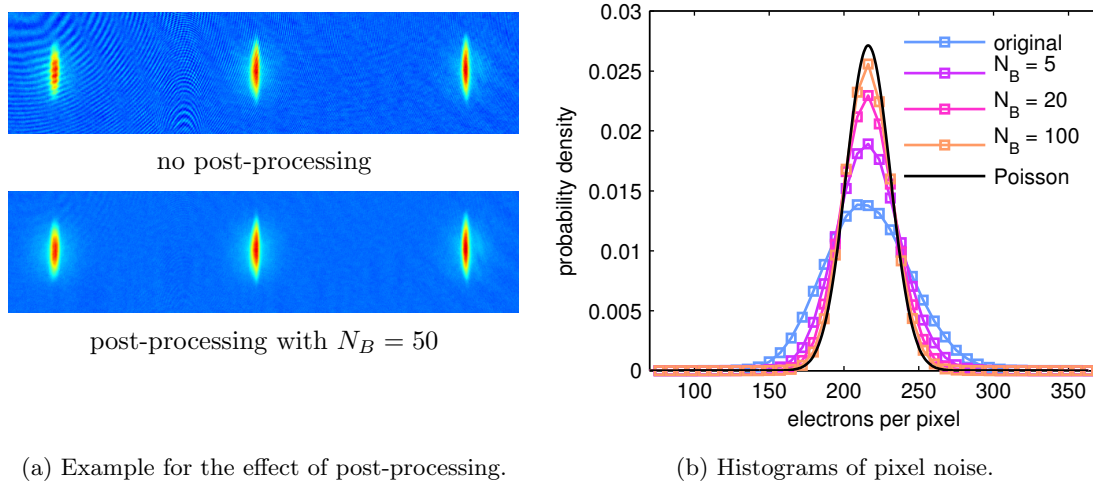


Figure 4.1: Temporal autocorrelation of interference fringe patterns. Several oscillations most probably of mechanical origin can be identified, the most pronounced one at ≈ 17 Hz. The correlation is computed as an average $c(\Delta t) = \langle \langle I_{ij}(t_2)I_{ij}(t_1) \rangle_{i,j} \rangle_{t_2-t_1=\Delta t}$ over time and pixels, from normalized images $I(t)$ (with average $\langle I_{ij}(t) \rangle_{i,j} = 0$ and standard deviation $\langle I_{ij}^2(t) \rangle_{i,j} = 1$). The images have been taken at intervals of 2 ms using a high-speed CMOS camera.



(a) Example for the effect of post-processing.

(b) Histograms of pixel noise.

Figure 4.2: Reduction of interference fringes by post-processing with an N_B -element basis. Histograms are based on a 200×200 pixel section from 10 random test images. For these histograms, the artificial reference image has been subtracted from the test images, instead of dividing the test images by the artificial reference image.

since the fringes only move a little and cycle their phase, it might be that a different reference image \tilde{I}^{ref} from the same series of experiments, or a linear combination $\sum_n c_n I^{\text{ref},n}$, fits better. The idea of our algorithm, which goes back to work in the group of W. Ertmer at the Universität Hannover, is to construct an optimal reference image $I_{\text{opt}}^{\text{ref}}$ for a given absorption image from a series of reference images taken with identical parameters.

The algorithm has been used in our group from the beginnings of the BEC project, and has already been described in detail in Michael Erhard's PhD thesis [57]. In the following paragraph, we give a short summary for completeness.

Images I , represented as two-dimensional arrays $I_{i,j}$ of $N_x \times N_y$ pixel values, form a real vector space $\mathbb{R}^{N_x \times N_y}$, and standard linear algebra methods may be used. The first step towards an optimal reference image is to construct an orthogonal basis from the set of all reference images. This is done using the Gram-Schmidt [80] orthonormalization scheme. The result is a set of pseudo-images $\{B^n, n = 1 \dots N_B\}$ that fulfill $(B^n, B^m) = \delta_{nm}$, where (\cdot, \cdot) is the canonical scalar product in $\mathbb{R}^{N_x \times N_y}$, i.e. $(A, B) \equiv \sum_{i,j} A_{i,j} B_{i,j}$. The optimal reference image is then calculated by projecting each absorption image onto this basis,

$$\tilde{I}^{\text{ref}} = \sum_n (I^{\text{abso}}, B^n) B^n. \quad (4.2)$$

This artificial reference image can then be used in (4.1) instead of I^{ref} . In a last step, the reference image is scaled such that $n_{\text{OD}} = 0$ on average *outside* a specified region which contains all atoms in all images. This improves the precision of particle numbers calculated by simply summing the optical density over all pixels. Without this step, summed-up particle numbers suffer from a fluctuating offset in the optical density. However, the rescaling factors are generally very close to one.

Together with diploma student Martin Brinkmann [112], we have had a closer look at the algorithm, in order to improve it further and test its limitations.

Since constructing the basis is rather costly in terms of computing time (proportional to N_B^2) and memory, the number of elements in the basis is practically limited to ≈ 100 . In contrast, a series of reference images can comprise several hundred images easily. It is thus necessary to pick a subset *before* actually computing the orthonormal basis.

For any given basis, the best choice to add is that normalized reference image which has a minimum projection on the existing basis, or, in other words, which is "maximally orthogonal".

We have developed a fast algorithm [112] to bring the raw reference images into near optimal order, such that it is then easy to pick as many as needed. The computing time needed for this ordering is short compared to the Gram-Schmidt calculation, but ensures that the subset of reference images used for the basis is as diverse and representative as possible. Since the algorithm is based on reduced images with a lower number of pixels (about 1% of the original pixels), the order is not exactly optimal, but large errors turn out to be rare in daily use.

As can be seen (see Fig. 4.2a), post-processing dramatically improves the quality of absorption images. One possibility of quantifying the improvement, disregarding, however, the structured nature of the interferences, is to look at the spread of pixel values in a homogeneously illuminated portion of the CCD. The read-out values of CCD pixels illuminated with a constant intensity, or average number of photons per time and pixel, are expected to obey a Poissonian distribution characterized by the average number of electrons released in the pixel.² The numbers of electrons N_{el} and photons N_{ph} are related

²Other sources of noise, e.g. quantization and read-out noise, are small at typical experimental param-

by the quantum efficiency $q = N_{\text{el}}/N_{\text{ph}}$, which is ≈ 0.6 for the camera used (SenSys ME3200+). The number of electrons is related to the final pixel value by a known constant (e.g. 2.9 electrons per count – see datasheet of the ME3200+), and in the example is ≈ 220 per pixel [112]. In fact, the noise level of images can be reduced to nearly the *shot-noise limit*, with an rms value of $\sqrt{N_{\text{el}}} \approx 15$ (see Fig. 4.2b). The small remaining discrepancy may well be caused by read-out noise. This result, obtained for a basis size of 100 elements, is an impressive demonstration of the capabilities of the post-processing algorithm, and has been observed here for the first time to our knowledge.

Finally, it is worth noting that, since the number of pixels $N = N_x \times N_y$ in any image is finite, the corresponding vector space is also finite-dimensional. This means that in principle, using a sufficiently large number of elements, the resulting orthonormal basis spans the whole space $\mathbb{R}^{N_x \times N_y}$. Obviously, the result of the post-processing algorithm will be a blank image in this case, regardless of any noise or structure in the original image, even if all images show only shot noise. However, $N_x \times N_y$ is typically > 3 orders of magnitude larger than the number of basis elements.

Now consider two random vectors in $\mathbb{R}^{N_x \times N_y}$, $\mathbf{v} = (v_1, \dots, v_N)$ and $\mathbf{b} = (b_1, \dots, b_N)$, representing a test image and an arbitrary basis vector both showing shot-noise only. The elements v_i and b_i each follow a probability distribution, $P_v(v_i)$ with $\langle v_i \rangle = 0$ for simplicity and $\langle v_i^2 \rangle = \sigma_v^2$, and analogously for b_i . \mathbf{v} and \mathbf{b} are independent quantities, i.e. the joint probability distribution is the product of the individual ones, $P(v_i, b_j) = P_v(v_i)P_b(b_j)$. The same is true for different components of each vector, and as a result $\langle v_i v_j \rangle = \sigma_v^2 \delta_{ij}$ and $\langle b_i b_j \rangle = \sigma_b^2 \delta_{ij}$. The projection of \mathbf{v} on the subspace orthogonal to \mathbf{b} results in a “shorter” (on average) vector $\tilde{\mathbf{v}} = \mathbf{v} - \frac{(\mathbf{v}, \mathbf{b})}{\|\mathbf{b}\|^2} \mathbf{b}$, whose norm is

$$\|\tilde{\mathbf{v}}\|^2 = \|\mathbf{v}\|^2 - \frac{|(\mathbf{v}, \mathbf{b})|^2}{\|\mathbf{b}\|^2}. \quad (4.3)$$

The average reduction in “length” can be calculated using the assumption that \mathbf{v} and \mathbf{b} are independent quantities,

$$\left\langle \frac{|(\mathbf{v}, \mathbf{b})|^2}{\|\mathbf{b}\|^2} \right\rangle = \left\langle \frac{\sum_{i,j} v_i b_i v_j b_j}{\sum_n b_n^2} \right\rangle \quad (4.4)$$

$$= \sum_{i,j} \langle v_i v_j \rangle \left\langle \frac{b_i b_j}{\sum_n b_n^2} \right\rangle, \quad (4.5)$$

and that the individual components are uncorrelated,

$$= \sum_i \langle v_i^2 \rangle \left\langle \frac{b_i^2}{\sum_n b_n^2} \right\rangle = \sigma_v^2. \quad (4.6)$$

On the other hand, $\langle \|\mathbf{v}\|^2 \rangle = N\sigma_v^2$, and the observed rms pixel noise

$$v_{\text{rms}} \equiv \sqrt{\frac{1}{N} \sum_i v_i^2} = \sqrt{\frac{\|\mathbf{v}\|^2}{N}} = \sigma_v \quad (4.7)$$

eters. In the case of Fig. 4.2b, the average number of electrons per pixel is ≈ 220 , corresponding to a count of ≈ 100 and quantization noise of the order of 1%, while read-out noise is specified at $8e^-$ rms.

is reduced by a factor of

$$\frac{\tilde{v}_{\text{rms}}}{v_{\text{rms}}} = \sqrt{\frac{\|\tilde{\mathbf{v}}\|^2}{\|\mathbf{v}\|^2}} = \sqrt{1 - \frac{1}{N}} \approx 1 - \frac{1}{2N}. \quad (4.8)$$

Since the number of pixels $N = N_x \times N_y$ is always several orders of magnitude larger than the number of basis vectors N_B , the total reduction of shot noise in a $N_x \times N_y$ test image by N_B basis vectors containing shot as well can be approximated as

$$\frac{\tilde{v}_{\text{rms}}}{v_{\text{rms}}} \approx 1 - \frac{N_B}{2N_x N_y} \quad (4.9)$$

and is obviously negligible for realistic numbers.

4.1.3 Random scattering: imaging with spatially incoherent light

Interference fringes result from light taking different paths to the same detector; the pattern seen by a spatially resolved detector reflects the differences in optical path length. One way of destroying unwanted patterns is thus to remove the large-scale correlation of optical path length difference and detector position. Inserting a scattering disk somewhere between source and detector will scramble the phases along different optical paths and will result in a random small-scale speckle pattern at the detector instead of large-scale fringes.

Unfortunately, this speckle pattern generally has a much higher contrast than the original fringes. Some sort of *averaging* is thus indispensable. Two effects may be considered to achieve averaging:

- *spatial averaging* over the area of a detector element (pixel) is effective if the characteristic speckle size is much smaller than pixel size. Since the speckle size is ultimately limited only by the optical wavelength ($\approx 1 \mu\text{m}$) which is much smaller than typical pixel dimensions ($\approx 10 \mu\text{m}$), this option appears to be feasible in principle. However, as discussed below, the speckle size is actually limited by the resolving power of the imaging system which is usually significantly larger than the pixel size in order to avoid unnecessary blurring.
- *temporal averaging* is achieved by moving or modulating the phase-scrambling element.³ The averaging effect is expected to be proportional to the speed of movement or modulation, and anti-proportional to the speckle size. Since the exposure time in our experiments is very short ($50 \mu\text{s}$), e.g. compared to conventional microscopy applications, care has to be taken to achieve a speckle size as small as possible even though spatial averaging remains out of reach. Still, implementing a sufficiently high rate of change is challenging.

Characteristics of laser speckle

Laser speckle has been known since the development of cw lasers, and has been the subject of systematic study since the early 1960s [116]. In its analysis, usually one of two limiting-case geometries is considered (see Fig. 4.3),

³This amounts to making use of the same mechanisms that otherwise lead to moving fringes, and in fact the same effect could in principle be achieved by artificially shaking some optical elements in the conventional detection setup. However, the considerations for speckle patterns applied to fringes quickly show that this is impractical.

- the “*free space*” geometry where the light scattered by a coherently illuminated object is observed on a screen (in most cases in the far field), and
- the “*imaging*” configuration, where a real image of the scattering object is projected on a screen by optical means.

The characteristics discussed below apply equally well to both cases, when correctly interpreted.

More complex assemblies, as they would be used in our experiment, are in general equivalent to one of the two cases. We have studied both configurations, but have achieved promising results only with the “free space” equivalent, and therefore restrict our discussion to this case.

Our setup differs from its “free space” equivalent in two ways.

- The lens L_1 , with the scattering cell mounted at one focal length f_1 distance, generates a virtual image of the cell at infinite distance, while preserving the viewing angle $2 \tan \theta = d_0/f_1$. Thus L_1 simulates the far field situation, but concentrates the scattered light to the region of interest, saving orders of magnitude of laser power compared to the actual “free space” geometry. Note that the aperture of L_1 does *not* enter in the characteristic size of the speckle pattern produced. The latter is determined solely by the viewing angle θ . However, D_1 determines the illuminated region and must be larger than the object of interest.
- Instead of directly observing the far-field speckle pattern produced in the principle plane of L_1 , it is projected onto a CCD camera through one or two imaging assemblies L_2 and L_3 , which ideally just transfer the intensity distribution from one plane to another. This is necessary in general because both the CCD camera and the object of interest must be physically separated from each other as well as from the lens L_1 . In our experiment, this is particularly true because the object of interest is a BEC trapped in a vacuum cell with limited optical and physical access. The apertures D_2 and D_3 impose additional restrictions on the speckle size by effectively limiting the viewing angle to $2 \tan \theta \leq \min(D_2/s_2, D_3/s_3)$.

Since laser speckle is a random phenomenon, it must be described by statistical methods. The most important characteristics of speckle are the *contrast* (or for more complete information, the probability density of the intensity) and the typical speckle size (or the autocorrelation of the spatial intensity distribution).

Random-walk arguments based on quite general assumptions of the scattering object [117] lead to the conclusion that the intensity in the observation plane obeys an *exponential probability distribution*,

$$\mathcal{P}(I) = \frac{1}{\bar{I}} e^{-I/\bar{I}} dI \quad (4.10)$$

with $\langle I \rangle = \sqrt{\langle I^2 \rangle} = \bar{I}$. Note that the contrast $c = \sqrt{\langle I^2 \rangle} / \langle I \rangle = 1$, and even excursions much larger than one standard deviation still occur with a high probability, making a stationary speckle pattern appear very spiky.

The Wiener-Kinchine theorem states that the autocorrelation function $C(\delta x, \delta y)$ of the intensity distribution $I(x, y)$ is the Fourier transform of its Wiener or power spectrum

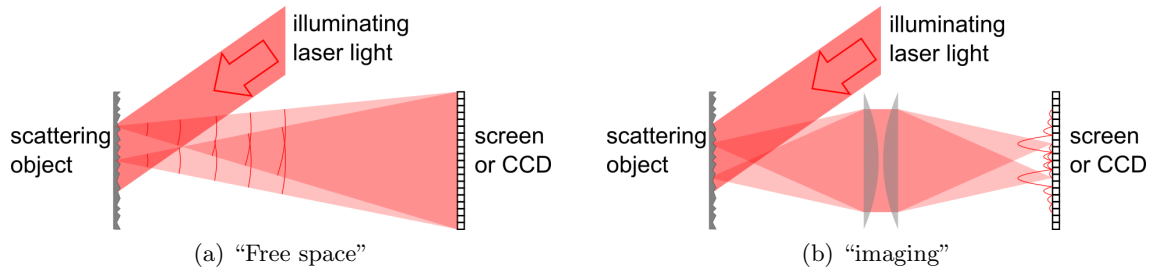


Figure 4.3: The two fundamental geometries in which laser speckle is observed.

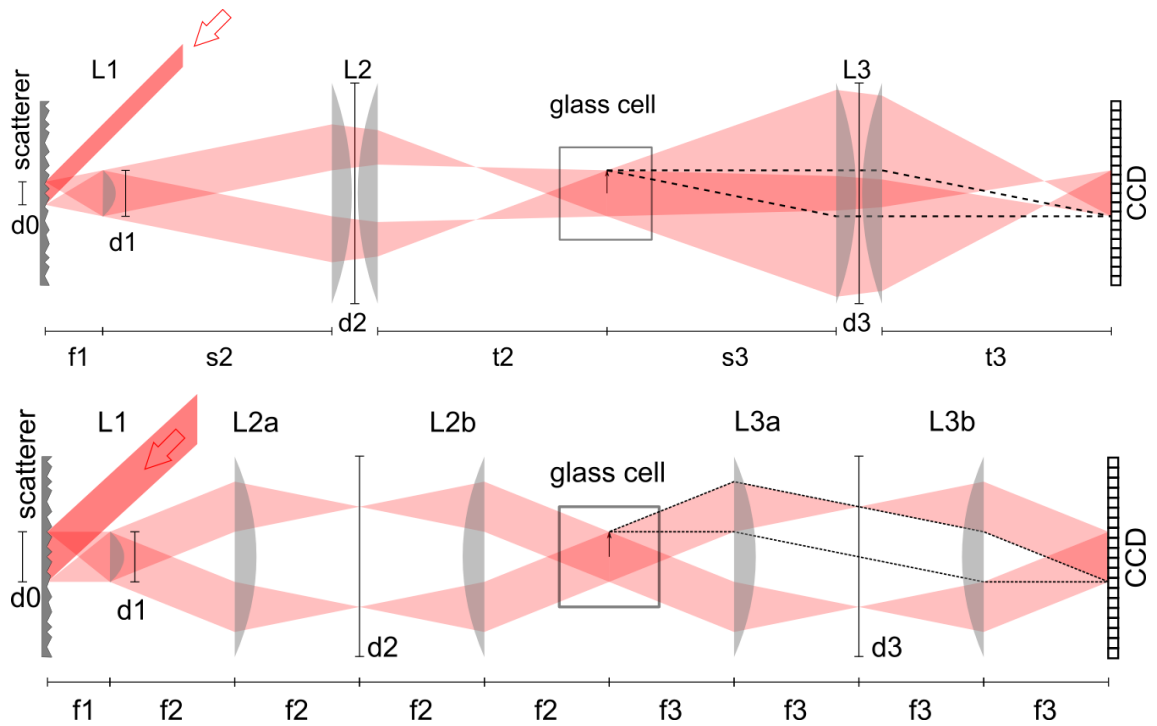


Figure 4.4: TOP: Actual geometry used in the experiment, equivalent to “free space”. Each pair of s_i, t_i satisfies the Gaussian lens formula, $\frac{1}{s_i} + \frac{1}{t_i} = \frac{1}{f_i}$. BOTTOM: Image transfer (4f) geometry, mapping both phase and intensity from the object to the image plane.

$|F(k_x, k_y)|^2$, where $F(k_x, k_y)$ in turn is the Fourier transform of $I(x, y)$,

$$\begin{aligned} C(\delta x, \delta y) &\propto \iint (I(x, y) - \bar{I})(I(x + \delta x, y + \delta y) - \bar{I}) dx dy \\ &= \iint |F(k_x, k_y)|^2 e^{i(k_x \delta x + k_y \delta y)} dk_x dk_y \end{aligned} \quad (4.11)$$

In the far field approximation, a single Fourier component in the image plane with a wave vector (k_x, k_y) corresponds to an “elementary” interference fringe, resulting from point sources separated by $(\lambda z k_x, \lambda z k_y)$ in the object plane, where z is the distance from the scatterer to the observation plane [117]. The larger the viewing angle Θ , the higher the wave numbers $k = \frac{\tan \Theta}{\lambda}$ contributing to the power spectrum, and the narrower the autocorrelation. The width Δx of the autocorrelation peak, characterizing the speckle size, is inversely proportional to the width of the power spectrum Δk , $\Delta k \Delta x \approx 2\pi$. With $\Delta k \approx \frac{\tan \Theta_{\max}}{\lambda}$, we obtain the order of magnitude of the typical speckle size

$$\Delta x \approx \lambda \frac{2\pi}{\tan \Theta_{\max}}. \quad (4.12)$$

More precisely, the power spectrum is proportional to the self-convolution of the *illuminating* power distribution $R(x', y')$ on the scattering object [117],

$$|F(k_x, k_y)|^2 \propto \iint R(x', y') R(x' - \lambda z k_x, y' - \lambda z k_y) dx' dy', \quad (4.13)$$

up to a delta-function at $k_x = k_y = 0$ which accounts for the non-negative average intensity \bar{I} .

A fluid scattering cell

Instead of e.g. a rotating scattering disk, we chose to try a scattering fluid, hoping that this would be more adequate to our requirements due to the smaller particle size and the potentially higher speed. We use a suspension of highly dispersible alumina or boehmite (Disperal[®] 40 by Sasol, kindly provided for free by the manufacturer), prepared according to the standard recipe given in the data sheet.⁴

The fluid scattering cell basically consists of a two-piece aluminum body housing two parallel microscope slides at a distance of 1 mm and leaving a free aperture of $20 \times 40 \text{ mm}^2$. Fluid is guided through the resulting $L = 40 \text{ mm}$ long channel of $W = 20 \text{ mm} \times H = 1 \text{ mm}$ rectangular cross section. Fig. 4.5 elucidates the geometry, which is known in fluid dynamics as *duct flow*. The scattering fluid is illuminated through one of the slides at an angle of about 45° , to avoid direct light in both the forward and the backward scattering geometry. A small centrifugal pump circulates the suspension in a closed loop.

The laminar solution of the Navier-Stokes equation in this geometry is known as *plane Poiseuille flow* and exhibits a parabolic velocity profile $u(h) = \hat{u} \frac{4h}{H} (1 - \frac{h}{H})$ across the smallest dimension. The Reynolds number is defined as $\text{Re} = \hat{u} H / \nu$, where ν is the kinematic viscosity of the fluid, and the volume flow rate is $\dot{V} = \frac{2}{3} \hat{u} W H$. The critical Reynolds number for the transition to turbulence in the given geometry is $\text{Re}_c = 5772$ [118].

⁴First experiments have proven the suitability of full-fat milk as well, but practical considerations strongly suggest a less perishable liquid.

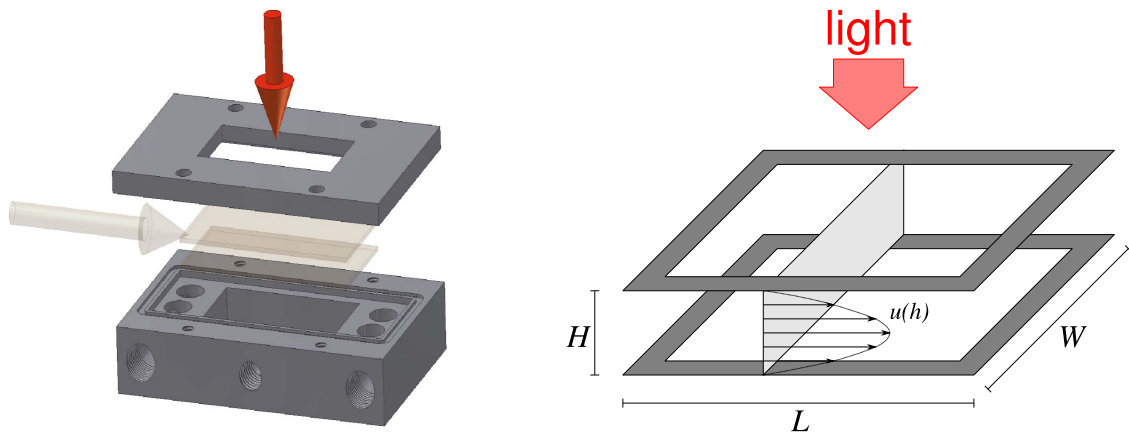


Figure 4.5: Mechanical construction and schematic flow geometry of the scattering cell

At a maximum flow rate of about $2 \ell/\text{min} = 33 \text{ cm}^3/\text{s}$, the maximum velocity assuming laminar flow is $\hat{u} = 2.5 \text{ m/s}$ and the Reynolds number assuming the viscosity of water, $\nu = 10^{-6} \text{ m}^2/\text{s}$, is $\text{Re} = 2500$, which is still significantly less than $\text{Re}_c = 5772$. The viscosity of the Disperal[®] 40 suspension is larger or at least the same as water. Thus it is in fact safe to assume laminar flow in our scattering cell. In particular, the particle velocity is purely in-plane, and the Doppler effect for scattered light can be made zero to first order if the line of sight is perpendicular to the plane of flow.

Note that the actual velocity distribution of the scatterers depends on the depth of penetration in the suspension. The fluid velocity is maximal at the center plane between the microscope slides, i.e. at a depth of penetration of 0.5 mm , while it is zero at the boundaries. Since a significant fraction of the light shines through the scattering cell, it is probably safe to assume an average velocity of the scattering particles of the same order of magnitude as \hat{u} .

Besides the velocity profile discussed above, the scattering particles also move due to Brownian motion. At room temperature $T = 293 \text{ K}$ and with an average mass of the alumina nanoparticles of $m = 4.2 \times 10^{-17} \text{ kg}$, we have a mean velocity of $\bar{v}_{3D} = \sqrt{3kT/m} = 0.017 \text{ m/s}$, or $\bar{v}_{2D} = \sqrt{2kT/m} = 0.014 \text{ m/s}$ in plane and $\bar{v}_{1D} = 0.01 \text{ m/s}$ out of plane. While the in-plane Brownian velocity is negligible, the out-of-plane velocity leads to a Doppler effect of the order of $\frac{\Delta f}{f} = \frac{\bar{v}}{c} = 3 \times 10^{-11}$, which appears to be negligible but amounts to $\approx 10 \text{ kHz}$ at optical frequencies. Compared to the linewidth of ^{87}Rb , however, this is still small. The example also emphasizes the importance of avoiding a longitudinal Doppler effect from the average fluid velocity, since that would be two orders of magnitude larger.

Brownian motion also leads to a continually evolving speckle pattern, even without mean flow. A statistically independent new speckle pattern may be expected when the particles have travelled a distance of the order of the inter-particle separation, in our case $d \equiv \sqrt[3]{n} \approx 0.75 \mu\text{m}$ where $n \approx 2.4 \times 10^{18} \text{ m}^{-3}$ is the concentration of particles. Since due to Brownian motion the rms displacement of a particle grows in time as $s(t) = \sqrt{\frac{kT}{2\pi\eta r} t}$, the displacement is $s(\tau) = d$ after a typical time $\tau = \frac{2\pi\eta r}{kT} d^2$. Again assuming the viscosity of water, we arrive at $\tau = 0.13 \text{ s}$ – by far large enough to regard a $20 \mu\text{s}$ exposure as instantaneous, but short enough to observe a “swarming” motion in live video at 10 frames per second.

Characterization of light scattered by fluid

The fluid scattering cell is intended as a way to avoid interference fringes in the detection of BEC. Together with Diploma student Lars Neumann, we have conducted several systematic tests in an external test setup in order to check the potential usefulness of the method. The test setup consists of a glass slide resolution target⁵ illuminated from behind with light backscattered from the fluid cell, and is imaged on a CCD camera⁶ (pixel size $6.8 \mu\text{m} \times 6.8 \mu\text{m}$) using the Halle custom-made objective (Section 3.3) configured for a magnification of 2.58 – corresponding to L_3 in Fig. 4.4. The CCD images of the resolution target contain areas of statistically homogeneous speckle where the slide is transparent, and at the same time allow to determine directly the resolution achieved.

We start our discussion by looking at a “still” image, i.e. with the fluid at rest and using the shortest possible exposure time $20 \mu\text{s}$. Fig. 4.6 shows the tools of the preceding section applied to images taken with the scattering cell placed at the shortest possible distance behind the slide and illuminated by a laser beam of $\approx 10 \text{ mm}$ diameter. As discussed in detail below, this configuration leads to the smallest possible speckle size.

The intensity statistics shows a very prominent exponential tail as expected, but has a maximum somewhat below the average intensity, indicating some spatial or temporal averaging. Since the fluid is at rest and the Brownian motion is negligible on the time scale of the exposure time, temporal averaging can be excluded. On the other hand, the autocorrelation function is obviously pixel-limited, and spatial averaging due to speckles of the order of the pixel size or less appears to be plausible. The numerical value of 1.7 pixels for the width of the autocorrelation is calculated from the power spectrum, because this method is more robust for nearly delta-correlated data.

Further averaging occurs when the fluid is pumped through the cell. Fig. 4.7 shows how the speckle contrast goes down as the exposure time of the camera becomes larger. The data has been taken in the realistic double imaging configuration of Fig. 4.4 with a volume flow rate of $\dot{V} \approx 9 \text{ cm}^3/\text{s}$, corresponding to a laminar peak velocity of $\hat{u} \approx 0.7 \text{ m/s}$. The speckle contrast at the shortest exposure time of $20 \mu\text{s}$ is about $3\times$ smaller than in the stationary case, equivalent to an average of $3^2 \approx 10$ statistically independent realizations of the speckle pattern. As expected, the contrast roughly follows the $\propto T^{-1/2}$ dependence that results from this intuitive picture, until it is limited by shot noise.

During the shortest exposure time of $20 \mu\text{s}$, the fluid particles move only $14 \mu\text{m}$, even assuming maximum velocity. The number of 10 statistically independent speckle patterns that result from this movement is roughly compatible with the inter-particle distance of $0.75 \mu\text{m}$.

Instead of increasing the exposure time, it is also possible to increase the speed or volume flow rate. From the $\propto T^{-1/2}$ dependence it follows that in order to achieve a speckle contrast equivalent to the shot-noise level at $T = 50 \mu\text{s}$, which is our typical exposure time for absorption detection, it is necessary to increase the flow speed by a factor of ≈ 4 . This should be technically feasible using a thinner fluid cell in combination with a pump capable of sufficient pressure.

Fig. 4.8 provides an overview of measurements showing the influence of setup parameters on the speckle characteristics. Two important conclusions can be drawn from this graph.

⁵Edmund Optics 1951 USAF Glass Slide Resolution Target

⁶Hamamatsu C8484-05G

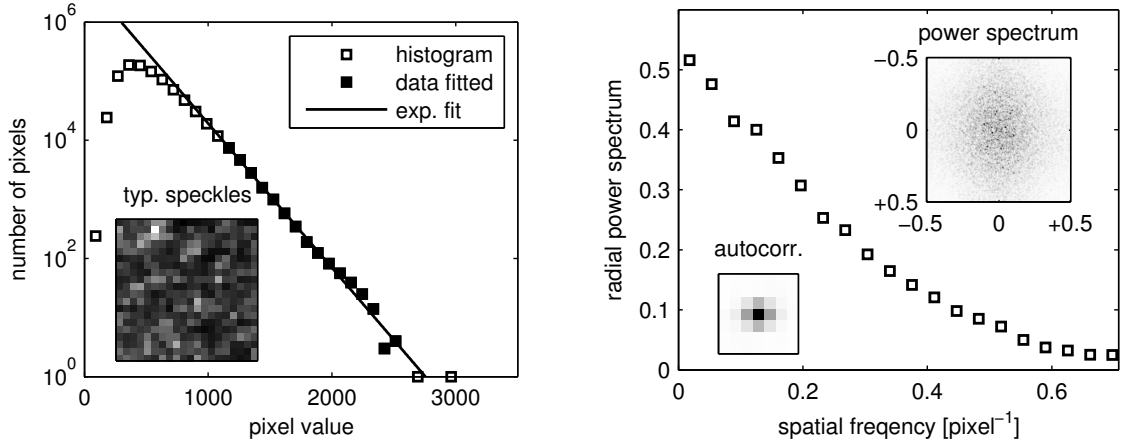


Figure 4.6: Intensity statistics and autocorrelation of a still picture (exposure time $20 \mu\text{s}$) of speckles. The contrast in this example is 0.42 at an average intensity (pixel value) of 522, and the average spatial frequency is $\frac{k}{2\pi} = 0.29 \text{ pixel}^{-1}$, corresponding to a width of the autocorrelation of $\pi/k = 1.7$ pixels.

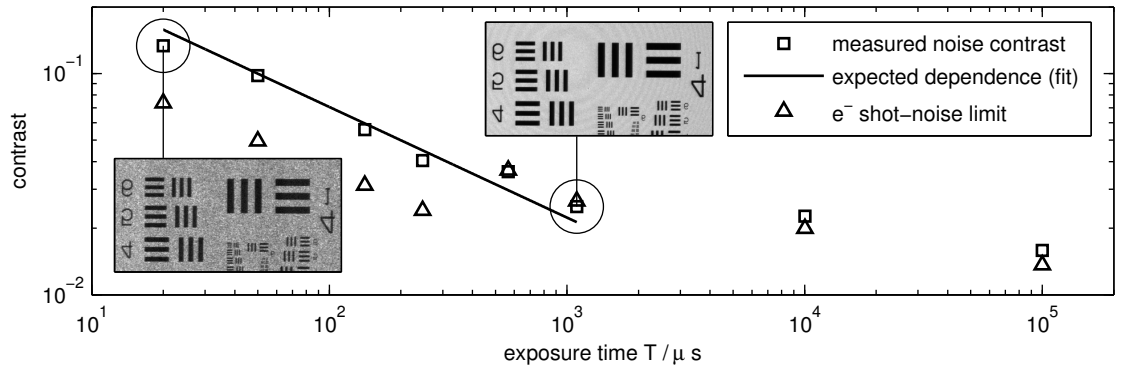


Figure 4.7: Contrast versus exposure time, measured in the double-imaging configuration and with illumination by a laser beam of $\approx 10 \text{ mm}$ diameter. The shot-noise estimate is calculated from the average number of electron per pixel assuming Poisson statistics. The conversion factor from intensity to electrons per pixel is $\frac{3.8}{5}$ for the Hamamatsu C8484 camera; this includes an additional internal gain of 14 dB. The two rightmost data points were taken with no additional gain. Note that the size of the speckle does not change, as is also reflected in the autocorrelation.

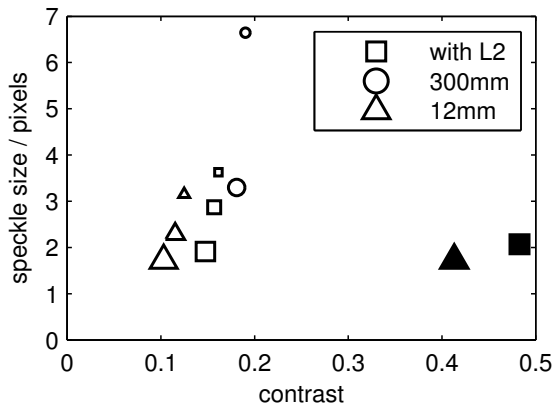
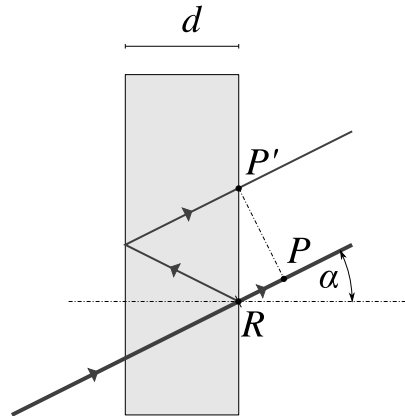


Figure 4.8: Map of speckle size versus contrast in various configurations: the marker type indicates whether the imaging lens L_2 was used or not, and in the latter case the distance between L_1 and the resolution target; the marker size indicates the illumination spot size from $\approx 10 \text{ mm}$ to tightly focused; solid symbols indicate stationary fluid.

Figure 4.9: Interference fringes from an incoherently illuminated etalon. The optical path length difference $\delta = RP' - RP$ depends on the angle α , $\delta = 2d \left(\frac{n-1}{\cos \alpha} + \cos \alpha \right)$. For small angles, $\delta \approx 2d(n + \alpha^2(n-2))$. n is the index of refraction inside the etalon; on the outside it is assumed to be one.



- In accordance with the general argument correlating the speckle size to the spatial frequency content of the light, smaller illumination spot sizes lead to coarser speckles. Increasing the distance of L_1 to the resolution target introduces an additional aperture and has the same effect, which however can be largely neutralized using the double-imaging configuration ($L_2 + L_3$, see Fig. 4.4).
- Contrary to what one might expect, the spot size only has a small effect on contrast, suggesting that there is no direct relationship between speckle size and contrast. The significantly larger contrast in imaging configuration thus remains puzzling, in particular since the contrast is also larger without averaging by fluid motion.

So unlike the original design goal, it may in fact be more useful to have a smaller spot size and larger speckles, depending on the dimensions of the object one is interested in. We have also reason to expect that the speckle contrast will not increase much when changing to larger magnification ($10\times$), as spatial averaging seems to be of secondary relevance.

Close inspection of strongly averaged images also shows the appearance of interference fringes of unknown origin when the speckle contrast decreases. These fringes do not influence the contrasts measured in Fig. 4.7 due to a suitably chosen pixel region, but of course the appearance of fringes is not quite what was intended by the use of scattered light. The purpose of using randomly scattered light is not just to hide interference fringes behind a curtain of additional noise.

It is only a certain class of fringes, however, that appears, and with a contrast of only about 3%. Compared to images taken with fully coherent illumination, where there are all kinds of fringe patterns with a total contrast of typically 20%, this is still an improvement. In terms of optical density that can be resolved in absorption imaging, the visibility is improved by a factor of 10 without any post-processing, which is fully compatible with incoherent illumination.

As an example of how interference fringes occur even under incoherent illumination, consider a flat glass plate (etalon) inserted between a source of incoherent light and a camera (Fig. 4.9). Interference occurs between light transmitted through the etalon and light reflected once back and forth between the partially reflecting parallel surfaces. The optical path length difference δ between these two rays of light in general depends on the position on the plate and on the detector. Light incident at a particular position of the camera may have passed the plate at any point. For *plane wave illumination*, an interference pattern, i.e. a systematic variation of the intensity with the position in the imaging plane, has maximum contrast if the optical path difference does *not* depend

on the position on the plate. Otherwise, averaging reduces the contrast. For *incoherent* illumination, the phase of the wavefront at any point of the etalon plane is random, and rays crossing it at different points will not interfere constructively, even if the crossing angle is the same. However, any remaining modulation of the resulting speckle pattern at the imaging plane will still be maximum under the above condition.

More formally, using ABCD-matrices, the distance r to the optical axis and the angle α of a ray crossing the etalon is related to r' and α' in the imaging plane by a transfer matrix

$$\begin{pmatrix} r' \\ \alpha' \end{pmatrix} = \begin{pmatrix} A & B \\ C & D \end{pmatrix} \begin{pmatrix} r \\ \alpha \end{pmatrix}. \quad (4.14)$$

The maximum possible fringe contrast is achieved for $A = 0$, i.e. when all rays crossing the etalon at angle α arrive at the same position r' , independent of r . The transfer matrix may be a product of several matrices each corresponding to a specific optical element. For example, a simple air space (distance d) is associated with the matrix

$$T_{\text{free}} = \begin{pmatrix} 1 & d \\ 0 & 1 \end{pmatrix} \quad (4.15)$$

and a thin lens (focal length f) is described by

$$T_{\text{Lens}} = \begin{pmatrix} 1 & 0 \\ -1/f & 1 \end{pmatrix}. \quad (4.16)$$

Obviously, a simple air space will never produce optimum contrast since $A = 1$, however the relative size of B to A becomes more favorable the larger d . In an imaging arrangement consisting of a space s , a lens f and another space b , the transfer matrix is the product

$$T = \begin{pmatrix} 1 & b \\ 0 & 1 \end{pmatrix} \begin{pmatrix} 1 & 0 \\ -1/f & 1 \end{pmatrix} \begin{pmatrix} 1 & s \\ 0 & 1 \end{pmatrix} = \begin{pmatrix} 1 - \frac{b}{f} & s + b - \frac{bs}{f} \\ -1/f & 1 - \frac{s}{f} \end{pmatrix} \quad (4.17)$$

In this case, maximum contrast is possible for $b = f$, i.e. if the etalon is in the focal plane of the lens.

If s and b fulfill an imaging relation, $1/s + 1/b = 1/f$ or $B = 0$, but the etalon is situated at distance Δs to the object plane, an equivalent way of looking at the problem is to transfer the camera backwards into the object plane and thus reduce the setup to the free space geometry.

The above arguments strongly hint at the fluid scattering cell itself, namely the glass window at the output, as the most probable source of interference fringes, since this is situated at a relatively large distance to the object plane in our setup. The glass substrate of the resolution slide, on the other hand, is not a plausible cause for the fringes because it is more or less in the object plane. The same applies to the glass cell in the actual experimental setup.

The radius of the central disk of the interference pattern of an etalon can be determined from the condition $\delta(\alpha_0) - \delta(0) = \lambda/2$. Applying the small-angle approximation, we obtain $\alpha_0 = \sqrt{\frac{\lambda}{4d|n-2|}}$. For a window of thickness 1 mm and $n = 1.5$ at 780 nm, the radius is $\alpha_0 \approx 0.02$. The diameter of the central disk in the images is roughly 0.25 mm, indicating an effective distance of 12.5 mm to the window of the fluid cell. This would mean that the imaging plane corresponding to the CCD camera through L_2 and L_3 was this distance off the plane of L_1 in our measurements, which appears quite plausible. Also, L_1 produces a

sharp image of the interference fringes at a distance f_1 which is of the same order, and it is well possible that by chance L_2 and L_3 were aligned to image that plane rather well, leading to a relatively large contrast.

In conclusion, absorption imaging with light scattered from a moving fluid is indeed technically feasible and promising. An improved setup, achieving a speckle contrast of the order of the pixel noise without fringes, requires a higher flow speed (about $4\times$) and an anti-reflection coated fluid cell.

4.1.4 Ultrashort pulses: absorption imaging in the Rabi regime

The idea to use ultrashort pulses for absorption detection is based on the observation that light from mode-locked lasers does not produce the speckle pattern otherwise common to coherent light sources. The reason is the spectral width of mode-locked lasers, which can be easily 100 nm e.g. in Ti:Sa lasers. To give an example, a mode-locked laser producing $\tau_p = 100$ fs long pulses has a corresponding spectral width of the order of $1/\tau = 10$ THz, corresponding to 23 nm centered around 830 nm. This broad range of wavelengths leads to averaging of interference patterns.

Using spectrally broad light appears to be in gross contrast to the usual requirements of absorption imaging. However, it is actually possible to make a virtue of necessity: pulses much shorter than the lifetime of the excited state $5^2P_{3/2}$, $\tau_{exc} \approx 26$ ns, manipulate the atomic state in the coherent regime. Assuming a two-level system, it is then e.g. possible to choose a pulse length corresponding to a π -pulse, driving the population completely to the excited state. In the language of absorption imaging, this corresponds to absorption of exactly one photon per atom per pulse. Choosing the repetition rate of the pulsed light source low enough to give the excited atoms time to decay, $T_{rep} \gg \tau_{exc}$, every pulse starts with all atoms prepared in the ground state and ends with all atoms having absorbed exactly one photon. Thus, the number of photons per atoms absorbed for one image is in principle exactly controllable.

The simple arguments given in the preceding paragraphs afford a first evaluation of the feasibility of the scheme. The source of pulsed light has to meet several demands.

- The spectrum should be centered around 780 nm, to a precision given by the spectral width of the pulsed source.
- Pulses must be shorter than the excited state lifetime, of the order of a few ns. Calculating with $\tau_p = 1$ ns, the spectral width is thus of the order of 1 GHz or 2×10^{-3} nm.
- In order to average out fringes from Fabry-Perot-like parasitic resonators, the spectral width should be larger than the free spectral range (FSR) of the resonator. Probably the smallest distance between any pair of surfaces leading to significant interference is our glass cell with $L = 20$ mm and an FSR of $c/(2L) = 7.5$ GHz, corresponding to 15×10^{-3} nm.
- On the other hand, to avoid optical pumping, the spectral width should be either small enough to resolve the excited states $F' = 3$ and $F' = 2$ ($\Delta\nu_{2/3'} = 267$ MHz corresponding to $1/\Delta\nu_{2/3'} = 3.7$ ns), or larger than the ground state hyperfine splitting ($\Delta\nu_{12} = 6.834$ GHz corresponding to $1/\Delta\nu_{12} = 0.16$ ns).

- The light intensity I is related to the resonant Rabi frequency Ω_0 by $\frac{I}{I_{\text{sat}}} = 2 \left(\frac{\Omega_0}{\Gamma}\right)^2$, where $I_{\text{sat}} = 1.67 \text{ mW/cm}^2$ is the saturation intensity⁷ and $\Gamma = \tau_{\text{exc}}^{-1} = 2\pi \times 6 \text{ MHz}$ is the decay rate from the excited state. Thus in order to achieve a π -pulse, the light intensity I_p during the pulse duration τ_p is given by $\frac{I_p}{I_{\text{sat}}} = \sqrt{\frac{4\pi}{\Gamma\tau_p}}$. For $\tau_p = 1 \text{ ns}$, $I_p \approx 18 \times I_{\text{sat}}$ or 30 mW/cm^2 .
- The repetition rate must be a small fraction of the decay rate, but large enough to absorb of the order of 100 photons in a typical exposure time of $100 \mu\text{s}$. A rate $1/T_r$ of a few MHz appears to satisfy both conditions. For $1/T_r = 5 \text{ MHz}$, the probability of atoms remaining in the excited state after T_r is only $e^{-\Gamma T_r} \approx 5 \times 10^{-4}$. Thus, we are talking about pulses with a duty cycle of the order of 10^{-3} .

Mode locked Ti:Sa lasers offer ultrashort pulses of typically 100 fs duration at a repetition rate, given by the cavity length, of the order of 80 MHz and in a suitable spectral range around 800 nm. The repetition rate may be reduced to the required value by extra-cavity pulse pickers or intra-cavity ‘‘cavity dumpers’’. Such systems are commercially available (e.g. from Coherent Inc.). The spectral width may be reduced by Fourier-transform pulse-shapers, at the cost of intensity, however.

Semiconductor lasers or amplifiers offer the potential to fast gain modulation by switching the current. Electronically pulsed diode lasers with pulse durations down to 0.1 ns are commercially available (PicoQuant/Toptica). To avoid the difficulties involved in tuning and stabilizing a switched laser diode with better than GHz precision, the pulsed diode could be seeded by a cw extended-cavity laser. Tapered amplifiers are by far less sensitive to varying currents and offer the additional advantage of higher power.

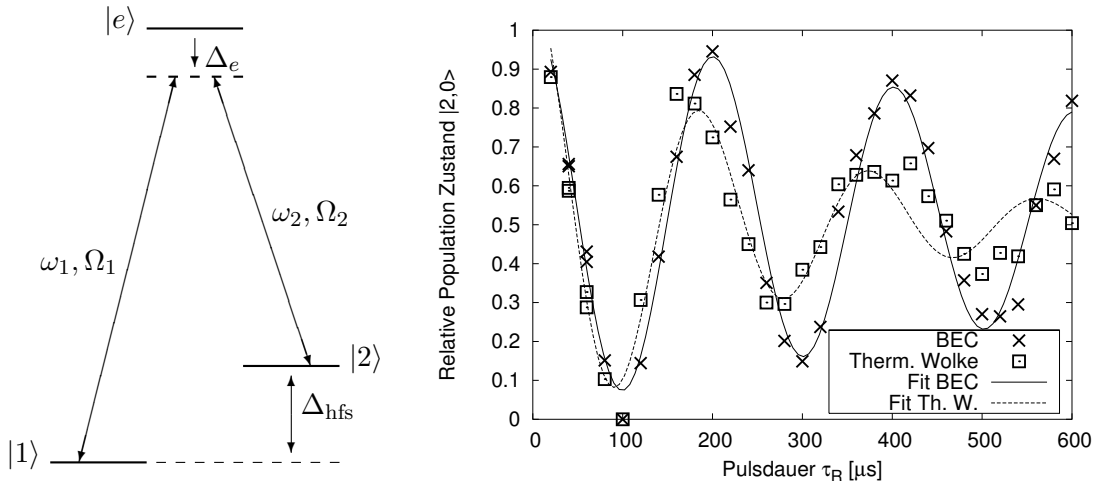
External switching of any suitable cw laser by an electro-optic or acousto-optic modulator would also be possible, but the necessary electronic and physical bandwidth poses a major technological challenge. Standard AOMs as those used in our MOT laser system (Crystal Technology Inc.) have rise times, limited by the speed of sound in the crystal, of $\tau_R > 10 \text{ ns}$, which is by far too slow. Commercial EOMs (e.g. Linos LM0202) claim a bandwidth of 100 MHz, probably limited by the relatively large capacitance of 100 pF⁸, which is also too slow. Pockels cell based Q-switches might provide the necessary rise time, but are generally limited to repetition rates in the kHz range at most. EOM- ($\tau_R = 5 \text{ ns}$) and AOM- ($\tau_R = 15 \text{ ns}$) switched laser pulses of 80 ns duration have been utilized to observe optical free-induction decay on the D_2 -line of ^{85}Rb [119]. Even though this experiment does not resolve optical Rabi oscillations, it obviously does enter the regime of coherent optical excitation.

In a recent publication [120], J. Dingjan et al. demonstrate a *pulsed, frequency-doubled laser system* based on telecommunication components, explicitly designed to coherently manipulate the ^{87}Rb $F = 2 \rightarrow F' = 3$ transition. Optical π -pulses of 4 ns duration, at a repetition rate of 5 MHz, from this laser source have been utilized by the same authors to trigger *controlled single-photon emission from a single trapped two-level atom* [121], claiming an excitation efficiency of $95 \pm 5\%$.

Questions regarding the feasibility of the coherent-absorption scheme remain. In particular, in a situation where the optical density of the atomic cloud is not small, the pulse

⁷For the cycling transition $F = 2, m_F = \pm 2 \rightarrow F' = 3, m_F = \pm 3$. For spectrally broad pulses, the excited hyperfine manifold, with splittings of the order of a few 100 MHz, cannot be resolved, effectively lowering I_{sat} . However, the D_1 line at 795 nm is sufficiently far detuned to be ignored.

⁸Charging 100 pF to 250 V in less than 1 ns requires a charging current exceeding 25 A.



(a) Schematic Λ transition. In the example to the right, $|1\rangle \equiv |F = 1, m_F = 0\rangle$ and $|2\rangle \equiv |F = 2, m_F = 0\rangle$.

(b) Rabi oscillations on the Raman transition $|F = 1, m_F = 0\rangle \leftrightarrow |F = 2, m_F = 0\rangle$. The plot shows the relative population of $|2, 0\rangle$ versus the duration of the laser pulse at resonance. Taken from [57].

amplitude (and possibly shape) will vary on its way through the cloud. In this case, the propagation of a pulse has to be calculated using the combined Maxwell- and optical Bloch equations [58, 119]. This kind of study has not been possible within this work. Other open questions involve repumping atoms that relax to the $F = 1$ manifold [121] and possible nonlinear effects at short pulse widths and high intensity.

4.2 Raman laser system

4.2.1 State manipulation via Raman transitions

Our Raman laser system is a coherent bichromatic light source, intended to drive Λ transitions between the hyperfine ground states $5^2S_{1/2}$ of ^{87}Rb , $|1\rangle$ and $|2\rangle$ with $F = 1$ and $F = 2$, respectively, via a virtual state near the excited manifold $|e\rangle$ $5^2P_{3/2}$. If the single-photon detuning Δ_e between the virtual and the actual excited state is large enough, the population of the virtual state, and with it the spontaneous decay rate, will be negligible. The virtual state can then be adiabatically eliminated from the equations of motion, and the three-level Raman process is reduced to a Rabi-like coupling between the two lower states $|1\rangle$ and $|2\rangle$. Assuming the two-photon detuning $\delta = \omega_2 - \omega_1 - \Delta_{\text{hfs}}$ is zero, the Rabi frequency of the two-photon transition is [57]

$$\Omega_R = \frac{\Omega_1 \Omega_2}{2\Delta_e}, \quad (4.18)$$

while the spontaneous scattering rate from the excited level is

$$\Gamma_{\text{sc}} = \frac{\gamma_e}{4\Delta_e^2} \left(\frac{\Omega_1'^2 \rho_{11} + \Omega_2'^2 \rho_{22}}{\rho_{11} + \rho_{22}} \right). \quad (4.19)$$

The term in brackets is a weighted average according to the ground state populations. The effective Rabi rates $\Omega_{1,2}'$ take additional excited levels into account. Obviously it is

favorable to choose a large Δ_e , since the ratio of Rabi frequency to scattering rate increases proportionally to Δ_e . However, the maximum detuning that can be used to still achieve a given Rabi frequency is eventually limited by the laser power available.

The hyperfine ground states $|1\rangle$ and $|2\rangle$ can also be coupled by microwave radiation (Section 3.5). The technical setup necessary for microwave manipulation consists largely of ready-made equipment and modules and is much less complex than the laser setup described below. However, the specific advantage of using light is the possibility of *local manipulations*, on a length scale much smaller than the extension of the BEC.

The Raman laser system has been used in our experiments on Bose condensation at constant temperature and in the observation of a mixed-spin Feshbach resonance [57], both part of Michael Erhard's PhD thesis. Although the capability of local manipulation has not been used in these experiments, the Raman laser system has proven useful for state preparation and population transfer between the $F = 2$ and $F = 1$ manifold. As an example, Fig. 4.10b shows Rabi oscillations of the two-photon transition $|F = 1, m_F = 0\rangle \leftrightarrow |F = 2, m_F = 0\rangle$. The two-photon resonance is shifted by $2\pi \times 8$ kHz with respect to the nominal hyperfine splitting due to slightly different AC Stark shifts of the two states. The damping can be explained by local dephasing across the laser beam diameter. Both effects are discussed in detail in [57].

Future experiments using the Raman laser will exploit its capability of local spin state manipulation, e.g. to produce *filled solitons*. Solitons have been observed in single-component BEC and are either *dark* [122, 123], i.e. manifest themselves as holes in the atomic density while the BEC serves as a nonlinear medium, or *bright*, which essentially means stable drops of atoms in an (at least) 1D waveguide. The dark variety can be prepared by imprinting a π phase step on the condensate wave function, while the bright variety may form spontaneously but requires either attractively interacting atoms [99, 100] or an artificially modified dispersion relation [124]. *Filled* solitons may exist in two-component condensates and as the name suggests consist of a π phase step in one component, while the resulting hole in the density distribution is filled with the other component [125].

The preparation of a filled soliton, starting from a pure $F = 1$ BEC, can be done by imprinting the π phase step on the $F = 1$ component and at the same time locally transferring the population to $F = 2$. Using the Raman laser, this can be done in a single step, using a light pulse equivalent to a full Rabi oscillation between $F = 1$ and $F = 2$. When this light is used to image the edge of a razor blade onto the BEC, the spin state of the atoms is not changed where the light is either fully screened off (0π -pulse) or not at all (2π -pulse). However, the 2π -pulse imprints an additional phase of π relative to the atoms that remain dark.⁹ Due to the limited imaging resolution, the light intensity will change smoothly from zero to full at the image of the edge, and so will the imprinted phase. In addition, about half-way across the edge, the pulse area will be π only, leading to full transfer of atoms to $F = 2$ at this point. More elaborate schemes can be realized using a spatial light modulator and possibly using a second off-resonant laser to decouple population transfer from phase imprinting.

⁹Consider a two level system, $|a\rangle$ and $|b\rangle$ with energies $\hbar\omega_a$ and $\hbar\omega_b$, resonantly coupled with Rabi frequency Ω_0 . The state of the system is a linear superposition $|\psi(t)\rangle = \alpha(t)|a\rangle + \beta(t)|b\rangle$ of the two energy eigenstates. In rotating wave approximation, the probability amplitudes evolve as $\alpha(t) = \cos(\Omega t/2) e^{-i\omega_a t}$ and $\beta(t) = \sin(\Omega t/2) e^{-i(\omega_b t - \phi)}$, starting from $\alpha(0) = 1$. In contrast, the uncoupled system evolves as $\tilde{\alpha}(t) = e^{-i\omega_a t}$ and $\tilde{\beta}$ correspondingly. For a 2π pulse, $\Omega t_{2\pi}/2 = \pi$ and $\alpha(t_{2\pi}) = -\tilde{\alpha}(t_{2\pi}) = e^{i\pi} \tilde{\alpha}(t_{2\pi})$.

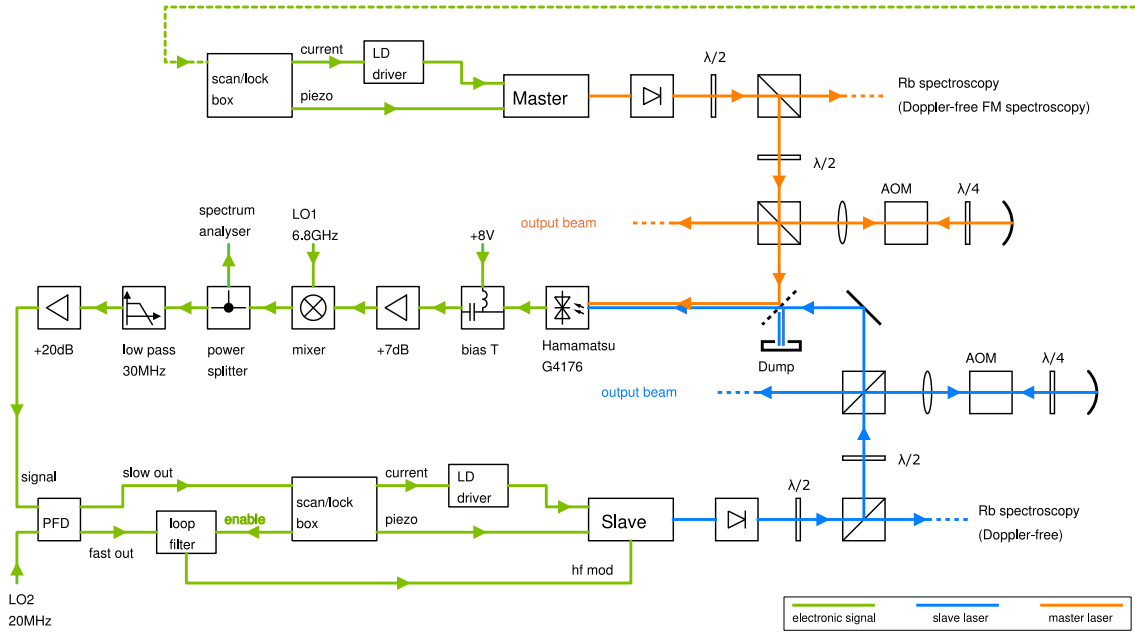


Figure 4.10: Schematic optical and electronic setup of the Raman laser system. For application at the experiment, both output beams are coupled into the same optical fiber.

4.2.2 A phase-locked diode laser system

We employ two extended cavity diode lasers (ECDL) at 780 nm, actively stabilized to maintain a frequency difference corresponding to the hyperfine splitting $\Delta_{\text{hfs}} \approx 2\pi \times 6.8 \text{ GHz}$. One of them (“Raman Master”) is free-running or frequency stabilized by Doppler-free ^{87}Rb spectroscopy, the other one (“Raman Slave”) is locked relative to the master in an optical phase-locked loop (OPLL) [126, 127], according to the schematic in Fig. 4.10. The phase of the two lasers is compared by overlapping them on a photodiode, acting as a mixer for LO^{10} and RF signals in the optical frequency domain, and an IF bandwidth in the GHz range. This phase is compared in two steps to that of two local oscillators, which together set the desired laser frequency difference. The output of the final phase-frequency discriminator (PFD) is fed back to the slave laser via a suitable control amplifier or loop filter.

Phase-locked lasers have been set up and used in a number of quantum optics experiments. Compared to other laser locking schemes, e.g. frequency stabilization by spectroscopy, the main challenge of an optical phase-locked loop is the *large bandwidth* necessary to compensate laser frequency fluctuations. This bandwidth has to be of the order of the laser linewidth, which is of the order of MHz for our extended cavity diode laser. The main design goals of our particular Raman laser system have been *simplicity* and *stability*.

- We use as much of the traditional spectroscopy-lock electronics as possible, only substituting the spectroscopy input signal with the low-frequency component of the PFD signal. Our ECDL can be tuned by modulating the diode current and by varying the external cavity length with a piezo-mounted grating acting as outcoupling mirror. Our traditional lock box feeds the amplified and filtered (PID-controller)

¹⁰Mixer terminology: LO = local oscillator, RF = radio frequency, IF = intermediate frequency.

error signal back to the diode current via the modulation input of the current driver, and moves the piezo-mounted grating in such a way as to minimize the need for current modulation. This combined, relatively low-bandwidth loop suffices to keep the Raman slave on average in lock.

- The high-frequency component of the PFD error signal is amplified and filtered separately and is added directly to the diode current via a current combining filter network located close to the laser diode. Potential ground loops are eliminated by the use of a RF transformer. The path from the PFD output to the combiner network is designed as a $50\ \Omega$ transmission line circuit and is thus modular. The control amplifier can be a simple attenuator (P-Controller) or an optimized filter and amplifier, and can be substituted by any other $50\ \Omega$ component without the need to change any settings.
- The use of a digital phase-frequency discriminator (Analog Devices AD9901), in contrast to a conventional mixer, makes the OPLL less sensitive to occasional large excursions of the relative phase. Although it does not prevent “cycle slip” [126, 127, 128], its saturation characteristic quickly drives the OPLL back into lock. The same feature also simplifies the locking procedure, extending the capturing range far beyond the loop bandwidth. In contrast to other digital PFD designs, the AD9901 features constant phase gain near the locking point, leading to low phase noise comparable to analog mixers [129]. We use an IF of 20 MHz and a 3rd order Bessel filter with 6 MHz corner frequency to remove the IF after the AD9901.
- Our OPLL has proven to remain in lock for hours. Large excursions and cycle slips have not been observed under reasonable operating conditions; if they occur, then only at a rate low enough to be ignored for our purposes.¹¹ In lock, the residual rms phase noise is $\approx 25^\circ = 0.44\ \text{rad}$, which is reasonably competitive [126, 127, 130, 131, 128].

4.2.3 Characteristics of the Raman laser system

The quality of the phase lock can be assessed looking at the output of the PFD, which is a direct measure of the phase error as long as it is within the linear regime, or by looking at the beat spectrum, where phase noise shows up as broadening of the beat note (“carrier” in rf communications terminology).

The rms phase error $\langle\phi^2\rangle$ as a measure of short-term lock quality is related to the fraction η of total power contained in the carrier as [126]

$$\eta = e^{-\langle\phi^2\rangle}, \quad (4.20)$$

assuming $\langle\phi^2\rangle \ll 1$. Alternatively, $\langle\phi^2\rangle$ can be directly calculated from the error signal, however, it is then subject to the 6 MHz bandwidth limitation given by the PFD low pass filter.

¹¹Our application requires a rigid phase relationship only for the duration of a sequence of pulses. This duration is limited by the lifetime of the condensate to several seconds at most, however, typically it may only be a fraction of a second. Cycle slips occurring from shot to shot are irrelevant. Using OPLLs for precision measurements, e.g. in a frequency chain, requires keeping track of the phase for hours or days. For this application, phase-slip-counting PFDs have been developed [126, 128].

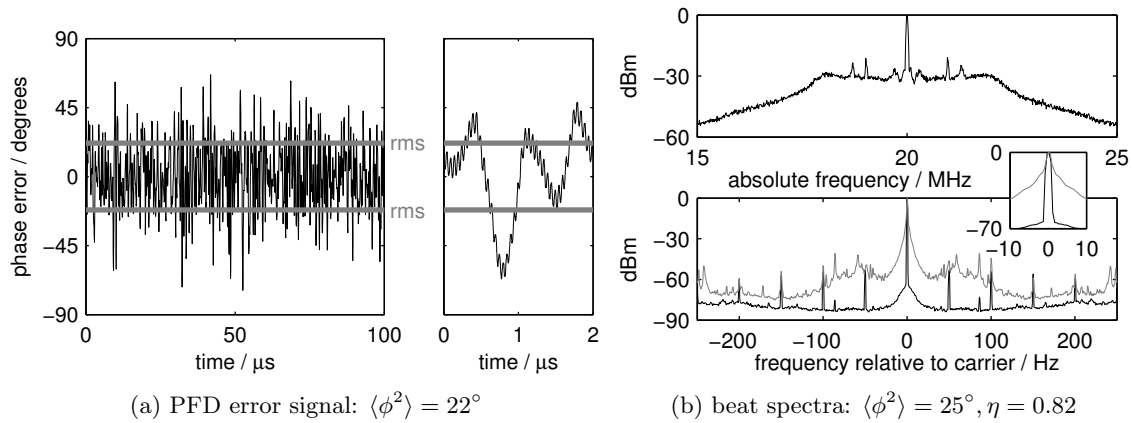


Figure 4.11: Different ways to determine the rms phase error of the OPLL. Spectra are either of the same beat signal used for feedback (top; bottom – lower curve) or recorded after transmission through 10 m optical fiber (bottom – higher curve, shaded).

Fig. 4.11 demonstrates that both methods indeed result in the same rms phase error of $\approx 25^\circ = 0.44$ rad. Both error signal and beat spectrum show residual IF modulation at 20 MHz, which is however negligible compared to the overall phase noise. In addition, the spectrum has several sharp features. Some of them can be traced to specific sources of interference, e.g. there are sidebands at multiples of the 50 Hz line frequency; another sideband at 972 kHz carries NDR Info, a radio channel which is broadcast at this frequency (AM) from a nearby transmitter station.¹²

After coupling into and transmission through 10 m of single-mode optical fiber, the beat note is significantly broadened, in particular in the 100 Hz range. In fact, the width of the carrier is limited by the 1 Hz resolution of the spectrum analyzer when the beat is recorded before fiber transmission, while after the fiber it is clearly noise dominated (see inset of Fig. 4.11). This is most probably due to acoustic noise modulating the optical path either spatially before the fiber, or via modulation of the index of refraction in the fiber. The latter effect should be suppressed when the polarization of the beams in the fiber is the same, since only differential changes of the index of refraction lead to noise in the beat note. The broadening could be eliminated by obtaining the OPLL feedback signal out of light transmitted through the fiber.

¹²Using a spectrum analyzer capable of AM demodulation and equipped with an headphone jack, it is even possible to listen to NDR Info when tuned to the corresponding sideband of the beat note. The signal is encoded in the relative phase of the laser light; it disappears when the light path is obstructed.

Chapter 5

Spin dynamics of a transversely magnetized state

*The fully transversely magnetized state as a particular superposition of Zeeman states can be seen as the fixed point of the present work. This chapter, covering those of our spinor BEC experiments that can be analyzed under the single-mode paradigm, is the heart of this thesis. The content of the following sections has been the subject of two peer-reviewed publications: work on $F = 1$ can be found in Kronjäger et al., Phys. Rev. A **72**, 063619 (2005) [2], work on $F = 2$ in Kronjäger et al., Phys. Rev. Lett. **97**, 110404 (2006) [1].*

5.1 Why this initial state?

The first experiments with spinor BEC in our group employed initial states that were either a single m_F -state prepared by rf adiabatic passage techniques, or superpositions produced by rf sweeps violating adiabaticity [57, 36] (Section 3.5). However, it turns out that single m_F states are not only eigenstates¹ of the single-particle Zeeman Hamiltonian, but also of the mean-field effective Hamiltonian (Section 2.3.1). This means that a pure single m_F state in the framework of the mean-field approximation simply does not evolve; dynamics observed starting from $m_F = 0$ [36] is a result of instability and is highly sensitive to imperfections of the preparation. On the other hand, superpositions produced by non-adiabatic sweeps suffer from ill-defined relative phases and sensitive dependence of the populations on the sweep speed.

Early experiments aiming at the inherent dynamics of spinor BEC [37, 38, 7] have started from a pure $m_F = 0$ state, and consequently have suffered from its instability, obscuring coherent oscillations. Numerical studies related to this type of experiment usually employ a small *seed* population in other states to induce dynamics, e.g. [36, 90, 93]. The instability of the $m_F = 0$ state and the resulting spatio-temporal dynamics, on the other hand, is an interesting phenomenon of its own, and has recently been observed in experiment [41]. Coherent superposition states, produced by rf pulse techniques, have been employed in experiments on two-component mixtures [26, 39], but their usefulness as an initial state of coherent spinor dynamics has been realized only recently [75, 50, 2].

¹Strictly speaking, since the interaction Hamiltonian is a nonlinear operator within the framework of mean-field theory, one cannot simply speak of eigenstates. However, there are extremal states, i.e. states for which the energy functional is extremal, and which are thus stationary states (compare Section 2.3.3).

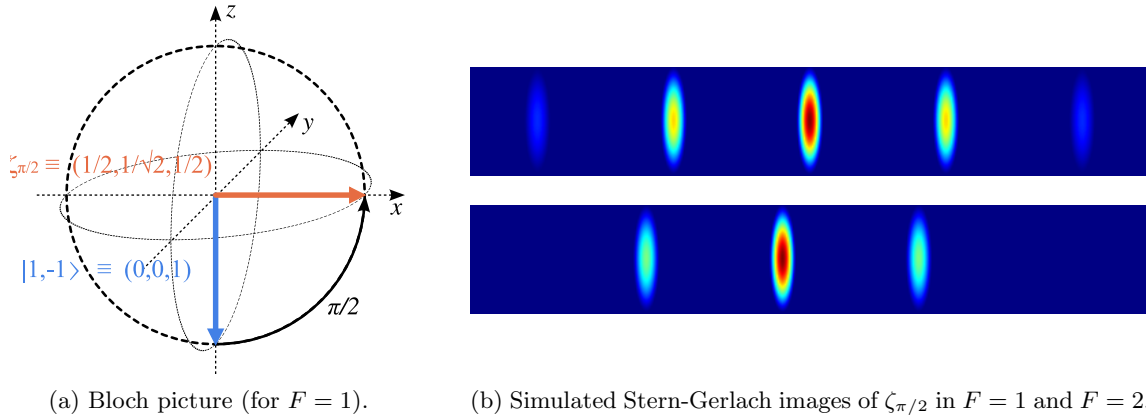


Figure 5.1: The fully transversely magnetized state $\zeta_{\pi/2}$ on the Bloch sphere and in Stern-Gerlach separated absorption images (compare Section 2.2.2 and Section 3.3). The spin vector $(\langle \mathbf{F}_x \rangle, \langle \mathbf{F}_y \rangle, \langle \mathbf{F}_z \rangle)$ is rotated from initially $(0, 0, -F)$ to $(F, 0, 0)$. The orientation of the rotated state in the xy -plane is arbitrary and has been chosen to give a real, symmetric state vector $(1/2, 1/\sqrt{2}, 1/2)$ and $(1/4, 1/2, \sqrt{3}/8, 1/2, 1/4)$ for $F=1$ and $F=2$, respectively.

The fully transversely magnetized states $\zeta_{\pi/2}$ as superpositions of all m_F states with well-defined phase are of particular relevance due to several reasons.

- They are easily and reliably prepared from the magnetically trapped state using a radio frequency $\pi/2$ -pulse (Section 3.5).
- In the limit of vanishing interaction, the dynamics induced by the Zeeman effect is strictly limited to the phases of the m_F components (Section 2.2.1), i.e. the populations remain constant. Therefore, any effect of interactions will immediately show up as population dynamics.
- On the other hand, in the limiting case of zero magnetic field the fully transversely magnetized states are equivalent to the original stretched state: orientation is irrelevant due to the absence of a symmetry-breaking magnetic field. All stretched states are then stationary due to the symmetry of the interaction Hamiltonian. A small magnetic field however will break the symmetry and lead to an observable evolution.
- For $F=1$, an analytic solution of the nonlinear SMA equation of motion, starting from $\zeta_{\pi/2}$, exists [74]. This solution exhibits a resonance phenomenon that can be traced back to the fundamental competition between Zeeman- and interaction-driven phase dynamics and is therefore present in $F=2$ as well.
- Finally, $\zeta_{\pi/2}$ is closely related to classical techniques such as Rabi- and Ramsey-experiments.

Since in both limiting cases (vanishing magnetic field or negligible interaction) the fully transversely magnetized state is stationary except for trivial phase dynamics, the driving mechanism behind the phenomena described in detail in the following sections is *the competition between Zeeman and interaction energy*. Perturbative solutions (Section 2.3.4) indeed show small population oscillations whose amplitude is proportional to

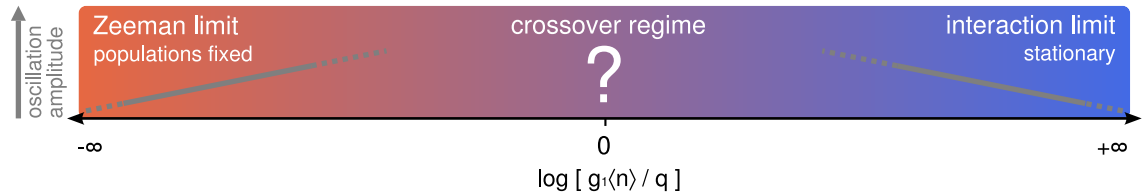


Figure 5.2: Definition of Zeeman and interaction regime. The fully transversely magnetized state is stationary (up to trivial phase dynamics) in the limiting cases. Oscillation amplitudes obtained by perturbative methods are indicated schematically.

- the quadratic Zeeman energy q in the regime dominated by interactions², i.e. $|q| \ll |g_1 \langle n \rangle|$ (*interaction regime*),
- the interaction energy $g_1 \langle n \rangle$ in the regime dominated by the quadratic Zeeman effect, i.e. $|g_1 \langle n \rangle| \ll |q|$ (*Zeeman regime*).

Obviously, there must be a crossover region $|q| \approx |g_1 \langle n \rangle|$ where large effects may be expected. Fig. 5.2 illustrates the regimes and limiting cases. An alternative interpretation in terms of *four-wave mixing*, where the competition between Zeeman and interaction energy amounts to *phase matching* taking into account a linear dispersion as well as an intensity dependence of the index of refraction, is discussed in Section 2.3.5.

5.2 Probing coherence in the Zeeman regime ($F = 1$)

Besides being invaluable tools for experimental characterization and preparation (Section 3.5), rf- and microwave driven oscillations also provide insight into the question of coherence. Fig. 5.4 and Fig. 5.5 show examples of such oscillations in $F = 1$ spinor condensates, for simplicity named after their two-level equivalents Rabi- and Ramsey-oscillations (Section 2.2.2). Simulations based on mean-field theory and the single-mode approximation (Section 2.3.2) indicate that in $F = 1$ interactions should have negligible effect on Rabi as well as Ramsey oscillations at high magnetic field, i.e. in the Zeeman regime $|g_1 \langle n \rangle| \ll |q|$. We therefore stick to the non-interacting case for the interpretation of Fig. 5.4 and Fig. 5.5.

Rabi oscillations

Driven continuously by a radio frequency signal at the Larmor frequency (Fig. 5.4), the relative populations in the *condensed fraction* in fact closely follow the single-atom predictions, the only difference to the well-known two-level case being a beat note due to the quadratic Zeeman effect. Oscillations can be tracked for up to 100 ms without significant deviation from a theoretical curve. The Rabi frequency and the detuning are fit parameters, while the radio frequency and the quadratic Zeeman effect are known³.

In contrast, the *thermal fraction* exhibits strong damping on this time scale. Shot-to-shot fluctuations of e.g. the Rabi frequency cannot be responsible for the damping, since

²we mainly consider the g_1 term of interactions, since this is present for any $F = 1$ as well as $F = 2$, and in the latter case plays the dominant role (Section 2.3.4).

³Strictly speaking, the quadratic Zeeman effect is related to the Larmor frequency, which differs from the rf by a small detuning of the order of 0.1%. This is small enough to be neglected, and calculations of the quadratic Zeeman effect are thus generally based on the radio frequency applied.

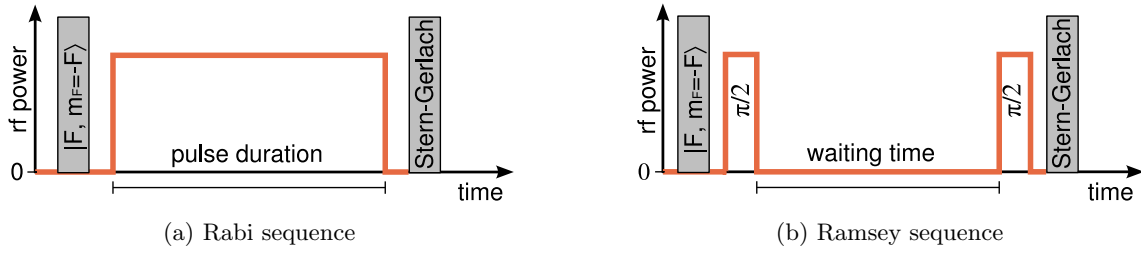


Figure 5.3: Schematic rf pulse sequence for the Rabi- and Ramsey experiments.

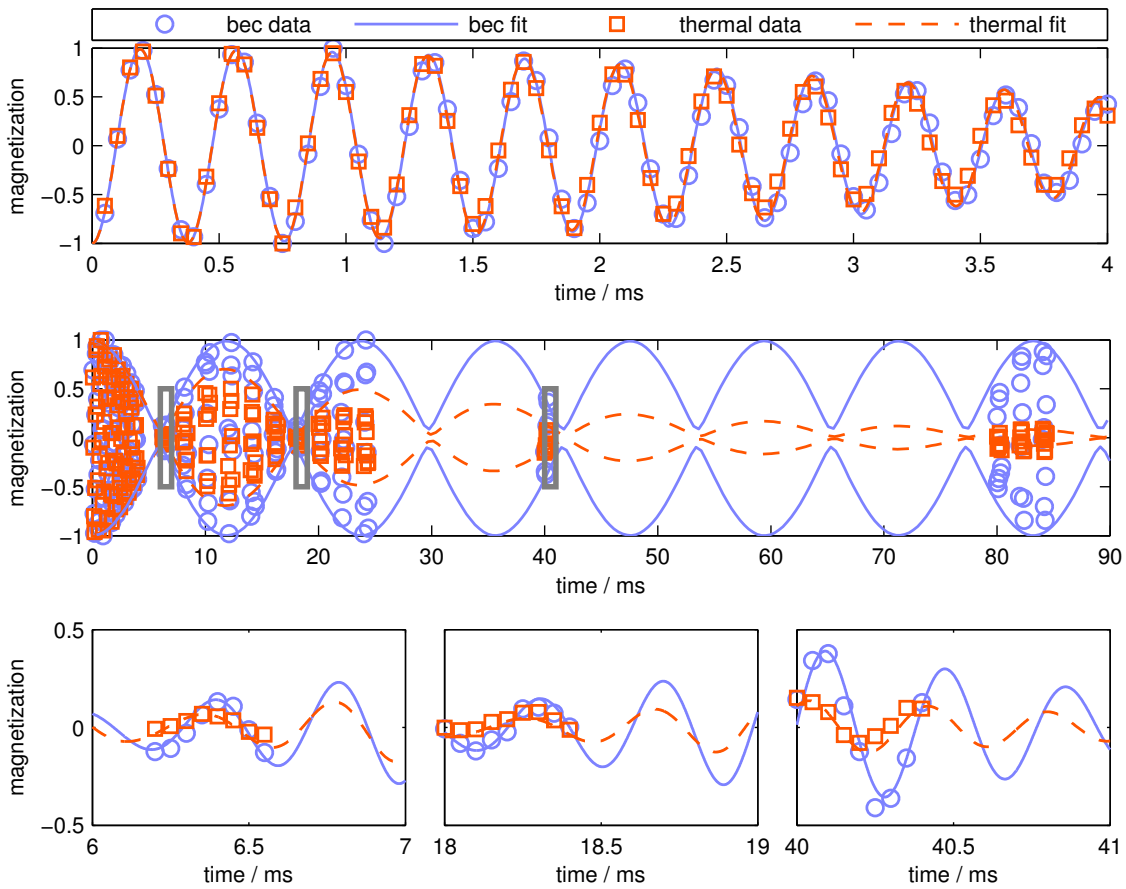


Figure 5.4: Rabi oscillations of a BEC with a significant thermal component in $F = 1$. Fits are calculated using the super-operator formalism and include damping ($\gamma^2 = 40$, estimated) for the thermal component. Parameter values obtained from a least-squares fit are Rabi frequency $\Omega_0 = 2\pi \times 5.274\text{Hz}$ and detuning $\Delta = -2\pi \times 194\text{Hz}$ for the BEC, $\Omega_0 = 2\pi \times 5284\text{Hz}$ and $\Delta = -2\pi \times 168\text{Hz}$ for the thermal cloud. While the difference in detuning is insignificant in view of the much larger Rabi frequency, the difference in Rabi frequency is in fact noticeable over the observation time of 100 ms (bottom row).

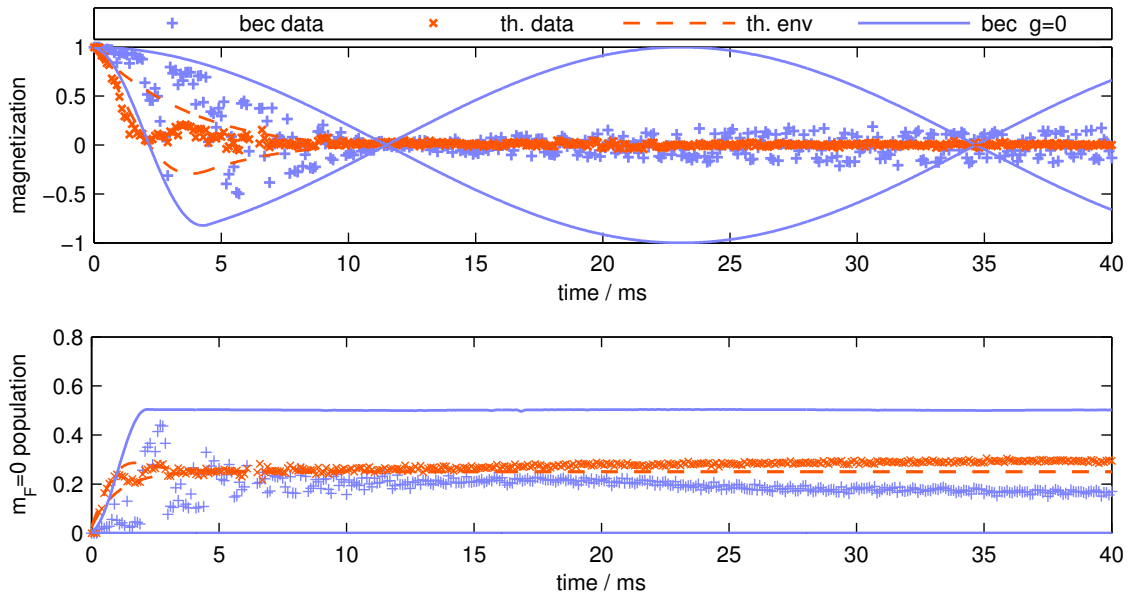


Figure 5.5: Ramsey experiment in $F = 1$. (For another example of a $F = 1$ Ramsey experiment, see Section 3.4.) The population of $m_F = 0$ oscillates at twice the Larmor frequency.

they would still lead to data filling the full envelope. However, thermal atoms can be viewed as a stochastic ensemble of individual non-interacting particles subject to a time-varying Zeeman Hamiltonian, as a result of different trajectories in space in conjunction with gradients. This applies to the offset field defining the Larmor frequency as well as the Rabi frequency given by the driving rf field. Taking into account the gradient of the offset field in the simplest possible form, i.e. a Lindblad operator $\mathbf{L} = \gamma \mathbf{F}_z$ (Section 2.2.3), leads to exponential damping. It is not possible however to accurately describe the data in this way, as is evident from the fact that the exponential damping assumed for the theoretical curve in Fig. 5.4 overestimates the actual envelope at short times but underestimates it at long times.

This is possibly explained by the fact that the variations in detuning expected from magnetic field gradients are of the order of 100 Hz (Section 3.4) and much smaller than the Rabi frequency Ω_0 . Thus they enter only quadratically into the local oscillation frequency $\Omega = \sqrt{\Omega_0^2 + \Delta^2}$, and the damping observed is probably caused by variations of the Rabi frequency Ω_0 rather than the detuning Δ . One can also think in terms of dressed states (compare [28]), where the Hamiltonian including rf coupling becomes diagonal with energy eigenvalues that are to first order given by the Rabi frequency near resonance. In this basis, the initial state $|1, -1\rangle$ is a superposition and dephasing by fluctuations of the energy levels could again be described by a diagonal Lindblad operator.

Ramsey oscillations

Ramsey oscillations (Fig. 5.5) occur at the Larmor frequency which is subject to shot-to-shot fluctuations large enough to obscure phase evolution after a few milliseconds (Section 3.4). Therefore, information has to be gained from the envelope only. Again, shot-to-

shot fluctuations will not change this envelope⁴. From Fig. 5.5 it is obvious that Ramsey oscillations are much more strongly damped in both condensed and thermal fraction – in fact not even a second node of the beat can be distinguished.

The damping of the thermal component can again, in principle, be explained in terms of a fluctuating Hamiltonian and modeled by a diagonal Lindblad operator $\mathcal{L} = \gamma \mathbf{F}_z$ (Section 2.2.3). However, the simple exponential does not seem to fit the data well. In any case, the much smaller time constant compared to Rabi oscillations indicates that inhomogeneities of the offset field are more pronounced than those of the driving rf field: the former enter linearly into the phase of the Ramsey oscillation, but are suppressed quadratically in the effective Rabi frequency $\Omega = \sqrt{\Omega_0^2 + \Delta^2}$ as discussed in the preceding section.

Magnetic field gradients may also explain damping in the BEC fraction, however, since in the framework of mean-field theory all particles are supposed to populate the same quantum mechanical state or wave function, the Lindblad formalism is not adequate. Instead, spatial inhomogeneities may lead to deviations from the SMA paradigm, i.e. spatially structured wave functions for the individual spin components. Depending on the size and direction of these structures, they will not be resolved in our images and instead may show up as apparent damping in global quantities like e.g. relative populations. The length scale of spin structures is bounded from below by the spin healing length, which in our experiment and for $F = 1$ typically is $4.3 \mu\text{m}$ (Section 2.3.6). Thus, in the astigmatic dipole trap, the extension of condensates in the direction of the detection beam (y -direction) is large enough to allow for domain formation which would not be observable in absorption images.

Formation of *spin patterns* has been observed in the crossed-beam dipole trap in the context of magnetic field compensation (Section 3.4, Fig. 3.6). The rate of dephasing due to gradients across the condensate is of the order of at least 20 Hz (Section 3.4), resulting in complete (π) dephasing after less than ≈ 25 ms; this is consistent with the observed timescale of damping in Fig. 5.5. Gradient induced spin structure is thus a plausible explanation for the damping of the BEC component in the Ramsey experiment.

Spatial structure formation also plays a role in the experiments aiming at interaction effects (Section 5.3 and Section 5.4) and is covered in more detail in the context of breakdown of the SMA (Section 5.6). In the elongated dipole trap, the formation of spin structure has been directly observed both in the interaction and in the Zeeman regime (Chapter 6). However, none of the above experiments detects the phases of spin components or, in other words, the transverse components of the spin vector – in contrast to the Ramsey experiment.

On the other hand, *thermalization effects*, which are discussed in Section 5.5, lead to population redistribution between the thermal cloud and the condensed part. This redistribution also shows up as a damping of the coherent dynamics, on a time scale compatible with observations. The relative phases of m_F states may also be expected to vary randomly from shot to shot, reflecting the statistical nature of the process. Since the Ramsey experiment is sensitive to these phases, the complete absence of large magnetization values at time > 10 ms is not compatible with the assumption of a condensate wave function with a spatially homogeneous phase. Thus, if thermalization is responsible for

⁴While in the Rabi case the envelope is simply calculated by plotting only the extrema of the underlying oscillation, a more sophisticated technique is used in the Ramsey case. The full dynamics is calculated for a number of detunings chosen randomly from a limited range, and the resulting maximum and minimum magnetization is evaluated at each time step.

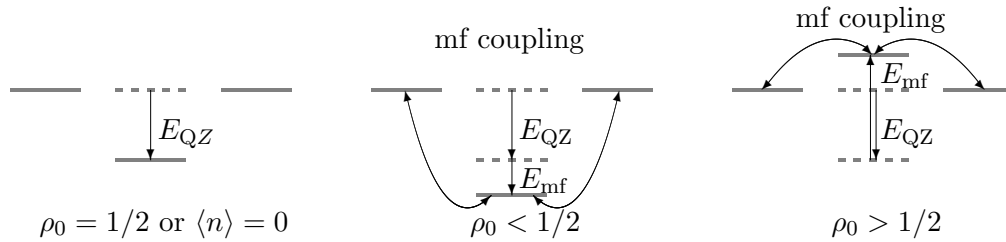


Figure 5.6: Level schemes of ^{87}Rb $F = 1$ including quadratic Zeeman energy E_{QZ} and mean-field energy E_{mf} . Note the sign convention, positive coefficients q and g_1 correspond to negative energies, i.e. lower $m_F = 0$. For ^{87}Rb $F = 1$, $q > 0$ and $g_1 < 0$. Also schematically shown is the coupling of m_F states by the mean-field Hamiltonian.

the observed damping, its effects must go beyond what can be described in single-mode approximation (SMA).

5.3 Effects of interaction in the Zeeman regime ($F = 1$)

Looking for signs of spin-dependent inter-atomic interaction, it has turned out that for realistic magnetic fields $B > 150$ mG (limited by the frequency range of the rf generator and amplifier, which are needed for state preparation and possibly analysis) an influence on the shape of Rabi or Ramsey oscillations is barely noticeable even in simulations. Additionally, Ramsey oscillations are highly sensitive to dephasing through Larmor frequency variations, which are on the other hand irrelevant for interaction effects due to rotational symmetry. In fact, it is more promising to perform an incomplete Ramsey experiment only, omitting the second $\pi/2$ -pulse. This amounts to preparing of the *fully transversely magnetized state* $\zeta_{\pi/2}$ and watching it evolve.

In the following, we will first develop an intuitive picture of the dynamics of this state under the influence of interactions and a magnetic field. In order to fit experimental data, we use an analytic solution of the SMA equations of motion, that may also serve as a check for the intuitive picture. The latter turns out to pertain to the case of $F = 2$ where no analytic solution is available.

Understanding spin dynamics in $F = 1$

Population dynamics of the fully transversely magnetized state is a result of spin-dependent interaction, which in the mean-field picture introduces off-diagonal matrix elements into the spin Hamiltonian. The matrix elements of the effective interaction Hamiltonian depend on the state, and in particular on the relative phases of the m_F -components (Section 2.3.2). Phase dynamics in turn is driven by energy differences represented by diagonal elements. In this simplified picture, the crossover between Zeeman and interaction regime is a result of competition between the Zeeman effect, lowering the $m_F = 0$ level relative to $m_F = \pm 1$, and mean-field energy lifting or lowering it further depending on the spin state and the sign of g_1 (as illustrated in Fig. 5.6).

One possibility to write the nonlinear spinor equations of motion (2.73) (for $F_z = 0$)

in the form of an effective (“mean-field”) Hamiltonian is

$$\mathbf{H}_{\text{mf}} = 2\hbar g_1 \langle n \rangle \begin{pmatrix} |\zeta_0|^2 & \zeta_0 \zeta_{-1}^* & 0 \\ \zeta_0^* \zeta_{-1} & |\zeta_{+1}|^2 + |\zeta_{-1}|^2 & \zeta_0^* \zeta_{+1} \\ 0 & \zeta_0 \zeta_{+1}^* & |\zeta_0|^2 \end{pmatrix} \quad (5.1)$$

$$= 2\hbar g_1 \langle n \rangle \begin{pmatrix} \rho_0 & 0 & 0 \\ 0 & 1 - \rho_0 & 0 \\ 0 & 0 & \rho_0 \end{pmatrix} \quad (5.2)$$

$$+ 2\hbar g_1 \langle n \rangle \sqrt{\frac{\rho_0(1-\rho_0)}{2}} \begin{pmatrix} e^{-i(\theta_0-\theta_{-1})} & 0 & \\ e^{i(\theta_{-1}-\theta_0)} & 0 & e^{i(\theta_{+1}-\theta_0)} \\ 0 & e^{-i(\theta_{+1}-\theta_0)} & 0 \end{pmatrix}. \quad (5.3)$$

The diagonal part, shifting the energies of the m_F states, only depends on the *population* of $m_F = 0$. For $\rho_0 = 1/2$, as in the case of the fully transversely magnetized state $\zeta_{\pi/2}$, the diagonal elements are all equal and have no influence on the dynamics. In contrast, the off-diagonal elements, coupling different m_F states, depend on *relative phases*. They vanish only in the case of $\rho_0 = 0$ or $\rho_0 = 1$, i.e. a pure $m_F = 0$ state, and consequently there is no population dynamics in these cases.

In the Zeeman regime, the mean-field energy is small and phase dynamics dominated by the Zeeman energy, introducing a linearly growing phase shift of $m_F = 0$ relative to $m_F = \pm 1$. As a result, the phase-dependent off-diagonal terms oscillate at the frequency $\omega_{\text{QZ}} = q/\hbar$, driving in turn a population oscillation at twice the frequency and with an amplitude proportional to the period of oscillation. In the opposite case, where the mean-field energy dominates, both phase and population oscillate: an increasing phase shift induces an increasingly rapid changing population, which in turn slows down and finally reverses phase dynamics. The balanced condition for this oscillation is $E_{\text{QZ}} = E_{\text{mf}}$. Since one turning point of the resulting oscillation is the initial state $\zeta_{\pi/2}$, the amplitude grows proportionally to q while the period remains fixed in the limit of small q . Asymptotic evolution occurs at resonance, when q and $g_1 \langle n \rangle$ are balanced such that the equilibrium condition $E_{\text{QZ}} = E_{\text{mf}}$ is approached only for an extremal population, i.e. $\rho_0 \rightarrow 0$ or $\rho_0 \rightarrow 1$. This picture is analogous to optical four-wave mixing with nonlinear phase matching (Section 2.3.5).

In $F = 1$, the only parameter determining interactions is $g_1 \langle n \rangle$, and the behavior of the system is fully characterized by the ratio

$$k = \frac{g_1 \langle n \rangle}{q} \quad \begin{cases} |k| \ll 1 & : \text{ Zeeman regime} \\ |k| \gg 1 & : \text{ interaction regime} \end{cases} \quad (5.4)$$

The time scale of evolution is given by q or $g_1 \langle n \rangle$, depending on which parameter is dominant.

Analytic results for $F = 1$

For $F = 1$, the mean-field equations of motion (2.73) can be identified with those of a classical non-rigid pendulum [75]. The classical phase space for this system (Fig. 5.7) is two-dimensional and parameterized by the $m_F = 0$ phase and the population (θ_0, ρ_0) . There are generally two distinct regions, separated by a critical trajectory. *Running phase* trajectories are periodic orbits closed across the θ_0 -boundaries of the rectangular domain

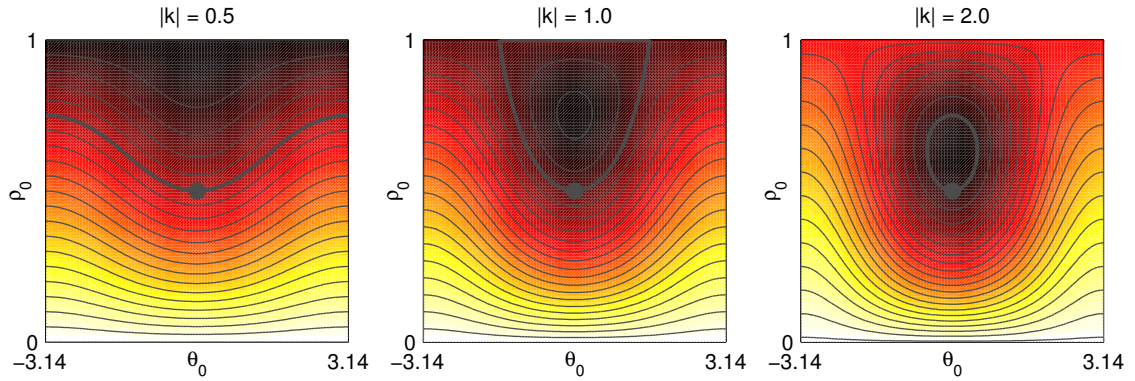


Figure 5.7: Classical phase space for the non-rigid pendulum, equivalent to $F = 1$ spin dynamics. Colors and contour lines indicate curves of constant energy, i.e. possible trajectories. The initial state $\zeta_{\pi/2}$ and the corresponding trajectory are highlighted. This plot has been calculated using the energy functional from [75].

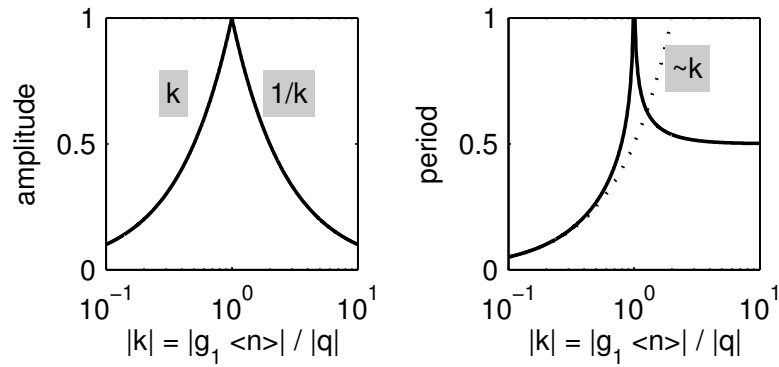


Figure 5.8: Amplitude and period of population oscillations in $F = 1$, according to the analytic solution (5.5). The period diverges to infinity at $|k| = 1$.

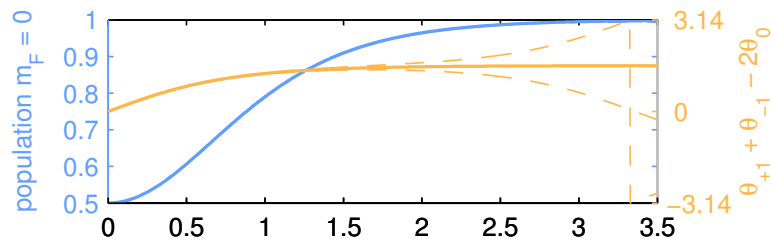


Figure 5.9: Population and phase dynamics at and around resonance $k = -1.00 \pm 0.01$, starting from $\zeta_{\pi/2}$.

$[0, 2\pi] \times [0, 1]$ or, in other words, wrapping around the cylinder formed by joining these boundaries. They correspond to a *rotating* pendulum. *Oscillating phase* trajectories are closed within the rectangular domain and correspond to a pendulum oscillating around its stable equilibrium position. The critical trajectory or *separatrix* is not closed but ends in singular points, meaning that time evolution must come to a standstill approaching these points. This corresponds to a pendulum having just enough energy to reach its unstable equilibrium position. In the context of spin dynamics, the initial state $\zeta_{\pi/2}$ lies in the domain of running phase solutions for $|k| < 1$ (Zeeman regime) and in the domain of oscillating phase solutions for $|k| > 1$ (interaction regime). For $|k| = 1$, it is part of the separatrix (resonance) and in time asymptotically approaches the unstable equilibrium state $\rho_0 = 1$.

For the special case of the initial state $\zeta_{\pi/2}$, the equations of motion (2.73) can be solved analytically (Patrick Navez [74]) in terms of Jacobi elliptic functions (Section 2.3.4). The directly measurable populations evolve according to

$$|\zeta_0(t)|^2 = (1 - k \operatorname{sn}_k^2(qt))/2, \quad (5.5a)$$

$$|\zeta_{\pm}(t)|^2 = (1 + k \operatorname{sn}_k^2(qt))/4. \quad (5.5b)$$

In the limiting cases of vanishing magnetic field or interaction, the solution simplifies to ordinary harmonic oscillations:

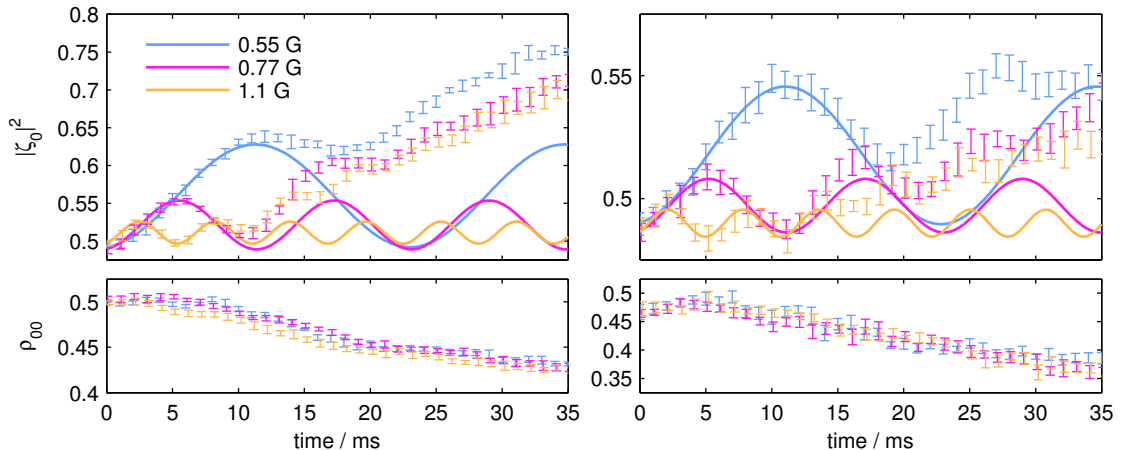
- For small $|k| \ll 1$, the Jacobi elliptic functions can be approximated by ordinary trigonometric ones, i.e. $\operatorname{sn}_k(x) \approx \sin(x)$, $\operatorname{cn}_k(x) \approx \cos(x)$, $\operatorname{dn}_k(x) \approx 1$. Thus, in the Zeeman regime the populations of (5.5) oscillate with an amplitude given by $|k|$, and a period of $\pi/|q|$.
- For large $|k| \gg 1$, the identity $\operatorname{sn}_k(x) = \frac{1}{k} \operatorname{sn}_{1/k}(kx)$ leads to the trigonometric approximation $\operatorname{sn}_k(x) \approx \sin(kx)/k$. Therefore, in the interaction regime, the populations oscillate with amplitude $1/|k|$ and period of $\pi/|g_1 \langle n \rangle|$.

The crossover region $|k| \approx 1$ exhibits a maximum of the amplitude while the oscillation period diverges. In other words, at $|k| = 1$ the evolution becomes aperiodic, and the $m_F = 0$ population asymptotically approaches 1. Fig. 5.8 shows both amplitude and period across two decades of k . The analytical solution for the special case of the fully transversely magnetized state supports the general considerations of the preceding section.

Experimental results

Across the range of magnetic fields under consideration within this work, ^{87}Rb $F = 1$ is well in the Zeeman regime, i.e. the spin-dependent interaction energy is small compared to the quadratic Zeeman effect. From Patrick Navez' analytic solution [74], we expect small oscillations of the m_F populations in this regime. The fact that the oscillation frequency approaches a value given by the quadratic Zeeman effect makes it possible to measure the effect of an interaction that otherwise is too weak to be observed directly: at low magnetic field, when interaction energy dominates, the period of oscillation is too long to be reliably observed before thermalization effects set in.

Fig. 5.10 confirms the behavior expected in the Zeeman regime: population oscillations are clearly visible for the condensed fraction, with the expected scaling of the frequency $\propto B^2$ and of the amplitude $\propto 1/B$. For the first 10 ms, the analytic solution (with k as a fit parameter) describes the data very well within error bars. The thermal fraction,



(a) “hot” – 27% cond. fraction ($\approx 3 \times 10^5$ atoms)
From fit: $|g_1 \langle n \rangle| \approx 33 \text{ s}^{-1}$, $\langle n \rangle \approx 1.9 \times 10^{14} \text{ cm}^{-3}$

(b) “cold” – 75% cond. fraction ($\approx 4 \times 10^5$ atoms)
From fit: $|g_1 \langle n \rangle| \approx 12 \text{ s}^{-1}$, $\langle n \rangle \approx 0.7 \times 10^{14} \text{ cm}^{-3}$

Figure 5.10: Population oscillations on the condensed fraction (top) demonstrating spin-dependent interaction in ^{87}Rb $F = 1$. In contrast, no significant oscillation is visible in the thermal component (bottom). Data points are averaged over several repetitions of the experiment (error bars), theoretical curves (lines) are computed from the analytic solution (5.5) with k and additional offsets in time and population as fit parameters, fixed by a least-squares algorithm.

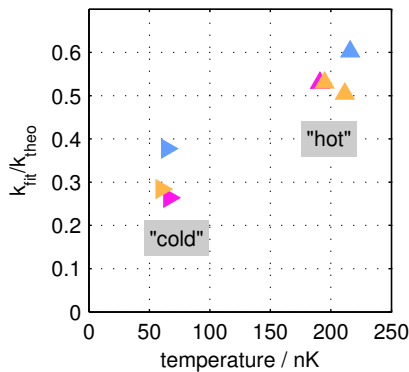


Figure 5.11: k values determined by a fit to experimental data compared to values obtained using known scattering lengths (Section 2.3.1) and a density determined from trapping frequencies and particle number. Colors correspond to Fig. 5.10.

in contrast, does not show significant oscillations. It is an interesting question whether in principle there could be coherent mean-field driven spin oscillations in the thermal component; in any case, however, the thermal density of particles is much smaller than that of the BEC, rendering the effect, if it exists, invisibly small.

From the fit parameters k and the quadratic Zeeman energies q , estimates of the interaction parameter $g_1 \langle n \rangle$ can be obtained in the two cases “hot” and “cold” (see figure caption of Fig. 5.10), enabling extrapolation to the interaction regime. The resonance point would be at 0.27 G (“hot”) and 0.16 G (“cold”), respectively. This is well within the limits of technical possibilities, but the period of oscillation in the interaction regime $\pi/|g_1 \langle n \rangle|$ would be 95 ms or 260 ms, respectively. Comparing this value to the time scale of Fig. 5.10, the pointlessness of trying to observe the crossover or interaction regime becomes obvious.

Oscillations for both “hot” and “cold” samples are strongly damped after about 15 ms due to thermalization effects. The mechanism behind these effects is discussed in detail in Section 5.5. Similar to the case of Ramsey oscillations, formation of spin domains may also

lead to apparent damping; however, spontaneous structure formation in $F = 1$ has been observed [41] and predicted [44, 90, 93] only at low magnetic field, i.e. in the interaction regime. Structure formation in $F = 2$ is also considered in Section 5.6 in the context of deviations from the SMA, and the Zeeman regime turns out to be much more robust than the interaction regime in that case. We have observed $F = 2$ structure formation in *both* regimes in an elongated geometry, but on a longer time scale; this will be the subject of Chapter 6. In conclusion, one can safely assume that the formation of spin domains as a mechanism of damping is of minor relevance in the Zeeman regime, at least on the time scale of the given experiment.

The value for $k = g_1 \langle n \rangle / q$ obtained from fitting to our data can be compared with calculations based on predictions [79] and an independent measurement [78] of the scattering length difference $a_0 - a_2$ (Section 2.3.3). The average density $\langle n \rangle$ entering through the single-mode approximation can be determined from the measured particle numbers N and the trapping frequencies (Section 3.2) via the chemical potential $\hbar\mu_{TF}$ in Thomas-Fermi approximation,

$$\langle n \rangle = \frac{4}{7} \frac{\mu_{TF}}{g_0} \quad \text{and} \quad \mu_{TF} = \frac{\bar{\omega}}{2} \left(\frac{15Na}{\bar{a}} \right)^{2/5}, \quad (5.6)$$

where $\bar{\omega} = \sqrt[3]{\omega_x \omega_y \omega_z}$ is the average trap frequency, $\bar{a} = \sqrt{\hbar/(m\bar{\omega})}$ is the corresponding harmonic oscillator length and $g_0 = \frac{4\pi\hbar a}{m}$ is the spin-independent interaction parameter corresponding to the “spin-independent” scattering length $a = \frac{2a_2 + a_0}{3}$. The “hot” sample has been prepared in a deeper as well as steeper trap, and the resulting increase in condensate density by far overcompensates the loss in density caused by the lower condensate fraction compared to the “cold” sample. The absolute number of condensate atoms in the “hot” sample is actually smaller than in the “cold” sample by about 20%.

Fig. 5.11 shows that the ratio of theoretical k_{theo} and fitted k_{fit} is fixed within each class (“hot” or “cold”) of samples, though far from one. While the presumably large error of the absolute particle number (a factor of two is a common assumption) may account for a part of the deviation, the origin of the rather large difference between the classes is not known. Besides true finite temperature effects, one possible source of trouble is the geometry of the optical trap and the fact that the “hot” sample was prepared in a significantly deeper trap than the “cold” one (see also the discussion in Section 3.2):

- Gravitational sag in a not truly harmonic potential may alter the scaling of trap frequencies with laser power (Section 3.2). Trap frequencies have been measured at the same laser power used for the “cold” sample; for the “hot” sample, less sag would lead to higher trap frequencies than expected by scaling, thus reducing $k_{\text{fit}}/k_{\text{theo}}$ towards the “cold” value.
- The trapping potential may not be sufficiently harmonic at all, and thus the scaling of the condensate density with the trapping frequency may differ from Tab. 3.1. This possibility is supported by the fact that the condensate fraction measured is not compatible with the fraction calculated from the measured temperature assuming a harmonic trap.

In conclusion, our data as it appears in Fig. 5.10 clearly confirms the validity of the SMA mean-field theory and the analytic solution (5.5). The origin of deviations is a worthy subject of its own, providing insight into much more fundamental questions in the context of condensate formation; this is discussed in Section 5.5. In addition, the fact that

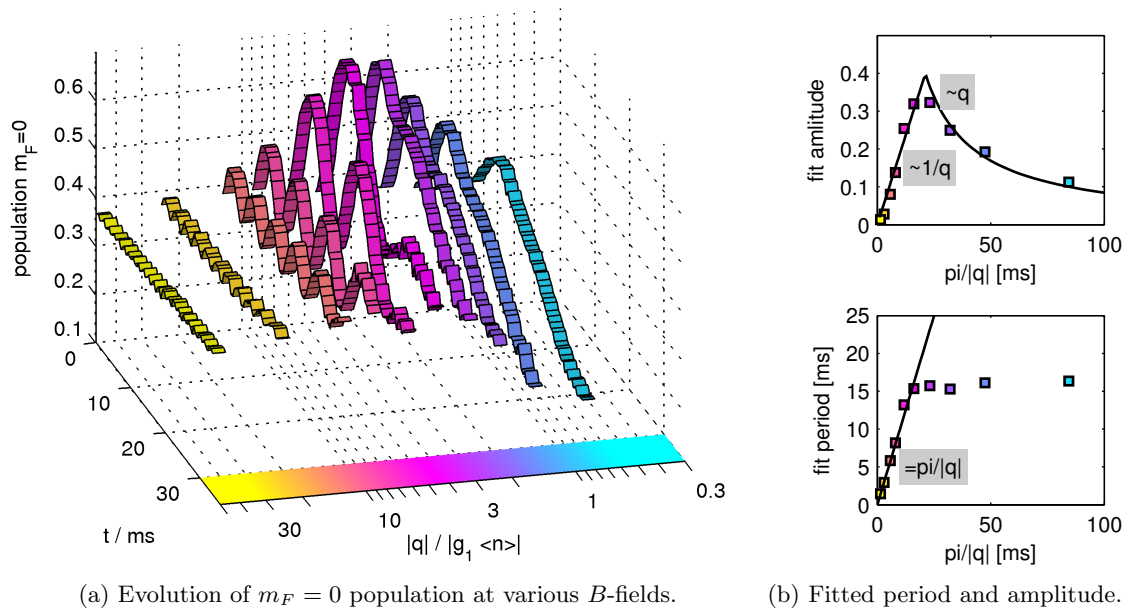


Figure 5.12: Resonance phenomenon in $F = 2$. The B -field is used as a parameter in terms of $q/(g_1 \langle n \rangle)$, where $q \sim B^2$ is the quadratic Zeeman energy and $g_1 \langle n \rangle$ the first spin-dependent mean-field energy (processes up to $\Delta m_F = 1$). In this figure, $g_1 \langle n \rangle = 47 \text{ s}^{-1}$ (corresponding to a density of $1 \times 10^{14} \text{ cm}^{-3}$) is used as a reference value. This value is obtained from SMA theory fits (see Fig. 5.14).

the $m_F = 0$ population grows initially is an independent confirmation that $^{87}\text{Rb } F = 1$ is indeed ferromagnetic ($g_1 < 0$) [2].

Similar coherent oscillations have been independently observed in the Georgia Tech group [50]. In their experiments, the authors could demonstrate the coherent manipulation of trajectories in phase space (Fig. 5.7) by switching the magnetic field, thereby modifying the energy landscape. Probably due to their different trapping geometry, the authors were also able to follow the oscillations over several 100 ms, allowing them to go to the interaction regime at low magnetic field.

5.4 Observation of the crossover resonance ($F = 2$)

While experiments in the previous section have shown the validity, at least for a limited time, of the SMA theory and the analytic solution for $F = 1$ in the Zeeman regime, it has turned out to be not feasible to actually reach the crossover region $|q| \approx |g_1 \langle n \rangle|$. As discussed in the previous Section 5.3, the reason is that in $F = 1$ at typical densities the frequency corresponding to the spin-dependent energy $g_1 \langle n \rangle$ is too small to lead to a full oscillation within the ≈ 15 ms available for coherent dynamics, before thermalization effects play a dominant role.

Although the analytic solution describing the resonance effect is limited to $F = 1$, the mechanism is generic, and a similar phenomenon is in fact observable in $F = 2$ (Fig. 5.12). The experimental procedure there is fully equivalent to the $F = 1$ case, i.e. preparation of $\zeta_{\pi/2}$ at a given B -field followed by a variable hold time and Stern-Gerlach analysis. Looking only at the $m_F = 0$ population, oscillations are clearly visible, with a maximum

amplitude at $|q|/|g_1(n)| \approx 3$ or $|k| \approx 1/3$, corresponding to a magnetic field of $B_0 \approx 0.6$ G. Analogous to $F = 1$, the oscillation frequency increases with $q \propto B^2$ in the high field (Zeeman) regime, whereas it is constant towards lower fields (interaction regime). At and below resonance, oscillations are heavily damped, to a degree where only one (upper) turning point is discernible. This damping also impedes the observation of the divergence of the oscillation period, which is expected by analogy and is also reproduced in numerical solutions of the $F = 2$ SMA mean-field equations. It is probably caused by *domain formation* rather than thermalization effects, since it happens on a shorter time scale and does not affect the Zeeman regime. The mechanism is discussed in detail in Section 5.6 and, in the context of an experiment where domain formation is actually observed, in Chapter 6.

Amplitudes and periods (Fig. 5.12) are obtained by fitting a squared sine to the first 15 ms (Zeeman regime, where oscillations are visible) or 10 ms (interaction regime) of the data. In the latter case, the “period” is defined as twice the time to the first turning point. Amplitude and period as a function of the quadratic Zeeman energy qualitatively follow the same laws as for $F = 1$, except that a clear resonance is missing due to the heavy damping. In the Zeeman regime, the prediction of the perturbative solution (2.81) can be verified, in particular the period of oscillation is in fact given by the quadratic Zeeman effect in this regime.

This is the first experimental observation of a resonance in coherent spinor BEC dynamics that has its origin in *many-particle* interactions leading to nonlinear dynamics. Work on $F = 1$ in the Georgia Tech group [50] has demonstrated coherent oscillations in both the interaction and Zeeman regime and the latter showed the typical scaling of frequency $\sim B^2$. However, a divergence of the period or the corresponding maximum of the amplitude has not been observed⁵. Our result is also fundamentally different from the observation [43, 132] of coherent Rabi-oscillations in the effective two-level system formed by two $F = 1$ atoms interacting at the individual sites of an optical lattice. While this is also an effect of the same spin-dependent interaction, it is fully described by (linear) two-level quantum mechanics. On the other hand, in reducing the complexity of the interacting many-particle system to the lowest non-trivial level, this experiment allows to e.g. extract precise numbers for the scattering lengths also used to parameterize the mean-field model (Section 2.3.3).

5.5 Thermalization effects ($F = 1$)

In the previous sections the focus has been on coherent phenomena. However, it is also obvious from the data that decohering mechanism play a significant role even on the time scale of 10 ms. Domain formation has been identified as one such mechanism that, although in principle coherent, leads to locally dephased oscillations and apparent damping of the dynamics of averaged quantities; this will be discussed in more detail in Section 5.6. The present section elucidates the role of a different mechanism of damping, involving thermal atoms and truly decoherent.

⁵Partly, this is due to a different choice of the initial state. The fully transversely magnetized state $\zeta_{\pi/2}$ is singular in being the ferromagnetic ground state at $B = 0$, which is the reason why the oscillation amplitude goes to zero in this limit. The Georgia Tech group used different initial states with non-zero magnetization, e.g. $\rho_{+1} = 0, \rho_0 = \rho_{-1} = 1/2$. $\zeta_{\pi/2}$ is a particularly suitable choice since the resonance shows up in both amplitude and period of oscillations.

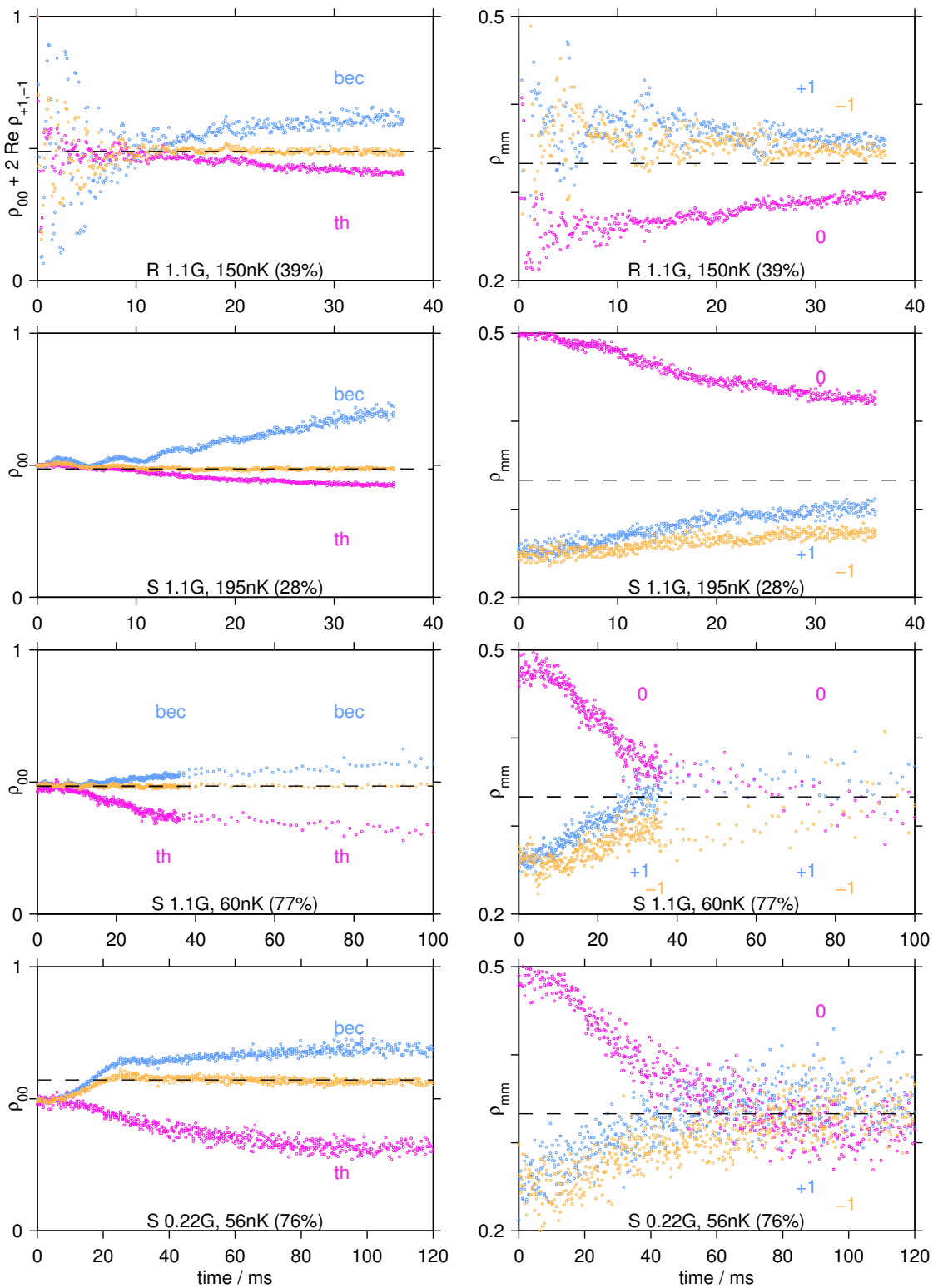


Figure 5.13: Short-term thermalization under various conditions. R = Ramsey type experiment; S = spin dynamics experiment.

Fig. 5.13 compares representative datasets from different experiments, taken at different parameter values with $F = 1$ spinor condensates. In all cases, a fully transversely magnetized state $\zeta_{\pi/2}$ is prepared and afterwards evolves freely for a certain time, until the populations of the final state are recorded by Stern-Gerlach analysis. In the case of a Ramsey experiment, a second $\pi/2$ -rotation is applied before Stern-Gerlach analysis, converting phases to populations. The thermal and the condensed parts are separated computationally by fitting a bimodal density distribution.

Assuming the respective ensemble can be described by a density matrix⁶ ρ , the effect of a $\pi/2$ pulse is

$$\bar{\rho} = \exp(i\frac{\pi}{2}\mathbf{F}_y) \rho \exp(-i\frac{\pi}{2}\mathbf{F}_y). \quad (5.7)$$

Only the diagonal elements of $\bar{\rho}$ are relevant, since only populations are measured by the Stern-Gerlach analysis. These diagonal elements are

$$\bar{\rho}_{00} = \frac{1}{2}(\rho_{+1+1} + \rho_{-1-1}) - \text{Re} \rho_{+1-1} \quad (5.8)$$

$$\bar{\rho}_{+1+1} = \frac{1}{2}\rho_{00} + \frac{1}{4}(\rho_{+1+1} + \rho_{-1-1}) + \frac{1}{2}\text{Re} \rho_{+1-1} + \frac{1}{\sqrt{2}}\text{Re}(\rho_{0+1} + \rho_{0-1}) \quad (5.9)$$

$$\bar{\rho}_{-1-1} = \frac{1}{2}\rho_{00} + \frac{1}{4}(\rho_{+1+1} + \rho_{-1-1}) + \frac{1}{2}\text{Re} \rho_{+1-1} - \frac{1}{\sqrt{2}}\text{Re}(\rho_{0+1} + \rho_{0-1}) \quad (5.10)$$

These equations can be inverted to give the $m_F = 0$ population *before* the $\pi/2$ -pulse, ρ_{00} , up to some oscillating coherences, as a function of the populations *after* the pulse only.

$$\rho_{00} + 2\text{Re} \rho_{+1-1} = \bar{\rho}_{+1+1} + \bar{\rho}_{-1-1} - \bar{\rho}_{00} \quad (5.11)$$

This makes it possible to compare the ‘‘Ramsey’’ type experiment to ‘‘spin dynamics’’ experiments missing the final $\pi/2$ -pulse, as in the upper row of Fig. 5.13.

The four datasets of Fig. 5.13 have in common a short ($\approx 10 \dots 15$ ms) period of damped coherent evolution in the condensed component⁷, followed by a period (up to 100 ms) of obviously incoherent ‘‘drifting’’ population dynamics (note that the time axes are scaled differently). Characteristic features of this ‘‘drifting’’ are:

- An increasing difference between the (average) $m_F = 0$ populations of the thermal and the condensed component, while initially both are prepared at $\rho_{00} = 1/2$. At the same time, the *total* $m_F = 0$ population remains fixed, at a value defined by the initial short period of coherent dynamics.⁸
- Convergence of the thermal populations $\rho_{mm}(m = -1, 0, +1)$ towards equipartition, $\rho_{mm} = 1/3$.

Incoherent dynamics thus clearly is the result of a redistribution between thermal and condensed population *within each spin state*. The probable cause of this redistribution

⁶This is true for the thermal component, which can be understood as a statistical ensemble of non-interacting particles; for the condensed part, a density matrix description can be used to take into account a spatially varying spin composition in terms of a distribution of the frequency of occurrence.

⁷Oscillations of the thermal fraction exist in the Ramsey case, but are very heavily damped, on a timescale one order of magnitude shorter than the condensed fraction.

⁸E.g. at 0.22 G, the initial increase in total $m_F = 0$ population from its prepared value of 1/2 is due to coherent dynamics. In other cases, the difference between prepared and asymptotic total population is negligible.

becomes manifest in the bottom row of Fig. 5.13. In all cases, the thermal spin components tend towards an equal population as expected for near-degenerate states. At a temperature of 100 nK, the mean kinetic energy per ^{87}Rb atom is $\frac{3}{2}kT \approx h \times 3 \text{ kHz}$. This is much smaller than the linear Zeeman energy of $\approx h \times 700 \text{ kHz/G}$ – changing magnetization thus is not an issue. However, the quadratic Zeeman energy is only $\approx h \times 90 \text{ Hz}$ at 1.1 G, so the equilibrium $m_F = 0$ fraction will be mainly determined by maximum entropy and thus uniformly distributed.

The classical collision rate $\tau^{-1} = \sigma nv$ in a thermal cloud provides a first estimate of the time scale on which thermalization processes occur. In our experiments, estimating the average velocity⁹ $v = \sqrt{3k_B T/m} \approx 0.05 \text{ cm/s} \times (T/\text{nK})^{1/2}$, the peak density¹⁰ $n = \zeta(3/2)\lambda_{\text{th}}^{-3} \approx 1.3 \times 10^{10} \text{ cm}^{-3} \times (T/\text{nK})^{3/2}$ and the elastic scattering cross-section $\sigma = 8\pi a^2 \approx 7 \times 10^{-12} \text{ cm}^2$, the inverse rate $\tau \approx 230 \text{ s} \times (T/\text{nK})^{-2}$ varies from about 60 ms at 60 nK to 6 ms at 200 nK. A second timescale is set by the rate of condensate formation, which has been shown to be smaller than the thermal collision rate (or the time scale larger, respectively) by about one order of magnitude under typical experimental conditions [133, 134, 135]. The “hot” data in Fig. 5.13 is roughly consistent with these numbers, while for the “cold” data the period of observation is too short to draw conclusions, but it is clear that the rapid convergence of the thermal populations observed in the first 30 ms does not fit these simple arguments.

These results can be viewed in the context of earlier work in our own group, namely on Bose-Einstein condensation at constant temperature [57, 3]. In the latter experiment, Bose-Einstein condensation in the initially unpopulated $F = 1, m_F = 0$ state is achieved by conversion of $m_F = \pm 1$ pairs to $m_F = 0$ at a very small rate of the order of 1 s^{-1} . In the temperature bath provided by the $m_F = \pm 1$ thermal components, a thermal cloud of $m_F = 0$ atoms grows until it reaches the critical particle number and a condensate appears. In [57], the process of thermalization which leads to the formation of a thermal cloud, although presumably the atoms are transferred from the condensed fractions of $m_F = \pm 1$, is assumed to be much faster than the rate of transfer. In the framework of a rate-equation model the corresponding rate is 13 s^{-1} , while the condensate appears only after 5 – 10 s. What has been observed in the work at hand can thus be viewed as a direct observation of precisely those fast thermalization processes that had to be assumed previously.

A related phenomenon termed “decoherence-driven cooling” is known from two-component quasi-spin-1/2 condensates [28], e.g. ^{87}Rb $F = 1, m_F = -1$ and $F = 2, m_F = +1$. Consider a finite-temperature condensate with all atoms in the same internal state. This can be seen as a single-component or scalar BEC, and in thermal equilibrium a certain fraction of atoms populate the condensed state, such that the phase space density of the non-condensed part is just at the critical value $g_{3/2}(1) \approx 2.612$. This is true, if the atoms are in one of their two energy eigenstates, as well as for any coherent superposition state. However, *decoherence* in the thermal cloud destroys the coherent superposition there, leaving an incoherent two-component mixture, each component having only half the critical phase space density. By redistribution of atoms from the condensed to the thermal parts, the phase space density is brought back to the critical value for each component

⁹In a partly condensed, non-interacting ensemble, the average kinetic energy per thermal particle is $E_{\text{kin}} = \frac{3}{2}k_B T \frac{\zeta(4)}{\zeta(3)} \approx 0.9 \times \frac{3}{2}k_B T$ [51].

¹⁰This applies in a partly condensed, non-interacting ensemble at the minimum of the trapping potential [51]. The thermal wavelength is defined as $\lambda_{\text{th}} = \sqrt{\frac{2\pi\hbar^2}{mk_B T}}$

separately. At the same time, the *temperature* of the system *decreases*, since the kinetic energy available is distributed between a larger number of particles. The mechanism of particle exchange allowing the system to relax to the thermal equilibrium is the same in this case as in our $F = 1$ experiments, and is also included in the rate-equation model of [57].

Temperature data from our $F = 1$ experiments, based on the time-of-flight expansion of the thermal cloud, is not conclusive, but a slight decrease in temperature is compatible. However the condensed fraction, calculated separately for each spin component, increases in $m_F = 0$ and decreases in $m_F = \pm 1$, as the thermal populations approach equipartition. Interpreting the $m_F = 0$ component as an independent single-component system, an increase of the condensed fraction in spite of a decrease in the total particle number implies a lower temperature.

5.6 Validity of the SMA ($F = 2$)

In both $F = 1$ and $F = 2$ data, SMA theory fits the data remarkably well¹¹ for a certain time interval, after which deviations become significant. For $F = 1$, these deviations are likely due to thermalization effects, which set in after ≈ 15 ms in accordance with Fig. 5.13 and cause a damping of the coherent oscillations as well as a slow increase of the $m_F = 0$ population in the condensate. Structure formation in $F = 1$, implying the breakdown of the single-mode approximation, has been observed in the groups of Chapman [50] and Stamper-Kurn [41] in the interaction regime on a time scale of 100 ms, but is not expected to be an issue in our experiments on $F = 1$.

The case is different for $F = 2$, where we are in the crossover and interaction regime, and the time scale of purely interaction-driven dynamics is well within the limit set by thermalization. In fact, the time span, over which the SMA description remains valid (see Fig. 5.12 and Fig. 5.14), depends on $g_1 \langle n \rangle / q$ and is significantly longer in the Zeeman regime. This can be understood in a local density picture, noting that the pscillation frequency depends strongly on the local density in the interaction regime, and spatial structure will emerge assuming nothing but local dynamics. In contrast, this is not the case in the Zeeman regime and consequently the whole density distribution remains in phase. We will get back to the local density argument in Chapter 6.

Direct observation of local dynamics is possible in the nearly isotropic crossed-beam trap (Fig. 5.15). On the time scale of a few ms, pronounced modulations in the density of

¹¹Note e.g. that for $F = 2$ the numerical solution reproduces even details like the subtle asymmetry of the oscillation at large q .

Figure 5.14: Validity of the SMA in the astigmatic trap (see page 91): individual fits (lines) to the datasets (markers) of Fig. 5.12. Times are in milliseconds. The parameter q is fixed by the known radio frequency, $g_1 \langle n \rangle$ is a fit parameter, as well as time- and population-offsets. The interval used for fitting extends from zero to the time indicated by the dotted line and has been determined by visual judgement. BOTTOM RIGHT: Residuals of a fit with fixed $g_1 \langle n \rangle = 47 \text{ s}^{-1}$ and time offset for varying fit intervals, for three representative datasets (triangular markers). NOTE: Fits have been calculated including the g_2 term, assuming a fixed ratio of g_2/g_1 according to the values of Tab. 2.2. However, setting g_2 to zero has only minor influence on the fit parameters as well as on the validity of the SMA. E.g., the average $g_1 \langle n \rangle$ with $g_2 = 0$ is 54 s^{-1} , compared to 47 s^{-1} at $g_2/g_1 = -2.1$.

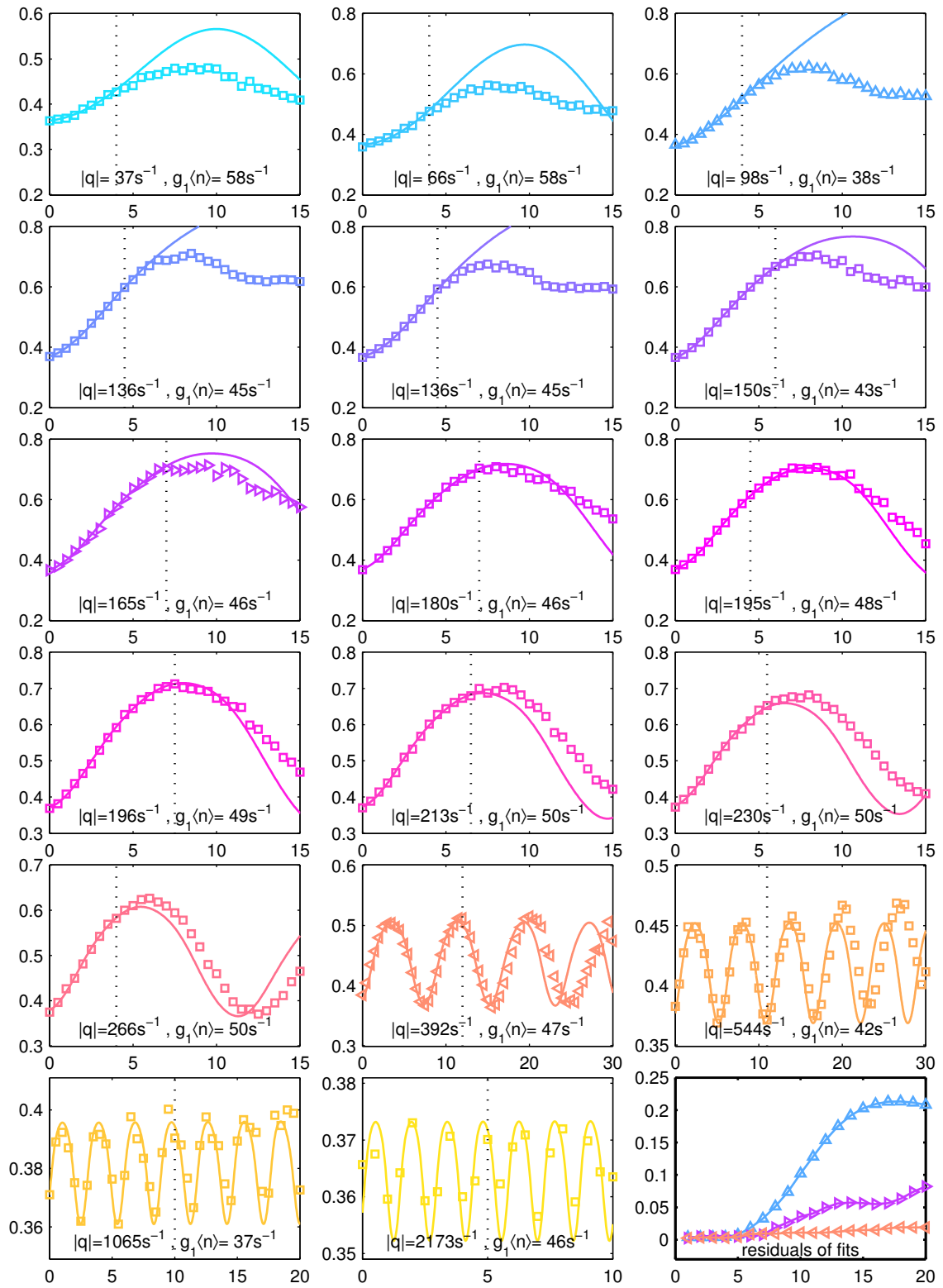


Figure 5.14: Validity of the SMA in the astigmatic trap (see page 90).

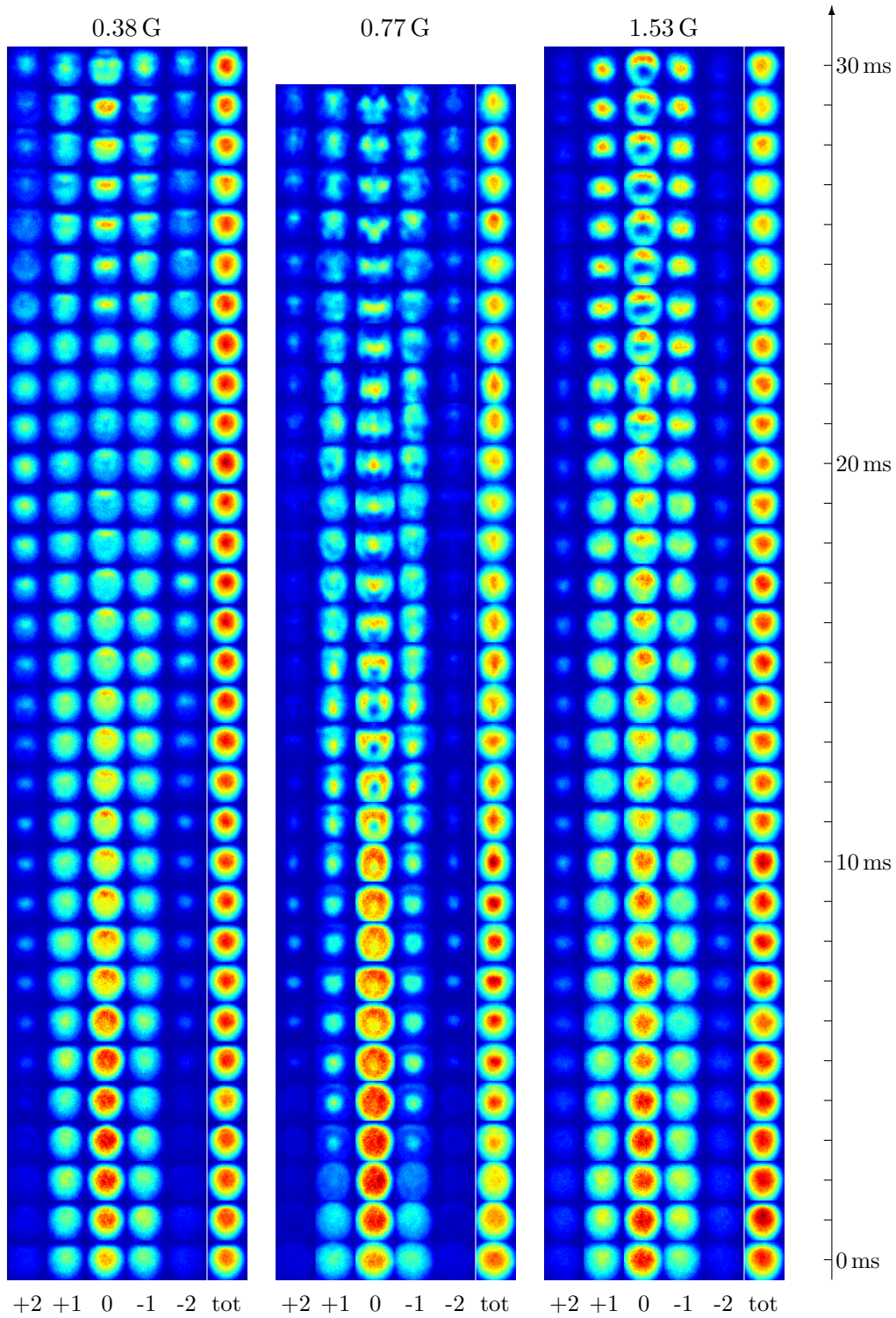


Figure 5.15: Structure formation in the nearly isotropic crossed-beam dipole trap. Stern-Gerlach images show the atomic column density in each spin state, plus the computed total density, at different magnetic fields: in the interaction regime (0.38 G), close to resonance (0.77 G) and in the Zeeman regime (1.53 G). Note that the Stern-Gerlach images and the computed total density are scaled and colored separately.

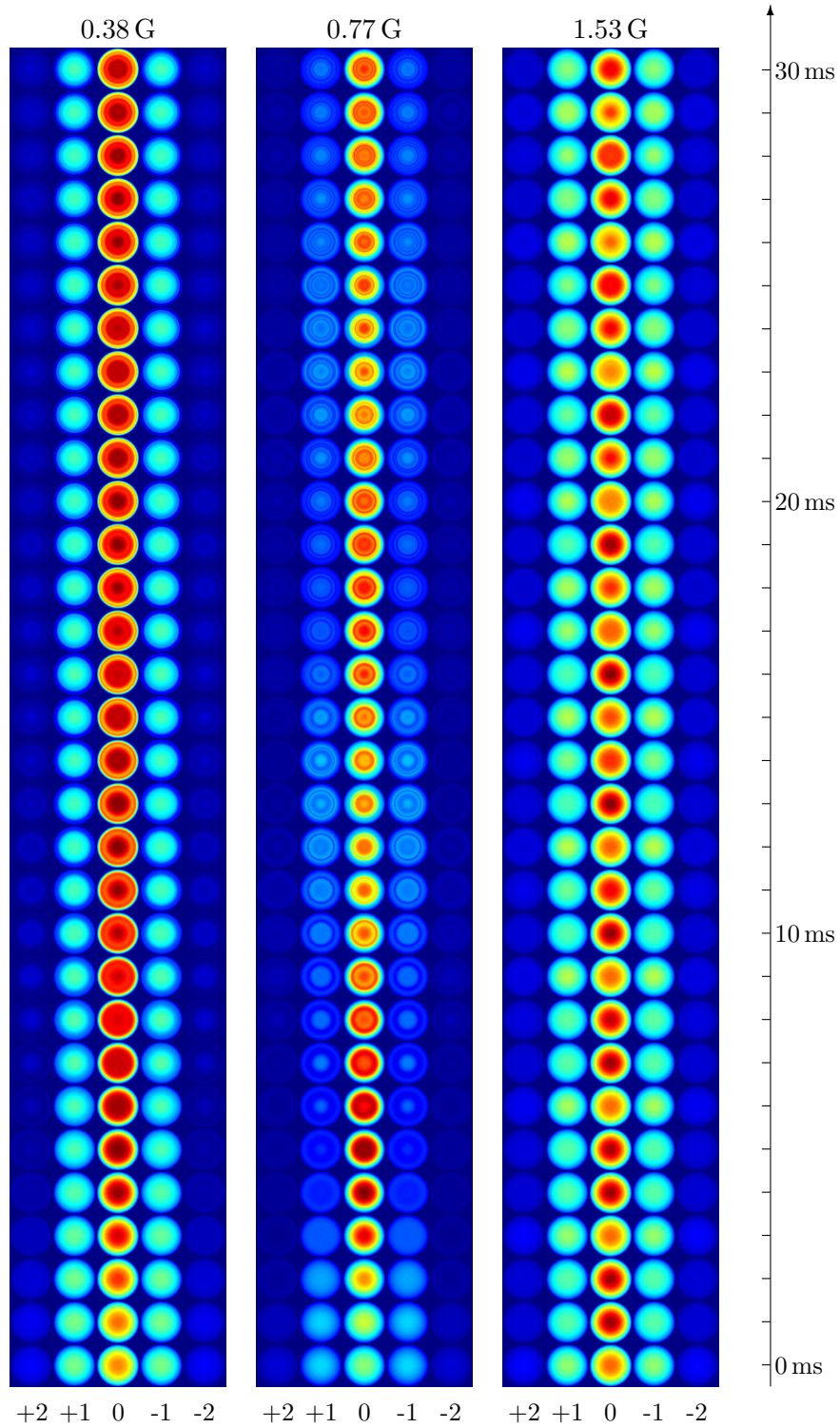


Figure 5.16: Local density simulation, based on the SMA equations of motion assuming a spherical parabolic density distribution. The picture shows the column integrated densities for each spin component. Symmetry with respect to $+m_F \rightarrow -m_F$ is assumed in the equations of motion, both $+m_F$ and $-m_F$ are shown for clarity only. The magnetic field values chosen here correspond to those of Fig. 5.15 assuming $g_1 \langle n \rangle \approx 107 \text{ s}^{-1}$, such that the intermediate field $B = 0.77 \text{ G}$ is close to resonance.

individual m_F -components emerge, while the total density profile, reconstructed by overlapping the Stern-Gerlach images, remains largely unchanged. The perfect reproducibility and the high degree of symmetry of the patterns at first sight seem to counter-indicate a dynamical instability [44] as their origin.

On the other hand, a numerical simulation in the local density approximation, i.e. based on the SMA equations of motion and a density distribution $n(r)$ leading to a spatially varying interaction parameter $g_1 n(r)$, is only able to reproduce some features in the very beginning of the evolution. E.g., the appearance of a sharp central peak in $m_F = \pm 1$ after about 10 ms in the resonant case is recognized as a local density effect. However, the pronounced “hole” forming after 25 ms in the Zeeman regime is not reproduced. Also not reproducible in the simulation is the large relative population of $m_F = \pm 2$ that comes up in the interaction regime after 15 ms. In fact, in any regime, the population of $m_F = \pm 2$ apparently never exceeds the initial value significantly, according to SMA calculations. The complex non-spherically symmetric patterns, on the other hand, that are particularly characteristic of the resonant case, may be the result of the gravitational sag deforming the density distribution.

Experiments in an elongated geometry (Chapter 6) also suggest the existence of an additional mechanism of structure formation beyond local density effects, which becomes relevant on a time scale of several times $(g_1 \langle n \rangle)^{-1}$, in both the Zeeman and the interaction regime. This topic will be discussed in detail in Chapter 6.

Concluding, it can be seen from experimental data and simulations that while the local density picture *does* provide an explanation for the more extended validity of the (global) SMA in the Zeeman regime, it is also applicable in a transitional regime only. At longer times, pattern formation based on different mechanisms such as linear instability or finite temperature effects take over. For $F = 1$ and $B = 0$, this kind of transition has been observed in numerical simulations [93]. Although not strictly applicable to our case (^{87}Rb $F = 1$ is ferromagnetic in contrast to $F = 2$, and $B \neq 0$), these simulations may serve as an example illustrating the underlying idea.

Chapter 6

Structure formation in elongated spinor Bose-Einstein condensates

Evidence of spontaneous pattern formation in anti-ferromagnetic $F = 2$ ^{87}Rb condensates as well as a critical analysis thereof is presented in this chapter. Similar phenomena have been observed before in ferromagnetic spinor condensates only, where they are easily interpreted as spontaneous symmetry breaking or demixing of components. This interpretation is not applicable to our observations. Possible explanations discussed here include a dynamical instability or a twisting of the order parameter by magnetic field gradients, both leading to the breakdown of the single-mode approximation.

6.1 Spinor dynamics beyond single-mode approximation

Our understanding of the coherent dynamics in spinor condensates, as it has been developed in this work, is largely based on the single-mode approximation. The popularity of the SMA lies in the fact that it reduces the mean-field description of spinor BEC to a small number of internal degrees of freedom. While important aspects of the interplay of mean-field and magnetic energy are accurately described in this approximation (in particular the resonance phenomenon discussed in Section 5.3 and Section 5.4), there is also clear evidence of dynamics involving more than a single common spatial mode (Section 5.6).

The transition from single-mode to spatially resolved dynamics involves two key ingredients. Spatial dependence may enter through the *parameters* of the single-mode description, density and magnetic field.

- In the *local density approximation*, SMA arguments remain valid in any infinitesimal volume element. Neighboring volume elements are independent in this limit. Mathematically, the equations of motion are still ordinary differential equations with respect to time, depending on the position as a parameter.
- When the spin state varies in space, the *kinetic energy* connected with the gradient of the wave-function introduces a coupling between neighboring volume elements. The equations of motion are now nonlinear partial differential equations in space and time (equations (2.60)-(2.62)).

Structured *ground states* induced by magnetic field gradients have been observed early in the history of spinor Bose-Einstein condensates [23, 77] and are well understood (see the

discussion in Section 2.3.3). *Dynamically induced* structure as a result of the density profile of a trapped condensate has been observed in ^{87}Rb $F = 2$ [38, 6] and has been proposed as a reason for apparent damping of coherent spin oscillations in $F = 2$ [1, 95] (Section 5.6). All these effects can be interpreted in terms of the local density approximation. On the other hand, local density arguments can hardly explain the strongly modulated patterns which we have observed in an isotropic trap (Section 5.6).

A different mechanism that can lead to *spontaneous* structure formation, even in the absence of locally varying fields as a driving force, relies on kinetic energy and the possible *linear instability* of the nonlinear partial differential equations of motion (Section 2.3.2). It is based on the fact that certain Fourier modes may experience an exponential amplification in linear approximation, when superimposed on a homogeneous solution of the nonlinear equations. An initial population of these modes due to e.g. random noise will then grow and produce a pattern of characteristic size corresponding to the wavelength of the unstable mode.

The present chapter addresses the dynamics of very elongated spinor Bose-Einstein condensates. The quasi-1D geometry offers two important advantages: a large axial extension of the condensates enables the observation of long-wavelength modes, while a comparatively tight transverse confinement suppresses structure formation in the direction of detection, which otherwise would be averaged and appear as damping or loss of contrast (compare Section 5.6).

6.2 Preparation and analysis of elongated BEC

Elongated BEC are prepared in a single-beam dipole trap (Section 3.2) by loading a near-degenerate spin-polarized ensemble from our magnetic trap and subsequently lowering the optical power over 10 s down to just above the power necessary to overcome gravity. At the final power of 22 mW, the transverse trap frequency is $\omega_y = \omega_z = \omega_{\text{rad}} = 2\pi \times 120$ Hz assuming cylindrical symmetry. Gravitational sag, however, is expected to lower the trap frequency at least in the vertical direction (compare Section 3.2). The axial trap frequency ω_{ax} , estimated from the shape of a Gaussian beam¹, is less than $2\pi \times 1$ Hz.

In order to verify that this trap is in fact quasi-1D for the purpose of spin dynamics, it is necessary to check that the spin healing length ξ_s is larger than the radial extension of the condensate. We can estimate the atomic density and the chemical potential $\hbar\mu$ from the spin dynamics parameter $g_1\langle n \rangle \approx 30 \text{ s}^{-1}$ (Fig. 6.5) and $\mu \approx g_0\langle n \rangle \approx 2.8 \times 10^3 \text{ s}^{-1}$. Assuming the Thomas-Fermi approximation, the radial harmonic potential is filled up to a radial distance of $R_{\text{TF}} = \sqrt{2\hbar\mu/m}/\omega_{\text{rad}} \approx 2.7 \mu\text{m}$. This has to be compared to the spin healing length $\xi_s = \sqrt{\hbar/(2mg_1\langle n \rangle)}$. The ratio of the two characteristic length scales is

$$\frac{\xi_s}{R_{\text{TF}}} = \frac{\omega_{\text{rad}}}{g_1\langle n \rangle} \sqrt{\frac{g_1}{g_0}} \approx 2.6 \quad . \quad (6.1)$$

This means that the formation of transverse structure formation will indeed be suppressed to a high degree. For comparison, in the nearly isotropic dipole trap of Fig. 5.15 in Section 5.6 $\xi_s/R_{\text{TF}} \approx 1$, and in the astigmatic dipole trap of Fig. 5.12 in Section 5.4 $\xi_s/R_{\text{TF}} \approx 1.5$ in the direction of detection.

¹For a dipole trap at the focus of a Gaussian beam, the ratio of radial and axial trapping frequencies is $\omega_{\text{rad}}/\omega_{\text{ax}} = \sqrt{2\pi}w_0/\lambda$, where w_0 is the beam waist and λ is the wavelength of the laser light.

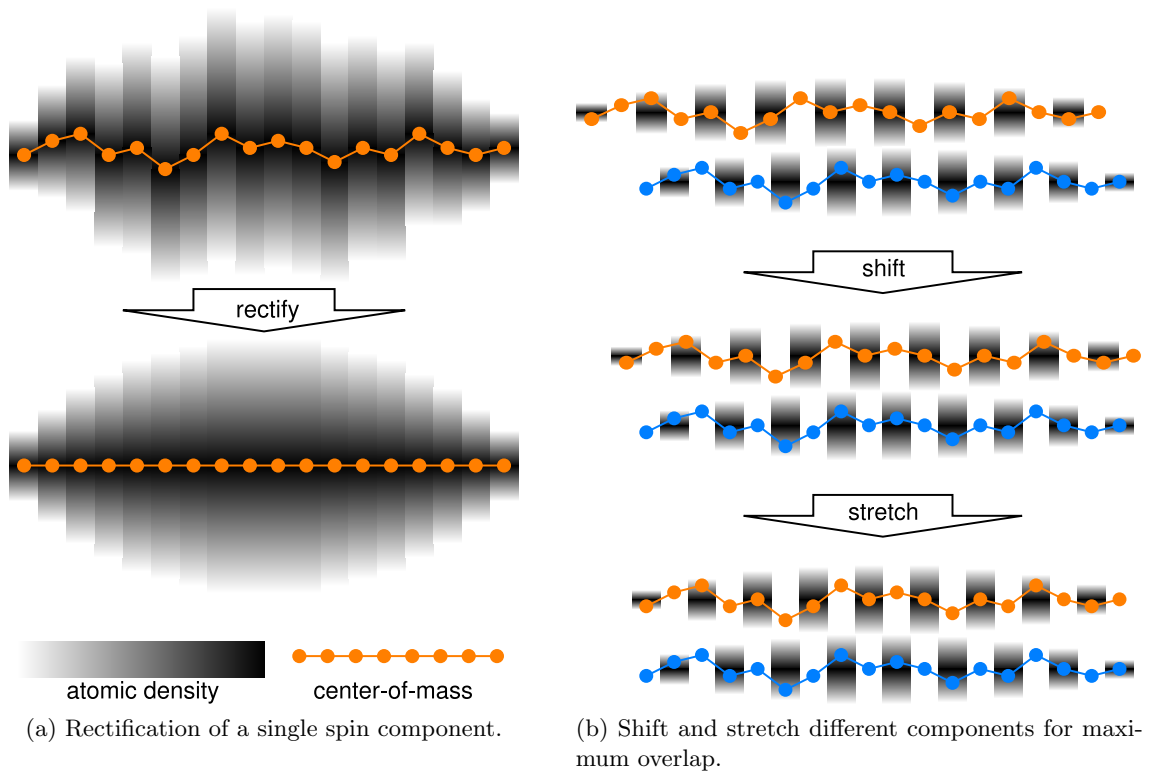


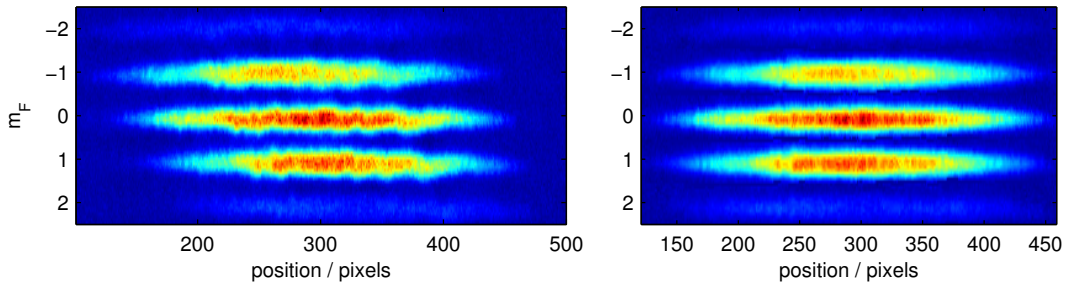
Figure 6.1: Shift and stretch algorithm (schematic).

In the single-beam trap, condensates extend over approximately $750\ \mu\text{m}$ along the horizontal axis. Since the horizontal separation of the spin components by the usual Stern-Gerlach procedure is much smaller than this extension, in particular if the time of flight is kept small, the Stern-Gerlach procedure has to be modified for this series of experiments in order to achieve *vertical* separation. This is done in two steps,

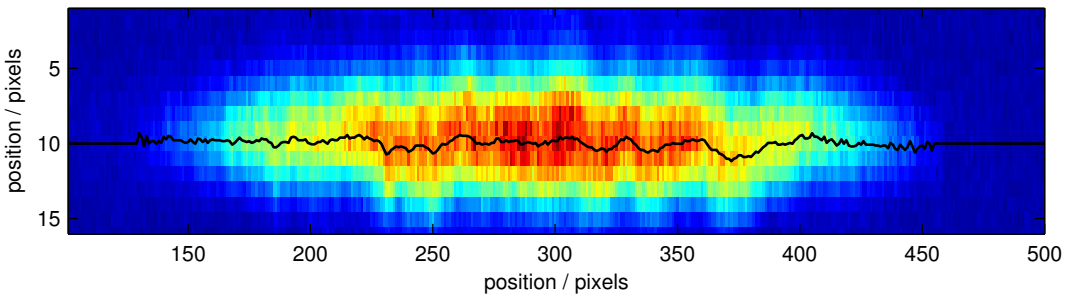
1. after 1 ms of time-of-flight, apply the usual Stern-Gerlach field (Section 3.3) for 1 ms in order to preserve the horizontal quantization axis (this also leads to some horizontal separation),
2. switch on the full gradient, as used for the MOT, plus a vertical offset field, thus shifting the field zero vertically away from the condensate to achieve vertical separation. This second step takes 4 ms; the total time-of-flight from switching off the trap to the detection light pulse is 6.4 ms.

A drawback of this method is that the separation of the spin components is not purely transversal to the trap axis, impeding the spatial correlation of patterns in different spin components. Even worse, the remaining axial shift slightly varies along the condensate, since the extension of the cloud is not negligible compared to the distance from the field zero, and the separation is radial following field lines.

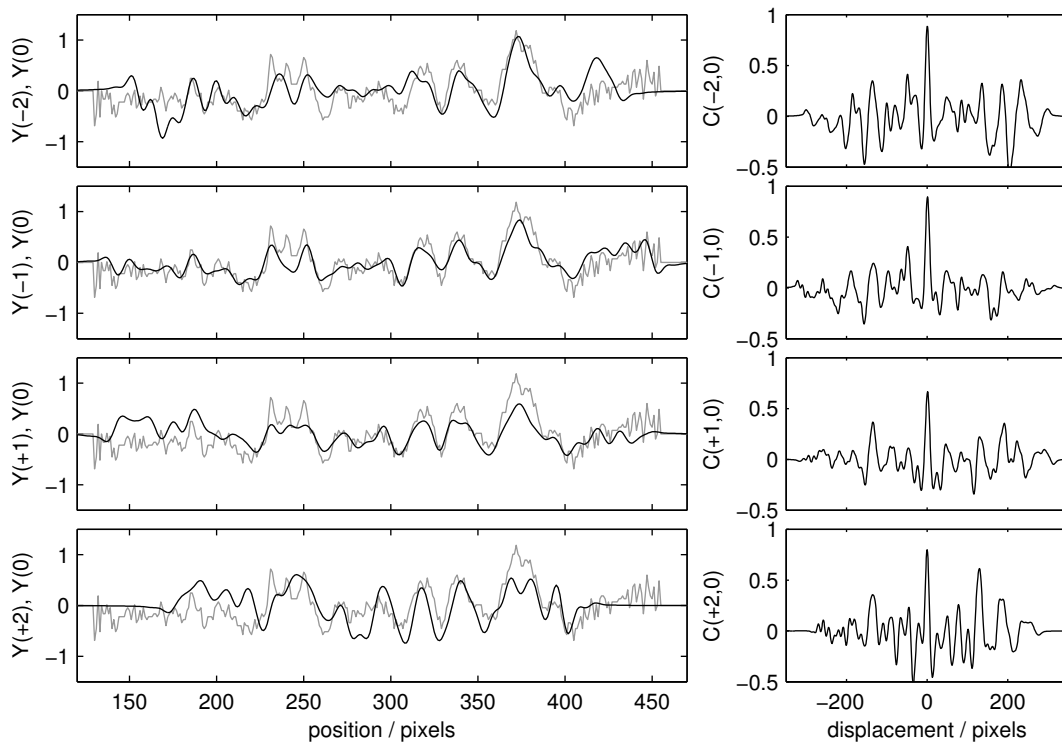
To overcome this complication, we have developed an algorithm that determines these shifts *a posteriori* from the images, based on *transverse excitations* of the condensate wave function that are *identical for all spin components* Fig. 6.2. The algorithm first rectifies each spin component by determining the vertical position of the center of mass in each pixel column and shifting accordingly. As a by-product, we obtain the transverse excursion as a



(a) LEFT: Vertically separated Stern-Gerlach image of an elongated condensate, illustrating horizontal shift and transverse excitations. RIGHT: Shift- and stretch-compensated rectified image, using optimal coefficients (see Fig. 6.3). Note that the aspect ratio in this graph is different from the pixel ratio.



(b) $m_F = 0$ component of the above image with corresponding transverse excursion function.



(c) LEFT: Transverse excursion Y (in pixels) of the above image, $m = \pm 1, \pm 2$ components (solid black) compared to $m = 0$ (grey). Optimal shift and stretch compensation has already been applied. RIGHT: Cross-correlation functions C of the same transverse excursions. Excursion functions have been bandpass-filtered for more clarity.

Figure 6.2: Transverse excitations in elongated condensates.

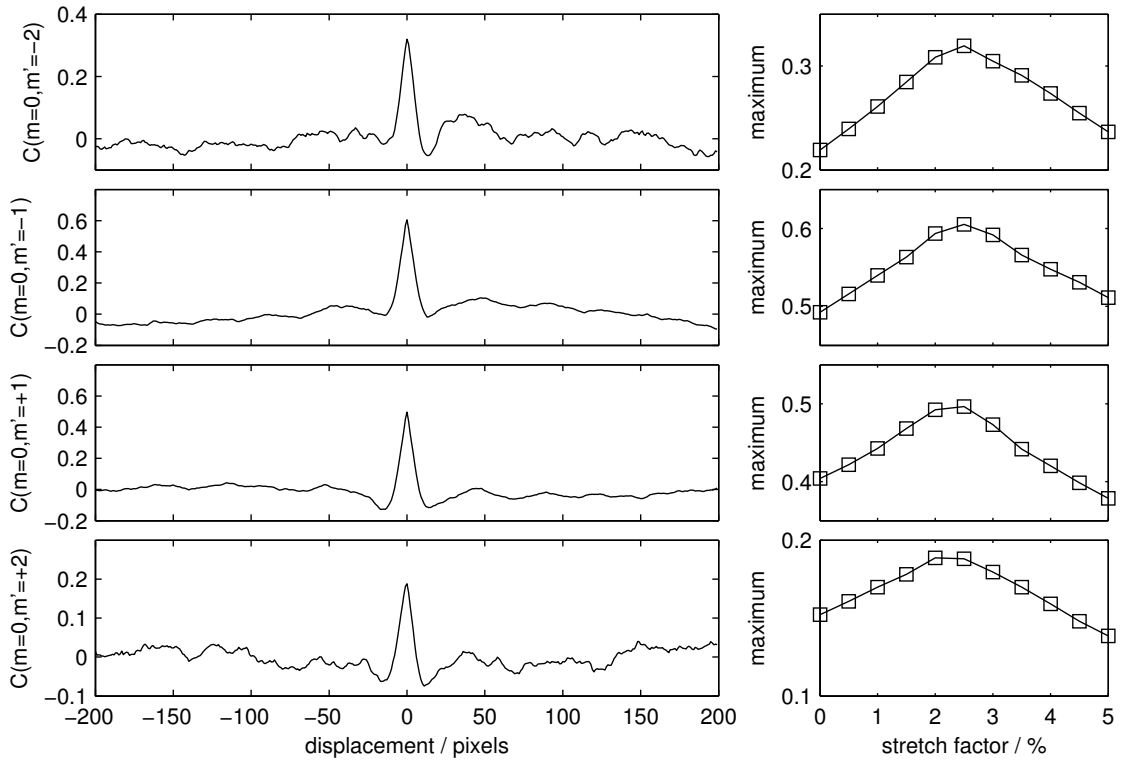


Figure 6.3: Horizontal shift and stretch compensation scheme. LEFT: Cross-correlation of transverse excursions at optimum stretch factor of $m_F \times 2.5\%$. All cross correlations show a prominent peak at zero displacement, indicating that the horizontal shifts applied are correct. RIGHT: Maximum of cross-correlation versus stretch factor. At a stretch factor of $m_F \times 2.5\%$, the peaks of all cross-correlations are maximal. The cross-correlations shown are averaged over 170 images covering the whole series of measurements (more than 600 images). Only images that do not show significant spin structure enter the cross-correlation. $m = 0, m' = \pm 2$ correlations appear smaller and noisier because the $m_F = \pm 2$ population is generally small and the determination of the transverse excursion is not as reliable as in $m_F = \pm 1$.

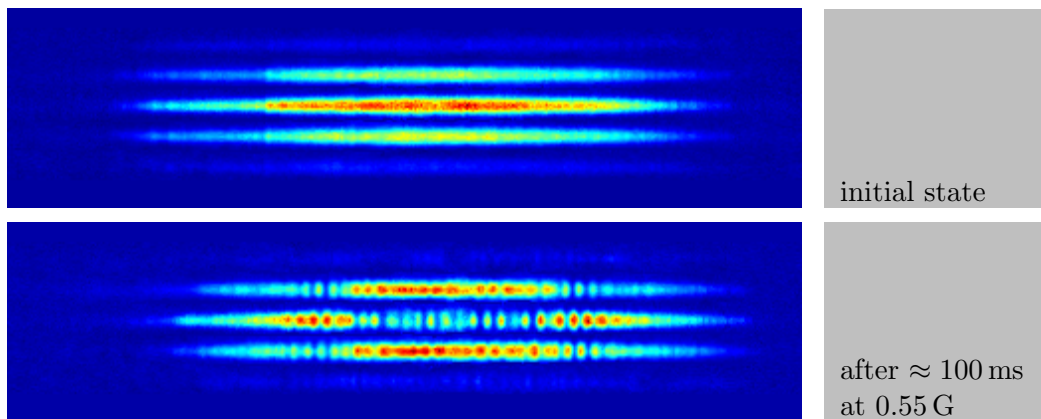


Figure 6.4: Example of structure formation in an elongated spinor BEC.

function of the axial position for each spin component. An optimal linear transformation (shift and stretch) reversing the horizontal shifts can be found by maximizing the cross-correlation of the transformed excursion functions. Fig. 6.1 and Fig. 6.3 illustrate the procedure in detail. It turns out that the inhomogeneity of the Stern-Gerlach field induces a m_F -dependent stretch of the images by about $m_F \times (2.5 \pm 0.5)\%$. The uncertainty of the stretch factor corresponds to about 3 pixels or $8 \mu\text{m}$ maximum over the length of the condensate. The absolute positioning uncertainty is about 1 pixel ($2.7 \mu\text{m}$).

In the following, all Stern-Gerlach images in elongated geometry will be rectified and shift-stretch-compensated (Fig. 6.4 shows an example). Additionally, it is useful to produce images where the transverse shape of the condensate is fully eliminated, i.e. color-coded plots of the column sums of each component. The vertical edges produced this way make it easier to judge the relative arrangement of structures in different spin components by eye.

The analysis of *correlations* between patterns of different m_F components turns out to provide an important insight into the characteristics of structure formation. In order to suppress density fluctuations, our analysis will be based on local relative spin populations $\rho_m(x) \equiv |\zeta_m(x)|^2$, where $\zeta_m(x)$ is a normalized spinor wave function as in equation (2.59) of Section 2.3.1.

Denoting by $\tilde{\rho}_m(x_i)$ the deviation of the relative population in state $m_F = m$ from its mean value at axial position (pixel) x_i ,

$$\tilde{\rho}_m(x_i) = \rho_m(x_i) - \frac{1}{N} \sum_{i=1}^N \rho_m(x_i), \quad (6.2)$$

the correlation coefficients $c_{mm'}$ are defined as an average over all axial positions (pixels),

$$c_{mm'} = \frac{1}{N} \sum_{i=1}^N \tilde{\rho}_m(x_i) \tilde{\rho}_{m'}(x_i), \quad (6.3)$$

The diagonal element c_{mm} is the square of the rms amplitude of fluctuations in $m_F = m$, and normalizing an off-diagonal element $c_{mm'}$ by the product of the two corresponding rms values $\sqrt{c_{mm}c_{m'm'}}$ results in a value between +1 and -1, indicating fully correlated ($c_{mm'} = 1$) or anti-correlated ($c_{mm'} = -1$) fluctuations in $m_F = m$ and $m_F = m'$.

If the $\tilde{\rho}_m$ were uncorrelated independent variables, one would expect

$$\frac{c_{mm'}}{\sqrt{c_{mm}c_{m'm'}}} = \delta_{mm'} = \begin{cases} 1 & m = m' \\ 0 & m \neq m' \end{cases} \quad (6.4)$$

However, since the relative populations are normalized, $\sum_m \tilde{\rho}_m(x) = 0 \quad \forall x$, the $\tilde{\rho}_m$ are inherently anti-correlated to some degree. Assuming a generalized relation

$$\frac{c_{mm'}}{\sqrt{c_{mm}c_{m'm'}}} = \delta_{mm'} + \alpha(1 - \delta_{mm'}) = \begin{cases} 1 & m = m' \\ \alpha & m \neq m' \end{cases} \quad (6.5)$$

this inherent anti-correlation α can be determined by summing twice over m, m' and solving for α ,

$$\alpha = -\frac{1}{2} \frac{\sum_m c_{mm}}{\sum_{m' > m} \sqrt{c_{mm}c_{m'm'}}} \quad (6.6)$$

Correlation coefficients in the following are generally shifted by this value α , calculated separately for each image, to make the distinction between additional correlation ($c_{mm'} - \alpha > 0$) and additional anti-correlation ($c_{mm'} - \alpha < 0$) clearer. Note that this shift may lead to correlation coefficients $c_{mm'} - \alpha$ larger than one.

6.3 Observation of a dynamical instability in $F = 2$

As in Chapter 5, we prepare elongated condensates in the *fully transversely magnetized state* $\zeta_{\pi/2} = (1/4, 1/2, \sqrt{3/8}, 1/2, 1/4)$ (see Fig. 5.1). To gain a first impression of spin dynamics in the elongated trap, we can compare the evolution of the global population of $m_F = 0$ (Fig. 6.5), disregarding any visible structure, to that observed in the much tighter astigmatic trap (Fig. 5.12). Both cases agree qualitatively: a maximum of $m_F = 0$ population occurs at intermediate magnetic fields and oscillations are observed in the Zeeman regime, while the dynamics in the interaction regime appears to be heavily damped. Structure formation below the limit of spatial resolution, or in a direction not observable in our experimental setup, has already been pointed out as a possible source of damping in Section 5.6, and we may expect to gain insight into this mechanism from the present case where structure formation is directly visible.

Over the magnetic field range covered in the elongated geometry experiments, the emergence of structure takes place in two successive steps, which are characterized by a *large-scale correlated (in-phase)* or *small-scale anti-correlated (out-of-phase)* spatial modulation of the relative $m_F = \pm 1$ populations, respectively.

In the beginning, on a time scale of several 10 ms, a predominantly long-wavelength in-phase structure appears, which can be understood in terms of the local density approximation using the homogeneous (or SMA) equations of motion. The wavelength of the modulation in this model is *not* given by some natural length scale, but depends on the density gradient $\partial n/\partial x$ and *varies in time*. This regime is more pronounced at low and intermediate magnetic fields (see Figures 6.8-6.11), which is compatible with our expectation that the time scale of evolution depends more strongly on density in this limit than in the Zeeman regime. In the local density approximation, $F_z = 0$ remains fixed everywhere and for all times.

As an example of the local density mechanism of structure formation, consider a condensate with a typical parabolic density profile $n(x)$ at negligible magnetic field, i.e. in the interaction regime². The $m_F = 0$ population at any position x then oscillates at $\omega \approx 4g_1 n(x)$ (Section 2.3.4, equation (2.82)), and two points separated by Δx dephase at a rate of $\Delta\phi \approx 4g_1 \frac{\partial n}{\partial x} \Delta x$. We estimate the density gradient as $\frac{\partial n}{\partial x} \approx \frac{2n_0}{L} \approx \frac{4\langle n \rangle}{L}$, where L is the extension of the condensate. The characteristic wavelength λ of the resulting pattern, defined by a dephasing of $\Delta\phi = 2\pi$ across $\Delta x = \lambda$, is given by

$$\lambda \approx \frac{2\pi L}{16g_1 \langle n \rangle t}. \quad (6.7)$$

The local density approximation thus leads to patterns with a characteristic length inversely proportional to the time of evolution. The approximation breaks down when $\lambda/(2\pi)$ approaches the spin healing length ξ_s .³

²Since the density goes to zero at the ends of the condensate, only the central part is actually in the interaction regime. At low magnetic field, however, this is a large fraction of the total condensate.

³ The factor 2π results from the fact that for a sinusoidal modulation of wavelength λ , the maximum

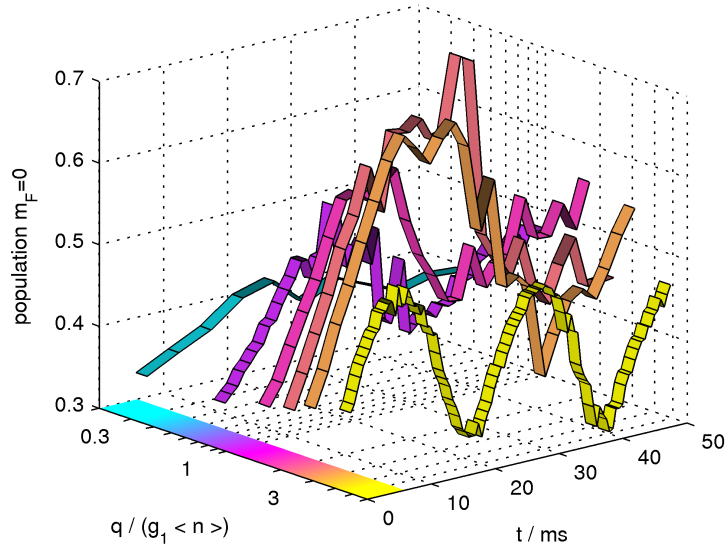


Figure 6.5: Global population dynamics of $m_F = 0$ in elongated geometry, compare to Fig. 5.12 (note the different viewing angle). The reference value $g_1 \langle n \rangle = 30 \text{ s}^{-1}$ for the interaction parameter, obtained from $q / (g_1 \langle n \rangle) \approx 2.5$ at resonance, is smaller than in Fig. 5.12, indicating a lower average density.

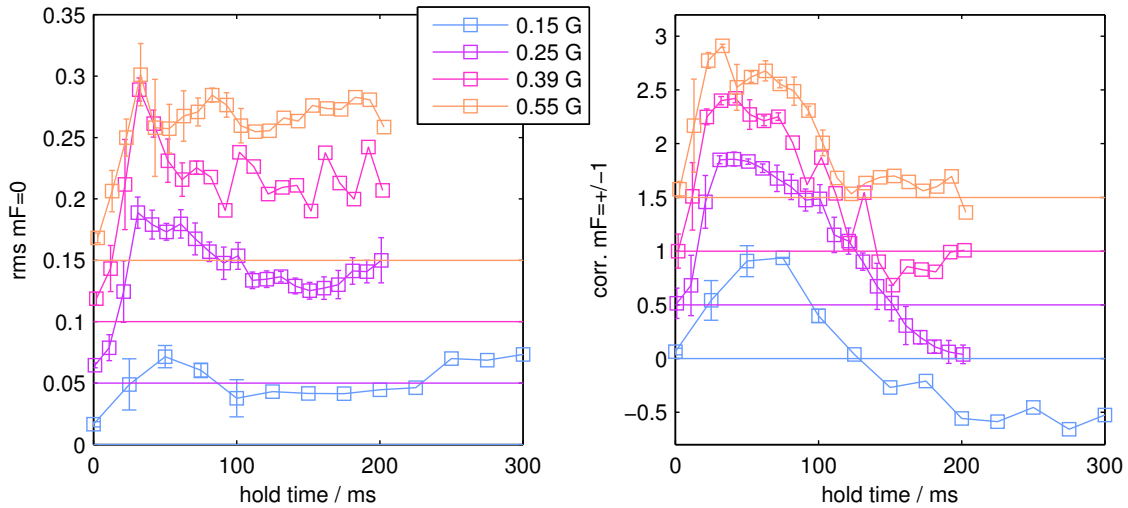


Figure 6.6: Emergence of longitudinal fluctuations in elongated geometry. LEFT: Rms fluctuations of the relative $m_F = 0$ population. An increase indicates the formation of spatial structure. RIGHT: Correlation between the fluctuations in the $m_F = +1$ and $m_F = -1$ component, normalized by the respective rms values and shifted to compensate for inherent anti-correlation (see Text). Positive values indicate correlated structure, negative values anti-correlated structure. NOTE: Curves have been offset vertically for clarity, as indicated by the zero baselines.

After about 100 ms, short-wavelength anti-correlated structure starts to appear on top of the large-scale modulations, and after 200 ms this is the dominant component of the fluctuations. The time scale for the onset of short-wavelength structure is roughly the same across the magnetic field range studied, but the patterns become prominent more quickly at larger magnetic field. In addition, while the resulting wave-like modulations are clearly out-of-phase at low and intermediate magnetic field, the “phase shift” between $m_F = \pm 1$ is closer to 90° than to 180° at the largest field value. In all cases, the anti-correlated pattern seems to decay in a chaotic way after several 100 ms, most quickly for $B = 0.39$ G, which corresponds to the largest transient total $m_F = 0$ population (“resonance”).

In Fig. 6.6, the rms amplitude $\sqrt{c_{00}}$ of the $m_F = 0$ fluctuations and the normalized correlation

$$\tilde{c}_{+1-1} = \frac{c_{+1-1}}{\sqrt{c_{+1+1}c_{-1-1}}} - \alpha \quad (6.8)$$

of the $m_F = \pm 1$ fluctuations are plotted versus time to demonstrate that they are suitable indicators of the two-step process mentioned. We concentrate on the $m_F = 0, \pm 1$ populations, because $m_F = \pm 2$ is only weakly populated from the start owing to our particular initial state. Only in the interaction regime at low magnetic field, a significant $m_F = \pm 2$ population comes up after some time, as can be seen in the images (Fig. 6.8-6.11). As an example, in the initial state only $1/8$ of the total population is in $m_F = \pm 2$, compared to $1/2$ in $m_F = \pm 1$. A local imbalance of the $m_F = \pm 2$ populations thus enters into F_z at half the weight of an imbalance in $m_F = \pm 1$.

Fig. 6.8-6.11 illustrate the spatial patterns at characteristic times and provide information on the length scale of the patterns as well as an overview of all m_F populations.

- 0 ms: Right after preparation, fluctuations are small and uncorrelated.
- 50 ms: Large-scale in-phase fluctuations are fully developed and still dominant. The normalized correlation between $m_F = \pm 1$ is positive.
- 100 ms: Small-scale out-of-phase fluctuations appear, the correlation approaches zero.
- 150 ms: Small-scale out-of-phase fluctuations are more or less fully developed, the correlation is down to zero or negative.
- 200 ms: Small-scale out-of-phase fluctuations are fully developed and begin to decay, the correlation has reached a more or less steady state at or below zero.

An important conclusion from the observation of anti-correlated local populations of $m_F = \pm 1$ is the *local non-conservation of magnetization* $F_z = 2(\rho_{+2} - \rho_{-2}) + (\rho_{+1} - \rho_{-1})$. This is a fundamental departure from the local density model, and a strong hint to a mechanism involving kinetic energy, such as *dynamical instability* as discussed in-depth in Section 2.3.2.

The small-scale patterns visible in Fig. 6.8-6.11 have a quite characteristic length scale of the order of $\lambda = 20 \mu\text{m}$, except for the lowest magnetic field $B = 0.15$ G where the length scale seems to be somewhat larger, $\lambda \approx 35 \mu\text{m}$. Comparing to the spin healing length $\xi_s = \sqrt{\frac{\hbar}{2mg_1\langle n \rangle}} \approx 3.5 \mu\text{m}$, their ratio λ/ξ_s is indeed of the order of 2π , a value predicted in this regime by *linear instability analysis* (Section 2.3.2 as well as the footnote on page 101). The *wave-like* patterns emerging are particularly impressive at low magnetic

gradient occurs at the zero crossings and is proportional to $\frac{2\pi}{\lambda}$. Since the definition of the (spin) healing length refers to the gradient of the density and spin composition, respectively, it has to be compared to $\frac{\lambda}{2\pi}$ in this case.

field, and Fig. 6.12 demonstrates the long-term behavior in this case. They correspond to amazingly regular, almost sinusoidal modulations of the axial spin expectation value F_z .

Spontaneous structure formation via dynamical instability has also been observed in an $F = 1$ spinor condensate [41] by the group of Stamper-Kurn. Apart from the fact that our experiments are done in $F = 2$, there are several other important differences regarding the setup as well as the outcome of the experiments.

- In [41], a spinor condensate is prepared in $m_F = 0$ with respect to an axial offset field, which is equivalent to a superposition of $m_F = \pm 1$ with respect to any transverse direction. In contrast, we prepare a spinor condensate in a state of zero axial, but maximum transverse magnetization, i.e. $m_F = +2$ with respect to some transverse direction.
- The initial state $|m_F = 0\rangle$ used in [41] is a state of *maximum* interaction energy relative to the ferromagnetic ground state of $F = 1$ ^{87}Rb , since $\vec{F} = 0$. For anti-ferromagnetic $F = 2$ ^{87}Rb , this role is played by the fully transversely magnetized state $|\zeta_{\pi/2}\rangle$ with $F_x = 2$.
- In [41], a spontaneous, locally varying *transverse* magnetization, but no longitudinal magnetization has been observed, which can be explained as domain separation of the immiscible $m_F = \pm 1$ components with respect to a locally varying transverse direction. In contrast, we observe a spontaneous, locally varying *longitudinal* magnetization. The transverse magnetization has not been directly observed in our experiment. However, $F_z \neq 0$ implies that the local magnetization is not purely transversal as prepared initially.
- In [41], the structure formed is rather irregular and at the length scale of the healing length ($2.4 \mu\text{m}$ in this case). The quadratic Zeeman energy is only 1.3s^{-1} and thus negligible compared to the interaction energy. In contrast, we observe much larger structures at a significantly larger magnetic field (150 mG, corresponding to $|q| = 10 \text{s}^{-1}$) that become smaller at higher field.
- Last but not least, ^{87}Rb $F = 1$ is ferromagnetic and is known to feature a dynamical instability, while $F = 2$ is *anti-ferromagnetic*. Even though a dynamical instability has been predicted for the pure $m_F = 0$ state [76] (Section 2.3.2), its interpretation in terms of spontaneous symmetry breaking as in $F = 1$ is less obvious and the question of the relative phase or correlation of the $+m$ and $-m$ modes, i.e. whether unstable modes lead to a modulation of F_z , has not yet been addressed.

Unpublished numerical simulations by M. Ueda [95, 76] for the case of an initially pure $F = 2, m_F = 0$ state show very similar behavior to that observed in our experiments. At low magnetic field, large-scale correlated patterns emerge as expected due to the local density mechanism, while at large magnetic field small-scale anti-correlated patterns appear, explaining the strong damping of spinor oscillations observed in [38]. However, the patterns in [95] lack the wave-like appearance observed here.

As already mentioned earlier, the state $m_F = 0$ differs from our initial state $\zeta_{\pi/2}$ in the amount of potential energy available for conversion to kinetic energy. The excess potential energy per particle, compared to the anti-ferromagnetic ground state, is (see Tab. 6.1 and

Table 6.1: Potential energies per particle of different $F = 2$ states (in SMA, see Section 2.3.2). Note that in ^{87}Rb $F = 2$, $g_1 > 0$, $g_2 < 0$ and $q < 0$.

description	state ζ	potential energy
pure $m_F = 0$	$(0, 0, 1, 0, 0)$	$\hbar \times \frac{g_2 \langle n \rangle}{8}$
fully transversely magnetized state	$(\frac{1}{4}, \frac{1}{2}, \frac{\sqrt{3}}{8}, \frac{1}{2}, \frac{1}{4})$	$\hbar \times (2g_1 \langle n \rangle + q)$
AF ground state [76]	$\frac{1}{\sqrt{2}}(1, 0, 0, 0, 1)$	$\hbar \times \left(\frac{g_2 \langle n \rangle}{8} + 4q \right)$

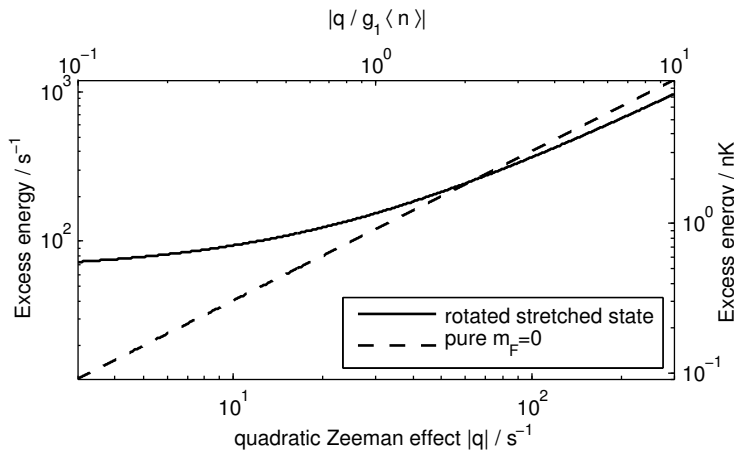


Figure 6.7: Excess potential energy as function of the quadratic Zeeman effect, in units of s^{-1} and nK. $g_1 \langle n \rangle = 30 \text{ s}^{-1}$, $|g_1| = |g_2|$. The curves intersect at $q = 2 \langle n \rangle (g_1 + g_2/16)$. Only if this condition is met, a free evolution starting in $\zeta_{\pi/2}$ can possibly end in $|0\rangle$.

Fig. 6.7)

$$E_0/\hbar = 4|q| \quad \text{for } \zeta = |0\rangle, \quad (6.9)$$

$$E_{\pi/2}/\hbar = 2 \langle n \rangle \left(|g_1| + \frac{1}{16} |g_2| \right) + 3|q| \quad \text{for } \zeta = \zeta_{\pi/2}. \quad (6.10)$$

Thus at low magnetic field $q \rightarrow 0$, there is not enough energy available in the $m_F = 0$ state to drive a dynamical instability at a small wavelength, corresponding to a high kinetic energy. This is reflected by the divergence of the minimum unstable wavelength λ_{\min} discussed in Section 2.3.2. Only the local density mechanism of structure formation remains, leading to correlated large-scale patterns. In contrast, the fully transversely magnetized state has an excess potential interaction energy even at $q = 0$ and thus will lead to the small-scale anti-correlated patterns connected with the dynamical instability in this limit, too.

An alternative explanation for the appearance of regular patterns at the length scale of $2\pi\xi_s$ may be the mechanism observed in a two-component Bose-Einstein condensate and described in [27] by the group of E. Cornell. A two-component condensate, e.g. ^{87}Rb $F = 2$, $m_F = +1$ and $F = 1$, $m_F = -1$, can be viewed as a quasi-spin-1/2 system (compare Section 2.2.1 and Section 2.2.2) and described by a $F = 1/2$ spinor order parameter, where the stretched states $|\pm \frac{1}{2}\rangle$ each correspond to one of the two basis states, and any other spinor state to a coherent superposition. In their publication [27] with the illustrative title “watching a superfluid untwist itself”, Matthews et al. show how such a spin-1/2 condensate “winds up” under the influence of a locally varying rate of evolution the authors call “differential torque”, much like in the case of local density dynamics described above.

When the size of the structures reaches the order of magnitude of $2\pi\xi_s$, the kinetic energy of the spinor wave function becomes relevant. Non-local evolution then leads to phase reversal and subsequent “unwinding” with increasing structure size, until the condensate is homogeneous once again and the sequence starts over.

In our case, the “differential torque” may result from either the local density mechanism as described above or from the residual magnetic field gradient of the order of 3 mG/cm (Section 3.4). Since we do not observe a decreasing structure size but rather small-scale patterns growing out of a large-scale background, we rule out the local density mechanism as the origin of a possible “twisting-untwisting” scenario. On the other hand, an axial magnetic field gradient leads to Larmor rotation at a locally varying rate, which is not observable with Stern-Gerlach detection⁴. Thus, only when the “phase reversal” takes place, rotating the spin vector out of the plane perpendicular to the axial magnetic field, structure in the axial spin component F_z becomes visible, and should then have a size of the order of $2\pi\xi_s$ from the start. At a residual gradient of $B' = 3 \text{ mG/cm}$ or $\omega' = \frac{g\mu_B}{\hbar}B' = 2\pi \times 2100 \text{ s}^{-1}\text{cm}^{-1}$, it takes $T \approx 1/(\xi_s\omega') = 250 \text{ ms}$ to “wind up” the order parameter down to the spin healing length. This is fairly consistent with the time scale observed, considering our limited knowledge of the residual gradient. However, we see no “unwinding” but rather a chaotic decay of the structures for evolution times larger than a few 100 ms. At this point, we can not fully exclude that at least the “twist” part of the mechanism plays a role at least at intermediate time scales.

Spin waves, as observed in thermal or partially condensed two-component ensembles [30, 29, 31] by the group of E. Cornell as well, are most likely unrelated to the phenomena observed here, since they appear at a much longer length scale, basically given by the condensate dimensions. In addition, the mechanism of spin propagation underlying these wave phenomena is indeed limited to thermal spinor gases, or condensates having a large thermal fraction.

In conclusion, we have evidence that what we observe in elongated ^{87}Rb $F = 2$ condensates may indeed be a dynamical instability leading to spontaneous pattern formation and local symmetry breaking. Additional structure formation preceding the growth of unstable modes can be identified as quasi-homogeneous dynamics in the local density approximation. A particularly intriguing feature of our experiments is the direct observation of characteristic wave-like modes.

In fact, we may assume that the formation of strongly modulated patterns we have observed in an isotropic dipole trap (Section 5.6) is also a consequence of dynamical instability rather than local density dynamics. On the other hand, the rapid damping of coherent oscillations observed in the astigmatic trap (Section 5.4) is likely to be caused by local density dynamics alone, since it appears in the interaction regime only, even though no visible structure has been observed in this case.

An alternative explanation of small-scale structures in elongated spinor BEC, relying on the residual magnetic field gradient, cannot be ruled out from the data available; experiments clarifying this point are possible and should be awaited for final assessment.

⁴A Ramsey sequence or final $\pi/2$ pulse would make the transverse spin visible in Stern-Gerlach images, see Section 2.2.1 and compare Section 5.2 as well as Section 5.5. However, this has not yet been applied to the elongated geometry.

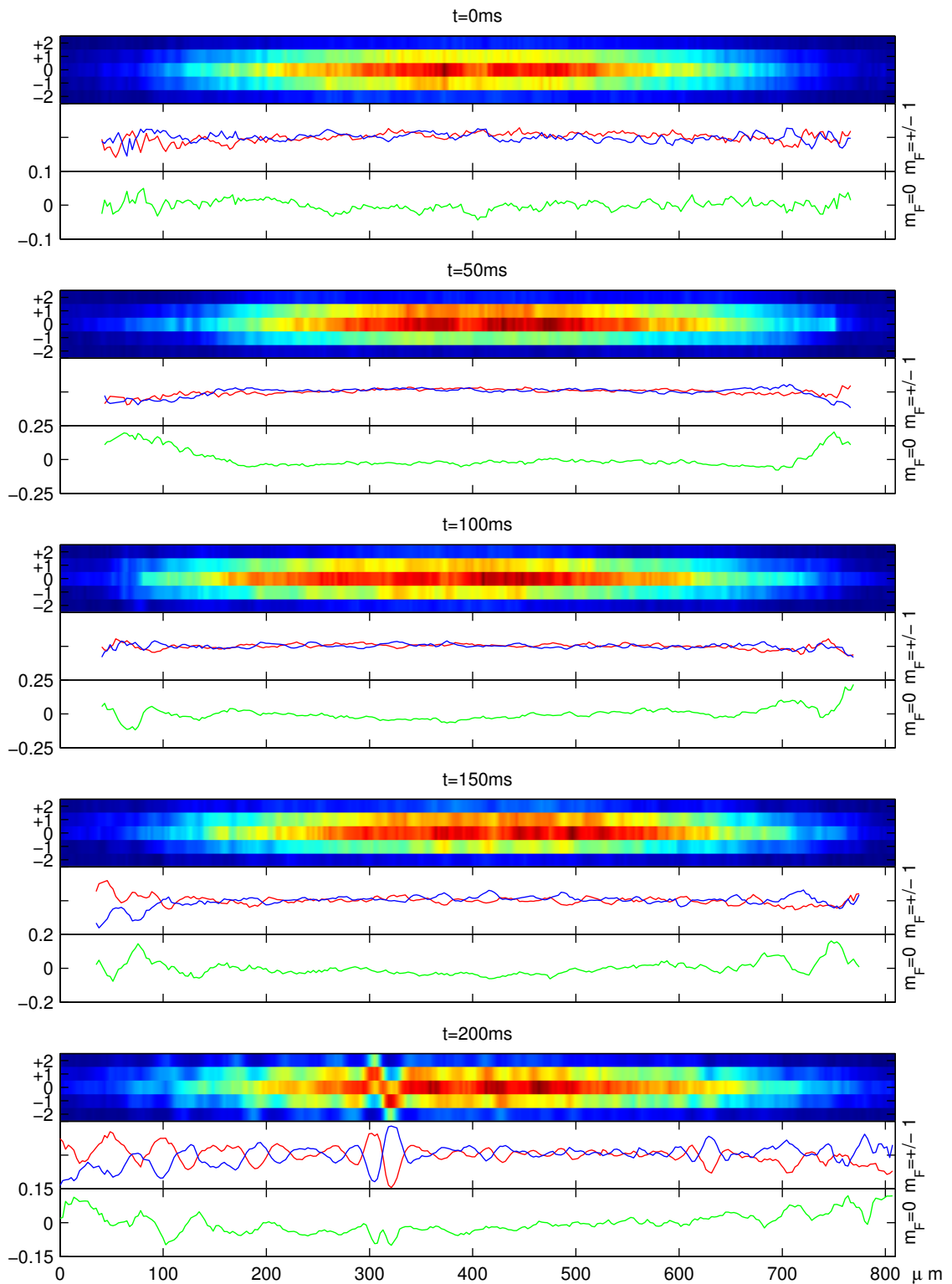


Figure 6.8: Emergence of spin structure at $B = 0.15 \text{ G}$, $|q|/|g_1 \langle n \rangle| \approx 0.34$.

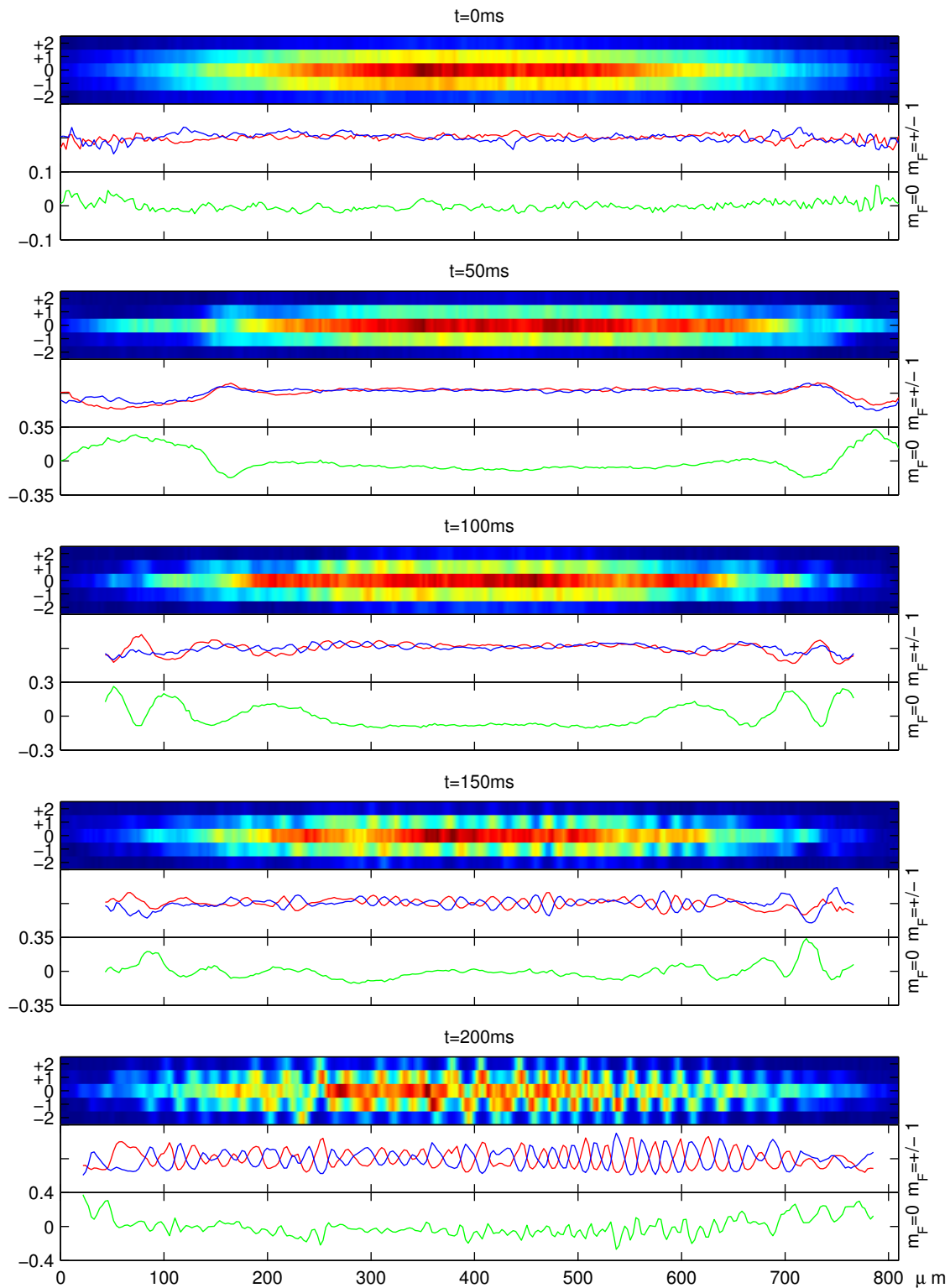


Figure 6.9: Emergence of spin structure at $B = 0.25$ G, $|q|/|g_1\langle n \rangle| \approx 0.95$.

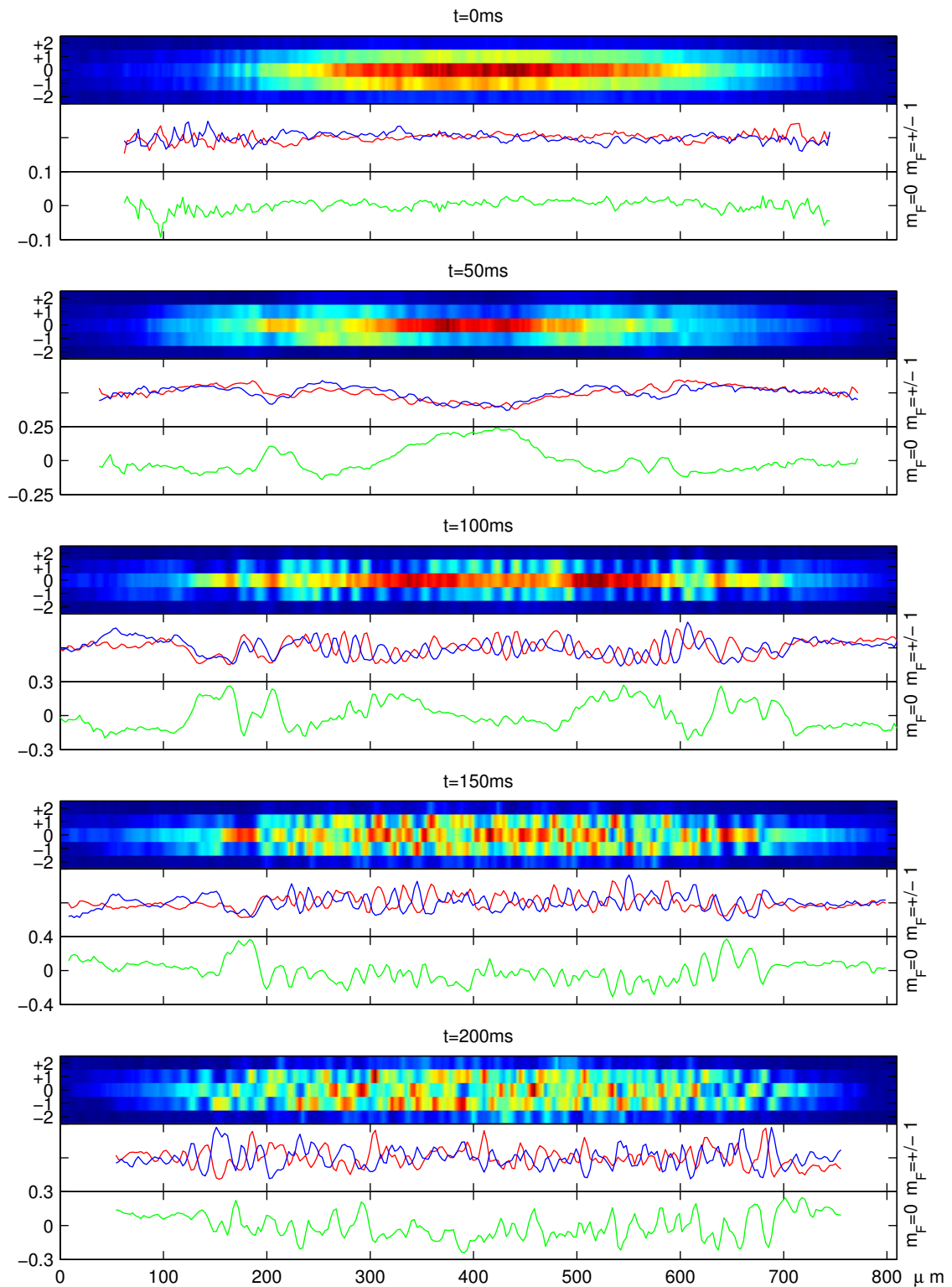


Figure 6.10: Emergence of spin structure at $B = 0.39$ G, $|q|/|g_1\langle n \rangle| \approx 2.3$.

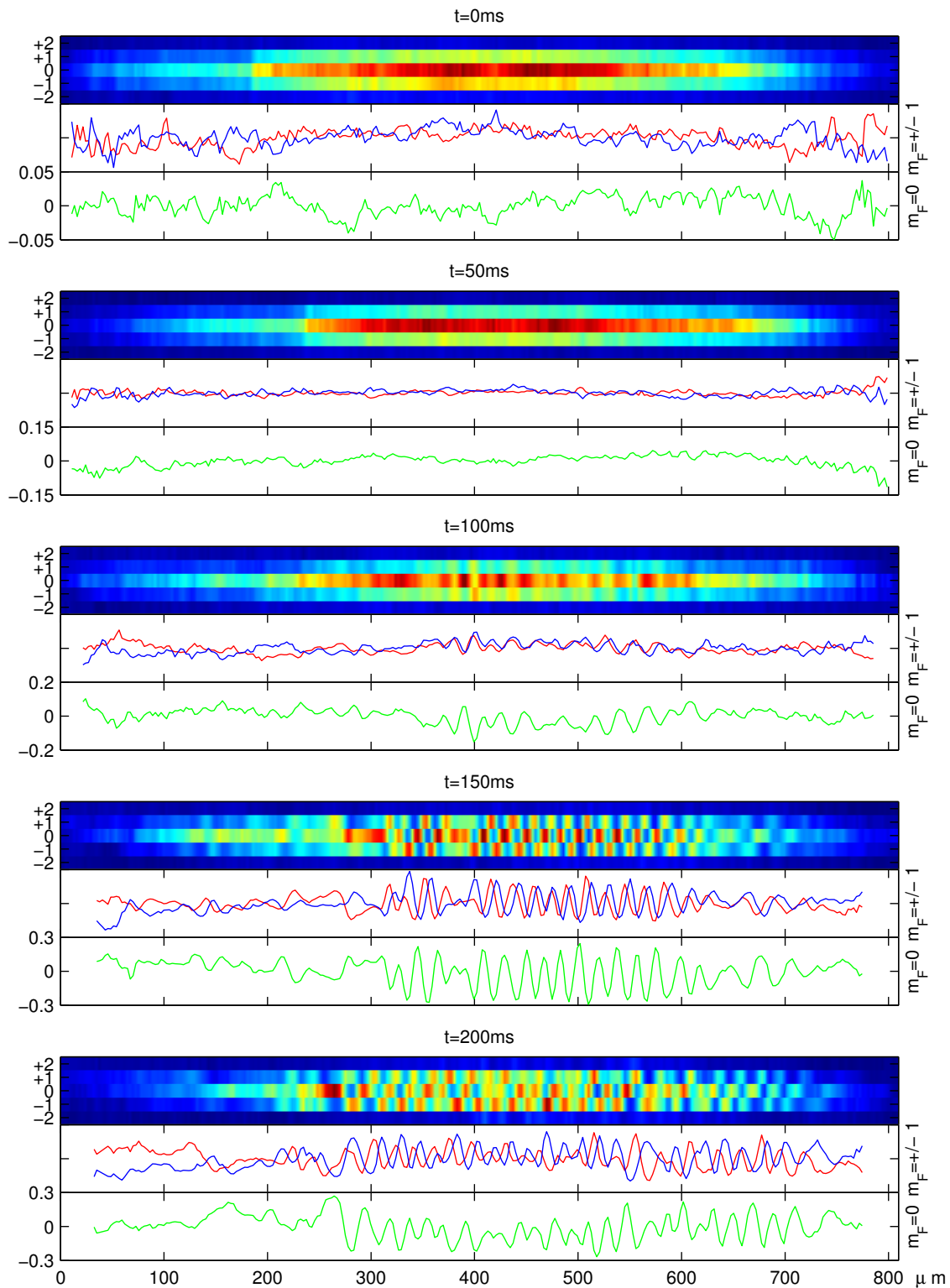


Figure 6.11: Emergence of spin structure at $B = 0.55$ G, $|q|/|g_1 \langle n \rangle| \approx 4.5$.

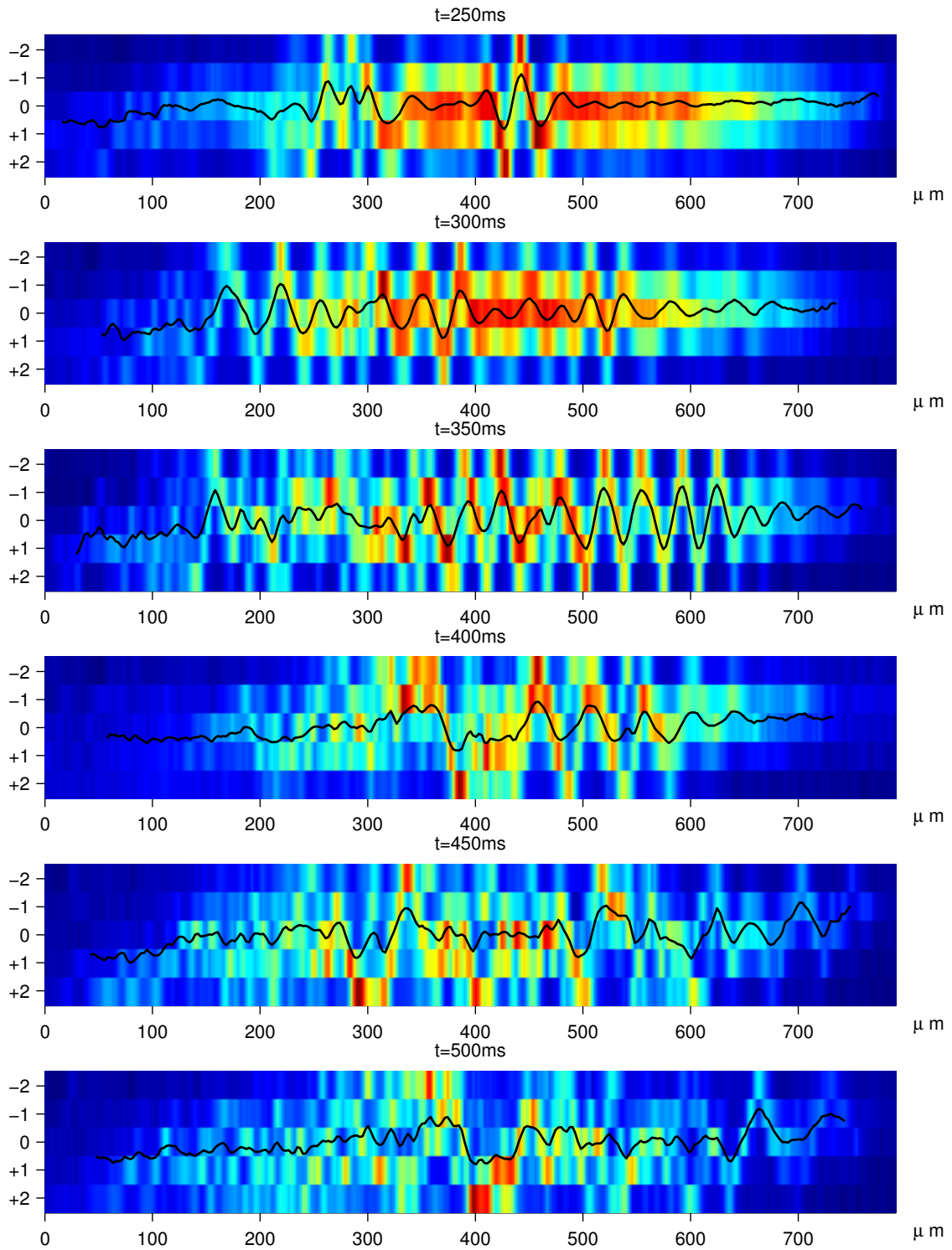


Figure 6.12: Emergence and decay of spin patterns at $B = 0.15$ G. SOLID LINE: Axial spin expectation value F_z . Tick marks correspond to m_F components in the image and at the same time set the scale for F_z .

Chapter 7

Chaotic dynamics in $F = 2$

A thorough numerical and analytical treatment of the equations of motion of symmetric $F = 2$ spin dynamics in the single mode approximation uncovers the complex and actually chaotic dynamics of this system. A comprehensive treatise of this topic is beyond the scope of the present work, but an attempt is made to introduce the reader to the beauty of nonlinear dynamics and deterministic chaos, which in fact is a ubiquitous phenomenon in nature.

7.1 Signatures of chaos

In the preceding Chapters 5 and 6, we have concentrated on common features of $F = 1$ and $F = 2$ spin dynamics in the single-mode approximation. We have shown in particular that both systems are governed by the competition of quadratic Zeeman energy q and interaction energy $g_1 \langle n \rangle$ and exhibit the same type of resonance in the crossover region between the Zeeman ($|g_1 \langle n \rangle| \ll |q|$) and the interaction ($|q| \ll |g_1 \langle n \rangle|$) regime (Fig. 7.1).

A close look at the simulated population curves of Fig. 5.12, however, already reveals that the solutions of the SMA equations of motion (2.76) (summarized again in Tab. 7.1) are no longer simply periodic, in contrast to $F = 1$. In addition, it turns out that the asymptotic case, which in $F = 1$ defines the position of the resonance $|q| = |g_1 \langle n \rangle|$ (Section 5.3), is much less robust in $F = 2$: obtaining an aperiodic numerical solutions

Table 7.1: Equations of motion of spin dynamics in $F = 2$, in single-mode approximation and restricted to the symmetric subspace $\zeta_{+m} = \zeta_{-m} \forall m$ (Section 2.3.2). This system of nonlinear ordinary differential equations is the basis of the present chapter. The g_2 interaction term is neglected in this chapter, since it only causes minor quantitative changes. $\zeta_m = \sqrt{\rho_m} e^{i\theta_m}$ is complex, with modulus $\sqrt{\rho_m}$ and phase θ_m . Note that in this chapter, the sign of the interaction parameter (positive in $F = 2$) and the quadratic Zeeman effect (negative in $F = 2$) is explicitly taken into account, and $g_1 \langle n \rangle, q > 0$ refers to the *modulus* of the respective quantity.

$$\begin{aligned}
 i\dot{\zeta}_2 &= \frac{g_1 \langle n \rangle}{2} A_2 2\zeta_1 - 4q\zeta_2 \\
 i\dot{\zeta}_1 &= \frac{g_1 \langle n \rangle}{2} A_2 \left[\sqrt{6}\zeta_0 + 2\zeta_2 \right] - q\zeta_1 \quad \text{with} \quad A_2 = 4\text{Re} \zeta_2 \zeta_1^* + 2\sqrt{6}\text{Re} \zeta_1 \zeta_0^* \\
 i\dot{\zeta}_0 &= \frac{g_1 \langle n \rangle}{2} A_2 2\sqrt{6}\zeta_1
 \end{aligned} \tag{7.1}$$

in the best possible approximation requires extremely fine tuning of the parameter $k = g_1 \langle n \rangle / q$ and results in different values depending on the numerical tools used (see Fig. 7.2).

These observations can be viewed as instances of two basic properties of chaotic systems [136, 137]: *recurrence*, meaning that trajectories in phase space return arbitrarily close to their starting point and do not e.g. asymptotically approach a stationary state, and *sensitivity* to initial conditions, implying that trajectories starting from two neighboring points in phase space separate exponentially with time. An intuitive picture of chaotic systems is that of *kneading the dough* [136]: by repeated *stretching* (sensitivity) and *folding* (recurrence), the ingredients are thoroughly mixed.

These first indications of chaos are supported by a mathematical analysis of the equations of spin dynamics. Spin dynamics in $F = 2$, represented by the symmetric single-mode mean-field equations (7.1), belongs to the class of *nonlinear conservative* systems. The latter means that the phase space volume is preserved along trajectories. As a consequence, there are no attractors such as stable fixed points, i.e. states that the system is asymptotically attracted to. Taking into account normalization $\sum_{i=0,1,2} \rho_i = 1$ and global gauge symmetry $|\zeta\rangle \equiv e^{i\theta} |\zeta\rangle \forall \theta \in \mathbb{R}$, the six real variables $\{(\zeta'_i = \text{Re } \zeta_i, \zeta''_i = \text{Im } \zeta_i), i = 1 \dots 3\}$ of (7.1) reduce to four degrees of freedom. Additionally, conservation of energy constrains dynamics further to a three-dimensional manifold in phase space. Two necessary conditions for the existence of chaos – nonlinearity and ≥ 3 degrees of freedom – are thus fulfilled. The system also is *bounded*, i.e. the phase space available to the system is finite, owing to the fact that populations and phases are bounded to $0 \leq \rho_i \leq 1$ and $0 \leq \theta_i \leq 2\pi$, respectively. For a conservative system, boundedness implies recurrence [137].

Sensitivity to small errors of the initial conditions is quantified in the *Lyapunov exponent* of a trajectory, which is defined as the long-term average rate of exponential separation from a second, infinitesimally close trajectory.¹ Positive values indicate unstable trajectories sensitive to initial conditions and perturbations, negative (zero) values mean the trajectory is (marginally) stable. Negative Lyapunov exponents, implying that the trajectory after a small perturbation converges exponentially back to the unperturbed one, only occur in dissipative systems. We will employ the Lyapunov exponent as a characteristic of individual trajectories and as a signature of chaos frequently in the present chapter.

Continuous systems, defined by ordinary differential equations, can be reduced to *discrete* ones by means of a *Poincaré section*. This is a suitably chosen hyper-surface in phase space that is crossed by trajectories $z(t)$ at times $t_i, i = 1, 2, 3 \dots$. The phase space points $z_i \equiv z(t_i)$ constitute a discrete series. The dynamical system $\dot{z} = F(z)$ can be reduced to a discrete map $\tilde{F} : z(t_i) \rightarrow z(t_{i+1}) = \tilde{F}(z_{t_i})$ relating a crossing point of any trajectory to the successive crossing of the same trajectory. Many properties of chaotic systems are more accessible in such a discrete formulation if the Poincaré section is chosen cleverly. Additionally, by reducing the dimension of the relevant manifold in phase space, Poincaré sections are important tools for visualizing chaotic dynamics. In the case of spin dynamics, the surface of section of a given energy shell is two-dimensional. In Section 7.3 we will make use of a suitable Poincaré section to visualize complex trajectories on a certain energy shell in a two-dimensional graph.

Conservative non-integrable systems possess an extremely complex phase space struc-

¹In fact, there is a whole spectrum of Lyapunov exponents according to the number of degrees of freedom. In this work, we refer to the *largest* exponent simply as *the* Lyapunov exponent. For details of the definition and numerical calculation of Lyapunov exponents, see Appendix B.

ture. Regions of regular and irregular motion coexist and are densely mixed. The theory of these systems [138, 139], compared to dissipative dynamics [137, 136], is rather involved. In the following, we will restrict ourselves to intuitive arguments and general notions of the theory of dynamic systems.

7.2 Trajectory statistics

In a first step, we take a closer look at the population dynamics starting from the *fully transversely magnetized state*, tying in with the experiments of Chapter 5. A typical trajectory (Fig. 7.2) from the crossover region, starting from the fully transversely magnetized state, clearly looks irregular in some way. However, we have to distinguish *pseudo-periodic* trajectories, which appear irregular on time scales less than the smallest common multiple of *all* cycle times², and truly chaotic trajectories. In the present section, several ways of characterizing trajectories are compared. As it turns out, they consistently indicate true chaos in certain parameter regions, revealing a rich structure in parameter space.

Periodic signals have a well-defined amplitude and cycle time, that can be obtained from the difference in value and time of each pair of minimum and maximum. Applying this method of measurement to an irregular signal such as the $m_F = 0$ population ρ_0 as in Fig. 7.2, we obtain a different amplitude and period for each minimum-maximum pair³:

$$\begin{aligned} \text{amplitude } A &\equiv \rho_0(t_{\max}) - \rho_0(t_{\min}) \\ \text{periodic time } T &\equiv t_{\max} - t_{\min} \end{aligned} \tag{7.2}$$

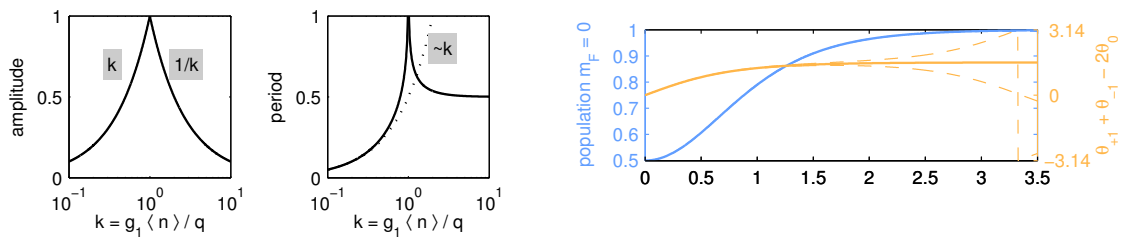
where $\rho_0(t)$ has a maximum at $t = t_{\max}$, equivalent to its time derivative having a zero crossing from positive to negative, $\dot{\rho}_0(t_{\max}) = 0 \searrow$ (t_{\min} correspondingly). This can also be interpreted as taking a Poincaré section with the surface $\dot{\rho}_0 = 0$, and thus allows to compare the results to one of the most popular routes to chaos, the *period doubling scenario*⁴. In this scenario, the transition from regular to chaotic motion takes place as a series of period doublings, which in the histogram of amplitudes appear as bifurcations. We will not go into detail, but Fig. 7.3 should provide an impression.

Applying the method to trajectories (in this case, the $m_F = 0$ population) starting from the fully transversely magnetized state $\zeta_{\pi/2}$, we obtain a histogram of amplitudes and periods as in Fig. 7.4. The plot shows, for a range of given parameters q (horizontal axis), the frequency of occurrence of an amplitude or period of a given value (vertical axis) as color-coded pixels. For these simulations, $g_1 \langle n \rangle = 1$ has been assumed which merely fixes the time scale. First of all, Fig. 7.4 demonstrates once again the prevalence of simple oscillations of decreasing amplitude in the limiting cases $q \rightarrow 0$ (interaction regime) and $q \rightarrow \infty$ (Zeeman regime). The broadening of the histograms as q approaches the crossover region indicates pseudo-periodicity, a fact supported by the Lyapunov exponent being zero outside the central crossover region $1.8 < q < 3.6$. In this central crossover region, parameter ranges leading to regular and chaotic motion alternate. Positive Lyapunov exponents and a characteristic “smearing” of the histograms are consistent indicators of

²A fact that has recently been exploited to simulate disorder in optical lattices, superposing two retro-reflected light beams of incommensurate frequencies [140].

³Actually, this definition yields twice the amplitude and half the periodic time, compared to the usual definitions.

⁴The period doubling scenario is a common route to chaos in *dissipative* systems, but also occurs in conservative ones. [137]



(a) Amplitude and period of population oscillations, according to the analytic solution (5.5). The period diverges to infinity at $k = 1$.

(b) Population and phase dynamics at and around resonance $k = 1.00 \pm 0.01$, starting from $\zeta_{\pi/2}$.

Figure 7.1: Spin dynamics resonance at the crossover from Zeeman to interaction regime, illustrated for $F = 1$. The same qualitative behavior has been observed in $F = 2$, see Chapter 5. Note that $k = g_1 \langle n \rangle / q$.

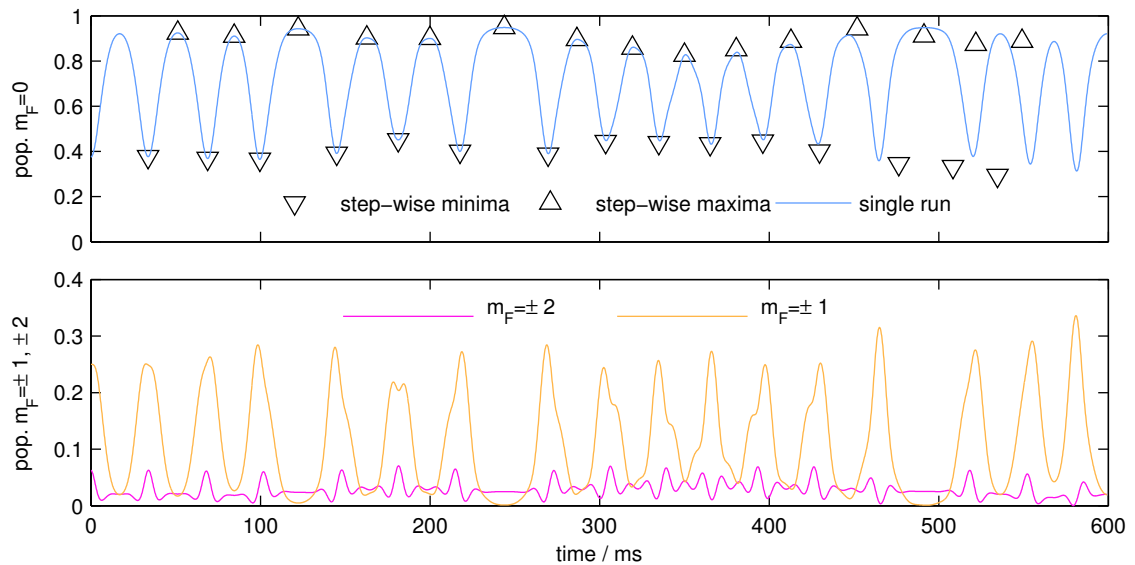


Figure 7.2: Simulated $F = 2$ population dynamics at $g_1 \langle n \rangle = 50 \text{ s}^{-1}$ and $q = 2.5 g_1 \langle n \rangle$, the initial state $\zeta_{\pi/2}$ is the same fully transversely magnetized state as in Chapter 5. Note how the indicated “step-wise” maxima and minima and the “single-run” trajectory start to diverge as a result of accumulated numerical errors. The “step-wise” and the “single-run” trajectory are calculated using the same code with a different choice of interpolation points.

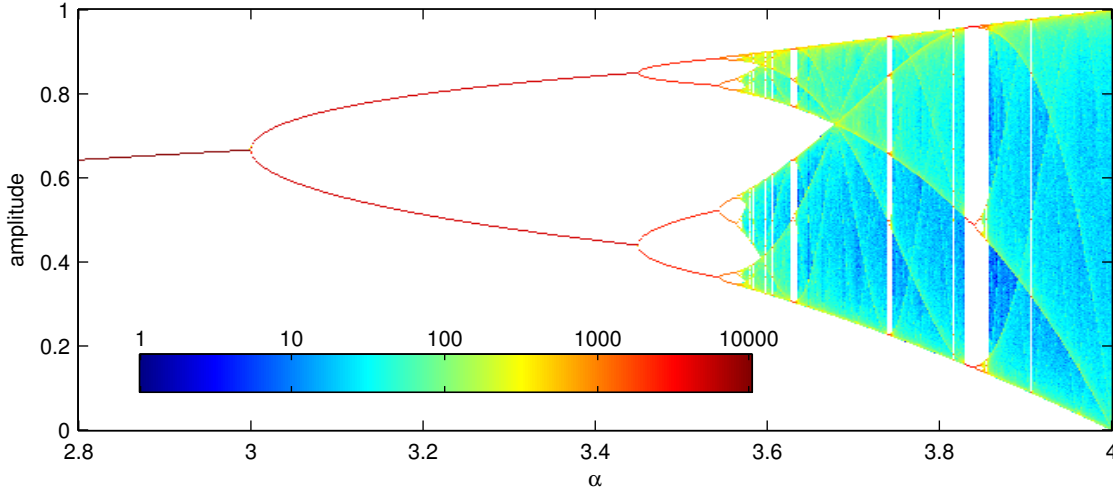


Figure 7.3: Histogram of amplitudes x_n of the so-called quadratic iterator, $x_{n+1} = \alpha x_n(1-x_n)$, $n = 1 \dots 10000$. This is an example of a discrete, dissipative system. Depending on the parameter α , the system state x_n is attracted by a fixed point (single line), a periodic cycle of period P ($P+1$ lines) and becomes chaotic for $\alpha > 3.5699\dots$ [136]. It may serve as an example of the period doubling scenario and is to be compared to Fig. 7.4, see text.

chaos. The sequence of chaotic and regular parameter ranges is very dense; the smallest structure resolved in parameter space consists of just a single grid spacing ($\Delta q \approx 10^{-3}$).

Comparing the histograms of spin dynamics to Fig. 7.3 demonstrating the period-doubling scenario, we note agreement in some aspects, but also obvious differences. First of all, the characteristic *period-doubling bifurcations* are *not seen* in spin dynamics. We merely observe a broadening of the histogram due to pseudo-periodic motion, in particular in the wings towards the Zeeman and interaction regime, or a completely smeared-out distribution in the chaotic regimes. This smearing out in the chaotic regime, on the other hand, is a common characteristic, as well as the interspersed *islands of order*, where the motion becomes (pseudo-)periodic for a narrow range of parameters q . One of them, at $q = 2.81$, will be studied in more detail in the following Section 7.3 using a different Poincaré surface of section to visualize trajectories.

Fitting power laws $A(q) = aq^\alpha$ and $T(q) = tq^\beta$ to the center-of-mass of the wings of the histograms, we recover the asymptotic behavior known from the analytic solution in $F = 1$, and expected from perturbative solutions in $F = 2$. The oscillation period is constant and of the order of one in the interaction regime, and follows q^{-1} in the Zeeman regime. The oscillation amplitude is maximal in the crossover region and decays both in the Zeeman regime and in the interaction regime. In the latter case, the best-fit exponent $\alpha \approx 1$ is in quantitative agreement with the perturbative solutions. In the Zeeman regime, the best-fit exponent deviates from the expected value $\beta = 1$, probably because at $q = 10$ we are not close enough to the limiting case.

As an alternative to the histogram technique, it is also possible to determine the spectral composition of trajectories by Fourier transformation of the population as a function of time. This has been done in Fig. 7.5, where similar to Fig. 7.4 the power spectrum of the $m_F = 0$ population for a given parameter q is color-coded in each pixel column. Comparison to Fig. 7.4 basically confirms the results of the preceding paragraph, clarifying in particular the pseudo-periodic high- q region. The dynamics there is governed by a set of

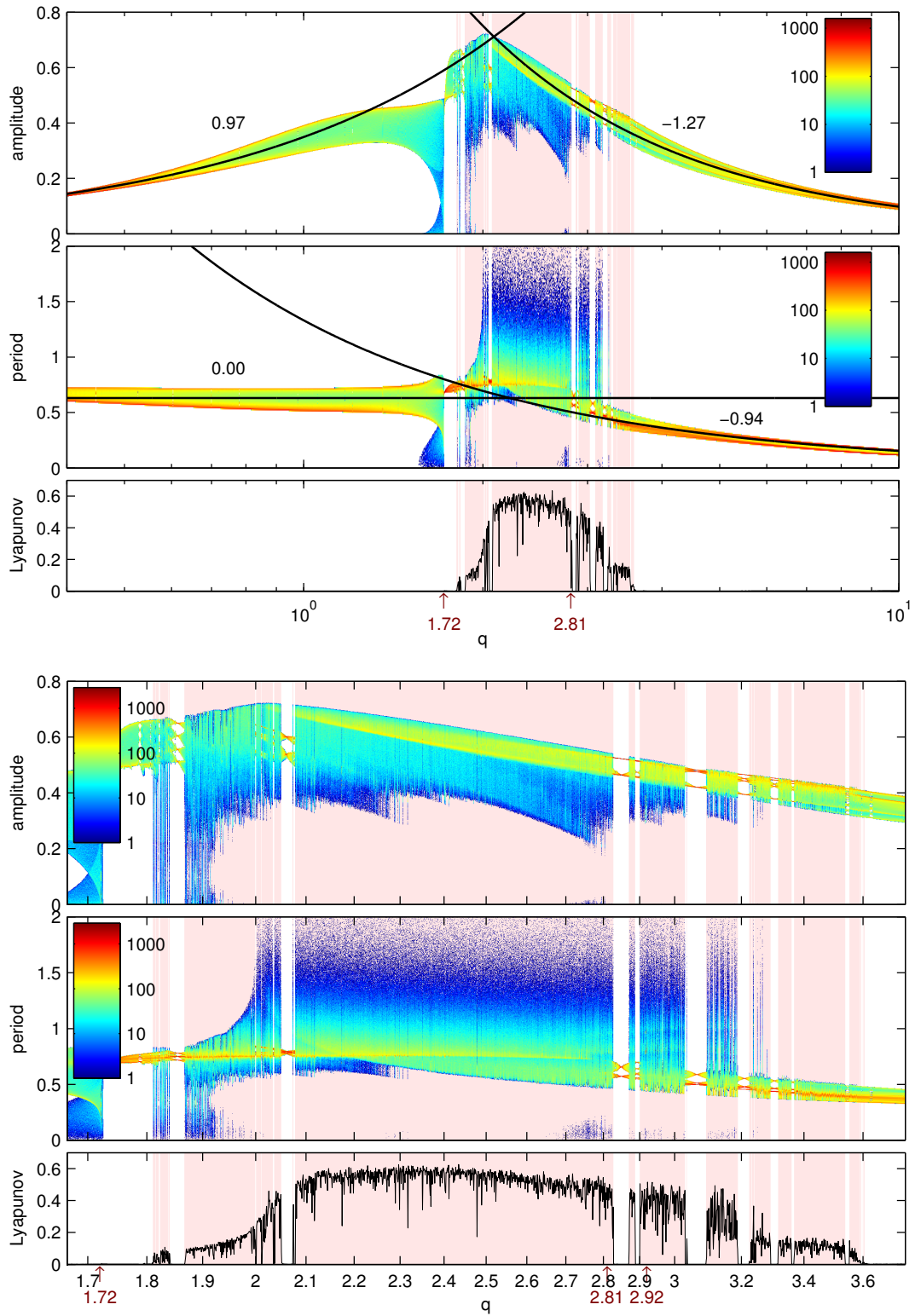


Figure 7.4: Histograms of amplitude and period (see text) of $m_F = 0$ population dynamics. Solid lines are power law fits to the center-of-mass curves calculated from the histograms, except for the low- q end of the period histogram, where the exponent has been fixed to zero. The respective exponents are indicated in the graphs. Regions of positive Lyapunov exponent (> 0.01) are marked in all graphs by a shaded background.

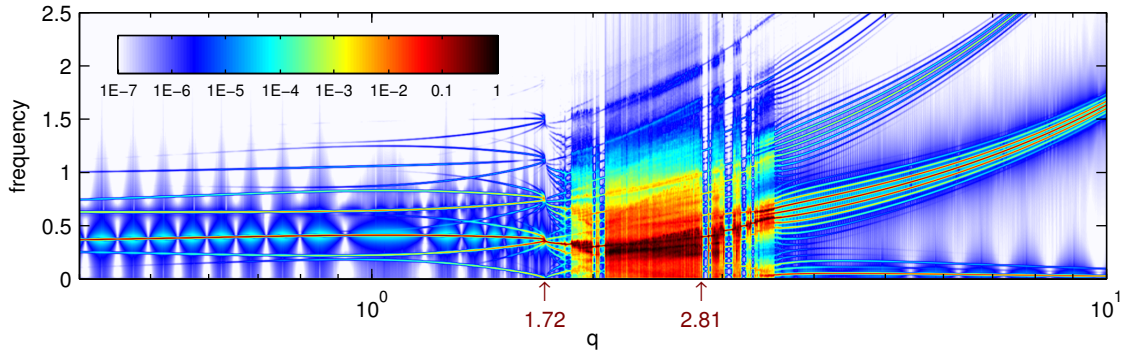


Figure 7.5: Fourier transforms of trajectories ($m_F = 0$ population) of fixed duration, comparable to those in Fig. 7.4. The Fourier transforms for each q have been normalized to the largest non-zero component. The periodically modulated background at the 10^{-6} level is probably an artefact, caused by the finite time of observation in conjunction with the period of the signal. This effect, known as *leakage*, depends on whether an integer number of periods fits into the time of observation or not. Adequate windowing (Hamming in this case) alleviates leakage, but doesn't fully remove the dependency.

several closely spaced modes of comparable spectral power, converging and/or dying out for $q \rightarrow \infty$. In contrast, in the interaction regime, there is a single dominant mode only.

Both histograms and Fourier plots exhibit another striking feature at $q \approx 1.72$. This becomes manifest in a *divergence* of amplitudes and periods in the histograms, and at the same time a *convergence* of characteristic frequencies as seen in the Fourier plot. The Lyapunov exponent is clearly zero at this point. The origin and impact of this feature is not understood. On the other hand, quite surprisingly, the “critical value” $q/g_1 \langle n \rangle = 2$, marking the boundary between F_x changing sign along a trajectory or not (see the following Section 7.3), does not at all show up in either of the graphs.

7.3 Phase space dynamics

The preceding Section 7.2 has brought up clear evidence for chaotic dynamics in the system of equations (7.1) describing single-mode spinor dynamics. For the purpose of characterizing this dynamics, it is not sufficient to just look at trajectories starting from a single initial condition, the fully transversely magnetized state. Rather, we have to look at the structure of the whole phase space available to the system at given parameter values.

In this section we get back to the concept of the Poincaré section as a powerful tool for the visualization of complex dynamics in phase space. We first point out a way of deriving equations of motion for arbitrary observables, and then proceed to pick suitable observables that allow to define a Poincaré section of physical relevance.

The equations of motion for the spinor $|\zeta\rangle$ (see Tab. 7.1 and Section 2.3.2) follow from a variational principle and an energy functional that is *not* just a quadratic form in $|\zeta\rangle$. However, in the present case, neglecting g_2 terms, the energy functional depends on the spinor via *expectation values of single-particle observables* only. In the subspace of spinors satisfying $\zeta_{+m} = \zeta_{-m} \forall m = -2 \dots 2$, $\langle F_y \rangle = \langle F_z \rangle = 0$ identically, and the energy functional can be expressed in terms of $\langle F_x \rangle$ and $\langle F_z^2 \rangle$ only:

$$\mathcal{H} = \frac{g_1 \langle n \rangle}{2} \langle \mathbf{F}_x \rangle^2 - q \langle \mathbf{F}_z^2 \rangle, \quad (7.3)$$

leading to an equation of motion for the spinor $|\zeta\rangle$

$$i\dot{\zeta}_m = \frac{\partial\mathcal{H}}{\partial\zeta_m^*} = \frac{\partial\mathcal{H}}{\partial\langle\mathbf{F}_x\rangle} \frac{\partial\langle\mathbf{F}_x\rangle}{\partial\zeta_m^*} + \frac{\partial\mathcal{H}}{\partial\langle\mathbf{F}_z^2\rangle} \frac{\partial\langle\mathbf{F}_z^2\rangle}{\partial\zeta_m^*}. \quad (7.4)$$

Returning to Hilbert space notation, we obtain $i|\dot{\zeta}\rangle = \mathbf{H}|\zeta\rangle$ with an effective Hamiltonian

$$\mathbf{H} = \frac{\partial\mathcal{H}}{\partial\langle\mathbf{F}_x\rangle} \mathbf{F}_x + \frac{\partial\mathcal{H}}{\partial\langle\mathbf{F}_z^2\rangle} \mathbf{F}_z^2 = g_1 \langle n \rangle \langle \mathbf{F}_x \rangle \mathbf{F}_x - q \mathbf{F}_z^2. \quad (7.5)$$

This reformulation of the equations of motion (7.1) makes it easy to directly calculate equations of motion for arbitrary observables A . Noting that $\langle \dot{\mathbf{A}} \rangle = \langle \dot{\zeta} | \mathbf{A} | \zeta \rangle + \langle \zeta | \mathbf{A} | \dot{\zeta} \rangle$ we arrive at the expression

$$\langle \dot{\mathbf{A}} \rangle = i \left[\frac{\partial\mathcal{H}}{\partial\langle\mathbf{F}_x\rangle} \langle [\mathbf{F}_x, \mathbf{A}] \rangle + \frac{\partial\mathcal{H}}{\partial\langle\mathbf{F}_z^2\rangle} \langle [\mathbf{F}_z^2, \mathbf{A}] \rangle \right]. \quad (7.6)$$

Now the question arises how the differences between $F = 1$ and $F = 2$ come into play, which lead to chaotic dynamics in $F = 2$ but not $F = 1$. As we have seen, equations of motion can be formulated without explicit reference to the spinor states, and thus have the same form for any F . The answer lies in the fact that the equation of motion for any observable will generally contain other observables which are products of the operators involved, and will thus not lead to a closed system of equations. As an example that will also be of use later, we consider $\langle \mathbf{F}_x \rangle$:

$$\langle \dot{\mathbf{F}}_x \rangle = -iq \langle [\mathbf{F}_z^2, \mathbf{F}_x] \rangle = q \langle \mathbf{F}_z \mathbf{F}_y + \mathbf{F}_y \mathbf{F}_z \rangle \quad (7.7)$$

The equation of motion of $\mathbf{F}_z \mathbf{F}_y + \mathbf{F}_y \mathbf{F}_z$ can be calculated along the same lines, but will contain products of three operators, and so on. However, since we are operating in a finite-dimensional Hilbert space, *all* observables can be expressed as linear combinations of a finite number of basis operators in this Hilbert space. Doing this one arrives at a closed set of at most⁵ $(2F + 1)^2$ equations of motion. For $F = 1$, these are at most nine equations, and the number can be further reduced by taking advantage of symmetries and constants of the motion. In $F = 2$, symmetries are the same but the number $(2F + 1)^2 = 25$ is much larger from the outset.

From the perspective of dynamic systems, using observables instead of spinor components may be seen as a change of variables, and it should be possible to fully describe the system (7.1) in terms of six suitably chosen observables instead of the real and imaginary parts of three spinor components $\zeta_n = \zeta_n^l + i\zeta_n^{\prime\prime}$, $n = 0, 1, 2$. Naturally, one chooses known constants of the motion as new variables. These are the “number of particles” N and the energy E ,

$$\begin{aligned} N &= 2(\zeta_2^{\prime 2} + \zeta_2^{\prime\prime 2} + \zeta_1^{\prime 2} + \zeta_1^{\prime\prime 2}) + \zeta_0^{\prime 2} + \zeta_0^{\prime\prime 2} \\ E &= 2g_1 \langle n \rangle \left[2(\zeta_2^l \zeta_1^l + \zeta_2^{\prime\prime} \zeta_1^{\prime\prime}) + \sqrt{6}(\zeta_1^l \zeta_0^l + \zeta_1^{\prime\prime} \zeta_0^{\prime\prime}) \right]^2 - q [8(\zeta_2^{\prime 2} + \zeta_2^{\prime\prime 2}) + 2(\zeta_1^{\prime 2} + \zeta_1^{\prime\prime 2})]. \end{aligned} \quad (7.8)$$

⁵In order to span the space of complex hermitian $N \times N$ matrices using only real coefficients, N^2 basis matrices are needed – N real diagonal matrices, $N(N - 1)/2$ real off-diagonal matrices and another $N(N - 1)/2$ imaginary off-diagonal matrices. In our case, $N = 2F + 1$. Compare Section 2.2.3, where similar arguments are applied to the density matrix. In this special case, the number of basis matrices is reduced by one due to the conservation of the trace of the density matrix.

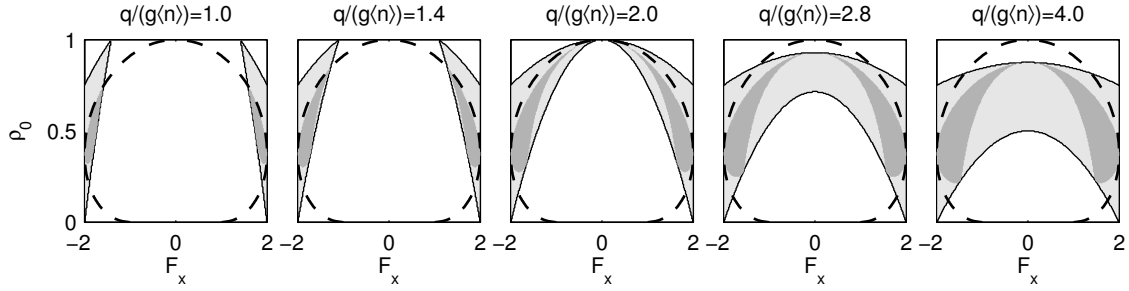


Figure 7.6: Valid regions in (ρ_0, F_x) phase space. The dashed line marks the limit imposed by the natural relationship of F_x and ρ_0 , while the lightly shaded areas indicate energy- and parameter-dependent restrictions in the case of $E = E(\zeta_{\pi/2})$ that apply to the full trajectory. However, only within the dark shaded areas (7.8) and (7.9) can be inverted to give a valid state on the surface of section $F_{zy} = 0$.

Additionally, we choose $F_x \equiv \langle \mathbf{F}_x \rangle$ and $F_{zy} \equiv \langle \mathbf{F}_z \mathbf{F}_y + \mathbf{F}_y \mathbf{F}_z \rangle / 2$ due to their intuitive meaning as the transverse component of the spin vector and its time derivative,

$$\begin{aligned} F_x &= 4(\zeta_2' \zeta_1' + \zeta_2'' \zeta_1'') + 2\sqrt{6}(\zeta_0' \zeta_1' + \zeta_0'' \zeta_1'') \\ F_{zy} &= 6(\zeta_2' \zeta_1'' - \zeta_2'' \zeta_1') + \sqrt{6}(\zeta_0'' \zeta_1' - \zeta_0' \zeta_1''). \end{aligned} \quad (7.9)$$

Finally, for compatibility with previous results, we take the population and phase of the $m_F = 0$ component,

$$\begin{aligned} \rho_0 &= \zeta_0'^2 + \zeta_0''^2 \\ \tan \theta_0 &= \frac{\zeta_0''}{\zeta_0'}. \end{aligned} \quad (7.10)$$

θ_0 is the only quantity influenced by the choice of the global phase, and consequently is arbitrary. Ignoring θ_0 amounts to projecting the phase space onto a plane of constant θ_0 , and the freedom of choice of the global phase ensures that the physically meaningful dynamics is fully captured in the projection.

It remains to be proven that this choice of quantities indeed constitutes a change of variables, i.e. that the relation between these quantities and the components of the spinor is (locally) invertible. First, the populations ρ_1 and ρ_2 can be calculated explicitly from (7.8). With $E_{QZ} = g_1 \langle n \rangle \langle \mathbf{F}_x \rangle^2 - E \geq 0$,

$$\begin{aligned} \rho_2 &= \frac{1}{6} (E_{QZ} - (N - \rho_0)) \\ \rho_1 &= \frac{2}{3} (N - \rho_0) - \frac{1}{6} E_{QZ}. \end{aligned} \quad (7.11)$$

The remaining phases are determined by (7.9)

$$\begin{aligned} F_x &= 4\sqrt{\rho_2 \rho_1} \cos(\theta_1 - \theta_2) + 2\sqrt{6}\sqrt{\rho_1 \rho_0} \cos(\theta_0 - \theta_1) \\ F_{zy} &= 6\sqrt{\rho_2 \rho_1} \sin(\theta_1 - \theta_2) + \sqrt{6}\sqrt{\rho_1 \rho_0} \sin(\theta_0 - \theta_1), \end{aligned} \quad (7.12)$$

which can be numerically solved for the phase differences $\theta_0 - \theta_1$ and $\theta_1 - \theta_2$. The global phase is irrelevant, but defined by $\tan \theta_0$ for formal completeness. From the populations and phases, the complex spinor components $\zeta_m = \sqrt{\rho_m} e^{i\theta_m}$ can be recovered.

Of the six variables $(N, E, F_x, F_{zy}, \rho_0, \theta_0)$, only F_x , F_{zy} and ρ_0 are dynamically relevant. In the following, we will further eliminate F_{zy} by defining a Poincaré surface of section $F_{zy} = 0$. For the remaining free variables, generally not the full domain $(\rho_0, F_x) \in [0 \dots 1] \times [-2 \dots 2]$ is physically accessible. Apart from the implicit relationship of $F_x = \langle \mathbf{F}_x \rangle$ and ρ_0 (7.12), the most important restrictions result from $0 \leq \langle \mathbf{F}_z^2 \rangle \leq 4$ and $0 \leq \rho_{1,2} \leq 1$. For the specific energy shell of the fully transversely magnetized state, $E = 2g_1 \langle n \rangle - q$ with $N = 1$, and $g_1 \langle n \rangle, q > 0$ we have the following non-trivial constraints:

$$F_x^2 \geq 4 - \frac{2q}{g_1 \langle n \rangle} \quad \rho_0 \geq \frac{g_1 \langle n \rangle}{2q} (4 - F_x^2) \quad \rho_0 \leq \frac{1}{4} \left(3 + \frac{g_1 \langle n \rangle}{2q} (4 - F_x^2) \right) \quad (7.13)$$

The two conditions on ρ_0 coincide only in the limiting case $|F_x| = \sqrt{4 - \frac{2q}{g_1 \langle n \rangle}}$ where $\rho_0 = 1$ necessarily. For $q/(g_1 \langle n \rangle) > 2$, the conditions remain valid but do not constrain F_x any more. Fig. 7.6 illustrates the domains of validity for the different cases. It must be stressed that these domains correspond to *projections* of the full phase space of triplets (ρ_0, F_x, F_{zy}) (neglecting $\tan \theta_0$) onto a $F_{zy} = \text{const}$ surface. The projection of the *full* trajectory must lie within the indicated limits.

On the Poincaré surface of section $F_{zy} = 0$, even further restrictions apply as indicated in Fig. 7.6. The final criterion is simultaneous solvability of (7.9), i.e. whether it is possible to find, for given populations ρ_i , phases such that actually $\langle \mathbf{F}_x \rangle = F_x$ and $\frac{1}{2} \langle \mathbf{F}_y \mathbf{F}_z + \mathbf{F}_z \mathbf{F}_y \rangle = 0$. The shaded areas in Fig. 7.6 have been calculated numerically by trying to invert (7.9) on a dense grid in (ρ_0, F_x) phase space.

Note the different meaning of allowed domains on the Poincaré section, as opposed to a projection of the full phase space. In the former case, a trajectory may “jump” from one domain to another, even if they are not connected. However, the projection of the trajectory between intersections with the Poincaré surface is still subject to conditions as explained previously. Thus for $q/g_1 \langle n \rangle < 2$, F_x can never change sign, but for $q/g_1 \langle n \rangle > 2$ it does even though the dark shaded areas in Fig. 7.6 may not actually meet.

Having found suitable variables and a Poincaré surface of section, we now turn to applying this technique to gain a deeper knowledge of the dynamical structure of our system. First of all we note that the Poincaré surface of section $F_{zy} = 0$ corresponds to points of the trajectory where F_x is minimal or maximal (turning points). (F_x, ρ) phase space is symmetric under $F_x \rightarrow -F_x$, i.e. for any trajectory $(F_x(t), \rho(t))$ there is a mirror image $(-F_x(t), \rho(t))$. Minima and maxima of F_x are reversed in the mirror image. Thus, instead of plotting a Poincaré section of e.g. minima (zero crossings of F_{zy} with positive slope) in the full range $F_x = -2 \dots 2$, it is equivalent to plot only half the range but using both minima and maxima. Also, $\langle \mathbf{F}_z^2 \rangle = (g_1 \langle n \rangle \langle \mathbf{F}_x \rangle^2 / 2 - E) / q$ may be used instead of F_x when the sign is not important. In the following, we apply both ways of plotting the Poincaré section to numerical solutions of (7.1) in a series of parameter values q , while $g_1 \langle n \rangle = 1$ without loss of generality. We look at the energy shell $E = 2g_1 \langle n \rangle - q$, which is the energy of the fully transversely magnetized state. In this case, the relation of $\langle \mathbf{F}_z^2 \rangle$ and $\langle \mathbf{F}_x \rangle$ is

$$F_{qz} \equiv \langle \mathbf{F}_z^2 \rangle = 1 - \frac{2g_1 \langle n \rangle}{q} \left(1 - \frac{\langle \mathbf{F}_x \rangle^2}{4} \right), \quad 0 \leq F_{qz} \leq 1. \quad (7.14)$$

Figures 7.8-7.14 are the result of numerical simulations, in which trajectories starting from random initial conditions (up to 300) have been followed and the intersections with the surface of section $F_{zy} = 0$ recorded (typically 1000). The trajectories are calculated in

complex variables using (7.1), and the new variables F_x and ρ_0 are extracted at the time of plotting. Every dot in Fig. 7.8-7.14 corresponds to a single intersection of a trajectory with the surface of section, and is colored (Fig. 7.8 and 7.9) or shaded (Fig. 7.10-7.14) according to the Lyapunov exponent λ of the *whole* trajectory, black corresponding to $\lambda = 0$ and lighter colors or shades of grey to a larger Lyapunov exponent. White areas have not been visited by any trajectory. The stretched state, which has been used as the initial condition in the preceding Section 7.2 and in particular in Fig. 7.4, is marked at $F_x = 2, \rho_0 = 0.375$ or $F_{qz} = 1, \rho_0 = 0.375$. Additionally, in Fig. 7.10-7.14 (shaded), the intersection points for a set of trajectories from a small neighborhood of the fully transversely magnetized state (“neighborhood trajectories”) are indicated by thick dots, colored according to the direction of sign change of F_{zy} , i.e. whether they cross the drawing plane, corresponding to the surface of section, from back to front or vice-versa. The fully transversely magnetized state itself indeed does belong to the surface of section as a point of maximal F_x . Fig. 7.7 illustrates the different coloring schemes.

Figures 7.8-7.10 provide an overview of the crossover regime. Compare the images to the corresponding vertical slices of Fig. 7.4, and note how the behavior of the neighborhood trajectories is reflected in the histograms of amplitude and period of trajectories starting exactly from the stretched state.

At the low q end, trajectories are restricted to positive F_x and have a zero or very small Lyapunov exponent. Phase space is filled with regular structures resembling filo pastry. The trajectories neighboring the stretched state trace out a well-defined path along the shells. This is typical of regular motion.

At $q = 2$, the two lobes of admissible states, characterized by positive and negative F_x , just meet in $F_x = 0$, and some trajectories are able to squeeze through and change sign. At the same time, the Lyapunov exponent of a large number of trajectories becomes significantly positive. Neighborhood trajectories start to spread in an irregular way, reflecting the sensitivity to disturbance that is indicated by a positive Lyapunov exponent. For $q > 2$, intersections of positive and negative slope mingle as a result of F_x changing sign.

Also at $q = 2$, a particularly prominent example of phase space structure can be seen: a set of closed trajectories orbiting around a *fixed point* ($F_{qz} \approx 0.6662, F_x \approx 1.632, \rho_0 \approx 0.5806$) on the surface of section, corresponding to a *periodic cycle* of the full trajectory. Also at $q = 2.90$ and $q = 3.3$, the stretched state must be close to such a fixed point, since all trajectories from the neighborhood remain close to each other, trapped in or near a periodic cycle.

At intermediate values around $q \approx 2.5$, chaotic and regular motion coexist in phase space. The neighborhood of the stretched state obviously belongs to the chaotic part. Although the chaotic trajectories look as if they filled a whole area in phase space, this is not exactly the case, since in a conservative system chaotic and regular trajectories are generally mixed in a highly complicated way [138, 139].

Figure 7.11 attempts to shed light on the yet unexplained feature in the histograms (Fig. 7.4) at $q \approx 1.72$. There is no sign of chaos anywhere in phase space at this value of the parameter. There seems to be a geometrical change, however, that leads

to a sudden disruption of the continuous line of negative-slope intersection points (turning points of maximal F_x or F_{qz}) of the neighborhood, while at the same time connecting two previously separate branches of positive-slope points (minimal F_x or F_{sq}). This results in a dramatic decrease of the possible spread in vertical separation that a pair of consecutive extrema can have.

Figures 7.12-7.14 are a close-up of one of the “islands of order” that appear in the histograms (Fig. 7.4), e.g. at $q = 2.81$. Looking at the whole phase space (Fig. 7.12), we notice that its overall structure does not change over the narrow range of parameters chosen here. There is a large part densely filled with chaotic trajectories, changing shape only very slightly. However, the behavior of neighborhood trajectories varies dramatically with q , switching from chaotic motion to near-periodic cycles (compare Fig. 7.4). The reason becomes obvious in a close-up of the neighborhood of the fully transversely magnetized state: trajectories become trapped when the fully transversely magnetized state happens to be close to a *periodic cycle*, which passes by as q varies. At $q = 2.850$, the fully transversely magnetized state nearly coincides with the intersection of the periodic cycle and the surface of section.⁶

The fully transversely magnetized state is an intersection point of negative slope since it has maximal $F_x = 2$ – exactly the same behavior is seen for the corresponding point of positive slope. Interestingly, part of the structure surrounding the periodic orbit seems to extend across the border of the accessible area. This shows up in the circular path traced by points of negative slope, half of which is at the high- F_x boundary and half of it at the low- F_x boundary of the permitted area. This points to a more complicated topology of the accessible phase space than can be caught in this projective visualization. There are points at the low- F_x and high- F_x boundary that must be dynamically equivalent.

The trapping of trajectories near a periodic cycle repeats at $q = 2.89$, where the fully transversely magnetized state happens to be close to a secondary periodic cycle, belonging to the same structure, and forming at slightly lower q . This is beautifully seen in the distribution of positive-slope points.

7.4 Discussion and outlook

The results of the preceding sections rely on the numerical analysis of a special case of an approximate description of the dynamics of spinor Bose-Einstein condensates. The question may be raised, how realistic these results in fact are, and whether they are observable in experiment.

First of all, we note that – in order to experimentally carry out the kind of analysis demonstrated here – it is necessary to follow trajectories for at least about 100 oscillations. At an optimistic period of oscillation of $2\pi/(g_1\langle n \rangle) \approx 50$ ms, this corresponds to 5 s of coherent evolution, which is hard to achieve in the presence of thermalization and losses. Also, non-destructive spin-sensitive detection [101] would be necessary to track the evolution of individual condensates, as extreme sensitivity to errors in the initial state is

⁶Note that this does *not* mean the fully transversely magnetized state is stationary at $q = 2.85$ – ρ_0 oscillates at high amplitude over the whole crossover region. However, at or near this particular q the oscillation becomes *periodic*, returning to exactly the same state at regular intervals.

characteristic of chaotic system and forbids the usual way of tracking time evolution by repeated destructive observation of identically prepared samples.

Second, our analysis relies on the single-mode approximation, and we have seen in Section 5.6 that this breaks down in the interaction and crossover regime. In fact, Chapter 6 deals with the experimental observation of spontaneous formation of spatial structure, and identifies a *dynamical instability* as the most likely reason. The chaotic dynamics that is the subject of the present chapter, however, is caused by the linear instability of the *homogeneous mode*. A spinor condensate may be stable with regard to homogeneous perturbations, or may have a zero Lyapunov exponent in the language of the preceding sections, but may still be unstable with respect to a spatially modulated disturbance. In order to experimentally observe homogeneous, or SMA, dynamics only, the condensate has to be much smaller than the spin healing length (typically $\xi_s \approx 2 - 3 \mu\text{m}$ at realistic densities). This could be achieved in a one-dimensional, deep *optical lattice*, which amounts to having a chain of closely-spaced (of the order of half the laser wavelength) individual condensates (see Chapter 8 for more details on the prospects of optical lattices).

Third, our analysis also ignores a possible instability with respect to homogeneous, but *asymmetric* perturbations. Although the total magnetization $F_z = 0$ is conserved, redistribution of population between $m_F = \pm 1$ and $m_F = \pm 2$ in an asymmetric way is in principle possible as long as $2\rho_{+2} + \rho_{+1} = 2\rho_{-2} + \rho_{-1}$. This has never been observed experimentally, though. A theoretical analysis of Lyapunov exponents for this generalized type of disturbance is possible from within the symmetric subspace – only the *tangential space* of a trajectory has to be extended. However, this analysis has not been carried out yet.

Last, but not least, what we observe is *not* quantum chaos in the conventional sense⁷ [141]. Rather, it is classical chaos in the dynamics of a mean-field approximation to many-body quantum mechanics, leading to nonlinear equations of motion. Nevertheless, one might ask the question whether and how this is reflected in true quantum many-body properties such as correlations.

In any case, the results presented in this chapter are doubtlessly a beautiful example of nonlinear chaotic dynamics, and the merging of techniques from both nonlinear quantum mechanics and the theory of dynamics systems has proven fruitful and fascinating. Experimental observation will be challenging, but is not out of reach of current experimental possibilities.

⁷Chaotic systems are governed by *nonlinear* equations of motion, such as they may arise in classical mechanics. Classical mechanics, on the other hand, is just a limiting case of quantum mechanics, obtained by the “correspondence principle”. Quantum mechanical evolution obeys the *linear* Schrödinger equation, which does not feature chaotic solutions. The fundamental question underlying *Quantum Chaos* is how chaotic behaviour of a nonlinear classical system is reflected in the properties of the corresponding quantum mechanical system.

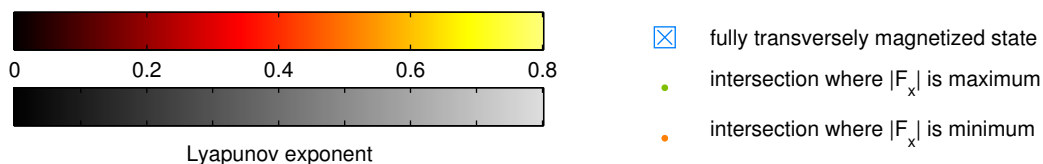


Figure 7.7: Coloring schemes and markers used in Fig. 7.8-7.14, see text as well.

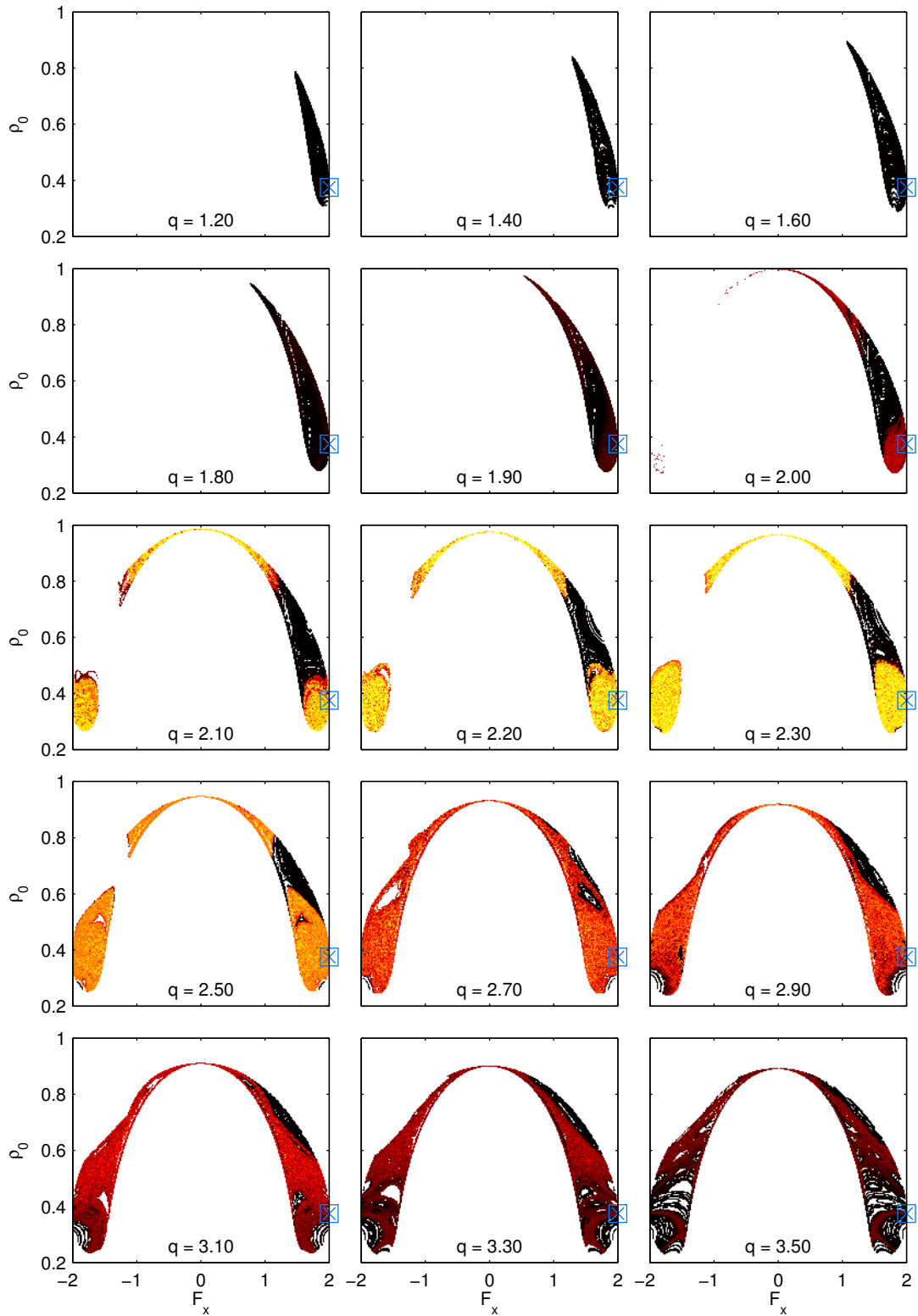


Figure 7.8: Dynamics in the Poincaré section F_x vs. ρ_0 . Overview of the whole crossover regime ($g_1 = 1$). Note how from $q = 2$ onwards, trajectories cross the border of $F_x = 0$, changing sign (initial states all have $F_x \geq 0$). At about the same time, regions of positive Lyapunov exponent emerge.

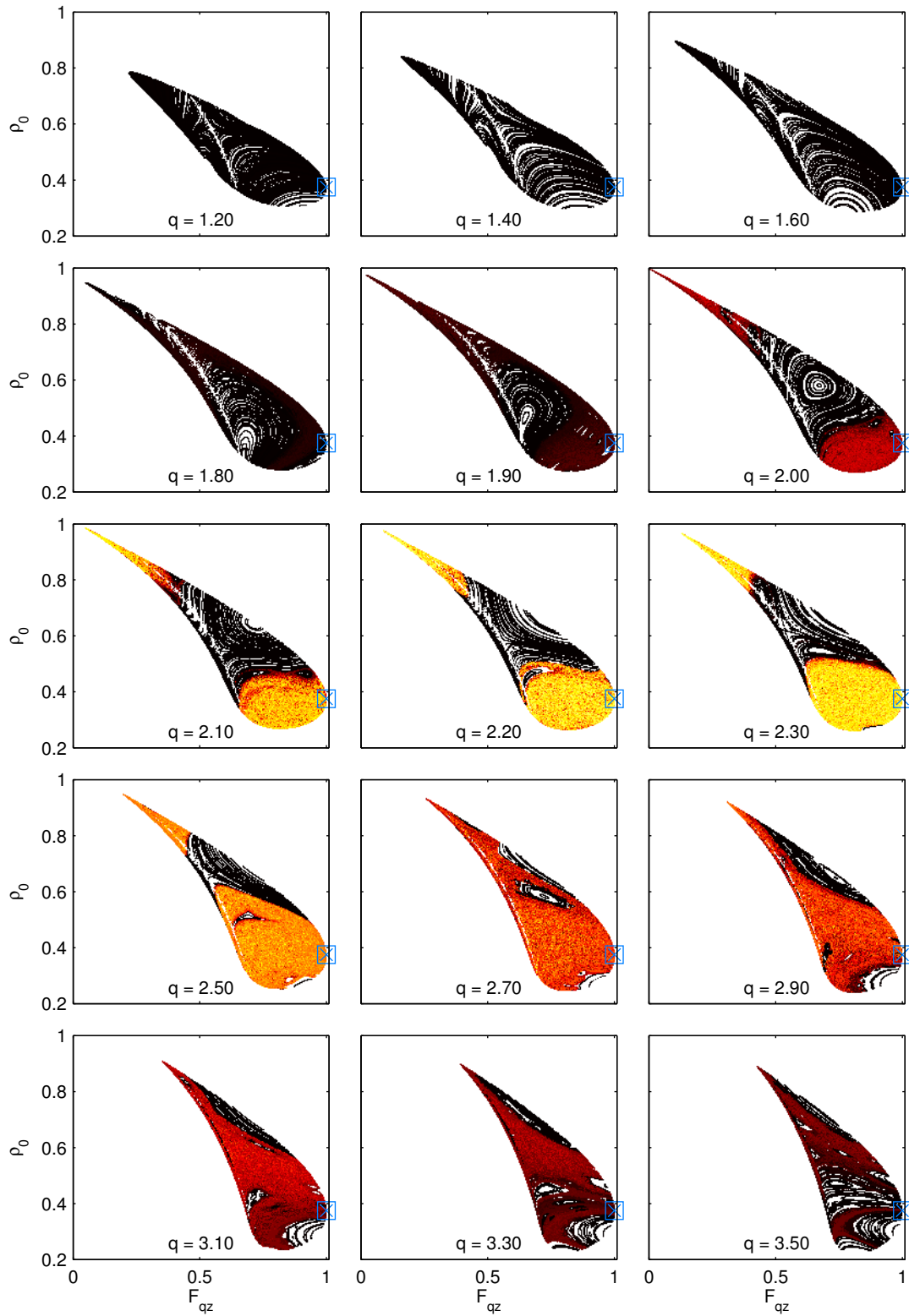


Figure 7.9: Dynamics in the Poincaré section $\langle F_z^2 \rangle$ vs. ρ_0 . Overview of the whole crossover region. Compare the different ways of portraying phase space as either (F_x, ρ_0) or $(F_{sq} \equiv \langle \mathbf{F}_z^2 \rangle, \rho_0)$. Note the prominent circular structure at $q = 2$, connected to a fixed point of the Poincaré plane.

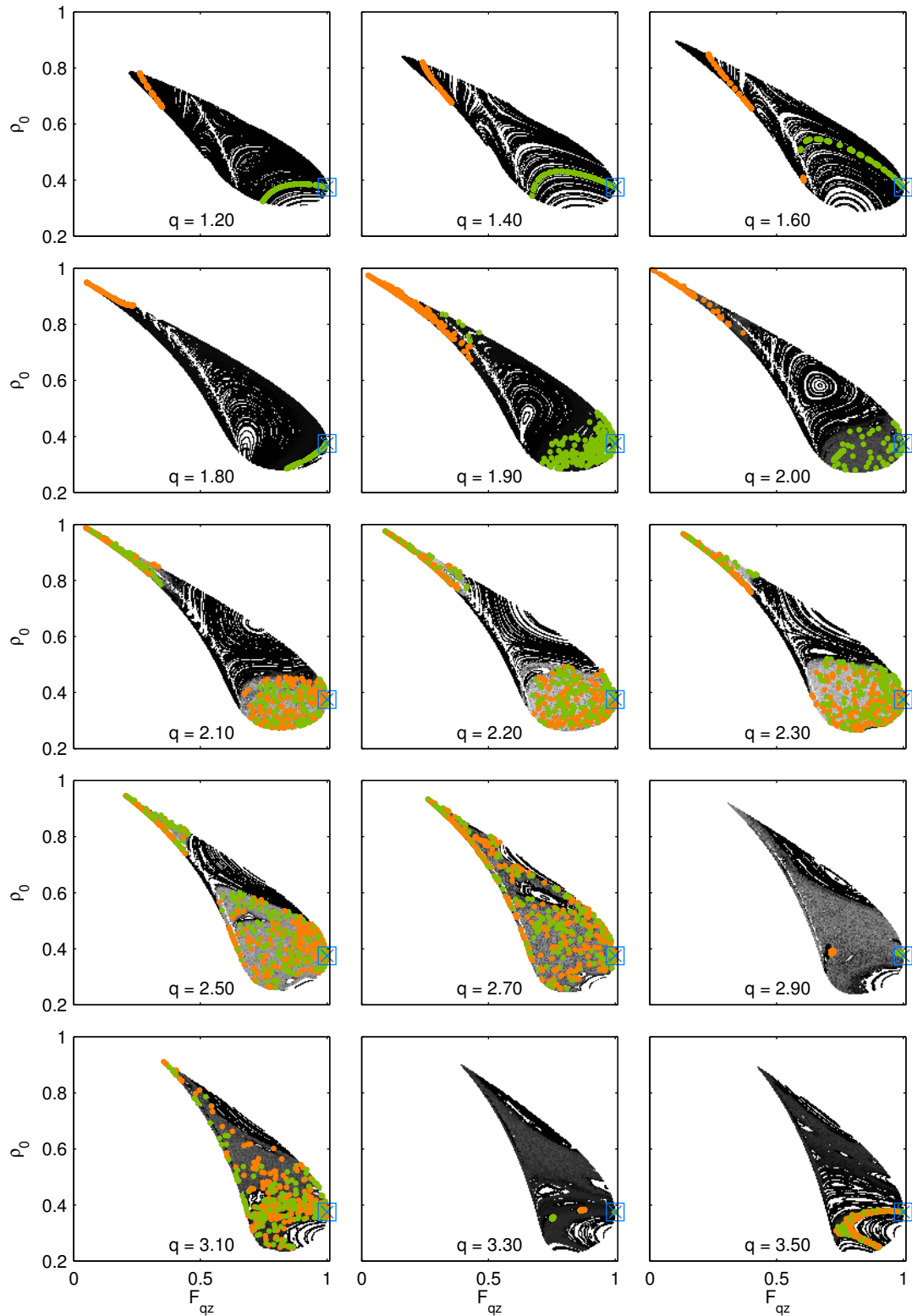


Figure 7.10: Dynamics in the Poincaré section (overview). Regions visited by trajectories starting near $\zeta_{\pi/2}$, indicated by the intersection points (zero crossings of F_{zy} of positive or negative slope). Note how the neighborhood of the fully transversely magnetized state is caught in a periodic cycle at $q = 2.90$.

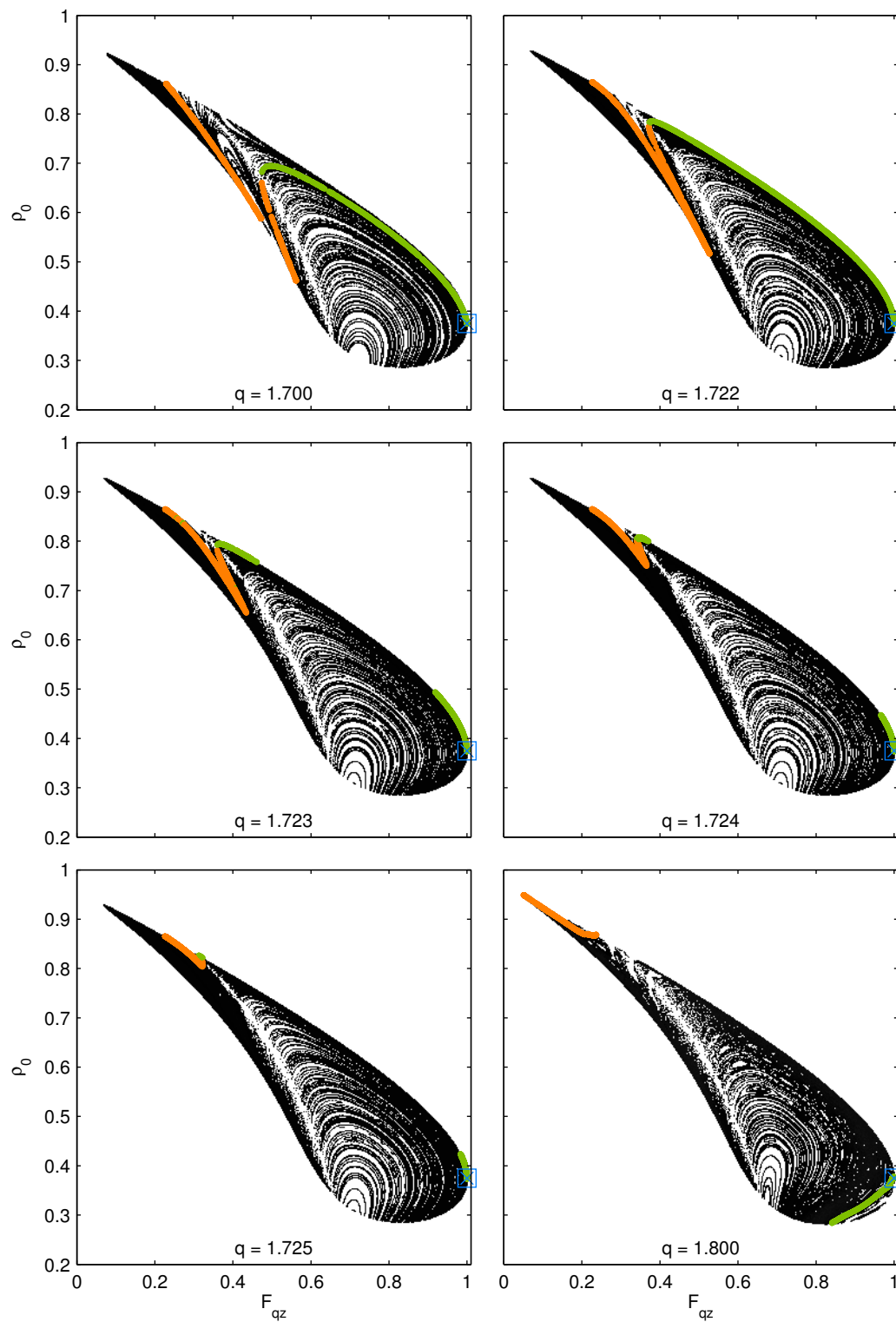


Figure 7.11: Dynamics in the Poincaré section: detail at $q = 1.72$. Note how at $q = 1.722$, the topology of the paths traced by intersection points changes.

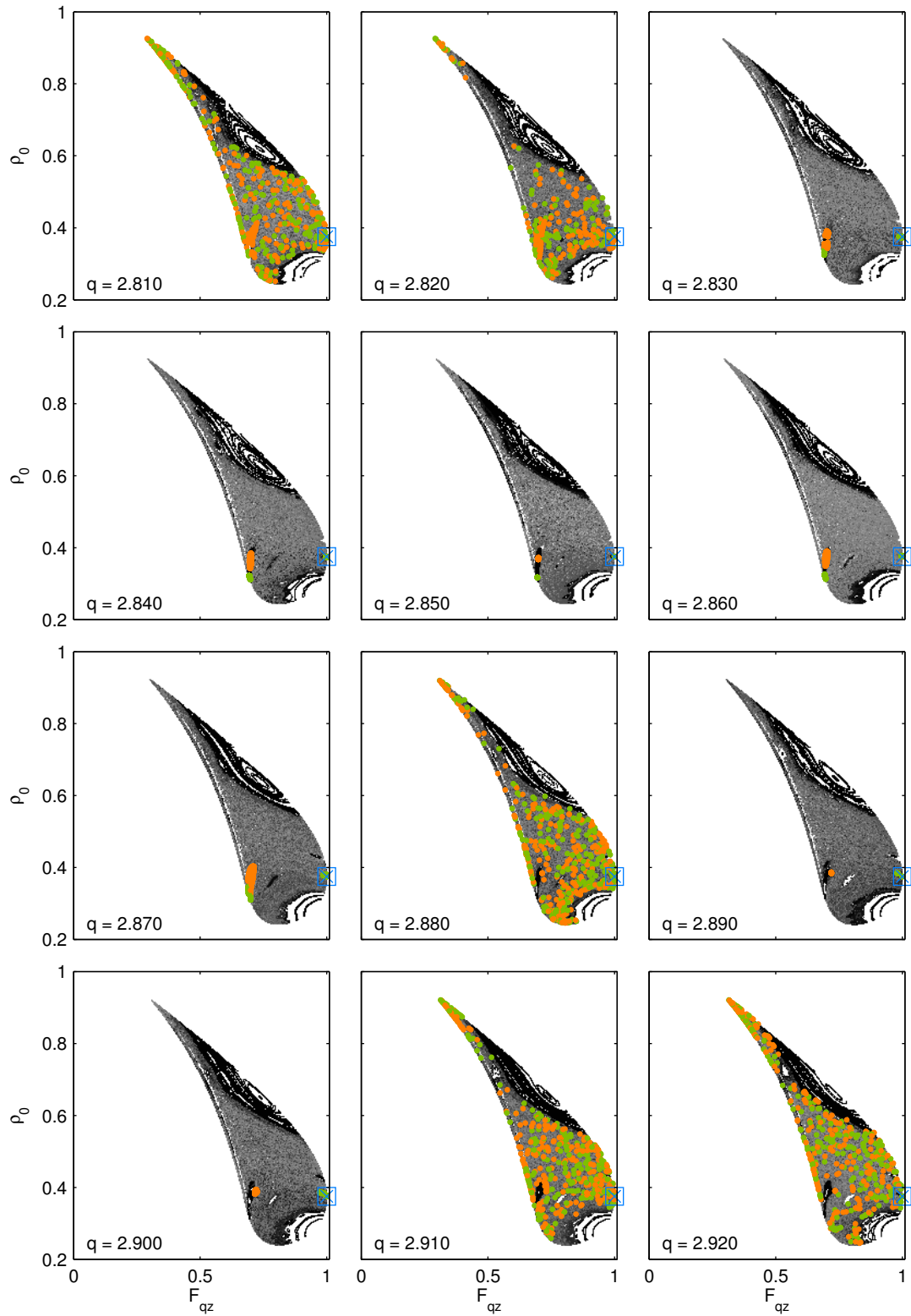


Figure 7.12: Dynamics in the Poincaré section: detail at $q = 2.81$. Overview of the whole phase space. Note once more how the neighborhood trajectories are caught by periodic cycles at q values corresponding to “islands of order” in the histograms of Fig. 7.4.

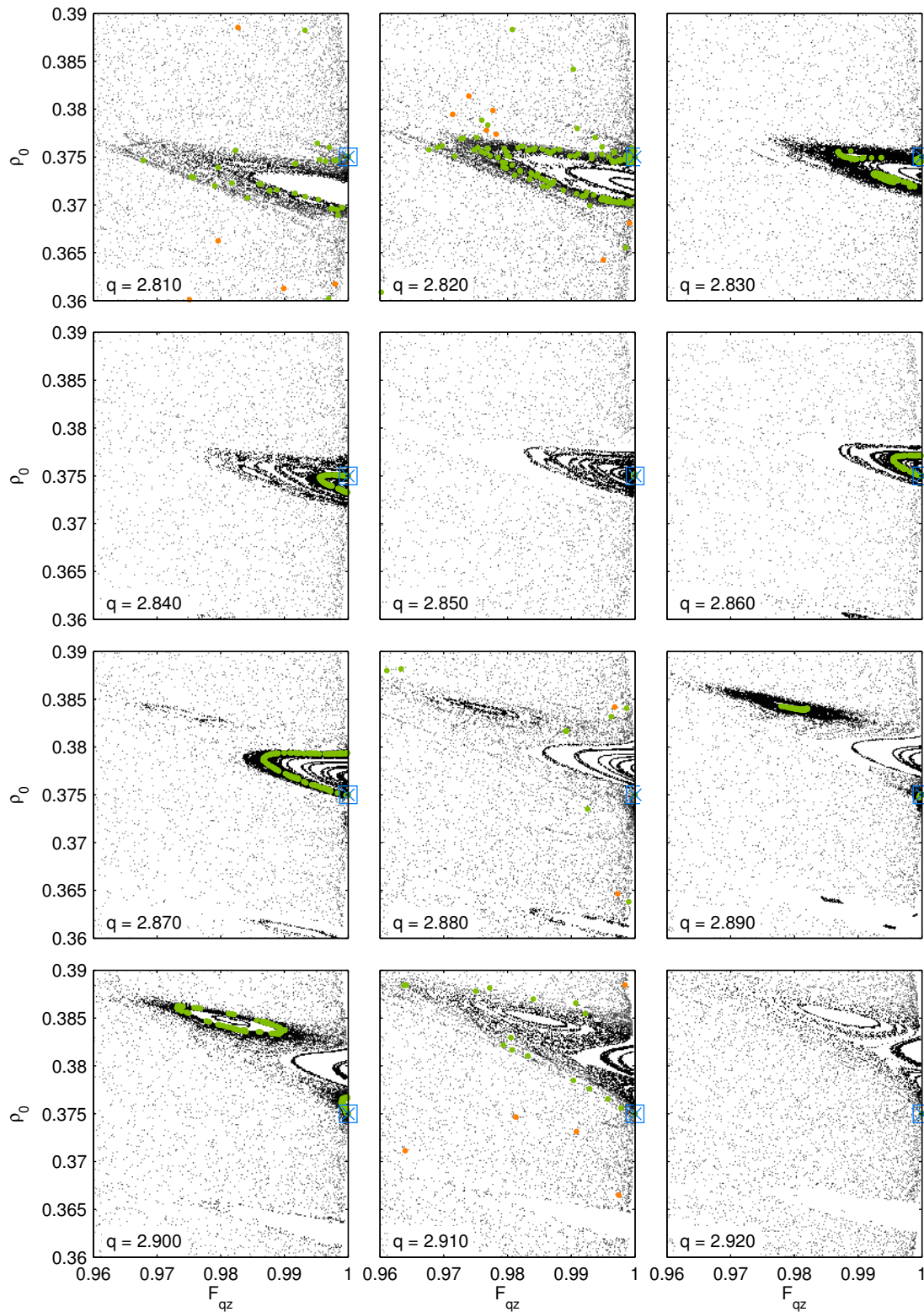


Figure 7.13: Dynamics in the Poincaré section: detail at $q = 2.81$. Close-up of the neighborhood of the fully transversely magnetized state. Note the periodic orbit structure passing the stretched state as a function of q .

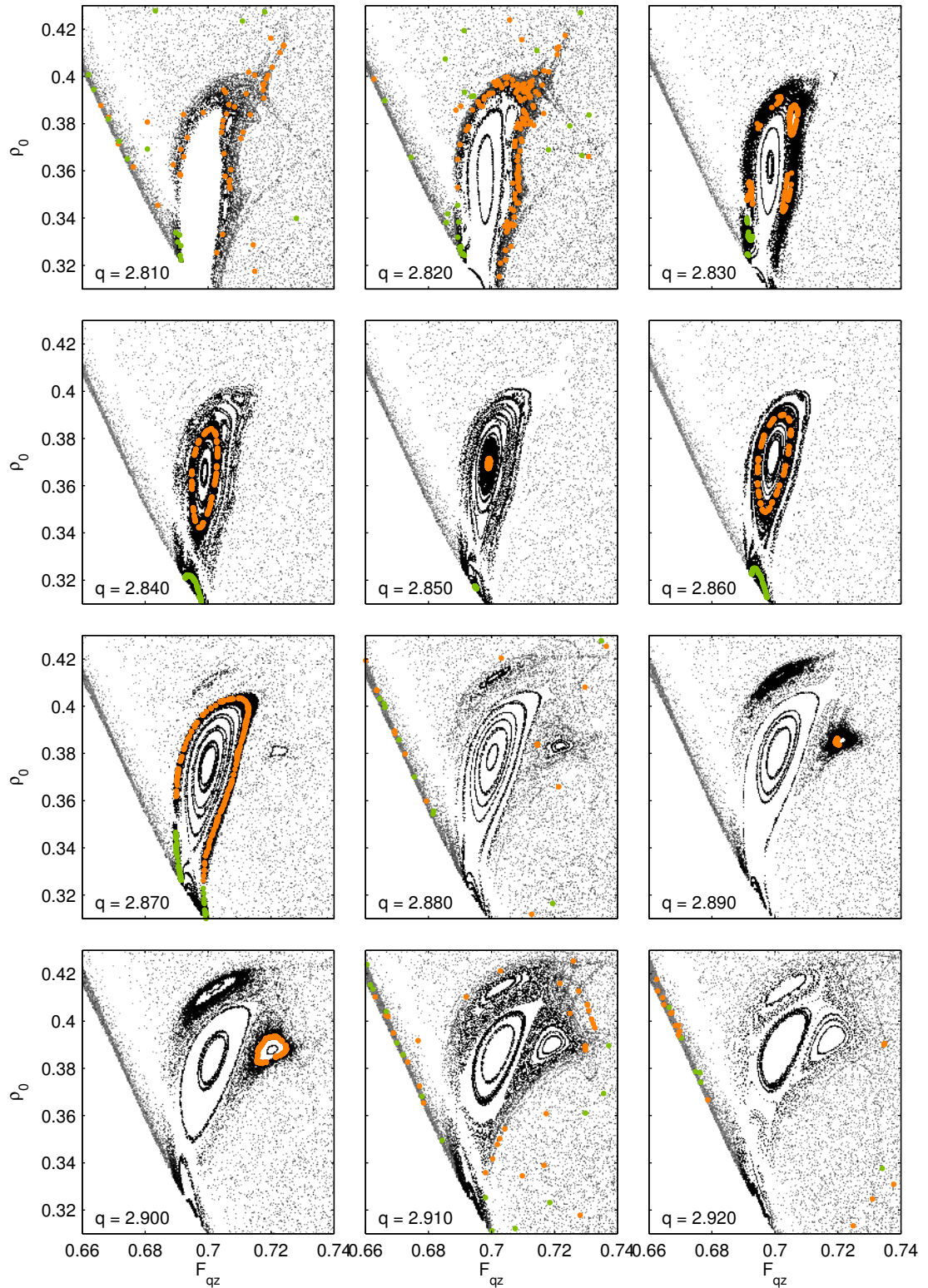


Figure 7.14: Dynamics in the Poincaré section: detail at $q = 2.81$. Close-up of the region where the periodic orbit starting from the stretched state intersects the Poincaré plane a second time with opposite slope.

Chapter 8

Summary and outlook

The present work is an important cornerstone of our current understanding of the physics of spinor Bose-Einstein condensates. In conjunction with recent experimental work in the group of Chapman [50, 37] and theoretical work by You [44, 75, 142, 73], Ueda [76, 90] and co-workers, it presents a consistent picture and a deep understanding of the topic of *single-mode coherent spinor dynamics*.

A recurring theme of this thesis are the *fully transversely magnetized states*, which as initial states of spinor dynamics have proven extremely enlightening. Coherent dynamics starting from a fully transversely magnetized state has shown the existence of a generic resonance phenomenon in spinor dynamics, irrespective of the ground state of the system. This resonance is analogous to *nonlinear phase-matching* in optical four-wave mixing, where the spin-dependent interaction provides the nonlinearity and the quadratic Zeeman effect plays the role of a linear dispersion.

Single-mode coherent spinor dynamics is constrained by *thermalization* and *spatial structure formation*. As ever so often in physics, the close inspection of these at first sight detrimental effects uncovers a whole realm of fascinating new phenomena.

Bose-Einstein condensates with their unique combination of a macroscopically populated quantum state and a finite-temperature environment provide an ideal testing ground for the paradigmatic situation of quantum system coupled to a thermal reservoir. Spinor BEC with their limited number of degrees of freedom simplify the control and analysis of such experiments. The processes observed and characterized in this thesis provide a deeper understanding of *thermalization in Bose-Einstein condensates* and connect to the fundamental questions of *condensate formation* [133, 134, 135] on the one hand, and *decoherence* [28] on the other hand.

Spatial structure formation is a classical field of nonlinear dynamics, and the results obtained with spinor BEC in this thesis – marvelous images of spin domain patterns like beads – merely touch its surface, leaving plenty of unknown terrain to discover. Spontaneous structure formation as a way of symmetry breaking also plays a prominent role in magnetism, e.g. in the formation of ferromagnetic domains. Previous results in spinor BEC were also limited to the ferromagnetic case [41], where the analogy is obvious. In this work, spontaneous domain formation is observed for the first time in an *antiferromagnetic quantum gas*, raising questions on its origin that could only be answered in part within the scope of this thesis.

While *inherent* spatial structure formation is a very promising route to follow, the future of spinor BEC experiments may lie in *external* spatial modulation, in the form of either *periodic potentials* or *tailored wave functions*.

Tailored wave functions of BEC in a conventional trap have been used in the past to generate *dark solitons* [122, 123] by imprinting a local phase-jump of π on the wave function. Spinor BEC on the one hand greatly increase the possibilities for manipulation of the wave function, and on the other hand possess several new types of topological defects [143, 144, 145, 46, 47, 146]. A particularly intriguing defect would be the *magnetic soliton*, consisting of a dark soliton or “hole” in one spin component, “filled” with another component. Solitons rely on the balance of the kinetic and the interaction energy associated with a local change of the wave function. Since the spin-dependent interaction is just a small fraction of the total interaction, filled solitons are expected to be larger (of the order of the spin healing length) and also longer-lived than dark ones.

In the course of this work, a Raman laser system suitable for the local manipulation of a spinor wave function has been set up. Using a *spatial light modulator*, which is currently being installed in our experiment, it will become possible to imprint arbitrary population and phase changes on ^{87}Rb spinor BEC. Besides producing single magnetic solitons, it will also be possible to study the interaction of several such excitations, as well as possibly other topological defects, depending on the dimensionality of the BEC.

Periodic potentials can be realized with standing light waves (“optical lattice”) acting as small-scale dipole traps [147, 148]. Ultracold quantum gases, be they bosonic or fermionic, in such a “crystal of light” form a model system of solid state physics not suffering from crystal defects and other complications present in real solids. The scientific potential of this technique is reflected by a rapidly growing number of experiments using it, as well as by a plethora of theoretical proposals. First experiments studying spinor gases in optical lattices have been performed in the group of Bloch [43, 78], but this rich and fascinating field remains largely unexplored to date.

In our group, a 3D optical lattice featuring *hexagonal symmetry* has been set up for the first time, opening new perspectives on spinor BEC as a quantum simulator of solid state magnetism. For example, a phenomenon thought to occur on a triangular grid is *spin frustration* [149]. On a square lattice, spins with anti-ferromagnetic interactions arrange their orientation in a staggered way, such that each pair of next neighbours is anti-parallel. On a triangular lattice, this is no longer possible, since for any pair of anti-parallel next neighbours, there is a third next-neighbouring site whose orientation is undefined.

The field of *spinor Bose-Einstein condensates* is still busy. Many fascinating ideas are being pursued and new proposals put forth, ranging from potential applications (e.g. magnetometry [150]) to fundamental aspects (e.g. exotic topological defects [146]). The greatly improved understanding of the *bulk* properties of spinor BEC, to which the work at hand has significantly contributed, provides a basis for mastering the challenges of future research on spinor BEC.

Appendix A

Coordinate systems

For historical reasons, the usual horizontal quantization axis of our experiment is labeled “ x -axis” and the vertical axis “ z -axis”. This coordinate system is used for *positions* as well as for *magnetic fields*. An *axial field* is thus expressed as $\vec{B} = B\vec{e}_x$, and the *transverse gradients* of the axial field are $\frac{\partial B_x}{\partial z}$ and $\frac{\partial B_x}{\partial y}$.

In contrast, the usual convention in quantum mechanics is to call the axis of quantization “ z -axis”, and we stick to this convention when talking about *spin*. This means that the *axial* component of the *spin* \vec{F} , which is also called *magnetization*, is F_z .

Effectively, we use two coordinate systems in parallel, which are rotated with respect to each other (Fig. A.1). Note that this does *not* apply to Chapter 2 – only in chapters referring to experiments, these complications have to be taken into account.

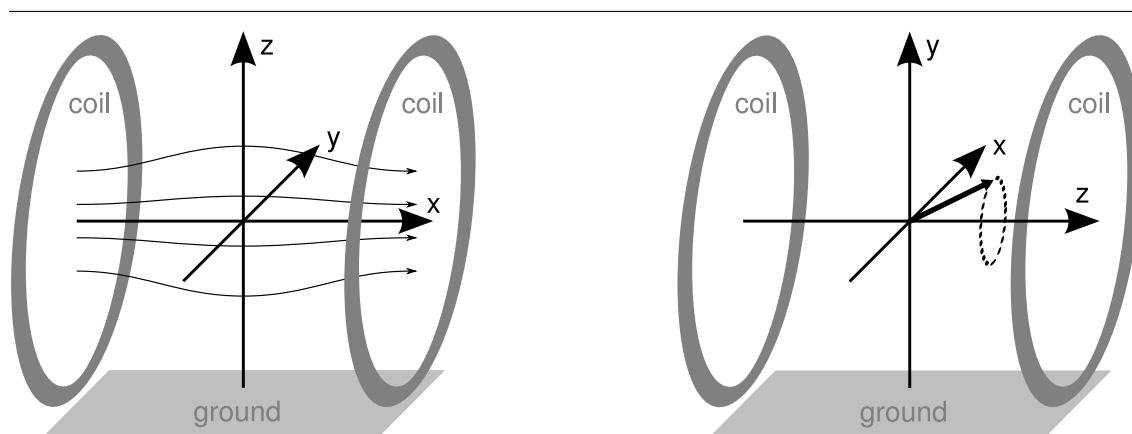


Figure A.1: Two different coordinate systems are used in parallel in this work. LEFT: Coordinate system for position and magnetic fields. RIGHT: Coordinate system for the spin.

Appendix B

Elementary nonlinear dynamics

Consider a *dynamical system* of N degrees of freedom, characterized by a *state vector* $\mathbf{z} = (z_1, \dots, z_N)$ in \mathbb{R}^N . Its time evolution is governed by a set of N coupled ordinary differential equations, or *equations of motion*,

$$\dot{\mathbf{z}} = \mathbf{F}(\mathbf{z}). \quad (\text{B.1})$$

A solution $\mathbf{z}(t)$ of this system is called a *trajectory*, with the *initial condition* $\mathbf{z}_0 \equiv \mathbf{z}(0)$. The set of all possible initial conditions constitutes the *phase space* of the system. Since any point of a trajectory can be seen as the initial condition of the trajectory from there on, the phase space defined this way in fact comprises *all states* the system can possibly occupy. Important special cases of trajectories are

- the *fixed point* or *stationary state* $\mathbf{z}(t) = \mathbf{z}_0 \forall t$, which is equivalent to the condition $\mathbf{F}(\mathbf{z}_0) = 0$, and
- the *periodic orbit* or *cycle*, a trajectory which returns to its initial condition in finite time, $\mathbf{z}(T) = \mathbf{z}(0)$, $0 < T < \infty$.

Now consider a particular solution $\mathbf{z}(t)$ and an infinitesimally small perturbation ζ on top of it. The equation of motion for the combined state is

$$\dot{\mathbf{z}} + \dot{\zeta} = \mathbf{F}(\mathbf{z} + \zeta). \quad (\text{B.2})$$

We obtain an equation of motion for the perturbation by *linearizing* \mathbf{F} in the neighborhood of the trajectory $\mathbf{z}(t)$,

$$\mathbf{F}(\mathbf{z} + \zeta) = \mathbf{F}(\mathbf{z}) + \partial\mathbf{F}(\mathbf{z})\zeta, \quad (\text{B.3})$$

where $\partial\mathbf{F}$ is the Jacobian matrix of \mathbf{F} and depends on \mathbf{z} . The equation of motion for the perturbation is linear, but time dependent via the trajectory $\mathbf{z}(t)$,

$$\dot{\zeta} = \partial\mathbf{F}(\mathbf{z}(t))\zeta. \quad (\text{B.4})$$

Solving this equation of motion, we obtain the time evolution operator $\mathbf{J}(z_0, t)$ that maps any initial perturbation ζ_0 to its value at time t ,

$$\zeta(t) = \mathbf{J}(z_0, t)\zeta_0. \quad (\text{B.5})$$

The *Lyapunov exponent* is a measure of how fast two infinitesimally close trajectories separate. Identifying one trajectory as $\mathbf{z}(t)$ and one as $\mathbf{z}(t) + \zeta(t)$, we define the Lyapunov exponent λ

$$\lambda = \lim_{t \rightarrow \infty} \frac{1}{t} \ln \frac{|\zeta(t)|}{|\zeta_0|}. \quad (\text{B.6})$$

Its value can be calculated from the linear approximation (following [151]),

$$\lambda = \lim_{t \rightarrow \infty} \frac{1}{t} \ln \frac{|\mathbf{J}(z_0, t)\zeta_0|}{|\zeta_0|} = \lim_{t \rightarrow \infty} \frac{1}{2t} \ln (\mathbf{n}^T \mathbf{J}^T \mathbf{J} \mathbf{n}), \quad (\text{B.7})$$

where in the latter variant the length of the initial perturbation has dropped out and the expression depends only on its orientation $\mathbf{n} = \zeta_0/|\zeta_0|$. The matrix $\mathbf{M} = \mathbf{J}^T \mathbf{J}$ is symmetric and positive, and therefore diagonalizable with real positive eigenvalues $\Lambda_1^2, \dots, \Lambda_N^2$. Choosing the respective eigenvectors as our initial orientation \mathbf{n} , we obtain a *spectrum of Lyapunov exponents*,

$$\lambda_i = \lim_{t \rightarrow \infty} \frac{1}{t} \ln \Lambda_i. \quad (\text{B.8})$$

Whether a trajectory is *stable* or not is determined by the *largest* Lyapunov exponent $\lambda_0 = \max\{\lambda_i\}$. If the orientation of an initial perturbation is not exactly perpendicular to the eigenvector \mathbf{u}_0 corresponding to λ_0 , i.e. if ζ_0 has a component in direction \mathbf{u}_0 , this component will grow exponentially at a rate larger than any other component of ζ_0 , and will thus dominate in (B.7). In other words, an arbitrary initial orientation (not perpendicular to \mathbf{u}_0) will be tilted over time towards the direction of the maximal growth rate.

The largest Lyapunov exponent can be numerically determined by solving the equations of motion (B.1) and (B.4) simultaneously for a set of perturbations of length $|\zeta| = 1$ and different initial orientations. Since the length $|\zeta|$ of the perturbation grows exponentially in time, it is necessary to *rescale* ζ to unity at regular intervals and record its logarithm. The sum of the logarithms, divided by the total time of evolution, is an approximation for the largest Lyapunov exponent. If the algorithm works as expected and produces a good approximation, the resulting Lyapunov exponent should be the same for all initial orientations (except for one, possibly).

Appendix C

Optical four-wave mixing

Following [84], we derive explicitly the coupled wave equations for the case of three optical modes and a third-order $\chi^{(3)}$ nonlinear susceptibility. We will see that this case is analogous the $F = 1$ spinor dynamics as described in Chapter 2. We further assume that all modes are collinear and linearly polarized in the same direction, with electric fields

$$\begin{aligned} E_j(\mathbf{r}, r) &= E(\omega_j)e^{-i\omega_j t} + E(-\omega_j)e^{i\omega_j t} \\ &= A_j(z)e^{i(k_j z - \omega_j t)} + \text{c.c.}, \end{aligned} \quad (\text{C.1})$$

where we have adopted the convention $E(-\omega_j) = E^*(\omega_j)$, and c.c. denotes the complex conjugate of the preceding expression. This way, $E_j(\mathbf{r}, t)$ is always real.

Each mode obeys a nonlinear wave equation

$$-\Delta E(\omega_n) - \frac{\omega_n^2}{c^2} \epsilon^{(1)}(\omega_n) E(\omega_n) = \frac{4\pi\omega_n^2}{c^2} P^{\text{NL}}(\omega_n), \quad (\text{C.2})$$

where $\sqrt{\epsilon^{(1)}}$ is the frequency-dependent linear index of refraction and

$$P^{\text{NL}}(\omega_n) = \sum_{\omega'_1, \omega'_2, \omega'_3} \delta(\omega_n, \omega'_1 + \omega'_2 + \omega'_3) \chi^{(3)} E(\omega'_1) E(\omega'_2) E(\omega'_3) \quad (\text{C.3})$$

is the polarization arising from third-order nonlinear processes.

Now assuming three modes $\omega_1, \omega_2, \omega_3$ with $2\omega_1 = \omega_2 + \omega_3$, we can write the nonlinear polarization explicitly, e.g. for the ω_1 mode,

$$\begin{aligned} P^{\text{NL}}(\omega_1) &= 3\chi^{(3)} E(\omega_1) E(-\omega_1) E(\omega_1) && \textit{self-PM} \\ &+ 6\chi^{(3)} [E(\omega_2) E(-\omega_2) + E(\omega_3) E(-\omega_3)] E(\omega_1) && \textit{cross-PM} \\ &+ 6\chi^{(3)} E(\omega_2) E(\omega_3) E(-\omega_1) && \textit{four-wave mixing} \end{aligned} \quad (\text{C.4})$$

or in terms of plane wave amplitudes

$$\begin{aligned} P^{\text{NL}}(\omega_1) &= 3\chi^{(3)} |A_1|^2 A_1 e^{ik_1 z} && \textit{self-PM} \\ &+ 6\chi^{(3)} [|A_2|^2 + |A_3|^2] A_1 e^{ik_1 z} && \textit{cross-PM} \\ &+ 6\chi^{(3)} A_2 A_3 A_1^* e^{i(k_2 + k_3 - k_1)z} && \textit{four-wave mixing} \end{aligned} \quad (\text{C.5})$$

Inserting $E(\omega_1)$ and $P^{\text{NL}}(\omega_1)$ into the wave equation we arrive at an equation for the amplitude A_1 ,

$$-\frac{\partial^2 A_1}{\partial z^2} - 2ik_1 \frac{\partial A_1}{\partial z} + k_1^2 A_1 = \left[\frac{\omega_1^2}{c^2} \epsilon^{(1)} + \frac{4\pi\omega_1^2}{c^2} \chi^{(3)} (3|A_1|^2 + 6|A_2|^2 + 6|A_3|^2) \right] A_1 + \frac{4\pi\omega_1^2}{c^2} \chi^{(3)} 6A_2 A_3 A_1^* e^{i(k_2+k_3-2k_1)z} \quad (\text{C.6})$$

In the plane wave ansatz $E(\omega_j) = A_j e^{ik_j z}$, fast oscillations are absorbed in the exponential term and A_j varies slowly as a function of z . In a linear medium, with $k_j = n(\omega_j) \frac{\omega_j}{c}$, A_j is actually a constant, and we use the same definition as a first-order approximation in the case of a nonlinear medium. The *slowly varying amplitude approximation* now neglects the second derivative $\frac{\partial^2 A_1}{\partial z^2}$, and the equation of motion reduces to

$$-2ik_1 \frac{\partial A_1}{\partial z} = \left[\frac{4\pi\omega_1^2}{c^2} \chi^{(3)} (3|A_1|^2 + 6|A_2|^2 + 6|A_3|^2) \right] A_1 + \frac{4\pi\omega_1^2}{c^2} \chi^{(3)} 6A_2 A_3 A_1^* e^{\frac{i}{c}(n(\omega_2)\omega_2 + n(\omega_3)\omega_3 - 2n(\omega_1)\omega_1)z} \quad (\text{C.7})$$

with the linear index of refraction $n = \sqrt{\epsilon^{(1)}}$. Without dispersion, i.e. if n does not depend on ω , the exponential drops out since $\omega_2 + \omega_3 - 2\omega_1 = 0$.

Similarly, equations for the mode A_2 can be derived,

$$-2ik_1 \frac{\partial A_2}{\partial z} = \left[\frac{4\pi\omega_2^2}{c^2} \chi^{(3)} (3|A_2|^2 + 6|A_1|^2 + 6|A_3|^2) \right] A_2 + \frac{4\pi\omega_1^2}{c^2} \chi^{(3)} 3A_1^2 A_2^* e^{-\frac{i}{c}(n(\omega_2)\omega_2 + n(\omega_3)\omega_3 - 2n(\omega_1)\omega_1)z}, \quad (\text{C.8})$$

and A_3 follows from swapping indices $2 \leftrightarrow 3$.

In the above equations, we have taken into account a possible dispersion in each individual wavenumber k_j . With this choice of k_j , $\epsilon^{(1)} \frac{\omega_j^2}{c^2} - k_j^2 = 0$ cancels in the equation of motion of all three modes, but at the cost of the non-vanishing exponent $n(\omega_2)\omega_2 + n(\omega_3)\omega_3 - 2n(\omega_1)\omega_1$.

Alternatively, we may as well choose $k_j = \bar{n} \frac{\omega_j}{c}$ with a constant average index of refraction $\bar{n} = \sqrt{\epsilon^{(1)}(\omega_1)}$. This way, a small part of the fast oscillation of the plane wave is shifted on to the amplitudes A_2 and A_3 . If the dispersion is small, however, this is just as good a first-order approximation as the first choice, and the variation of $A_2(z)$ and $A_3(z)$ is still slow. As a result, the exponential term vanishes, but at the cost of an additional term

$$\frac{\omega_m^2}{c^2} (\sqrt{\epsilon^{(1)}} - \bar{n}) A_m \quad (\text{C.9})$$

in the right-hand side of the equations of motion for $m = 2, 3$.

In the latter formulation, it becomes clear that dispersion, i.e. the variation of the linear index of refraction as a function of ω , plays the role of the *quadratic Zeeman effect* in spinor dynamics (Chapter 2). The mode A_1 , whose index of refraction serves as a reference, plays the role of the $m_F = 0$ spinor amplitude ζ_0 . The choice of $k_j = \bar{n} \frac{\omega_j}{c}$ in the plane wave ansatz is analogous to the transformation to a rotating frame in spinor dynamics, where Larmor rotation also drops out.

Bibliography

- [1] J. Kronjäger, C. Becker, P. Navez, K. Bongs and K. Sengstock. *Magnetically tuned spin dynamics resonance*. Phys. Rev. Lett. **97**, 110404 (2006). doi:10.1103/PhysRevLett.97.110404.
- [2] J. Kronjäger, C. Becker, M. Brinkmann, R. Walser, P. Navez, K. Bongs and K. Sengstock. *Evolution of a spinor condensate: Coherent dynamics, dephasing, and revivals*. Phys. Rev. A **72**, 063619 (2005). doi:10.1103/PhysRevA.72.063619.
- [3] M. Erhard, H. Schmaljohann, J. Kronjäger, K. Bongs and K. Sengstock. *Bose-Einstein condensation at constant temperature*. Phys. Rev. A **70**, 031602(R) (2004). doi:10.1103/PhysRevA.70.031602.
- [4] M. Erhard, H. Schmaljohann, J. Kronjäger, K. Bongs and K. Sengstock. *Measurement of a mixed-spin-channel Feshbach resonance in ^{87}Rb* . Phys. Rev. A **69**, 032705 (2004). doi:10.1103/PhysRevA.69.032705.
- [5] H. Schmaljohann, M. Erhard, J. Kronjäger, K. Bongs and K. Sengstock. *Dynamics and thermodynamics in spinor quantum gases*. Appl. Phys. B **79**, 1001 (2004). doi:10.1007/s00340-004-1664-6.
- [6] H. Schmaljohann, M. Erhard, J. Kronjäger, M. Kottke, S. van Staa, J. J. Arlt, K. Bongs and K. Sengstock. *Magnetism in ultracold quantum gases*. Journal of Modern Optics **51**, 1829 (2004). doi:10.1080/0950034042000200560.
- [7] H. Schmaljohann, M. Erhard, J. Kronjäger, M. Kottke, S. van Staa, L. Cacciapuoti, J. J. Arlt, K. Bongs and K. Sengstock. *Dynamics of $F = 2$ Spinor Bose-Einstein Condensates*. Phys. Rev. Lett. **92**, 040402 (2004). doi:10.1103/PhysRevLett.92.040402.
- [8] H. Schmaljohann, M. Erhard, J. Kronjäger, M. Kottke, S. van Staa, J. J. Arlt, K. Bongs and K. Sengstock. *Spin Evolution in Ultracold Quantum Gases*. Laser Physics **14**, 1252 (2004).
- [9] R. Gati, B. Hemmerling, J. Fölling, M. Albiez and M. K. Oberthaler. *Noise Thermometry with Two weakly Coupled Bose-Einstein condensates*. Phys. Rev. Lett. **96**, 130404 (2006). doi:10.1103/PhysRevLett.96.130404.
- [10] J. M. Obrecht, R. J. Wild, M. Antezza, L. P. Pitaevskii, S. Stringari and E. A. Cornell. *Measurement of the Temperature Dependence of the Casimir-Polder Force*. Phys. Rev. Lett. **98**, 063201 (2007). doi:10.1103/PhysRevLett.98.063201.

- [11] N. S. Ginsberg, S. R. Garner and L. V. Hau. *Coherent control of optical information with matter wave dynamics*. *Nature* **445**, 623 (2007). doi:10.1038/nature05493.
- [12] S. Tung, V. Schweikhard and E. A. Cornell. *Observation of Vortex Pinning in Bose-Einstein Condensates*. *Phys. Rev. Lett.* **97**, 240402 (2006). doi:10.1103/PhysRevLett.97.240402.
- [13] V. Schweikhard, I. Coddington, P. Engels, S. Tung and E. A. Cornell. *Vortex-Lattice Dynamics in Rotating Spinor Bose-Einstein Condensates*. *Phys. Rev. Lett.* **93**, 210403 (2004). doi:10.1103/PhysRevLett.93.210403.
- [14] V. Bretin, S. Stock, Y. Seurin and J. Dalibard. *Fast Rotation of a Bose-Einstein Condensate*. *Phys. Rev. Lett.* **92**, 050403 (2004). doi:10.1103/PhysRevLett.92.050403.
- [15] S. Fölling, F. Gerbier, A. Widera, O. Mandel, T. Gericke and I. Bloch. *Spatial quantum noise interferometry in expanding ultracold atom clouds*. *Nature* **434**, 481 (2005). doi:10.1038/nature03500.
- [16] M. Schellekens, R. Hoppeler, A. Perrin, J. V. Gomes, D. Boiron, A. Aspect and C. I. Westbrook. *Hanbury Brown Twiss Effect for Ultracold Quantum Gases*. *Science* **310**, 648 (2005). doi:10.1126/science.1118024.
- [17] W. Gerlach and O. Stern. *Der experimentelle Nachweis der Richtungsquantelung im Magnetfeld*. *Z. Phys. A* **9**, 349 (1922). doi:10.1007/BF01326983.
- [18] Wikipedia. *Stern-Gerlach-Versuch* — *Wikipedia, Die freie Enzyklopädie* (2007). URL <http://de.wikipedia.org/w/index.php?title=Stern-Gerlach-Versuch&oldid=31935845>. [Online; Stand 22. Mai 2007].
- [19] W. Heisenberg. *Zur Theorie des Ferromagnetismus*. *Z. Phys. A* **49**, 619 (1928). doi:10.1007/BF01328601.
- [20] D. M. Stamper-Kurn, M. R. Andrews, A. P. Chikkatur, S. Inouye, H.-J. Miesner, J. Stenger and W. Ketterle. *Optical Confinement of a Bose-Einstein Condensate*. *Phys. Rev. Lett.* **80**, 2027 (1998). doi:10.1103/PhysRevLett.80.2027.
- [21] T.-L. Ho. *Spinor Bose Condensates in Optical Traps*. *Phys. Rev. Lett.* **81**, 742 (1998). doi:10.1103/PhysRevLett.81.742.
- [22] T. Ohmi and K. Machida. *Bose-Einstein condensation with internal degrees of freedom in Alkali gases*. *J. Phys. Soc. Jap.* **67**, 1822 (1998). doi:10.1143/JPSJ.67.1822.
- [23] J. Stenger, S. Inouye, D. M. Stamper-Kurn, H.-J. Miesner, A. P. Chikkatur and W. Ketterle. *Spin domains in ground-state Bose-Einstein condensates*. *Nature* **396**, 345 (1998). doi:10.1038/24567.
- [24] H.-J. Miesner, D. M. Stamper-Kurn, J. Stenger, S. Inouye, A. P. Chikkatur and W. Ketterle. *Observation of Metastable States in Spinor Bose-Einstein Condensates*. *Phys. Rev. Lett.* **82**, 2228 (1999). doi:10.1103/PhysRevLett.82.2228.

- [25] C. J. Myatt, E. A. Burt, R. W. Christ, E. A. Cornell and C. E. Wieman. *Production of Two Overlapping Bose-Einstein condensates by sympathetic cooling*. Phys. Rev. Lett. **78**, 586 (1997). doi:10.1103/PhysRevLett.78.586.
- [26] D. S. Hall, M. R. Matthews, C. E. Wieman and E. A. Cornell. *Measurement of Relative Phase in Two-Component Bose-Einstein Condensates*. Phys. Rev. Lett. **81**, 1543 (1998). doi:10.1103/PhysRevLett.81.1543.
- [27] M. R. Matthews, B. P. Anderson, P. C. Haljan, D. S. Hall, M. J. Holland, J. E. Williams, C. E. Wieman and E. A. Cornell. *Watching a Superfluid Untwist Itself: Recurrence of Rabi Oscillations in a Bose-Einstein Condensate*. Phys. Rev. Lett **83**, 3358 (1999). doi:10.1103/PhysRevLett.83.3358.
- [28] H. J. Lewandowski, J. M. McGuirk, D. M. Harber and E. A. Cornell. *Decoherence-driven Cooling of a Degenerate Spinor Bose Gas*. Phys. Rev. Lett. **91**, 240404 (2003). doi:10.1103/PhysRevLett.91.240404.
- [29] H. J. Lewandowski, D. M. Harber, D. L. Whitaker and E. A. Cornell. *Observation of Anomalous Spin-State Segregation in a Trapped Ultracold Vapor*. Phys. Rev. Lett. **88**, 070403 (2002). doi:10.1103/PhysRevLett.88.070403.
- [30] J. M. McGuirk, H. J. Lewandowski, D. M. Harber, T. Nikuni, J. E. Williams and E. A. Cornell. *Spatial Resolution of Spin Waves in an Ultracold Gas*. Phys. Rev. Lett. **89**, 090402 (2002). doi:10.1103/PhysRevLett.89.090402.
- [31] J. M. McGuirk, D. M. Harber, H. J. Lewandowski and E. A. Cornell. *Normal-Superfluid Interaction Dynamics in a Spinor Bose Gas*. Phys. Rev. Lett. **91**, 150402 (2003). doi:10.1103/PhysRevLett.91.150402.
- [32] C. V. Ciobanu, S.-K. Yip and T.-L. Ho. *Phase diagrams of $F=2$ spinor Bose-Einstein condensates*. Phys. Rev. A **61**, 033607 (2000). doi:10.1103/PhysRevA.61.033607.
- [33] M. Koashi and M. Ueda. *Exact Eigenstates and Magnetic Response of Spin-1 and Spin-2 Bose-Einstein Condensates*. Phys. Rev. Lett. **84**, 1066 (2000). doi:10.1103/PhysRevLett.84.1066.
- [34] N. N. Klausen, J. L. Bohn and C. H. Greene. *Nature of spinor Bose-Einstein condensates in rubidium*. Phys. Rev. A **64**, 053602 (2001). doi:10.1103/PhysRevA.64.053602.
- [35] C. K. Law, H. Pu and N. P. Bigelow. *Quantum Spins mixing in spinor Bose-Einstein condensates*. Phys. Rev. Lett. **81**, 5257 (1998). doi:10.1103/PhysRevLett.81.5257.
- [36] H. Schmaljohann. *Spindynamik in Bose-Einstein Kondensaten*. Ph.D. thesis, Universität Hamburg (2004). urn:nbn:de:gbv:18-21508.
- [37] M.-S. Chang, C. D. Hamley, M. D. Barrett, J. A. Sauer, K. M. Fortier, W. Zhang, L. You and M. S. Chapman. *Observation of Spinor Dynamics in Optically trapped ^{87}Rb Bose-Einstein Condensates*. Phys. Rev. Lett. **92**, 140403 (2004). doi:10.1103/PhysRevLett.92.140403.

- [38] T. Kuwamoto, K. Araki, T. Eno and T. Hirano. *Magnetic field dependence of the dynamics of ^{87}Rb spin-2 Bose-Einstein condensates*. Phys. Rev. A **69**, 063604 (2004). doi:10.1103/PhysRevA.69.063604.
- [39] M. H. Wheeler, K. M. Mertes, J. D. Erwin and D. S. Hall. *Spontaneous Macroscopic Spin Polarization in Independent Spinor Bose-Einstein Condensates*. Phys. Rev. Lett. **93**, 170402 (2004). doi:10.1103/PhysRevLett.93.170402.
- [40] A. Griesmaier, J. Werner, S. Hensler, J. Stuhler and T. Pfau. *Bose-Einstein Condensation of Chromium*. Phys. Rev. Lett. **94**, 160401 (2005). doi:10.1103/PhysRevLett.94.160401.
- [41] L. E. Sadler, J. M. Higbie, S. R. Leslie, M. Vengalattore and D. M. Stamper-Kurn. *Spontaneous symmetry breaking in a quenched ferromagnetic spinor Bose-Einstein condensate*. Nature **443**, 312 (2006). doi:10.1038/nature05094.
- [42] J. Kobayashi, Y. Izumi, M. Kumakura and Y. Takahashi. *All-Optical Formation of Molecules with Spin Degree of Freedom in an Atomic Bose-Einstein Condensate*. Laser Physics **16**, 718 (2006). doi:10.1134/S1054660X06040293.
- [43] A. Widera, F. Gerbier, S. Fölling, T. Gericke, O. Mandel and I. Bloch. *Coherent Collisional Spin Dynamics in Optical lattices*. Phys. Rev. Lett. **95**, 190405 (2005). doi:10.1103/PhysRevLett.95.190405.
- [44] W. Zhang, D. L. Zhou, M.-S. Chang, M.-S. Chapman and L. You. *Dynamical instability and domain formation in a Spin-1 Bose-Einstein Condensate*. Phys. Rev. Lett. **95**, 180403 (2005). doi:10.1103/PhysRevLett.95.180403.
- [45] E. Müstecaplıoğlu, M. Zhang and L. You. *Nonlinear Dynamics of a Spinor Bose-Einstein Condensate in a Double-Well Potential*. Laser Physics **16**, 379 (2006). doi:10.1134/S1054660X06020319.
- [46] H. Saito, Y. Kawaguchi and M. Ueda. *Breaking of Chiral Symmetry and Spontaneous Rotation in a Spinor Bose-Einstein Condensate*. Phys. Rev. Lett. **96**, 065302 (2006). doi:10.1103/PhysRevLett.96.065302.
- [47] H. Saito, Y. Kawaguchi and M. Ueda. *Topological defect formation in a quenched ferromagnetic Bose-Einstein condensate*. Phys. Rev. A **75**, 013621 (2007). doi:10.1103/PhysRevA.75.013621.
- [48] L. I. Plimak, C. Weiß, R. Walser and W. P. Schleich. *Quantum dynamics of atomic coherence in a spin-1 condensate: Mean-field versus many-body simulations*. Opt. Comm. **264**, 311 (2006). doi:10.1016/j.optcom.2006.03.074.
- [49] F. Deuretzbacher, K. Bongs, K. Sengstock and D. Pfannkuche. *Evolution from a Bose-Einstein condensate to a Tonks-Girardeau gas: An exact diagonalization study*. Phys. Rev. A **75**, 013614 (2007). doi:10.1103/PhysRevA.75.013614.
- [50] M.-S. Chang, Q. Qin, W. Zhang, L. You and M. S. Chapman. *Coherent spinor dynamics in a spin-1 Bose condensate*. Nature Phys. **1**, 111 (2005). doi:10.1038/nphys153.

- [51] F. Dalfovo, S. Giorgini, L. P. Pitaevskii and S. Stringari. *Theory of Bose-Einstein condensation in trapped gases*. Rev. Mod. Phys. **71**, 463 (1999). doi:10.1103/RevModPhys.71.463.
- [52] C. J. Pethick and H. Smith. *Bose-Einstein Condensation in Dilute Gases*. Cambridge University Press (2002).
- [53] L. Pitaevskii and S. Stringari. *Bose-Einstein Condensation*. Oxford University Press (2003).
- [54] D. S. Hall, M. R. Matthews, J. R. Ensher, C. E. Wieman and E. A. Cornell. *Dynamics of Component Separation in a Binary Mixture of Bose-Einstein Condensates*. Phys. Rev. Lett. **81**, 1539 (1998). doi:10.1103/PhysRevLett.81.1539.
- [55] G. Modugno, M. Modugno, F. Riboli, G. Roati and M. Inguscio. *Two Atomic Species Superfluid*. Phys. Rev. Lett. **89**, 190404 (2002). doi:10.1103/PhysRevLett.89.190404.
- [56] T. Mayer-Kuckuk. *Atomphysik*. Teubner, Stuttgart (1997).
- [57] M. Erhard. *Experimente mit mehrkomponentigen Bose-Einstein-Kondensaten*. Ph.D. thesis, Universität Hamburg (2004). urn:nbn:de:gbv:18-22619.
- [58] L. Allen and J. H. Eberly. *Optical Resonance and Two-Level Atoms*. Dover Publications (1987).
- [59] C. Cohen-Tannoudji, B. Diu and F. Laloë. *Quantum Mechanics*. John Wiley and Sons (1997).
- [60] I. I. Rabi. *Space Quantization in a Gyration Magnetic Field*. Phys. Rev. **51**, 652 (1937). doi:10.1103/PhysRev.51.652.
- [61] N. F. Ramsey. *A Molecular Beam Resonance Method with Separated Oscillating Fields*. Phys. Rev. **78**, 695 (1950). doi:10.1103/PhysRev.78.695.
- [62] J. Mathews and R. L. Walker. *Mathematical Methods of Physics*. Addison-Wesley, 2nd edition (1970).
- [63] F. T. Hioe and J. H. Eberly. *N-Level Coherence Vector and Higher Conservation Laws in Quantum Optics and Quantum Mechanics*. Phys. Rev. Lett. **47**, 838 (1981). doi:10.1103/PhysRevLett.47.838.
- [64] G. Kimura. *The Bloch-Vector Space for N-Level Systems: the Spherical-Coordinate Point of View*. Open Sys. & Information Dyn. **12**, 207 (2005). doi:10.1007/s11080-005-0919-y.
- [65] K. Dietz. *Generalized Bloch spheres for m-qubit states*. J. Phys. A: Math. Gen. **39**, 1433 (2006). doi:10.1088/0305-4470/39/6/016.
- [66] S. Kryszewski and M. Zachcial. *Positivity of the $N \times N$ density matrix expressed in terms of polarization operators*. J. Phys. A: Math. Gen. **39**, 5921 (2006). doi:10.1088/0305-4470/39/20/019.

- [67] G. Lindblad. *On the Generators of Quantum Dynamical Semigroups*. Comm. Math. Phys. **48**, 119 (1976). doi:10.1007/BF01608499.
- [68] R. Alicki and K. Lendi. *Quantum Dynamical Semigroups and Applications*, volume 286 of *Lecture Notes in Physics*. Springer-Verlag, Berlin (1987).
- [69] D. Salgado and J. L. Sánchez-Goméz. *A formula for the Bloch vector of some Lindblad quantum systems*. Phys. Lett. A **323**, 365 (2004). doi:10.1016/j.physleta.2004.02.006.
- [70] A. Buchleitner and K. Hornberger (editors). *Coherent Evolution in Noisy Environments*, volume 611 of *Lecture Notes in Physics*. Springer-Verlag, Berlin (2002).
- [71] D. Salgado and J. L. Sánchez-Goméz. *Lindbladian evolution with self-adjoint Lindblad Operators as Averaged Random Unitary Evolution* (2002). arXiv:quant-ph/0208175v1.
- [72] Wikipedia. *Gell-Mann matrices — Wikipedia, The Free Encyclopedia* (2006). URL http://en.wikipedia.org/w/index.php?title=Gell-Mann_matrices&oldid=88095021. [Online; accessed 22-May-2007].
- [73] S. Yi, Ö. E. Müstecaplıoğlu, C. P. Sun and L. You. *Single-mode approximation in a spinor-1 atomic condensate*. Phys. Rev. A **66**, 011601(R) (2002). doi:10.1103/PhysRevA.66.011601.
- [74] P. Navez. Private communication.
- [75] W. Zhang, D. L. Zhou, M.-S. Chang, M.-S. Chapman and L. You. *Coherent spin mixing dynamics in a spin-1 atomic condensate*. Phys. Rev. A **72**, 013602 (2005). doi:10.1103/PhysRevA.72.013602.
- [76] H. Saito and M. Ueda. *Diagnostics for the ground-state phase of a spin-2 Bose-Einstein condensate*. Phys. Rev. A **72**, 053628 (2005). doi:10.1103/PhysRevA.72.053628.
- [77] T. Isoshima, K. Machida and T. Ohmi. *Spin-domain formation in spinor Bose-Einstein condensation*. Phys. Rev. A **60**, 4857 (1999). doi:10.1103/PhysRevA.60.4857.
- [78] A. Widera, F. Gerbier, S. Fölling, T. Gericke, O. Mandel and I. Bloch. *Precision measurement of spin-dependent interaction strengths for spin-1 and spin-2 ^{87}Rb atoms*. New Journal of Physics **8**, 152 (2006). doi:10.1088/1367-2630/8/8/152.
- [79] E. G. M. van Kempen, S. J. J. M. F. Kokkelmans, D. J. Heinzen and B. J. Verhaar. *Interisotope determination of ultracold rubidium interactions from three high-precision experiments*. Phys. Rev. Lett. **88**, 093201 (2002). doi:10.1103/PhysRevLett.88.093201.
- [80] I. N. Bronstein, K. A. Semendjajew, G. Musiol and H. Mühlig. *Taschenbuch der Mathematik*. Verlag Harri Deutsch (2001).
- [81] L. Deng, E. W. Haley, J. Wen, M. Trippenbach, Y. Band, P. S. Julienne, J. E. Simsarian, K. Helmerson, S. L. Rolston and W. D. Phillips. *Four-wave mixing with matter waves*. Nature **398**, 218 (1999). doi:10.1038/18395.

- [82] J. J. P. Burke, P. S. Julienne, C. J. Williams, Y. B. Band and M. Trippenbach. *Four-Wave Mixing in Bose-Einstein condensate systems with multiple spin states*. Phys. Rev. A **70**, 033606 (2004). doi:10.1103/PhysRevA.70.033606.
- [83] E. V. Goldstein and P. Meystre. *Quantum theory of atomic four-wave mixing in Bose-Einstein condensates*. Phys. Rev. A **59**, 3896 (1999). doi:10.1103/PhysRevA.59.3896.
- [84] R. W. Boyd. *Nonlinear Optics*. Academic Press, Boston (1992).
- [85] P. G. Kevrekidis and D. J. Frantzeskakis. *Pattern forming dynamical instabilities of Bose-Einstein condensates*. Modern Physics Letters B **18**, 173 (2004). doi:10.1142/S0217984904006809.
- [86] E. V. Goldstein and P. Meystre. *Quasiparticle instabilities in multicomponent atomic condensates*. Phys. Rev. A **55**, 2935 (1997). doi:10.1103/PhysRevA.55.2935.
- [87] L. D. Carr and J. Brand. *Spontaneous Soliton Formation and Modulational Instability in Bose-Einstein Condensates*. Phys. Rev. Lett. **92**, 040401 (2004). doi:10.1103/PhysRevLett.92.040401.
- [88] K. Kasamatsu and M. Tsubota. *Multiple Domain Formation Induced by Modulation Instability in Two-Component Bose-Einstein Condensates*. Phys. Rev. Lett. **93**, 100402 (2004). doi:10.1103/PhysRevLett.93.100402.
- [89] N. P. Robins, W. Zhang, E. A. Ostrovskaya and Y. S. Kivshar. *Modulational instability of spinor condensates*. Phys. Rev. A **64**, 021601(R) (2001). doi:10.1103/PhysRevA.64.021601.
- [90] H. Saito and M. Ueda. *Spontaneous magnetization and structure formation in a spin-1 ferromagnetic Bose-Einstein condensate*. Phys. Rev. A **72**, 023610 (2005). doi:10.1103/PhysRevA.72.023610.
- [91] H. Pu, C. K. Law, S. Raghavan, J. H. Eberly and N. P. Bigelow. *Spin-mixing dynamics of a spinor Bose-Einstein condensate*. Phys. Rev. A **60**, 1463 (1999). doi:10.1103/PhysRevA.60.1463.
- [92] W. Zhang and L. You. *An effective quasi-one-dimensional description of a spin-1 atomic condensate*. Phys. Rev. A **71**, 025603 (2005). doi:10.1103/PhysRevA.71.025603.
- [93] J. Mur-Petit, M. Guilleumas, A. Polls, A. Sanpera and M. Lewenstein. *Dynamics of $F = 1$ ^{87}Rb condensates at finite temperature*. Phys. Rev. A **73**, 013629 (2006). doi:10.1103/PhysRevA.73.013629.
- [94] J.-P. Martikainen and K.-A. Suominen. *Collective excitations in an $F = 2$ Bose-Einstein condensate*. J. Phys. B **34**, 4091 (2001). doi:10.1088/0953-4075/34/21/302.
- [95] M. Ueda. Unpublished.
- [96] C. A. Sackett, J. M. Gerton, M. Welling and R. G. Hulet. *Measurements of Collective Collapse in a Bose-Einstein Condensate*. Phys. Rev. Lett. **82**, 876 (1999). doi:10.1103/PhysRevLett.82.876.

- [97] J. M. Gerton, D. Strekalov, I. Prodan and R. G. Hulet. *Direct observation of growth and collapse of a Bose-Einstein condensate with attractive interactions*. Nature **408**, 692 (2000). doi:10.1038/35047030.
- [98] E. A. Donley, N. R. Claussen, S. L. Cornish, J. L. Roberts, E. A. Cornell and C. E. Wieman. *Dynamics of collapsing and exploding Bose-Einstein condensates*. Nature **412**, 295 (2001).
- [99] K. E. Strecker, G. B. Partridge, A. G. Truscott and R. G. Hulet. *Formation and propagation of matter-wave soliton trains*. Nature **417**, 150 (2002). doi:10.1038/nature747.
- [100] L. Khaykovich, F. Schreck, G. Ferrari, T. Bourdel, J. Cubizolles, L. D. Carr, Y. Castin and C. Salomon. *Formation of a Matter-Wave Bright Soliton*. Science **296**, 1290 (2002). doi:10.1126/science.1071021.
- [101] J. M. Higbie, L. E. Sadler, A. P. Chikkatur, S. R. Leslie, K. L. Moore, V. Savalli and D. M. Stamper-Kurn. *Direct Nondestructive Imaging of Magnetization in a Spin-1 Bose-Einstein Gas*. Phys. Rev. Lett. **95**, 050401 (2005). doi:10.1103/PhysRevLett.95.050401.
- [102] R. Grimm, M. Weidemüller, and Y. Ovchinnikov. *Optical dipole traps for neutral atoms*. Adv. At. Mol. Opt. Phys. **42**, 95 (2000). arXiv:physics/9902072v1.
- [103] S. van Staa. *Entwicklung und Realisierung einer optischen Dipolfalle für ^{87}Rb Bose-Einstein Kondensate*. Diplomarbeit, Universität Hamburg (2003).
- [104] S. Schnelle. *Aufbau eines optischen Gitters für ein ^{87}Rb Spinor-Bose-Einstein-Kondensat*. Diplomarbeit, Universität Hamburg (2006).
- [105] C. Becker. *n/a*. Ph.D. thesis, Universität Hamburg (to be published).
- [106] T. A. Savard, K. M. O'Hara and J. E. Thomas. *Laser-noise-induced heating in far-off resonance optical traps*. Phys. Rev. A **56**, R1095 (1997). doi:10.1103/PhysRevA.56.R1095.
- [107] W. Ketterle, D. S. Durfee and D. M. Stamper-Kurn. *Making, probing and understanding Bose-Einstein condensates*. In M. Inguscio, S. Stringari and C. E. Wieman (editors), *Proceedings of the International School of Physics - Enrico Fermi*, 67. IOS Press (1999). arXiv:cond-mat/9904034.
- [108] H. F. Hofmann and S. Takeuchi. *Quantum-State tomography for spin-1 systems*. Phys. Rev. A **69**, 042108 (2004). doi:10.1103/PhysRevA.69.042108.
- [109] G. Klose, G. Smith and P. S. Jessen. *Measuring the Quantum State of a Large Angular Momentum*. Phys. Rev. Lett. **86**, 4721 (2001). doi:10.1103/PhysRevLett.86.4721.
- [110] T. Garl. *Aufbau eines Bragg-Lasersystems für Kohärenzuntersuchungen an Spinor-Bose-Einstein Kondensaten*. Diplomarbeit, Universität Hamburg (2004).
- [111] L. Neumann. *Hochauflösende Detektion von Bose-Einstein Kondensaten*. Diplomarbeit, Universität Hamburg (2006).

- [112] M. Brinkmann. *Optimierung der Detektion und Auswertung von ^{87}Rb -Spinor-Kondensaten*. Diplomarbeit, Universität Hamburg (2005).
- [113] Wikipedia. *Erdmagnetfeld* — *Wikipedia, Die freie Enzyklopädie* (2007). URL <http://de.wikipedia.org/w/index.php?title=Erdmagnetfeld&oldid=28405284>. [Online; Stand 22. Mai 2007].
- [114] L. M. K. Vandersypen and I. L. Chuang. *NMR techniques for quantum control and computation*. *Rev. Mod. Phys.* **76**, 1037 (2005). doi:10.1103/RevModPhys.76.1037.
- [115] S. Ospelkaus and C. Ospelkaus. Private communication.
- [116] L. I. Goldfischer. *Autocorrelation Function and Power Spectral Density of Laser-Produced Speckle Patterns*. *J. Opt. Soc. Am* **55**, 247 (1965). URL <http://www.opticsinfobase.org/abstract.cfm?URI=josa-55-3-247>.
- [117] J. W. Goodman. *Some fundamental properties of speckle*. *J. Opt. Soc. Am* **66**, 1145 (1976). URL <http://www.opticsinfobase.org/abstract.cfm?URI=josa-66-11-1145>.
- [118] J. Schumacher. Private communication.
- [119] K. Toyoda, Y. Takahashi, K. Ishikawa and T. Yabuzaki. *Optical free-induction decay of laser-cooled ^{85}Rb* . *Phys. Rev. A* **56**, 1564 (1997). doi:10.1103/PhysRevA.56.1564.
- [120] A. Dingjan, B. Darquié, J. Beugnon, M. Jones, S. Bergamini, G. Messin, A. Browaeys and P. Grangier. *A frequency-doubled laser system producing ns pulses for rubidium manipulation*. *Appl. Phys. B* **82**, 47 (2006). doi:10.1007/s00340-005-2027-7.
- [121] B. Darquié, M. P. Jones, J. Dingjan, J. Beugnon, S. Bergamini, Y. Sortais, G. Messin, A. Browaeys and P. Grangier. *Controlled Single-Photon Emission from a Single Trapped Two-Level Atom*. *Science* **309**, 454 (2005). doi:10.1126/science.1113394.
- [122] S. Burger, K. Bongs, S. Dettmer, W. Ertmer and K. Sengstock. *Dark Solitons in Bose-Einstein Condensates*. *Phys. Rev. Lett.* **83**, 5198 (1999). doi:10.1103/PhysRevLett.83.5198.
- [123] J. Denschlag, J. E. Simsarian, D. L. Feder, C. W. Clark, L. A. Collins, J. Cubizolles, L. Deng, E. W. Hagley, K. Helmerson, W. P. Reinhardt, S. L. Rolston, B. I. Schneider and W. D. Phillips. *Generating Solitons by Phase Engineering of a Bose-Einstein Condensate*. *Science* **287**, 97 (2000). doi:10.1126/science.287.5450.97.
- [124] T. Anker, M. Albiez, R. Gati, S. Hunsmann, B. Eiermann, A. Trombettoni and M. K. Oberthaler. *Nonlinear Self-Trapping of Matter-Waves in Periodic Potentials*. *Phys. Rev. Lett.* **94**, 020403 (2005). doi:10.1103/PhysRevLett.94.020403.
- [125] T. Busch and J. R. Anglin. *Dark-Bright Solitons in Inhomogenous Bose-Einstein Condensates*. *Phys. Rev. Lett.* **87**, 010401 (2001). doi:10.1103/PhysRevLett.87.010401.

- [126] M. Prevedelli, T. Freearge and T. W. Hänsch. *Phase locking of grating-tuned diode lasers*. Appl. Phys. B **60**, S241 (1995).
- [127] R. Wynands and A. Nagel. *Precision spectroscopy with coherent dark states*. Appl. Phys. B **68**, 1 (1999). doi:10.1007/s003400050581.
- [128] L. Cacciapuoti, M. de Angelis, M. Fattori, G. Lamporesi, T. Petelski, M. Prevedelli, J. Stuhler and G. M. Tino. *Analog+digital phase and frequency detector for phase locking of diode lasers*. Rev. Sci. Instr. **76**, 053111 (2005). doi:10.1063/1.1914785.
- [129] Analog Devices. *Ultrahigh Speed Phase/Frequency discriminator AD9901 (Rev. B)* (1999). URL http://www.analog.com/UploadedFiles/Data_Sheets/AD9901.pdf.
- [130] H. Richter. *Phasenstabilisiertes Diodenlasersystem zur Dunkelresonanzspektroskopie an ^{85}Rb* . Diplomarbeit, Universität Hamburg (2002).
- [131] M. Chwalla. *Ein phasenstabilisiertes Diodenlaser-System bei 780 nm zur Spektroskopie an ^{87}Rb -Atomen*. Diplomarbeit, Universität Innsbruck (2002).
- [132] F. G. A. Widera, S. Fölling, O. Mandel and I. Bloch. *Resonant Control of spin dynamics in ultracold quantum gases by microwave dressing*. Phys. Rev. A. **73**, 041602(R) (2006). doi:10.1103/PhysRevA.73.041602.
- [133] H.-J. Miesner, D. M. Stamper-Kurn, M. R. Andrews, D. S. Durfee, S. Inouye and W. Ketterle. *Bosonic Stimulation in the Formation of a Bose-Einstein Condensate*. Science **279**, 1005 (1998). doi:10.1126/science.279.5353.1005.
- [134] M. Köhl, M. J. Davis, C. W. Gardiner, T. W. Hänsch and T. Esslinger. *Growth of Bose-Einstein Condensates from Thermal Vapor*. Phys. Rev. Lett. **88**, 080402 (2002). doi:10.1103/PhysRevLett.88.080402.
- [135] C. W. Gardiner, P. Zoller, R. J. Ballagh and M. J. Davis. *Kinetics of Bose-Einstein Condensation in a Trap*. Phys. Rev. Lett. **79**, 1793 (1997). doi:10.1103/PhysRevLett.79.1793.
- [136] H.-O. Peitgen, H. Jürgens and D. Saupe. *Chaos and Fractals*. Springer-Verlag (1992).
- [137] H. G. Schuster. *Deterministic Chaos*. VCH Verlagsgesellschaft, Weinheim (1988).
- [138] M. V. Berry. *Regular and Irregular Motion*. In S. Jorna (editor), *Topics in Nonlinear Dynamics*, volume 46 of *Am. Inst. Phys. Conf. Proc.* (1978).
- [139] R. H. G. Helleman. *Self-Generated Chaotic Behaviour in Nonlinear Mechanics*. In E. G. D. Cohen (editor), *Fundamental problems in Statistical Mechanics*, volume 5. North-Holland Publ., Amsterdam (1980).
- [140] L. Fallani, J. E. Lye, V. Guarrera, C. Fort and M. Inguscio. *Ultracold Atoms in a Disordered Crystal of Light: Towards a Bose Glass*. Phys. Rev. Lett. **98**, 130404 (2007). doi:10.1103/PhysRevLett.98.130404.
- [141] H.-J. Stöckmann. *Quantum Chaos. An Introduction*. Cambridge University Press, Cambridge (1999).

- [142] W. Zhang and L. You. *Bose-Einstein Condensation of trapped interacting spin-1 atoms*. Phys. Rev. A **70**, 043611 (2004). doi:10.1103/PhysRevA.70.043611.
- [143] U. A. Khawaja and H. Stoof. *Skyrmions in a ferromagnetic Bose-Einstein condensate*. Nature **411**, 918 (2001). doi:10.1038/35082010.
- [144] J.-P. Martikainen and K.-A. Suominen. *Creation of a Monopole in a Spinor Condensate*. Phys. Rev. Lett. **88**, 090404 (2002). doi:10.1103/PhysRevLett.88.090404.
- [145] A. E. Leanhardt, Y. Shin, D. Kielpinski, D. E. Pritchard and W. Ketterle. *Coreless Vortex Formation in a Spinor Bose-Einstein Condensate*. Phys. Rev. Lett. **90**, 140403 (2003). doi:10.1103/PhysRevLett.90.140403.
- [146] G. W. Semenoff and F. Zhou. *Discrete Symmetries and 1/3-Quantum Vortices in Condensates of $F = 2$ Cold Atoms*. Phys. Rev. Lett. **98**, 100401 (2007). doi:10.1103/PhysRevLett.98.100401.
- [147] D. Jaksch, C. Bruder, J. I. Cirac, C. W. Gardiner and P. Zoller. *Cold Bosonic Atoms in Optical Lattices*. Phys. Rev. Lett. **81**, 3108 (1998). doi:10.1103/PhysRevLett.81.3108.
- [148] M. Greiner, O. Mandel, T. Esslinger, T. Hänsch and I. Bloch. *Quantum phase transition from a superfluid to a Mott insulator in a gas of ultracold atoms*. Nature **415**, 39 (2002). doi:10.1038/415039a.
- [149] L. Santos, M. A. Baranov, J. I. Cirac, H.-U. Everts, H. Fehrmann and M. Lewenstein. *Atomic Quantum Gases in Kagomé Lattices*. Phys. Rev. Lett. **93**, 030601 (2004). doi:10.1103/PhysRevLett.93.030601.
- [150] M. Vengalattore, J. M. Higbie, S. R. Leslie, J. Guzman, L. E. Sadler and D. M. Stamper-Kurn. *High-Resolution Magnetometry with a Spinor Bose-Einstein Condensate*. Phys. Rev. Lett. **98**, 200801 (2007). doi:10.1103/PhysRevLett.98.200801.
- [151] P. Cvitanović, R. Artuso, R. Mainieri, G. Tanner, G. Vattay, N. Whelan and A. Wirzba. *Classical and Quantum Chaos (version 11)*. chaosbook.org <http://www.chaosbook.org/> (2004).

Danksagung

Diese Doktorarbeit wäre ohne die andauernde Unterstützung durch sämtliche Mitglieder der Arbeitsgruppe “Kalte Quantengase” nicht möglich gewesen. Ich möchte mich an dieser Stelle bei einigen Menschen namentlich bedanken, die besondere Aufmerksamkeit verdienen.

An erster Stelle steht dabei Klaus Sengstock, der als Gruppenleiter nicht nur für ein Labor und meine Bezahlung gesorgt hat, sondern auch in häufigen Diskussionen seine Gedanken beisteuerte. Das gleiche gilt für Kai Bongs, der daneben noch mehrfach die undankbare Aufgabe übernommen hat, unsere Ergebnisse werbewirksam und gleichzeitig politisch korrekt zu formulieren.

Michael Erhard und Holger Schmaljohann haben mir beigebracht, wie man Dinge gut macht – und nicht am Wochenende. Sie haben mir ein wohldurchdachtes und gut funktionierendes Experiment hinterlassen, das nur leider am falschen Ort stand. Immerhin, wir hatten eine schöne Zeit in der Jungiusstrasse (und sie haben beim Packen geholfen).

Silke und Christian Ospelkaus haben viele Schaltpläne von Holger und Michael geerbt, als sie ihr enorm erfolgreiches Bose-Fermi-Mischungs-Experiment aufgebaut haben, und haben sie mir in Form von hübschen Geräten, fertig zum Einbau, zurückgegeben. Mit ihrer unermüdlichen Hilfsbereitschaft haben sie mir das Leben des öfteren beträchtlich leichter gemacht.

Christoph Becker war seit dem Umzug in unser neues Labor mein Kollege und Freund, und war in der einen oder anderen Weise an schlicht sämtlichen Ergebnissen dieser Arbeit beteiligt, sei es im Labor oder im Gespräch. Ich schätze mich glücklich, in ihm einen Partner gehabt zu haben, der meine Vorstellungen von “Guter Praxis” geteilt hat. Obwohl ich es leider nie geschafft habe, Christoph mit der Elektronik zu befreunden, schätze ich doch seinen Versuch. Ich denke, mit mir und seinem Musikgeschmack ist es gerade umgekehrt.

Reinhard Mielck hat nicht nur immer sofort geholfen, wenn ich ihn gebeten habe, sondern sich auch sehr für seine Arbeit engagiert. Abgesehen davon hatte er immer ein paar aufmunternde Worte für mich übrig und ein gutes Gespür dafür, wann die nötig waren.

Victoria Romano hat sich zuverlässig um Papierkram, Abrechnungen und alles andere, was unter meiner Konfusion hätte leiden können, gekümmert. Im übrigen hatte sie ihre eigene Art, mich aufzuheitern, wenn sie sich auf leidenschaftliche Diskussionen mit Christoph eingelassen hat.

Ein besonderer Dank gilt Sibylle, Silke, Christian und Christoph für das Korrekturlesen meiner Arbeit. Ohne ihre Mühe hätte ich viele Inkonsistenzen und Sprachfehler sicher übersehen.

Ich möchte auch all denen danken, die für mich da waren, als ich sie brauchte. Besonders danke ich Frauke, für die zahlreichen elektronischen Unterhaltungen über Gott und die Welt (meist aber doch eher allzu Menschliches). Ebenso danke ich allen, die die Jahre in Hamburg zu einer schönen Zeit für mich gemacht haben.

Am Ende möchte ich meinen Eltern danken, die mich über die Jahre (eine ganze Menge Jahre) zuversichtlich unterstützt haben und die irgendwie immer wussten, wenn mal wieder eine Lieferung Schokolade nötig war.

Acknowledgments

This work would not have been possible without the continuing support by all members of the Quantum Gases Group. I would like to point out a few persons deserving special attention.

First of all, Klaus Sengstock as the head of the group not only provided laboratories and financing, but also contributed his thoughts in numerous discussions. The same applies to Kai Bongs, who also took over the laborious task of casting our results into eye-catching yet politically correct language for publication.

Michael Erhard and Holger Schmaljohann taught me how to do things well and not on a weekend, and they left me with a well thought-out and well working experiment, unfortunately in the wrong place. We had a very enjoyable time at Jungiusstraße 9 (and they did help with packing).

Silke and Christian Ospelkaus, building up their extraordinarily successful Bose-Fermi mixture apparatus, inherited lots of design ideas from Holger and Michael and gave them back to me as ready-to-use computer-designed gadgets. Always willing to help out, they have made my life a great deal easier on many occasions.

Christoph Becker has been my colleague and friend since we moved to our new laboratories, and has contributed to all of the results in this thesis in some way or another, be it in the lab or in discussions. I'm lucky to have had him as a partner, sharing my notions of what is "good practice". Unfortunately, I never managed to really bring electronics home to Christoph, but I proudly acknowledge his attempt. I guess it's just vice-versa with me and his taste of music.

Reinhard Mielck not only helped promptly whenever he was asked, but also took interest in everything he did, and did a good job. Besides, he was always able to cheer me up – and had a good sense for these moments.

Victoria Romano always trustily took care of paperwork and reimbursements, and had her own way of cheering me up by engaging in a fierce discussion with Christoph.

I'm grateful to Sibylle, Silke, Christian and Christoph for proof-reading my thesis. Many inconsistencies and bad language would have gone through unnoticed without their mindful reading.

I would also like to thank those who stood by me when I needed them – I appreciate particularly the numerous electronic conversations I had with Frauke on sometimes more but often less varying topics. Likewise, I'm grateful to all who made the past years a time of my life.

Finally, I would like to thank my parents for their confident support over the years (quite a lot of years) – somehow, they always knew when I was in desperate need of chocolate.

Errata

Section 2.3.3: In Tab. 2.2 on page 27, the numerical value as well as the units of the constant $4\pi a_B \hbar/m$ are wrong. The correct value is $4\pi a_B \hbar/m = 2\pi \times 7.73 \times 10^{-14} \text{ Hz cm}^3$. Note that the *correct* value has been used in Chapter 5, e.g. in Fig. 5.10.

This error has been corrected in the online version of this thesis.